Universidade de Brasília
Instituto de Geociências
Programa de Pós-graduação em Geologia

EMBASAMENTO PRÉ-MESOZOICO DOS TERRENOS AREQUIPA E ANTOFALLA: IMPLICAÇÕES GEODINÂMICAS E GERAÇÃO DE ARCOS MAGMÁTICOS NA REGIÃO BOLÍVIA-CHILE.

AREQUIPA AND ANTOFALLA TERRAINS PRE-MESOZOIC BASEMENT: GEODYNAMIC IMPLICATIONS AND GENERATION OF MAGMATIC ARCS IN THE BOLIVIA-CHILE REGION.

JULIANA REZENDE DE OLIVEIRA

Tese de doutorado N° 189

Orientadora: Prof. Drª. Natalia Hauser

Co-orientador: Prof. Dr. Amarildo Salina Ruiz

Brasília, 02/09/2022

Universidade de Brasília
Instituto de Geociências
Programa de Pós-graduação em Geologia

EMBASAMENTO PRÉ-MESOZOICO DOS TERRENOS AREQUIPA E ANTOFALLA: IMPLICAÇÕES GEODINÂMICAS E GERAÇÃO DE ARCOS MAGMÁTICOS NA REGIÃO BOLÍVIA-CHILE.

AREQUIPA AND ANTOFALLA TERRAINS PRE-MESOZOIC BASEMENT: GEODYNAMIC IMPLICATIONS AND GENERATION OF MAGMATIC ARCS IN THE BOLIVIA-CHILE REGION.

JULIANA REZENDE DE OLIVEIRA

Tese apresentada ao Programa de Pós-Graduação em Geologia – Instituto de Geociências – IG da Universidade de Brasília – UnB como requisito parcial obrigatório para a obtenção do título de Doutora em Geologia.

Área de concentração: Geologia Regional

Orientador: Prof. Drª. Natalia Hauser

Comissão Examinadora:

Prof. Dr. Luís Gustavo Ferreira Viegas (IG/UnB)

Prof. Dr. César Casquet Martín (IGEO, CSIC);

Prof. Dr. Victor Alberto Ramos (FCEN/ CONICET);

Prof. Dr. Catarina Laboure Bemfica Toledo (Suplente IG/UnB);

Re REZENDE DE OLIVEIRA, JULIANA
Embasamento pré-mesozoico dos terrenos Arequipa e Antofalla: Implicações geodinâmicas e geração de arcos magmáticos na região Bolívia-Chile / JULIANA REZENDE DE OLIVEIRA; orientador Natalia Hauser; co-orientador Amarildo Salina Ruiz. -- Brasília, 2022. 175 p.

Tese(Doutorado em Geologia) -- Universidade de Brasília, 2022.

1. Complexo Metamórfico Cerro Uyarani. 2. Complexo metamórfico Belén. 3. U-Pb/Hf em zircão. 4. Orogenia Sunsas Grenville. I. Hauser, Natalia, orient. II. Salina Ruiz, Amarildo, co-orient. III. Título.

AGRADECIMENTOS

Dedico todo o trabalho e o título de doutora aos meus pais, Reginaldo e Rose, vocês sempre foram e são até hoje o meu pilar, em meio a tantas alegrias e dificuldades que vivemos juntos durante a vida, o doutorado foi a jornada mais longa e exaustiva para mim. Agradeço o amor, paciência, suporte, abraços, colo, amizade e confiança de vocês em mim, mesmo quando eu mesma não acreditava. Foi me espelhando em vocês e colocando em prática tudo o que me ensinaram sobre ética, amor, responsabilidade, dedicação e fé que cheguei até aqui. Vocês me presentearam com uma família maravilhosa de avós, tios e primos que me amam e me amparam, obrigada!

Agradeço de todo coração aos meus amigos de Cuiabá-MT, mas principalmente à Sthephanny e Syrham por todo carinho e apoio dedicado a mim, que mesmo longe estiveram muito presentes. Agradeço também às tantas amizades construídas em Brasília, em especial a Carol, Frankie, Gabi, Jeninha, Lulu, Marina, Seba, Thassio e Well, vocês foram e são essenciais na minha vida. Faço aqui um agradecimento especialmente ao Pedro Cordeiro e ao Thassio Werlang. Pedro, por tantas discussões sobre a geologia das áreas, pelo apoio, amizade e carinho. Thassio, meu amigo, meu irmão, minha família, que me ajudou tantas e tantas vezes, que me acolheu e sempre fez com que eu me sentisse em casa, mesmo estando muito longe de lá.

Agradeço muito a todos os professores que me acompanharam até aqui! Especialmente aos meus queridos professores da UFMT Amarildo, Maria Zélia e Maria Eliza, que na graduação e mestrado me ensinaram e ajudaram tanto. Minha orientadora Natalia que mesmo diante das circunstâncias desfavoráveis se dedicou nessa parceria de tese. Aos técnicos dos laboratórios da UnB pela assistência na preparação e análise das amostras.

O presente trabalho foi realizado com apoio da Coordenação de Aperfeiçoamento de Pessoal de Nível Superior-Brasil (CAPES) – Código de Financiamento 001.

“...a gente já se acostumou que a alegria pode ser breve
Mostre o sorriso, tenha juízo, a inveja tem sono leve
A espreita pesadelos são como desfiladeiros, chão em brasa
Nunca se esqueça o caminho de casa”.

Emicida (Leandro Roque de Oliveira)

RESUMO

Na região dos Andes Centrais, especificamente na costa oeste da América do Sul, duas exposições do embasamento pré-andino, uma no Cerro Uyarani, na Bolivia e outra perto de Belén, no Chile, registram a história tectono-magmática e metamórfica do Paleoproterozoico, Mesoproterozoico a Neoproterozoico e Ordoviciano do embasamento pre-gondwanico. O estudo destas áreas de suma importância pois nestes terrenos está registrada a história de evolução da parte oeste da América do sul. O embasamento Paleoproterozoico do terreno Arequipa (18ºS a 14ºS) ocorre desde a costa oeste do Peru até o Altiplano boliviano. Este embasamento está exposto no Cerro Uyarani, no departamento de Oruro, Bolívia. O Complexo Metamórfico Cerro Uyarani (CMCU), este trabalho, é constituído por litotipos félsicos e máficos metamorfizados em fácies granulito. Este Complexo tinha sido considerado um fragmento de crosta continental afetado por eventos magmáticos e metamórficos de alto grau no Paleoproterozoico, e de mais baixo grau no Mesoproterozoico a Neoproterozoico. Nossos novos dados U-Pb (LA-ICP-MS) em zircão e dados inéditos de isotópicos de Hf revelam uma história distinta. O estudo de texturas de zircão combinados com as idades U-Pb revela dois eventos principais, um durante o Paleoproterozoico, revelado pelos núcleos de zircão magmático de 1.81-1.75 Ga, e raros núcleos metamórficos de 1.88 Ga e um segundo evento Mesoproterozoico, durante o qual os núcleos antigos foram recristalizados. Este segundo evento está caracterizado por um primeiro ciclo de migmatização do embasamento, em 1,19–1,17 Ga. . O segundo ciclo, em ~1,1–1,0 Ga, é registrado em bordas metamórficas e em novos cristais de zircão metamórfico pela transformação do embasamento migmatítico em fácies granulitos. Os dados isotópicos combinados U-Pb e Hf sugerem que o CMCU fazia parte da porção mais ao sul do terreno Arequipa pelo menos desde os ~1,74 Ga, acrescido ao terreno Paraguá e Cráton Amazônico em 1,19–1,17 Ga. O evento 2 é caracterizado por uma fase acrescionária - ciclo 1 seguido por uma fase colisional - ciclo 2 - no qual as condições de metamorfismo foram elevadas para fácies granulito. Os dados de U-Pb e εHfT em zircão apresentam similaridade com terreno Arequipa, do terreno Rio Apa, do SW do Cráton Amazônico e outros *inliers* grenvillianos.

O Complexo Metamórfico Belén é caracterizado principalmente por ortognaisses, seguidos de xistos, rochas ultramáficas e diques máficos e félsicos alojados ao longo deu uma faixa de aproximadamente ~20 Km, de direção NNW-SSE. Os dados de U-Pb/Hf (LA-ICP-MS) nos zircões destes litotipos permitem delinear a história evolutiva relacionada ao magmatismo Famatiniano nesta região. O magmatismo teve um pico entre 470 e 464 Ma com a geração de quartzo monzodioritos, granodioritos e tonalitos que foram intrudidos por diques máficos sin-plutônicos. Essas rochas encontram-se intensamente deformadas e metamorfizadas em fácies anfibolito-alto. Os valores de εHf_T indicam, como em outras áreas afetadas pelo magmatismo Famatiniano, um magmatismo juvenil com forte assimilação crustal para a região de Belén. Várias hipóteses foram postuladas para explicar como um magmatismo de fonte mantélica pode ter intensa assinatura crustal entre elas: 1) retrabalhamento de crosta antiga; 2) retrabalhamento de sedimentos subductados; ou 3) instalação do arco magmático em prisma acrescionário, todos envolvendo entrada de componente mantélico. Os poucos zircões herdados (1.97-1.95 Ga) encontrados no anfibolito e anfibólio gnaisse do CMB e os dados isotópicos de Hf sugerem o retrabalhamento do terreno Arequipa (CUMC como parte do terreno), o qual foi retrabalhado durante a Orogenia Sunsas-Grenville. O CMB representaria então um terreno retrabalhado no Mesoproterozoico intrudido por rochas plutônicas félsicas a máficas durante o Ordoviciano. Os novos dados U-Pb e os poucos dados de Hf, aportados até o momento nesta tese, são muito importantes no entendimento da evolução do Paleoproterozoico ao Ordoviciano, na parte oeste do continente sul-americano, um lugar com poucos afloramentos de embasamento.

Palavras-chave: Complexo Metamórfico Cerro Uyarani, Complexo metamórfico Belén, U-Pb/Hf em zircão, Orogenia Sunsas-Grenville, Magmatismo Famatiniano

ABSTRACT

In the Central Andes region, specifically on the west coast of South America, two exposures of the pre-Andean basement, in the Cerro Uyarani, in Bolivia and another near Belén, in Chile, record the tectono-magmatic and metamorphic history of the Paleoproterozoic, Mesoproterozoic, Neoproterozoic, and Ordovician pre-gondwanic basement. The study of these areas is of paramount importance because these terranes recorded the evolution history of the western part of South America. The Paleoproterozoic basement of the Arequipa terrane (18 to 14 ºS) occurs from the west coast of Peru to the Bolivian Altiplano. This basement crops out in the Cerro Uyarani area in Oruro department, Bolivia. The Cerro Uyarani Metamorphic Complex (CUMC) – this work, consists of felsic and mafic granulite facies metamorphic rocks. This exposure was recognized as a crustal fragment that experienced magmatic and high-grade metamorphic events in the Paleoproterozoic and lower-grade metamorphism in Mesoproterozoic-Neoproterozoic times. Our new zircon U-Pb (LA-ICP-MS) and first Hf isotopic data reveal a distinct geological history. The zircon textures study combined with U-Pb ages indicate two main events, one during the Paleoproterozoic, indicated by magmatic zircon cores of 1.81-1.75 Ga, and rare metamorphic cores of 1.88 Ga, and a second Mesoproterozoic event, during which the old cores were recrystallized. This second event include a first cycle with basement migmatization at 1.19–1.17 Ga. The second cycle at ~1.1–1.0 Ga recorded the transformation of the migmatitic basement into granulite facies. Hafnium and U-Pb isotopic data together suggest that the CUMC was part of the southernmost portion of the Arequipa terrane at least from ~1.74 Ga, and was added to the Paraguá terrane and Amazonian Craton at 1.19–1.17 Ga. The second event is characterized by a accretionary phase – cycle 1 - followed by a colisional phase – cycle 2 - when metamorphic conditions reached granulitic facies. The zircon U-Pb and εHf_T data show similarity with the Arequipa terrane, Rio Apa terrane, SW Amazon Craton, and other Grenvillian inliers.

The Belén Metamorphic Complex comprises mainly orthogneisses, and minor schists, ultramafic rocks, and mafic and felsic dykes emplaced along approximately 20 km extent exposure, in an NNW-SSE arrangement. The U-Pb/Hf (LA-ICP-MS) in these lithotypes zircon grains allow to trace the evolutionary history of Famatinian magmatism in this region. The magmatism flare-ups between 470 and 464 Ma with generation of quartz monzodiorite, granodiorite, and tonalite intruded by syn-plutonic mafic dikes. These rocks are intensely deformed and metamorphosed to upper amphibolite grade. The εHf_T values indicate, as in other areas affected by Famatinian magmatism, juvenile magmatism with high crustal assimilation to the Belén region. Several hypotheses have been postulated to explain how a mantle source magmatism can have an intense crustal signature among them: 1) reworking of old crust; 2) reworking of subducted sediments; or 3) installation of the magmatic arc in an accretionary prism, all involving mantle component input. A few inherited zircon grains (1.97-1.95 Ga) from amphibolite and amphibole gneiss of the CMB and the isotopic Hf data suggest reworking of the Arequipa terrane (CUMC being considered as part of this terrane), which was reworked during the Sunsas-Grenville Orogeny. Then, the BMC would represent a Mesoproterozoic reworked terrane intruded by felsic to mafic plutonic rocks during the Ordovician. The new U-Pb data and the few Hf data provided so far in this thesis are very important to the understanding of the tectonic evolution from the Paleoproterozoic to the Ordovician in the western part of the South America, a place with few basement outcrops.

Keywords: Cerro Uyarani Metamorphic Complex, Belén Metamorphic Complex, U-Pb/Hf in zircon, Sunsas-Grenville Orogeny, Famatinian magmatism

LISTA DE FIGURAS

Capítulo 1

Capítulo 2: Paper 1

Capítulo 3: Paper 2

Capítulo 4

SUMÁRIO

1 CAPÍTULO 1

1.1 APRESENTAÇÃO DO TEMA

O desenvolvimento de orógenos acrescionários e colisionais em escala global marca a formação de antigos supercontinentes. A configuração dos supercontinentes Columbia, Rodínia e Gondwana são fundamentados por evidências de paleomagnetismo (Buchan et al., 2001; Meert, 2001; Meert e Torsvik, 2003; Salminen et al., 2013; Dopico et al., 2021), estudo de zircões detríticos (Rainbird et al., 1998; Cawood et al., 2007; Wu et al., 2010; Kuznetsov et al., 2014; Turner et al., 2014), estudo de enxames de diques máficos (Ernst et al., 2008, 2010; Ernst e Srivastava, 2008; Ernst et al., 2013), informações paleontológicas, reconstruções paleogeográfica (Burrett e Berry, 2000; Hartz e Torsvik, 2002; Wingate et al., 2002; Meert e Torsvik, 2003; Franz et al., 2006; Bispo-Santos et al., 2013) e alinhamento de cinturões orogênicos (Berthelsen e Marker, 1986; Hoffman, 1991; Zhao et al. 2001; Wilde et al. 2002).

O estudo das exposições de embasamento pré-cambriano nos Andes Centrais (Fig. 1, Ramos, 2010) é importante para a compreensão da complexa evolução tectônica dos terrenos aglutinados na margem (hoje) ativa da América do Sul e que participaram da formação dos supercontinentes Columbia e Rodínia (Dalziel e Forsythe, 1985; Ramos 1988, 2008, 2010).

Assim também se faz necessário o melhor entendimento da orogenia Famatiniana, do Ordoviciano Inferior e Médio, desenvolvida ao longo da margem proto-andina do Gondwana (Ducea et al., 2017; Rapela et al., 2018).

O elo de correlação entre os terrenos Arequipa, Antofalla e o Cráton Amazônico, é a presença de cinturões granulíticos, entre 1.7 Ga e 1.0 Ga (Cobbing et al. 1977, Dalmayracet al. 1977, Shackleton et al. 1979, Priem et al. 1989, Wasteneys et al. 1995 e Casquet et al. 2010). A reativação da colisão entre os terrenos Arequipa e Antofalla no Ordoviciano é indicada pela geração de crosta oceânica, plataforma clástica (Ramos 1988; Sempéré 1995; Bahlburg et al. 2006) e geração de arco magmático (Ramos, 2008).

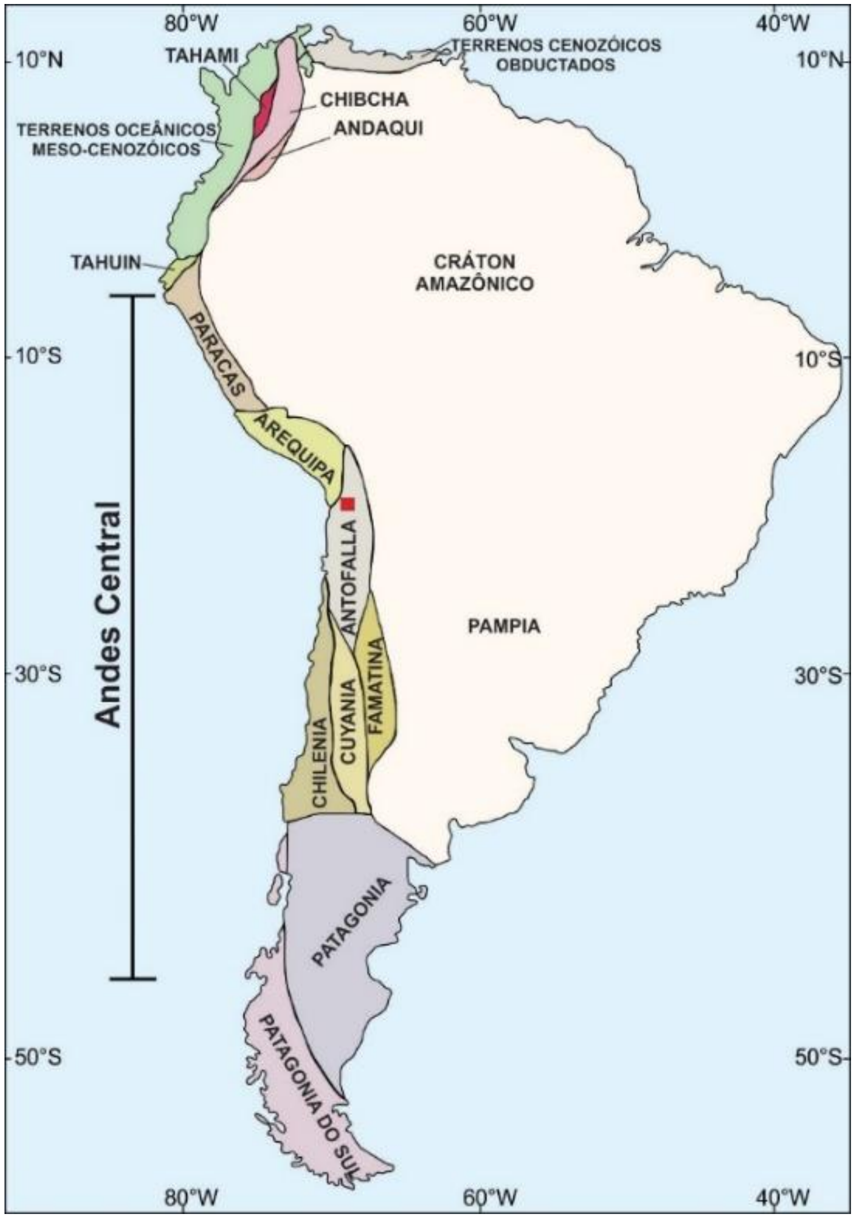

Figura 1. Configuração da América do Sul e localização dos terrenos de embasamento pré-andino na costa oeste da América do Sul, com a localização da área de estudo, quadrado vermelho, em relação aos Andes Centrais (Modificado de Ramos, 2010).

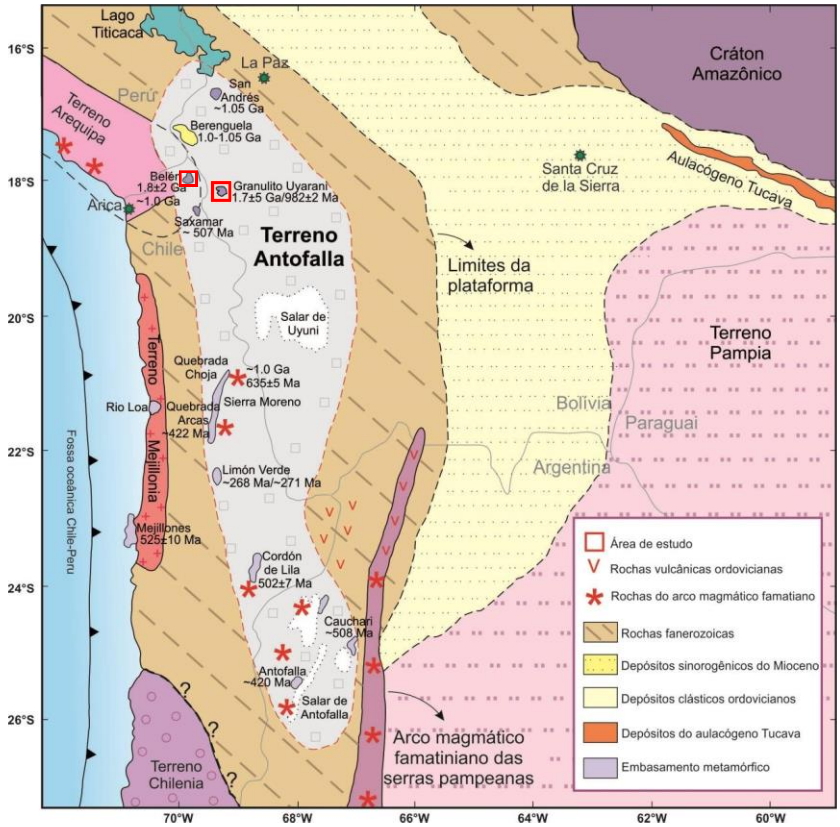

Figura 2. Posição do Terreno Antofalla em relação aos terrenos vizinhos como terreno Arequipa. Neste modelo de Ramos (2008), as duas áreas estudadas, Cerro Uyarani e Belén, são inseridas no terreno Antofalla.

Considerando os Terrenos Arequipa e Antofalla como um bloco único a partir de ~1.0 Ga , os Domínios Norte, Central e Sul, foram definidos de acordo com as idades de magmatismo e metamorfismo, isótopos de Pb e idades T_{DM} de Nd em rocha total (Fig. 3; Loewy et al., 2004). O Domínio Norte abrange o terreno Arequipa com magmatismo e metamorfismo paleoproterozoicos e arco magmático neoproterozoico; o Domínio Central tem magmatismo e metamorfismo mesoproterozoico seguido de magmatismo tardio Neoproterozoico, que considera a porção norte a central do terreno Antofalla, o Domínio Sul registra magmatismo e metamorfismo do Neoproterozoicos ao Ordoviciano, na porção sul do terreno Antofalla (Loewy et al., 2004).

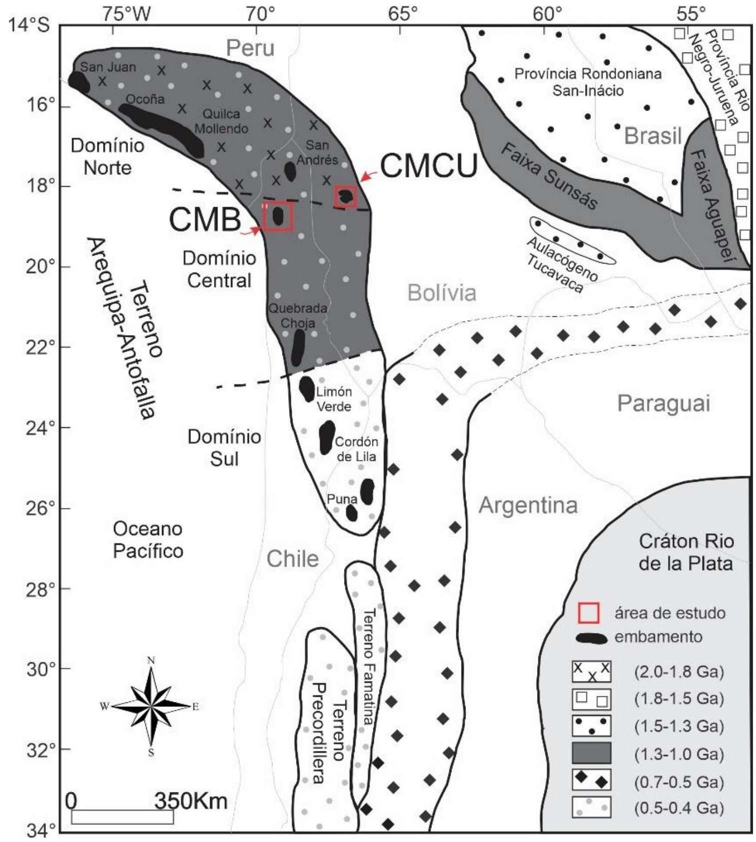

Figura 3. Localização do Complexo Metamórfico Cerro Uyarani (em inglês, Cerro Uyarani Metamorphic Complex: CUMC) e do Complexo Metamórfico Belén (em inglês, Belén Metamorphic Complex: BMC) considerando a divisão de domínios elaborada por Loewy et al. (2004).

Duas exposições do embasamento foram escolhidas para estudo de evolução tectônica. O Complexo Metamórfico Cerro Uyarani (CMCU) são rochas do Pré-Cambriano, que afloram na porção oeste da Bolívia e representam uma janela estrutural do terreno Arequipa (e.g., Wörner et al., 2000; Oliveira et al., 2022; Pankhurst et al., 2016) ou do Terreno Antofalla (Ramos 2008). Já o Complexo Metamórfico Belén que já foi considerado como uma exposição Pré-Cambriana (e.g., Tosdal, 1996; Garcia et al., 2004), atualmente é compreendido como uma exposição de rochas plutônicas e metamórficas geradas na construção do proto-Gondwana, a ~90 km a oeste do CMCU e que mostra indícios de retrabalhamento de crosta mais antiga (Pankhurst et al., 2016). Em relação aos domínios isotópicos (Loewy et al., 2004), as áreas de estudos deste trabalho, Complexo Metamórfico Cerro Uyarani e Complexo Metamórfico Belén, estão englobadas nos Domínios Norte e Central, respectivamente.

1.2 JUSTIFICATIVAS E OBJETIVOS

As duas áreas escolhidas como alvo deste trabalho possuem poucos trabalhos de reconhecimento de campo, não apresentam mapeamento detalhado publicado em artigos científicos, contam com poucas idades U-Pb em algumas das litologias, e poucos dados isotópicos e geoquímicos. É possível que, por se tratar de locais remotos da Bolívia e do Chile de difícil acesso e em altas atitudes, trabalhos mais robustos sejam escassos os nestes locais.

Ambas as exposições são relevantes por registrarem orogenias do Proterozoico (Complexo Metamórfico Cerro Uyarani) e do Paleozoico (Complexo Metamórfico Belén) ainda pouco entendidas tanto na própria região em que afloram quanto em relação às possíveis correlações de magmatismo, fonte e origem em relação a outros blocos, terrenos e crátons que configuram hoje a América do Sul.

Portanto, o objetivo dessa tese é sugerir uma evolução tectônica plausível com os dados obtidos. No caso do CMCU, em relação às orogenias do Paleoproterozoico ao Mesoproterozoico, indicar um posicionamento em relação à formação de supercontinentes (principalmente Rodinia). Para o CMB o objetivo é contribuir para o entendimento do magmatismo e metamorfismo do arco Famatiniano na região, comprar com as demais ocorrências deste arco heterogêneo e contribuir com dados que sugiram um modelo de geração magmática mais adequado para a área.

O Complexo Metamórfico Cerro Uyarani possui idades com erros altos e interpretações ainda em andamento, diferentes litotipos que não estão individualizados em mapa e relações de contato desconhecidas entre as unidades. Tais questões em aberto foram discutidas no artigo inserido no capítulo 2 dessa tese, corroborando assim para o conhecimento geológico por meio de novos dados de campo, descrição petrográfica, datação U-Pb e isótopos de Lu-Hf em zircão, que robusteceram na compreensão da evolução tectônica da área e nas correlações com o terreno Arequipa, Paraguá, Rio Apa, Cráton Amazônico e MARA cráton.

O Complexo Metamórfico Belén tem pouco litotipos datados, mapeamento restrito e conhecimento limitado do desenvolvimento magmatismo. No artigo do capítulo 3 apresentamos novas idades e isótopos de Hf inéditos que enriquecem o conhecimento do magmatismo Famatiniano e dão pistas para uma proposta diferente de desenvolvimento do arco na região, além de corroborar com o conhecimento do metamorfismo e deformação das rochas estudadas.

1.3 LOCALIZAÇÃO E VIAS DE ACESSO

A área de estudo da tese localiza-se na fronteira Bolívia-Chile e trata-se de 2 áreas chaves (Fig. 4). A área 1 localiza o Complexo Metamórfico Belén, no extremo norte do Chile, na região XV - Arica e Parinacota, na Província Parinacota, Comuna de Putre, com as coordenadas UTM 447187/7960868. O acesso à esta área é realizado por Arica, no litoral do Chile, pela Rota Internacional - CH 11 e via A-31, entre as Vilas Chapiquiña e Tignamar. Na área 2 encontra-se o Complexo Metamórfico Cerro Uyarani, no departamento de Oruro, Província Sajama, município de Turco, próximo às Vilas Água Rica e Iru Pampa e situa-se na porção ocidental da Bolívia, com as coordenadas UTM 535070/7958469. O deslocamento até a área 2 é feito via Rota Internacional - CH 11 no Chile e Rota Nacional 4 e 27 na Bolívia.

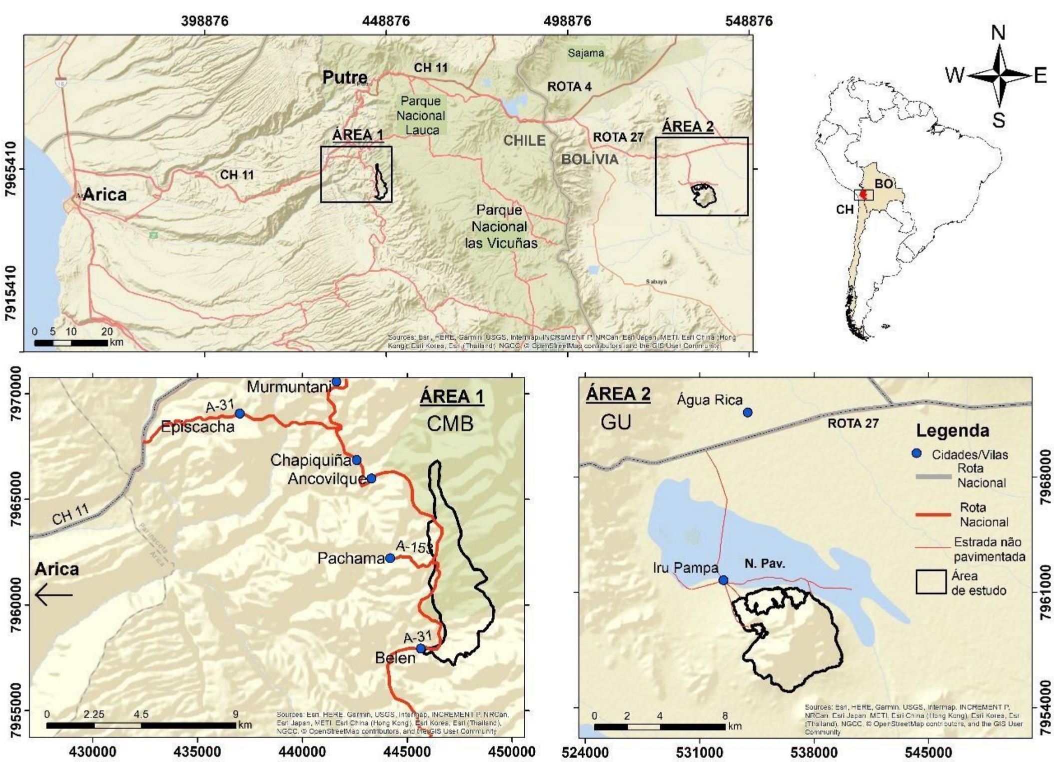

Figura 4. Mapa de localização e vias de acesso às áreas-chave de estudo. A área 1 localiza-se no extremo norte do Chile, e compreende o Complexo Metamórfico Belén. A área 2 fica na porção ocidental da Bolívia onde se encontra o Complexo Metamórfico Cerro Uyarani.

1.4 ESTRUTURA DA TESE

Esta tese de doutorado está estruturada em quatro capítulos. O Capítulo 1 contém informações gerais sobre a tese de doutorado apresentando introdução ao tema, justificativas da pesquisa, objetivos, localização e vias de acesso das áreas de estudo e materiais e métodos utilizados na pesquisa. O Capítulo 2 contém o artigo já publicado (disponível online em 14 de maio de 2022) referente ao Complexo Metamórfico Cerro Uyarani, intitulado "**The Cerro Uyarani Metamorphic Complex on the Bolivian Altiplano: New constraints on the tectonic evolution of the Central Andean basement between ~1.8 and 1.0 Ga**". O Capítulo 3 aborda a contextualização geológica e estudo das idades e isótopos de Hf do magmatismo do Complexo Metamórfico Belén, intitulado "**U-Pb/Hf isotopic composition of the Belén Metamorphic Complex, northern Chile: new constrains on the Ordovician Famatinian Magmatic arc**". O Capítulo 4 apresenta os dados de geoquímica das rochas do Complexo Metamórfico Belén. Finalmente, o Capítulo 5 aborda as conclusões e recomendações da tese.

1.5 MATERIAIS E MÉTODOS

Etapa Preliminar

Levantamento e estudo do acervo bibliográfico, seguido de interpretação geológica utilizando imagens LANDSAT 8 (*Land Remote Sensing Satellite*) e SRTM (*Suttle Radar Topography Mission*). Confecção de mapa geológico interpretativo preliminar e mapa-base em escala 1:50.000 e 1:25.000, utilizados no trabalho de campo.

Etapa de campo

Mapeamento do Complexo Metamórfico Cerro Uyarani e do Complexo Metamórfico Belén em escala 1:25.000, com coleta de amostras para estudo petrográfico (descrição macroscópica e de seções delgadas), geocronologia U-Pb em zircão e análises isotópicas de Hf em zircão. Foram realizadas duas etapas de campo, em 2016 e em 2019.

Análise Petrográfica

As amostras dos Domínio I, II e III do Complexo Metamórfico Cerro Uyarani foram coletadas no trabalho de campo do mestrado, de 2014 a 2015, das quais foram confeccionadas 48 lâminas delgadas no Laboratório de Laminação do Departamento de

Recursos Minerais (DRM/UFMT). Tais lâminas foram utilizadas nesta tese de doutorado. As amostras coletadas no Complexo Metamórfico Belén são exemplares de entre xistos, gnaisses e anfibolitos. Foram confeccionadas 27 lâminas delgadas no Laboratório de Laminação da Universidade de Brasília.

Geoquímica

Para determinação da composição química (elementos maiores, menores, traços e terras-raras) em rocha total (RT) foram selecionadas 20 amostras do CMB. As amostras foram britadas, moídas e pulverizadas no Laboratório de Geocronologia da Universidade de Brasília. Posteriormente foram enviadas para o ALS Global Analytical Laboratories Ltda (Belo Horizonte - Brasil). O pacote de método analítico escolhido foi o “CCP-PKG01”, com a utilização de espectrometria de emissão atômica com fonte de plasma (ICP-AES), fluorescência de raios-X (X-ray fluorescence - XRF) e espectrometria de massa com fonte de plasma (ICP-MS). A perda ao fogo (*loss on ignition* - LOI) é estimada pela diferença de peso após o aquecimento a 100°C. Para detalhamento do método laboratorial acesse o link www.alsglobal.com.

Geocronologia U-Pb em zircão

Seis amostras do Complexo Metamórfico Cerro Uyarani (3 de granulito félsico e 3 de anfibolito) e 11 amostras do Complexo Metamórfico Belén (ortognaisses, ortoxistos e de anfibolito) foram selecionadas para a datação de zircão. Essas amostras foram britadas, moídas e pulverizadas no Laboratório de Geocronologia da Universidade de Brasília. A metodologia utilizada foi Laser Ablation Inductively Coupled Plasma Mass Spectrometry (LA-ICP-MS), com modelo Thermo-Finnigan-Neptune HR-MC-ICP-MS aclopado a um sistema de laser Nd: YAG UP213 New Wave, com spot de 25-30 µm e laser a 10 Hz e 2-3 J/cm2, realizadas no Laboratório de Geocronologia da Universidade de Brasília. As análises seguiram o método de Albarède et al. (2004). O zircão GJ-1 (608 Ma, Jackson et al., 2004) foi o padrão utilizado para quantificar o fraccionamento no ICP-MS. O zircão 91500 (1065 Ma, Wiedenbeck et al. 1995) também foi analisado como padrão externo. As massas calibradas foram 238, 232, 208, 207, 206, 204 e 202. O ^{204}Pb comum foi monitorado com base nas massas ^{202}Hg e (^{204}Hg + ^{204}Pb). Não foi necessário corrigir a contribuição de Pb comum (^{204}Pb). O Microscópio de Varredura Eletrônica (MEV) gerou as imagens de Cathodoluminescence (CL) e Back-scattered electron microscopy (BSE) utilizados para a descrição da morfologia e texturas internas dos zircões analisados. Os dados brutos foram processados pelo software Evaluation, reduzidos em Excel, com a Macro Chronus 2.0 Alpha 3 (Oliveira, 2015), e as idades foram calculadas usando a Macro Isoplot 4.15 (Ludwig K R. 2003). Os processos analíticos e a redução de dados são descritos detalhadamente por Bühn et al. (2009).

Análise dos isótopos de Lu-Hf em zircão

Os isótopos Lu–Hf foram analisados no mesmo instrumento usado para a análise dos isótopos U–Pb. Os dados do isótopo Lu-Hf foram coletados ao longo de ablação de 40-50 s, usando um tamanho de furo de 40 μm de diâmetro e energia de 85%. A seleção dos cristais para análise de Lu-Hf foi baseada nos dados U-Pb concordantes (concordância de idades 6/8 e 7/6), complexidades (borda e núcleo de diferentes idades) e tamanho do cristal. Quando possível, o ponto de coleta do Lu-Hf foi colocado o mais próximo possível do ponto anterior feito para a análise de U-Pb. Os sinais dos isótopos livres de interferência ^{171}Yb, ^{173}Yb e ^{175}Lu foram monitorados durante a análise para corrigir interferências isobáricas de ^{176}Yb e ^{176}Lu no sinal de ^{176}Hf, utilizando os parâmetros de Chu et al. (2002). O fator de normalização de $^{173}Yb/^{171}Yb$ foi de 1,132685 (Chu et al., 2002). As razões de isótopos de háfnio foram normalizadas para o valor de $^{179}Hf/^{177}Hf$ de 0,7325 (Patchett, 1983). Uma descrição detalhada dos procedimentos e métodos é fornecida em Matteini et al. (2010). Os dados obtidos dos cristais de zircão foram processados em uma macro do Microsoft Excel (adaptado de Bertotti, 2012 e Bertotti et al., 2013) para calcular os valores corrigidos de $^{176}Hf/^{177}Hf$ e $^{176}Lu/^{177}Hf$. O cálculo dos valores de εHf_T utilizou a constante de decaimento $\lambda = 1,865*10-11$ após Scherer et al. (2006), e $^{176}Lu/^{177}Hf = 0,0332$ e $^{176}Hf/^{177}Hf = 0,282772$ CHUR valores segundo Blicert-Toft e Albarède (1997). A razão Lu/Hf crustal média permite calcular as idades T_{DM} de dois estágios a partir da composição isotópica inicial de Hf (Gerdes e Zeh, 2006, 2009; Nebel et al., 2007). Para o tempo de cristalização do zircão, as idades do modelo Hf do manto empobrecido de dois estágios (T_{DM} Hf) são calculadas usando $_{176}Lu/_{177}Hf = 0,0384$ e $^{176}Hf/^{177}Hf = 0,28325$ para o manto empobrecido (Chauvel e

Blichert-Toft, 2001) e ^{176}Lu /^{177}Hf valor de 0,0113 para a crosta média (Taylor e McLennan, 1985; Wedepohl, 1995).

2 CAPÍTULO 2 – PAPER 1

Journal of South American Earth Sciences 116 (2022) 103843

Contents lists available at ScienceDirect

Journal of South American Earth Sciences

journal homepage: www.elsevier.com/locate/jsames

The Cerro Uyarani Metamorphic Complex on the Bolivian Altiplano: New constraints on the tectonic evolution of the Central Andean basement between ~1.8 and 1.0 Ga

Juliana Rezende de Oliveira [a,*], Natalia Hauser [a], Wolf Uwe Reimold [a], Amarildo Salina Ruiz [b], Ramiro Matos [c], Thassio Werlang [a]

[a] Laboratory of Geochronology and Isotope Geochemistry, Geosciences Institute, University of Brasília, Asa Norte, Brasília, DF, CEP, 70910-900, Brazil [b] Geology Faculty, Geosciences School, University of Mato Grosso, Fernando Corrêa da Costa Avenue, 2367, Boa Esperança, Cuiabá, MT, 78060-900, Brazil ´ [c] Instituto de Investigaciones Geologicas y del Medio Ambiente, University Mayor of San Andrés, Street 27, Geology Pavilion, La Paz, Bolivia

ABSTRACT

The Cerro Uyarani Metamorphic Complex (CUMC) in Bolivia provides a record of complex Paleoproterozoic to Mesoproterozoic tectono-magmatic evolution, as revealed through U–Pb isotopic analysis of zircon from three litho-domains (DI – DIII). The Paleoproterozoic crystalline basement was subject to two stages of Mesoproterozoic reworking. This detailed study of zircon textures and geochronology, including determination of first Hf- isotope data, from felsic granulites, banded granulites and amphibolites reveals a first Paleoproterozoic event at 1.81–1.74 Ga in magmatic and some metamorphic zircon cores, with zircon ϵHf_T values of +6.3 to − 0.2. A subsequent Mesoproterozoic event can be divided into 2 cycles: a first one at 1.19–1.17 Ga is reflected by recrystallized rims and cores of zircon with ϵHf_T values of − 6.8 to − 3.6. This cycle is here associated with migmatization of the basement, during which the Paleoproterozoic crust was differentiated into DI-leucosome rich migmatite, DII-leucosome rich migmatite, DIII – our best proxy of Paleoproterozoic crust, melanosome, and paleosome. The second cycle at ~1.1–1.0 Ga is recorded in metamorphic rims and by newly grown metamorphic zircon with ϵHf_T values of − 15.1 to − 2.6. This event was responsible for the transformation of the CUMC migmatitic basement into granulite facies rocks. We interpret that the CUMC was part of the southernmost portion of the Arequipa terrane from, at least, ~1.74 Ga and that it then became attached to the Paraguá terrane and Amazon craton at 1.19–1.17 Ga. This collision generated migmatites, and then, with the arrival of Laurentia passing through the Arequipa terrane front (with CUMC at the Arequipa terrane), the conditions of metamorphism were raised to granulite facies. A younger event of lower metamorphic grade and likely associated with fluid-driven alteration is recognized in the partial retrograde transformation of mafic granulites into amphibolites. Our new U–Pb and εHf_T data indicate that the Paleo-to Mesoproterozoic history of the CUMC is, thus, similar to that of the Arequipa terrane, Rio Apa terrane, the SW Amazon craton, and other Grenville-age inliers; but it was distinct from the evolution of the Sierra de Maz and Pie de Palo of the hypothetical MARA craton.

Keywords:
Cerro Uyarani, Andean basement inliers Precambrian, Granulite metamorphism, Amphibolite metamorphism, U–Pb/Hf zircon analysis, Bolivian geology

2.1 INTRODUCTION

The understanding of Precambrian crustal growth towards the assembly of the South American continent has been focused mainly on the evolution of the Brazilian part, where the comparatively oldest rocks are exposed (e.g., Cordani et al., 2000; Santos et al., 2000; Tassinari and Macambira, 2004) and where the main events in terms of continent collisions and amalgamation between the Amazon, Sao Francisco, and ˜ other cratons have been investigated. The accessible basement in the western part of South America consists of scarce outcrops of Paleo- to Neoproterozoic rocks, generally in the form of inliers in younger sedimentary and/or volcanic terranes. Notably, most of this region is covered by Mesozoic to Cenozoic volcanic and sedimentary rocks of the Andean Orogen and related foreland basins (e.g., Harmon et al., 1984; Ramos, 2018). This cover, as well as the associated Andean deformation, have hindered the recognition of older basement, the study of which could have improved the understanding of the Precambrian evolution of the South American continent.

However, at least 10 inliers (Fig. 1) in southern Peru, western Bolivia, northern Chile, and northwestern Argentina have been identified (Loewy et al., 2004). The best-preserved inliers are exposed along the coastal region of southern Peru (e.g., Cobbing and Pitcher, 1972; Wasteneys et al., 1995; Casquet et al., 2010) and northern Chile (Ramos, 2008a), and extend into western Bolivia (Loewy et al., 2004; Mamani et al., 2008). These inliers, collectively recognized as the Arequipa terrane, had a complex, polycyclic magmatic and metamorphic evolution from the early Proterozoic to the early Paleozoic (e.g., Worner et al., ¨ 2000; Loewy et al., 2004; Ramos, 2008b; 2018). In the Andean foreland of central Argentina, the Sierra de Maz (Casquet et al., 2006, 2008a) corresponds to the western Sierras Pampeanas. Far to the east of the Andean active margin, in central-south Brazil and eastern Bolivia, the Rio Apa and Paraguá terranes (e.g., ´ Cordani et al., 2010; Teixeira et al., 2020; Boger et al., 2005; Nascimento et al., 2016; Redes et al., 2020; Ribeiro et al., 2020) have been investigated.

The segmented Arequipa terrane has also been interpreted as the manifestation of a single, coherent basement block with Paleoproterozoic ages (Cordani et al., 2000) and Archean sources and inheritance (Casquet et al., 2010). In contrast, the Antofalla terrane records mainly Paleozoic magmatic and metamorphic rocks with Precambrian inheritance (e.g., Pankhurst et al., 2016). Only a single Mesoproterozoic inlier, the Quebrada Choja, has been identified (Loewy et al., 2004).

The two terranes together have been discussed as the Arequipa- Antofalla basement (Ramos, 1988; Tosdal, 1996; Loewy et al., 2004). On the basis of isotopic data, this terrane has been divided into successively younger Northern, Central, and Southern domains (Loewy et al., 2004). In the southern part of the Northern Domain, on the Bolivian Altiplano, occurs a structural window of approximately 34 km^2, the Paleo- to Mesoproterozoic Cerro Uyarani inlier, which is largely covered by Neogene and Quaternary sedimentary and volcanic rocks.

The Cerro Uyarani Metamorphic Complex (CUMC), discovered by Tröeng et al. (1994), represents the only exposure of Precambrian basement in western Bolivia (Fig. 2). The chemical signature of this basement is alkali-calc to calc-alkaline, and metaluminous to peraluminous. Seemingly these rocks developed in an arc environment in association with tholeiitic basalts (Oliveira et al., 2017).

With the objective to better understand the source(s) and genesis of the Cerro Uyarani Metamorphic Complex (CUMC), we here present new U–Pb and some Lu–Hf isotope data obtained by LA-ICP-MS on zircon from various high-grade metamorphic rocks. The results will help to understand what happened between the time of dismemberment of the Columbia supercontinent (Paleoproterozoic) and the assembly of the Rodinia supercontinent through the Meso- and Neoproterozoic Sunsas and Grenville orogenies. This work will also constrain the paleogeographic relationship(s) of this inlier that has a strategic position within the neighboring terranes such as the Arequipa-Antofalla basement, Rio Apa terrane, and the Amazon craton. These new data will also help to better understand the crustal evolution of the South American continent.

2.2 GEOLOGICAL SETTING

The collision of the Laurentia and Amazonia continents during the Neoproterozoic assembly of the supercontinent Rodinia resulted in the formation of the Grenville and Sunsas (Fig. 1A) orogenic belts (e.g., Ramos, 1988; Ramos and Vujovich, 1993; Sadowski and Bettencourt, 1996; Loewy et al., 2004; Fuck et al., 2008). Eastern Laurentia dates to ~1.8–1.0 Ga and its extreme southeastern part comprises magmatic and metamorphic rocks of 1.3–1.0 Ga age (Ownby et al., 2004). The Grenville Orogen

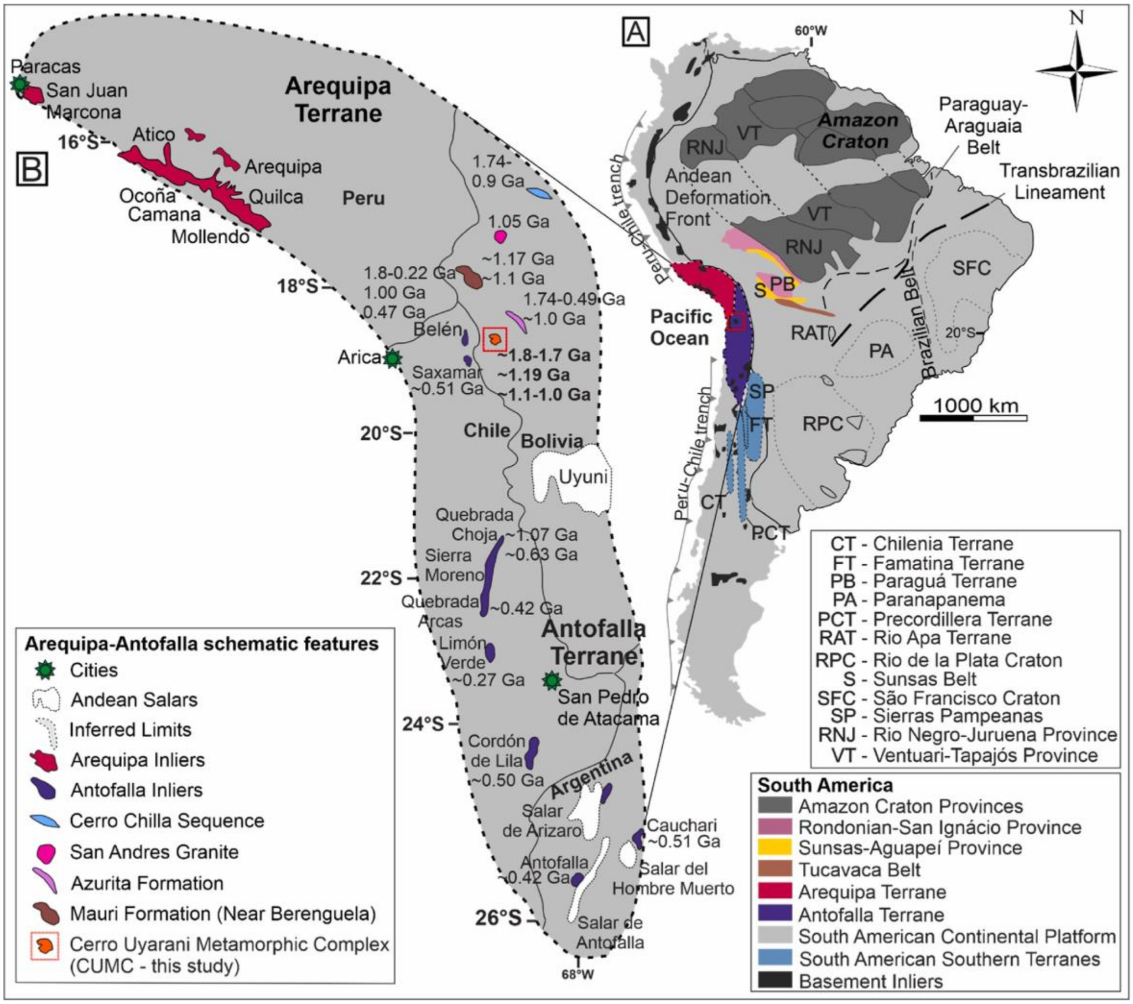

Figure 1 A) Schematic map of South America showing the Arequipa and Antofalla terranes after Ramos (2009), and the geological provinces of the Amazon craton after Cordani et al. (2009). B) Detail of the Arequipa (Casquet et al., 2010) and Antofalla exposures (Ramos et al., 1996). The position of the main inliers and related rocks of Bolivia are indicated: the Cerro Uyarani Metamorphic Complex (CUMC), the Cerro Chilla volcano-sedimentary sequence (Bahlburg et al., 2020), the San Andres metagranites (Lehmann, 1978), gneissic clasts in the Azurita/Potoco Formation (Evernden et al., 1977) and the Mauri Formation near Berenguela village (Tosdal, 1996). The boundaries of the Arequipa and Antofalla terranes are after Loewy et al. (2004). The acronyms are defined in the legend.

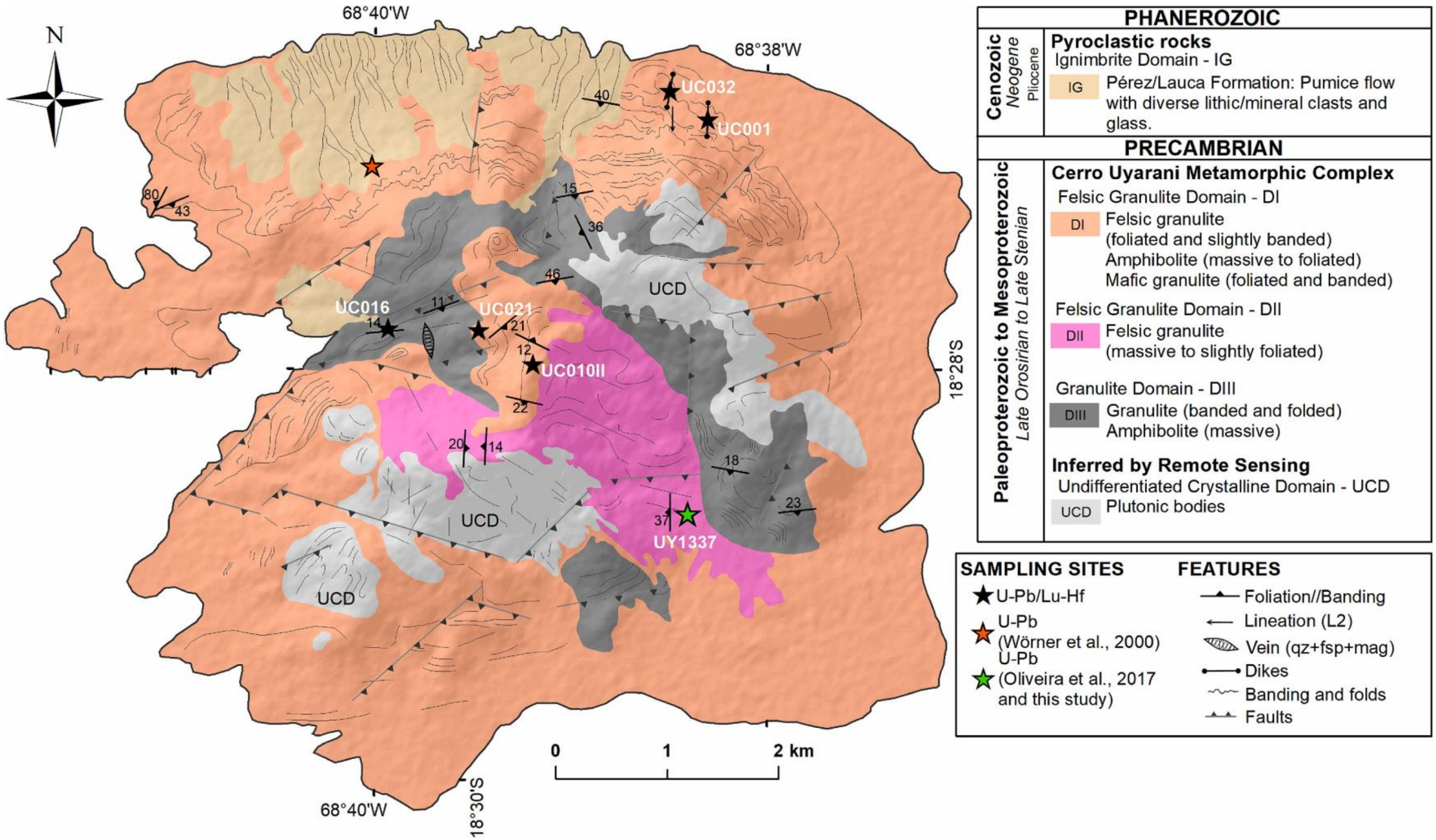

Figure 2. Geological map and main geological structures of the CUMC of western Bolivia (1:45,000 scale). The locations of the Felsic Granulite Domain I (DI), Felsic Granulite Domain II (DII), and the Banded Granulite Domain III (DIII), as well as the inferred limits of the Undifferentiated Crystalline Domain (UCD) and the Pleistocene ignimbrites (2.7 ± 0.01 Ma; Walfort et al., 1995) of the Peréz Formation (Troeng ¨ et al., 1994) are indicated.

on the eastern side of Laurentia, i.e., in today's southeastern North America, was a product of the progressive development of juvenile crust, crustal reworking, and addition of exotic terranes (e.g., Karlstrom et al., 1999; Sinha and McLelland, 1999; Hatcher et al., 2004).

The conjoined margin of the SW Amazon craton (Fig. 1A) was an active margin between 1.45 and 1.1 Ga (Santos et al., 2000, 2003, 2008) and between 1.2 and 0.95 Ga (e.g., Litherland et al., 1986, 1989; Teixeira et al., 2010). This margin comprises the Sunsas-Aguapeí province (Fig. 1A) formed by metasedimentary rocks and granitic bodies of low-grade metamorphic grade and includes three orogenic belts - Sunsas, Aguapeí, and Nova Brasilandia (e.g., ˆ Tohver et al., 2004a,b; Boger et al., 2005; Teixeira et al., 2010; Rizzotto et al., 2014; Quadros et al., 2021). The analogy between the Grenville and Sunsas orogens is spatial and temporal (Johansson et al., 2022), but the differences in tectonic evolution and isotopic composition (Pb–Pb and Sm–Nd data) demand the existence of two distinct collisional orogens (Loewy et al., 2003, 2004).

The ages of basement exposures to the west of the Sunsas orogenic belt have been interpreted to indicate a collision between SW Amazonia and small microcontinents that became amalgamated between Laurentia and Amazonia (Ramos, 1988, 2008a; Bahlburg and Hervé, 1997; Loewy et al., 2004). The Arequipa and Antofalla terranes exemplify these smaller basement blocks in this collisional region (e.g., Loewy et al., 2004; Fuck et al., 2008; Ramos, 2008a).

2.2.1 The Arequipa-Antofalla Precambrian basement

The scattered basement outcrops of the Arequipa terrane occur over about 800 km in southern coastal Peru (Cobbing and Pitcher, 1972). These inliers comprise orthogneisses, batholiths, metasedimentary rocks, volcanic sequences, migmatites and schists, all of which were metamorphosed to amphibolite and granulite grade (e.g., Shackleton et al., 1979; Martignole and Martelat, 2003; Casquet et al., 2010). These outcrops (Fig. 1B), known as Paracas, San Juan, Marcona, Lomas, Atico, Ocoña, Camana, Quilca, Mollendo, and Arequipa (e.g., ˜Wilson, 1975; Cobbing et al., 1977; Dalmayrac et al., 1977; Shackleton et al., 1979; Wasteneys et al., 1995; Loewy et al., 2004; Casquet et al., 2010; compare Fig. 1B), yielded ages between 2.0 and 0.99 Ga. The Antofalla terrane, just south of the Arequipa terrane, extends from the northern coast of Chile to the western portion of the Puna of Argentina, and includes the Belén, Quebrada Choja, Sierra Moreno, San Andres, Berenguela, Saxámar, Cauchari, Cordon de Lila, Lim´ on Verde and Antofalla outcrops ´ (Loewy et al., 2004, Ramos et al., 1996; compare Fig. 1B). This basement includes granitic and ortho- as well as para-derivate rocks of Precambrian to Paleozoic ages that are variably metamorphosed to granulite, amphibolite, and greenschist facies (Lehmann, 1978; Tosdal, 1996; Wörner et al., 2000¨ ; Loewy et al., 2004). The Cerro Uyarani (Cerro Uyarani Metamorphic Complex - CUMC) and Belen (Belén Metamorphic Complex - BMC) inliers are located on the limit between the Arequipa and Antofalla terranes or in the southern part of the northern domain and central domain, respectively, in the sense of Loewy et al. (2004). The correlation of these inliers with either the Arequipa or/and the Antofalla terranes has been discussed. The CUMC potentially relates to the Arequipa basement (Tröeng et al., 1994; Wörner et al., 2000¨ ; Oliveira et al., 2017, Fig. 1B), but the complex was also considered by Omarini et al. (1999) and Ramos et al. (1996) as Antofalla terrane basement based on the gravimetric data of Götze et al. (1994).

The Precambrian basement of western Bolivia (Fig. 1B) is also known in the form of red gneiss and granite boulders in the conglomerate of the Azurita/Potoco Formation (Evernden et al., 1977), as gneiss and granulite clasts in the Mauri Formation near Berenguela (Tosdal, 1996), and in the San Andres area where a borehole intersected the basement ´ (Lehmann, 1978). Recently, this basement was indirectly identified in the volcano-sedimentary sequences of the Chilla Beds and constrained in age through U–Pb dating of detrital zircon to 1.73–0.80 Ga by Bahlburg et al. (2020).

2.2.2 Age of the Cerro Uyarani Metamorphic Complex

A first attempt to date rocks from the CUMC was made by Troeng ¨ et al. (1994), who described leucocratic gneisses with inclusions of mafic rocks and obtained a Rb–Sr whole-rock age of 1859 ± 200 Ma, which was interpreted as the basement age. Wörner et al. (2000) ¨ dated these rocks with U–Pb on zircon by ID-TIMS. They obtained for a charnockite an upper intercept age of 2024 ± 133 Ma and a lower intercept age of 1157 ± 60 Ma, which were interpreted as the age of the igneous protolith and a subsequent metamorphic event, respectively. These authors also obtained a Sm–Nd mineral isochron

(1008 ± 16 Ma) and an ^{40}Ar-^{39}Ar amphibole plateau age (982.5 ± 1.7 Ma) for mafic granulite, which were interpreted as cooling ages after granulite facies metamorphism. A U–Pb SHRIMP zircon age of 1736 ± 5.1 Ma was interpreted as the age of crystallization of the igneous protolith by Oliveira et al. (2017). These chronological data suggested that the CUMC rocks could be related to the Antofalla (Pacci et al., 1980; Tosdal, 1996; Ramos, 2008a) and Arequipa basement (Wörner et al., 2000; Loewy et al., 2004), which is further supported by seismic (Dorbath et al., 1993), gravimetric, geochemical, and other isotopic data (Loewy et al., 2004; Mamani, 2006; Mamani et al., 2008, 2010).

2.3 ANALYTICAL METHODS

2.3.1 Remote sensing

The application of remote sensing data is useful in desert regions (e. g., Araujo and Mello, 2010; Fal et al., 2019) such as at Cerro Uyarani in Bolivia. Our study of satellite images defined color, tone, shape, boundaries, and textural criteria (Supplementary Table 01_Remote Sensing Data) for the study region. This detail, combined with field information, sample description, and geochemistry, allowed the definition of domains and preparing a first detailed geological map (Fig. 2), at the scale of 1:45,000, for the Cerro Uyarani Metamorphic Complex.

We prepared the geological map using three remote sensing datasets: 1) Sentinel-2A, 2) Landsat-8, and 3) DEM images, all projected with UTM at the 19N zone. In the first application of the Sentinel-2A data, we used image T19KEV 20210327T144729_TCI_10m (Copernicus Sentinel Data, 2020) with the following characteristics: one granule at level-1C, Top of Atmosphere (TOA) reflectance, and located at 19N UTM zone with 0% cloud cover and less than 10 m resolution. For the Landsat-8 application, we downloaded the image LC08_L1TP_001073_20200406_20200410_01_T1 (United States Geological Survey, 2013) that combines metadata ETM+, Operational Land Imager (OLI), and the Thermal Infrared Sensor (TIRS), with seasonal coverage of the global landmass at a spatial resolution of 30 m (visible, NIR, SWIR), 100 m (thermal), and 15 m (panchromatic). The third application of a Digital Elevation Model has the following characteristics: DEM ASTER Level 1A, with a spatial resolution of 15 m in the horizontal plane, and 0 % cloud cover. The ID of the acquired image is AP_17242_PLR_F6820_RT1 (ASTER, 2018).

The satellite images (Supplementary Material - Figures; Fig. 1) differentiate the local domains by texture, color, structure, and shape (Supplementary Table 01_Remote Sensing Data). The Sentinel-2 band combination R: 4, G: 3, B: 2 provided a naturally colored image (Drusch et al., 2012) similar to the authentic natural colors seen in the field. For the CUMC geological map, this image highlighted the DI felsic composition with a greater volume of mafic bodies and the main E-W structures, in comparison to DII and DIII. Two Landsat-8 images also supported the definition of the domains. The Landsat-8 image band combination of yellow tone (R: 10, G: 7, B: 3) coated DIII gray, lightened DII and IG, and defined the DIII and UCD boundaries (see below for Domain descriptions). The blue image (R: 1, G: 2, B: 5) highlights DI and UCD, and colors them more bluish and scratchier than DII and DIII. The Digital Elevation Model generates the shaded relief that exaggerates the natural relief, enhances main structures such as faults and contacts, and differentiates the appearances of the different domains.

2.3.2 Separation and preparation of zircon crystals

Zircon concentration was performed at the Laboratory of Geochronology of the University of Brasilia. Approximately 30 kg each of six samples were crushed in a jaw crusher, ground in a vibratory cup mill, and sieved to different grain sizes (<250 μm). This was followed by the separation of minerals by density. Then, the concentrate of heavy minerals underwent magnetic separation using a Frantz isodynamic separator. About 60–90 zircon grains were separated by handpicking from each sample. These grains were cast into an epoxy mount, polished to half thickness, and the polished surfaces were characterized by backscattered electron (BSE) and cathodoluminescence (CL) imaging using a FEI QUANTA 450 scanning electron microscope (SEM).

2.3.3 U–Pb isotope analysis

U–Pb isotope analysis on zircon was performed by LA-ICP-MS at the same Laboratory (Supplementary Table 2_U–Pb) with a Thermo-Fisher Neptune HR-MC-ICP-MS instrument, coupled to a Nd: YAG UP213 New Wave laser-ablation system. The analyses were performed based on the standard-sample bracketing method (Albarède et al., 2004) using the GJ-1 standard (Jackson et al., 2004) to control fractionation. The 91500 reference zircon (Wiedenbeck et al., 1995, 2004) was also analyzed as an unknown during analytical sessions. Tuned masses were 238, 232, 208, 207, 206, 204 and 202. Integration time was 1 s and ablation time was 40 s. Spot size was 30 μm and laser adjustment was 10 Hz and 2–3 J/cm^2. The $^{207}Pb/^{206}Pb$ and $^{206}Pb/^{238}U$ ratios were time-corrected. Data reduction was done with the in-house Chronus software of the UnB Geochronology Laboratory (Oliveira, 2015).

Common ^{204}Pb was monitored based on the ^{202}Hg and (^{204}Hg + ^{204}Pb) masses. It was not necessary to correct for the common Pb contribution (^{204}Pb). Analytical errors were propagated by the quadratic addition [(2SD ^ 2 + 2SE ^ 2) 1/2] (SD = standard deviation; SE = standard error) of external reproducibility and performance accuracy. External reproducibility is represented by the standard deviation generated from repeated analyses (n = 20, ~1.1% for $^{207}Pb/^{206}Pb$ and up to ~ 2% for $^{206}Pb/^{238}U$) of the GJ-1 zircon standard during the analytical sessions, and performance accuracy was taken as the standard error calculated for each analysis. The data are shown in Concordia diagrams with 2σ error ellipses, and weighted mean ages were calculated with the Isoplot-3/Ex. software (Ludwig, 2012). The geological time scale adopted here is the updated version of the scale by Cohen *et al.* (2013). More details about the U–Pb methodology on zircon at this laboratory can be found in Bühn et al. (2009).

2.3.4 Lu–Hf isotope analysis

Lu–Hf isotopes (Supplementary Table 3_Lu–Hf) were analyzed on the same instrument used for U–Pb isotope analysis. The Lu–Hf isotope data were collected over 40–50 s of ablation time, using a 40 μm diameter spot size, and an energy of 85%. The selection of crystals for Lu–Hf analyses was based on these parameters: concordant U–Pb data (concordance of 6/8 and 7/6 ages), complexities (rim and core of different ages), and crystal size. When possible, the Lu–Hf spot was placed as close as possible to the earlier spot for U–Pb analysis to analyze portions of the zircon grain with the same U and Pb isotopic characteristics. The signals of the interference-free isotopes ^{171}Yb, ^{173}Yb and ^{175}Lu were monitored during analysis to correct for isobaric interferences of ^{176}Yb and ^{176}Lu on the ^{176}Hf signal. The ^{176}Yb and ^{176}Lu contribution was calculated using the isotopic abundances of Lu and Hf proposed by Chu et al. (2002). The contemporaneous measurements of ^{171}Yb and ^{173}Yb provide a method to correct for mass-bias of Yb using a $^{173}Yb/^{171}Yb$ normalization factor of 1.132685 (Chu et al., 2002). Hafnium isotope ratios were normalized to the $^{179}Hf/^{177}Hf$ value of 0.7325 (Patchett, 1983). A detailed description of the procedures and methods is given in Matteini et al. (2010).

Data obtained from zircon crystals were processed in a Microsoft Excel macro (adapted from Bertotti, 2012 and Bertotti et al., 2013) to calculate the corrected values of $^{176}Hf/^{177}Hf$ and $^{176}Lu/^{177}Hf$. The calculation of $\varepsilon Hf_{(T)}$ values used the decay constant λ = $1.865 * 10^{-11}$ after Scherer et al. (2006), and the $^{176}Lu/^{177}Hf$ = 0.0332 and $^{176}Hf/^{177}Hf$ = 0.282772 CHUR values after Blichert-Toft and Albarède (1997). The average crustal Lu/Hf ratio allows to calculate two-stage T_{DM} ages from the initial Hf isotopic composition (Gerdes and Zeh, 2006, 2009; Nebel et al., 2007). For the time of zircon crystallization, the two-stage depleted mantle Hf model ages (T_{DM} Hf) are calculated using $^{176}Lu/^{177}Hf$ = 0.0384 and $^{176}Hf/^{177}Hf$ = 0.28325 for the depleted mantle (Chauvel and Blichert-Toft, 2001) and the $^{176}Lu/^{177}Hf$ value of 0.0113 for the average crust (Taylor and McLennan, 1985; Wedepohl, 1995).

Before Hf isotope measurements on zircon, replicate analyses of a 200 ppb Hf JMC 475 standard solution doped with Yb (Yb/Hf = 0.02) were obtained ($^{176}Hf/^{177}Hf$ = 0.282162 ± 13 2σ, n = 4). During the analytical session, replicate analyses of the GJ-1 reference zircon were done, which yielded an average $^{176}Hf/^{177}Hf$ ratio of 0.282006 ± 16 (2σ, for n = 25), in agreement with the reference value for the GJ standard zircon obtained by Morel et al. (2008).

2.4 Geology of the Cerro Uyarani Metamorphic Complex

Field work allowed to recognize two main units (see map, Fig. 2), the Tertiary volcaniclastic cover denominated the Ignimbrite Domain (IG), and the Paleoproterozoic to Mesoproterozoic granulitic to amphibolitic basement. The second unit had not been differentiated in previous works (Wörner et al., 2000; Oliveira et al., 2017). Here we distinguish four granulite domains (Table 1): the Felsic Granulite Domain I (DI), Felsic Granulite Domain II (DII), Banded Granulite Domain III (DIII), and an Undifferentiated Crystalline Domain (UCD). The latter one has not been explored yet in the field. The granulite domains are foliated and banded, and lithotypes maintain the compositional and structural segregation generated during migmatization. Based on the field characteristics and the aspects of zircons (Fig. 11.8–14), we interpret that these granulites represent a migmatite complex. The outcrops of felsic granulite in DI and DII comprise leucosome and in some cases mesosome. The banded granulites of DIII are interpreted as a mesocratic migmatite, and the amphibolite present in DI and, locally, in DII and DIII is interpreted as a melanosome.

Satellite images were used to confirm and delimit the extension of the domains differentiated by field characteristics and petrography. The features used to classify the domains based on the remote sensing data are summarized in Supplementary Table 1_Remote Sensing Data. In the following, each domain will be described. Brief petrographic descriptions of the recognized lithotypes are presented in Table 2. We inserted other field information in the outcrop map (Supplementary Material - Figures; Fig. 2).

2.4.1 Ignimbrite domain - IG: Perez Formation

The Pliocene ignimbrite deposit in the area of the CUMC corresponds to the Perez/Lauca Formation (Muñoz 1988b). The main occurrence of ˜ this formation, of approximately 3.9 km × 1.5 km, is in the northern portion of the Cerro Uyarani Metamorphic Complex.

The contact against granulites is distinct in the northeastern part. A second, smaller body occurs in the central-western portion of the study area. The ignimbrite forms plateaus in broad valleys and is characterized by flow banding. It is rich in light gray, very fine-grained, crystal rich pumice. Biotite phenocrysts, quartz crystaloclasts of millimeter to centimeter size, and centimeter-sized, dark gray, very fine-grained, red, mafic lithoclasts are embedded in an aphanitic matrix.

Table 1: Summary of geological aspects related with the main domains of CUMC

Domains/Samples	Coordinates	Rock type	Protolith at ~1.2 Ga	Mafic mineral index	Structure	Granulometry	Chemical composition
Felsic Granulite Domain I (DI)							
Foliated facies							
UY1422	Lat: 18° 26’ 26.92” S Long: 68° 38’ 22.87” W	Felsic granulite	Migmatite (Leucosome)	Leucocratic	Weakly foliated to foliated	Medium to coarse-grained	Granite
UC005	Lat: 18° 26’ 46.25” S Long: 68° 38’ 29.11” W						
Banded facies							
UC004	Lat: 18° 26’ 46.41” S Long: 68° 38’ 26.00” W	Banded granulite	Migmatite (leucosome and few melanosomes)	Mesocratic	Banded	Medium-grained	Granodiorite
UC021*	Lat: 18° 27’ 48.18” S Long: 68° 39’ 28.34” W						
Plagioclase rich foliated facies							
UC009	Lat: 18° 26’ 53.81” S Long: 68° 38’ 52.38” W	Felsic granulite	Migmatite (leucosome and few melanosomes)	Leucocratic	Weakly foliated to foliated	Medium-grained	Granodiorite to tonalite or quartz-diorite
Felsic Granulite Domain II (DII) – foliated facies							
UY1337*	Lat: 18° 28’ 41.91” S Long: 68° 38’ 24.30” W	Felsic granulite	Migmatite (Leucossome)	Leucocratic	Weakly foliated	Coarse-grained	Granite to Granodiorite
Banded Granulite Domain III (DIII)							

Leucocratic banded facies							
UC019	Lat: 18° 27’ 52.86” S Long: 68° 39’ 39.72” W	Banded granulite	Protolith or Migmatite (leucosome)	Leucocratic to mesocratic	Banded and a few foliated outcrops	Medium-grained	Granodiorite, tonalite and diorite
UC017	Lat: 18° 27’ 49.46” S Long: 68° 39’ 49.41” W						
UC016*	Lat: 18° 27’ 47.71” S Long: 68° 39’ 56.02” W						
Mesocratic banded facies							
UC024	Lat: 18° 27’ 45.65” S Long: 68° 39’ 51.22” W	Banded granulite	Protolith or Migmatite (melanosome and few leucosome)	Mesocratic to melanocratic	Banded	Medium-grained	Tonalite to diorite
Tabular mafic bodies							
UC007	Lat: 18° 26’ 51.43” S Long: 68° 38’ 47.20” W	Mafic granulite	Residuum or Paleosome	Melanocratic	Tabular, foliated or banded	Medium-grained	Gabbro
UC004	Lat: 18° 26’ 46.41” S Long: 68° 38’ 26.00” W						
Mafic bodies (melanosome)							
UC001*	Lat: 18° 26’ 46.40” S Long: 68° 38’ 18.40” W	Amphibolite	Paleosome or Melanosome	Melanocratic	Elongated, ovoid and sigmoidal	Very fine-grained to fine-grained	Alkali-gabbro, gabbro and syeno-gabbro
UC10II*	Lat: 18° 27’ 58.11” S Long: 68° 39’ 11.71” W						

UC032*	Lat: 18° 26’ 38.22” S Long: 68° 38’ 30.01” W						
UY1421	Lat: 18° 26’ 26.92” S Long: 68° 38’ 22.87” W						

Obs.: (*) Samples that were analyzed by U-Pb

Table 02: Summary of petrographic aspects related with the main domains of the CUMC.

Domains/Samples	Coordinates	Mineral assemblage	Disequilibrium features	Details	Granoblastic texture
Felsic Granulite Domain I (DI)					
Foliated facies					
UY1422	Lat: 18° 26’ 26.92” S Long: 68° 38’ 22.87” W	qz (~35%) + afs (~30%) + pl (~30%) + opx (5-10%) + phl (2-5%) ± cpx (<5%) ± amp (<2%) + hem + Ilm + mag (~2%) + ap + zrn + rt (~1%)	Rm*: ser + act-trem + musc + chl + ep + brown mica; opx uralitized with amp rims; simplectitic brown mica with pl; brown mica lamellae at opx fractures	Perthitic afs or microcline with graphic texture; quartz chessboard extinction; vermicular quartz included or intergrown with pl and afs; myrmekite; small mafic mineral crystals (amp + cpx + opx + phl) in nematoblastic levels; amphibole with brown mica inclusions	Polygonal and decussate
UC005	Lat: 18° 26’ 46.25” S Long: 68° 38’ 29.11” W				
Banded facies					
UC004	Lat: 18° 26’ 46.41” S Long: 68° 38’ 26.00” W	Felsic band: pl (25-35%) + qz (20-35%) + afs (35-40%) + opx (10%) ± cpx (<2%) + phl (2-5%) + mag (~3%) + ap + zrn + rt (~1%)	Rm*: act-trem + ser + brown mica + Musc; simplectitic brown mica with pl; second brown mica is poorly developed and interstitial at contacts with other minerals	Cpx and amp aggregates with rt exsolution (as sagenitic texture) in cpx; carbonate microveins; afs elongated and with perthite; microcline + afs; graphic texture in afs, some granular quartz grains occur at an irregular grain boundary with pl and afs; opx envelopes small, rounded quartz grains	Decussate
UC021*	Lat: 18° 27’ 48.18” S Long: 68° 39’ 28.34” W	Mafic band: afs (~35%) + pl (~25%) + qz (~20%) + opx (~10%) + amp (10%) ± cpx (<5%) + phl (~2%) + mag (~3%) + ap + zrn + rt (~1%)			
Plagioclase rich foliated facies					
UC009	Lat: 18° 26’ 53.81” S Long: 68° 38’ 52.38” W	pl (~50-55%) + qz (25-30%) + afs (~5%) + opx (~5-10%) + phl (~8%) + mag (~5%) ± cpx (<5%) + amp (<5%) + ap + zrn + ttn (~2%)	Rm*: cb + saussurite + brown mica	Carbonate microveins cutting the banding; quartz is granular to slightly elongated or shows vermicular intergrowth with afs+qz; phlogopite occurs associated with pyroxene; 43ith43ngsita43tion of feldspar (also secondary carbonate)	Decussate
Felsic Granulite Domain II (DII) – foliated facies					

UY1337*	Lat: 18° 28' 41.91" S Long: 68° 38' 24.30" W	pl (~40%) + qz (~30%) + afs (~20%)+ amp (~10%) + opx (~5%) + cpx (<3%) + phl (~2%) + mag (~3%) + ap + zrn + ttn (~2%)	Rm*: ser + clay minerals + chl + 44ith44ngsita-group minerals	Qz with irregular and ameboid limits, chessboard extinction; rounded and vermicular shapes of some quartz grains intergrown with tabular phlogopite; afs with perthite texture and partially replaced by clay-minerals	Decussate 44ith polygonal spots
Banded Granulite Domain III (DIII)					
Leucocratic banded facies					
UC019	Lat: 18° 27' 52.86" S Long: 68° 39' 39.72" W	pl (40-55%) + qz (15-30%) + afs (6-15%) + phl (5-10%) + opx (5-7%) + amp (<5%) ± cpx (<4%) + mag + hem (~5%) + ap + zrn + rt (~2%)	Rm*: ser + act-trem + brown mica + amp	Pl with myrmekite; afs with graphic texture; microcline or perthite afs; opx and cpx relics, practically all replaced by amphibole; qz + pl + bt microveins	Decussate, interlobate and ameboid
UC017	Lat: 18° 27' 49.46" S Long: 68° 39' 49.41" W				
UC016*	Lat: 18° 27' 47.71" S Long: 68° 39' 56.02" W				
Mesocratic banded facies					
UC024	Lat: 18° 27' 45.65" S Long: 68° 39' 51.22" W	pl (40-45%) + qz (15-20%) + afs (8-10%) + amp (10-20%) + opx (10-15%) + phl (~10%) + cpx (5-10%) + mag + hem (~5%) + ap + zrn (~2%)	Rm*: ser + musc + amp	Afs granular and slightly perthitic; weakly bent tabular reddish-brown mica (phl); opaque vermicular minerals; dark green amp partially replaced by pyroxene	Interlobate
Tabular mafic bodies					
UC007	Lat: 18° 26' 51.43" S Long: 68° 38' 47.20" W	amp (25-35%) + pl (15-30%) + cpx (~15%) + opx (~10%) + afs (5%) + mag + hem (~10%) + ap + rt (~2%)	Rm*: amp	Brown green to yellow green amphibole replaced partially by pyroxene and associated with small crystals of brown mica; high occurrence of opaque minerals; no quartz; felsic bands of pl + amp + mag	Polygonal
UC004	Lat: 18° 26' 46.41" S Long: 68° 38' 26.00" W				
Ovoid Mafic bodies					
UC001*	Lat: 18° 26' 46.40" S Long: 68° 38' 18.40" W	pl (40-60%) + amp (15-30%) + cpx (10-20%) ± phl (10-15%) + afs (~10%) + mag + hem	Rm*: amp + clay minerals and mica	A few replacement minerals; accumulationses of amp and px common; rare quartz grains	Polygonal and interlobate

UC10II*	Lat: 18° 27’ 58.11” S Long: 68° 39’ 11.71” W	(~10%) + zrn + ap + ttn (~3%) ± qz (< 1%)				
UC032*	Lat: 18° 26’ 38.22” S Long: 68° 38’ 30.01” W					
UY1421	Lat: 18° 26’ 26.92” S Long: 68° 38’ 22.87” W					

Obs.:

(*) Samples that were analyzed by U-Pb

Abbreviations for names of rock-forming minerals: afs – alkali feldspar; amp – amphibole; ap – apatite; bt – biotite; cpx – clinopyroxene; hem – hematite; ilm – ilmenite; mag – magnetite; opx – orthopyroxene; phl – phlogopite; pl – plagioclase; qz – quartz; rt – rutile; ttn – titanite (sphene) and zrn – zircon (Whitney and Evans, 2010).

***Rm – Retrometamorphism**

2.4.2 Felsic granulite domain I

A leucocratic, pinkish, medium-to coarse-grained felsic granulite with a granitic appearance alternating with foliated and banded layers dominates ca. 62% of the CUMC outcrops and defines Domain I (DI). Main minerals are quartz and feldspar, besides minor biotite, pyroxene, amphibole and magnetite. The foliation is emphasized by the orientation of mafic minerals (Fig. 3ATable 2). The banding (S2) is characterized by an intercalation of mafic and felsic bands of 0.5–5 cm width. The same compositions are observed in the foliated and leucocratic felsic granulite parts.

The well-marked foliation (S1) and discontinuous banding (S2, Fig. 3A) are generally parallel (S1//S2 of 197/27) and trend in E-W direction (Fig. 2). In the southern portion of the domain, S1/S2 become sub-horizontal, and in the western part, the structures dip shallowly to the SW (see also Oliveira et al., 2017). In the smaller body in the center of the complex (Fig. 2), S1 and S2 trend N–S. There are several open folds.

Several rounded to sigmoidal, centimeter wide amphibolite bodies, locally deformed into recumbent folds or boudinaged (Fig. 3B and D), and a few tabular and lens-shaped mafic granulite bodies with parallel banding (Fig. 3C) are associated with DI. The banding is locally highly deformed, with simple and complex folding, as, for example, observed at points UC004, UC021, UC007 and UC017 (Fig. 3A, B, 3D, 3F). Pegmatite veins of centimeter width extend parallel to foliation and banding. In some areas, this domain shows some characteristics of the precursor (e. g., at point UC007, where a discordant gneiss with an oblique orientation - in comparison to the foliation of the host rock – occurs (Fig. 3D). From ten samples collected from this domain, sample UC021 was selected for U–Pb/Hf analysis on zircon.

2.4.3 Felsic granulite domain II

Domain II (DII) is well defined in the south-central portion of the complex (Fig. 2). The Landsat-8 image provides clear contacts of this domain against both DI and DIII (Fig. 2). This domain is characterized by two main facies: a leucocratic, pinkish, and coarse-grained, massive facies with local occurrence of mafic enclaves (Fig. 3E), and a less abundant mesocratic, gray, plagioclase-rich, banded, medium-grained facies. Small mafic amphibolite or mafic granulite (Fig. 3E) bodies occur along the boundary between these facies. The leucocratic massive facies is composed of quartz and feldspar, with rare brown mica, brown pyroxene, and magnetite (Table 2). Local foliation is enhanced by mafic minerals, such as biotite and brown pyroxene. The mesocratic facies is banded and shows chevron folds and ovoid amphibolite enclaves. The enclaves have a nebulitic appearance and can extend parallel to the banding. A mafic band, 0.5–20 cm wide, is dark-gray, medium-grained, and rich in amphibole. Locally, as at point UCR015, the two facies occur parallel to each other (Fig. 3E). Sample UY1337 is representative of the leucocratic facies of Felsic Granulite Domain II and was selected for U–Pb/Hf isotopic analysis.

2.4.4 Banded Granulite Domain III

Domain III (DIII) occurs in the central part of the CUMC and as a smaller outcrop to the south of the main complex (Fig. 2). DIII has tonalitic composition and comprises two lithofacies (Fig. 3F): a gray, medium-grained, mesocratic type of bands, equivalent to the brown bands in the Sentinel-2 data, and yellowish, leucocratic, quartzofeldspathic bands, equivalent to the beige bands in the same image. These lithofacies are characterized by symmetrical and open folds, and crenulation. In the northwestern part, S1 is parallel to S2, and according to Oliveira et al. (2017), it is banded in NE-SW direction, changing to N–S direction in the southern outcrop.

The mesocratic gray and medium-grained facies shows millimeter to centimeter wide bands composed of pyroxene, amphibole, and dark mica, alternating with plagioclase, quartz, and rare alkali-feldspar rich bands. The leucocratic, yellowish to pinkish, medium-grained, banded facies contains accumulations of reddish-brown orthopyroxene. A few small amphibolite enclaves with sharp contacts and up to 30 cm wide, grayish, and medium-grained mafic bands composed of amphibole and pyroxene were noted.

The contact between domains DIII and DI is well distinguished by the lithological change from granitic aspect (samples UC021 and UC022 in Fig. 3B), to the gray tonalitic rock (represented by outcrop UC017 in Fig. 3F). Sample UC016 from Domain III was selected for U–Pb/Hf isotopic analysis.

2.4.5 Mafic bodies

Small, 3–5 m wide, rounded and elongated amphibolite bodies, and tabular, even smaller, lens-like bodies of mafic granulite, are hardly visible in the Sentinel-2 image.

Amphibolite bands and pods: Amphibolites, commonly associated with DI (Fig. 2), occur in little bodies of 5–50 cm size. They also occur locally associated with DII or DIII. These bodies are here interpreted as melanosome. These occurrences are tabular, pod-like or lensoid in shape, and in part boudinaged. In the central part of DI, they occur as deformed, lensoid or sigmoidal enclaves or as elongated, folded bodies (Fig. 3B). Contact with the felsic granulite host is mostly sharp but locally there are also more gradational to even nebulous transitions. The amphibolite occurrences are melanocratic, very fine-to fine-grained, dark gray, and massive to foliated. Amphibole and plagioclase are the main minerals, but pyroxene and opaque minerals may also be present. Representative amphibolite samples for U–Pb/Hf isotope analysis are UC001 and UC 10II, both of which were hosted by Felsic Granulite of Domain I (Fig. 2).

Mafic granulite: Melanocratic, dark gray, fine-to medium-grained, tabular, mafic bodies, 2–5 m in extent, occur mainly associated with DI (Fig. 3C). They have lenticular shapes and were identified at points UC004, UC005 and UC007 (Table 1). Laterally, the bodies are thin and segregate into lenses. Some show schollen character. The mineral composition is similar to that of the amphibolites. The mafic granulites are foliated and banded, and have centimeter-wide felsic bands of feldspar, besides amphibole or pyroxene (Fig. 3C). In thin section, the presence of orthopyroxene and clinopyroxene allows to classify this rock type as a mafic granulite.

2.5 Results

2.5.1 U–Pb

U–Pb isotopic data (Table 3) for zircon from felsic granulite samples UC021 (DI banded facies) and UY1337 (DII foliated facies) that both represent leucosome, for sample UC016 from a more tonalitic part interpreted as paleosome (DIII), and from three amphibolite samples from Domain I, UC032, UC010II and UC001, interpreted to represent melanosome, were obtained. All isotopic results are compiled in the Supplementary Data file CUMC U–Pb.

Sample UC021 - domain I

Zircon crystals from the Felsic Granulite of DI are 100–300 μm long, translucent, brownish, and strongly fractured. They may have inclusions of acicular apatite and magnetite. The crystals are mostly subhedral and prismatic, but a few are ovoid. BSE and CL imaging indicates that cores with oscillatory-zoning are truncated or overgrown by younger zoned domains, resorption domains, and so-called recrystallized rims (Kroner ¨ et al., 2014, Fig. 4). Forty-nine U–Pb analyses on cores and rims were obtained for this sample.

From thirty-one concordant ages, a Paleoproterozoic population with $^{207}Pb/^{206}Pb$ ages between 1757 and 1567 Ma and a Mesoproterozoic population with $^{207}Pb/^{206}Pb$ ages between 1209 Ma and 1154 Ma can be identified. An upper intercept age of 1742 ± 53 Ma (MSWD = 2.9) was obtained from twelve analyses on Paleoproterozoic cores with Th/U ratios between 0.35 and 1.05. According to the CL images, the zircon cores are relatively large, with a well-preserved oscillatory zonation (ZR 26C). There are also small core remnants with unidentifiable texture (ZR 8C). Seventeen zircon rims, with complex textural domains, gave an upper intercept age of 1190 ± 9.3 Ma (MSWD = 0.96). These grains have Th/U ratios of 0.04–0.51. CL analysis reveals oscillatory rims around Paleoproterozoic cores, in some cases cracked due to expansion of older cores (ZR 8R).

There are some grains with oscillatory zoned overgrowth that did not show any difference in age when core and rim were analyzed (ZR 11, Fig. 4). A few homogeneous younger rims cut ~1.19 Ga cores (ZR 18). This grain with a wide, homogeneous rim of high CL brightness (Fig. 4, inset) gave a concordant age of 1087 ± 17 Ma (Th/U ~0.36). The weakly zoned, medium luminescent, recrystallized rim of Zr 9 gave a 970 ± 20 Ma age (Th/U ~0.37) - the youngest age determined for this sample.

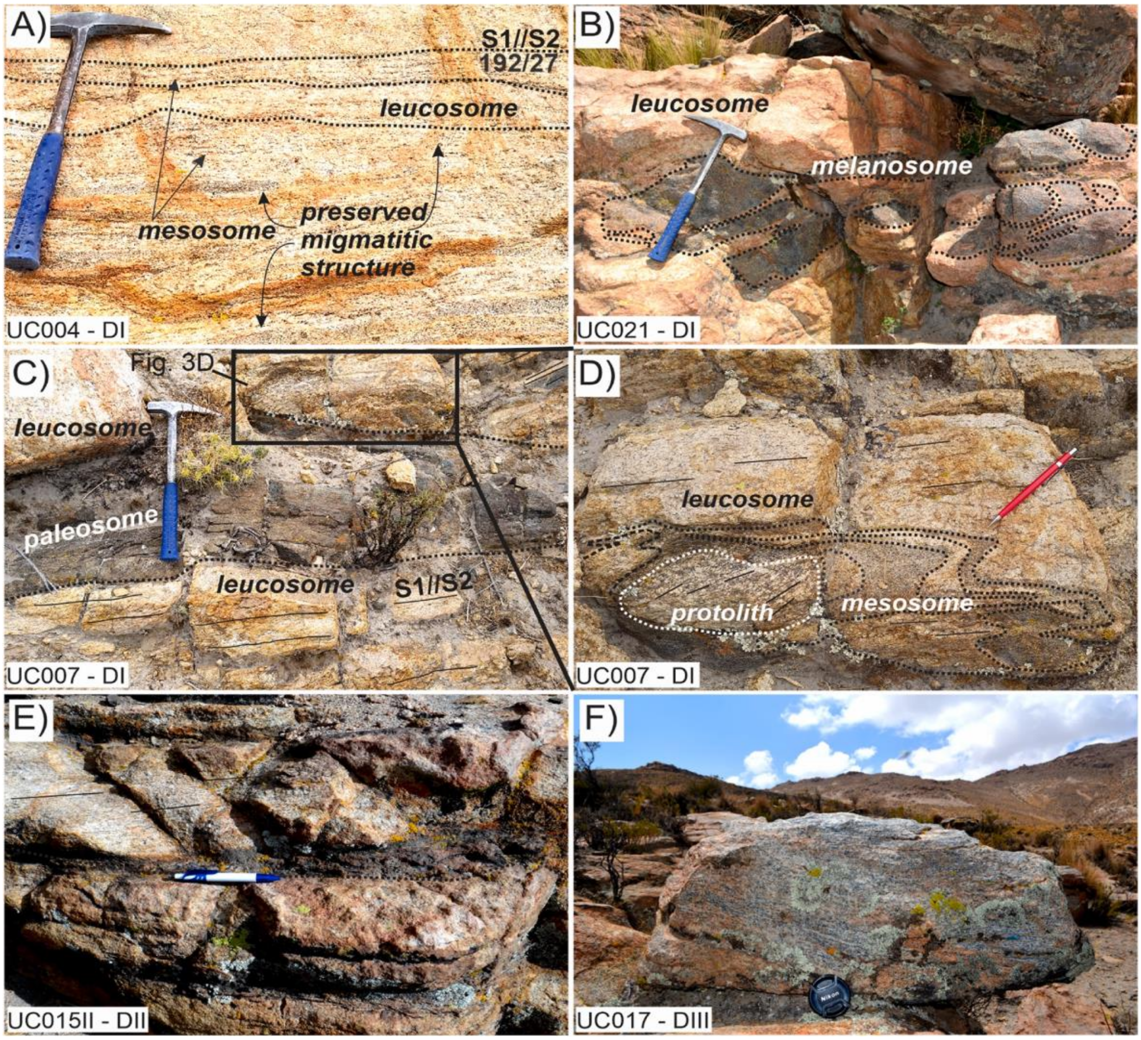

Figure 3. Field photographs from the Cerro Uyarani Metamorphic Complex. A) Aspect of the felsic granulite from Domain I in the NE part (UC006) and B) Felsic granulite in contact with a cm-sized folded and boudinaged amphibolite body at point UC021. The structures of the felsic granulite are not well-defined due to a low abundance of mafic minerals, and the reddish color is due to alteration of the alkali-feldspar. C) Abrupt contacts between mafic and felsic granulite (UC007). The tabular shape suggests a dyke or sill structure for the protolith, but as there is no lateral continuity, a raft structure of a paleosome would be our preferred interpretation. D) Detail of Fig. 3C, with a rare occurrence of a domain gneiss that may represent the original protolith for the migmatites. E) Aspect of the foliated felsic granulite from DII outcrop (UC015II). At the bottom of the photo, a contact of foliated felsic granulite with gneissic facies, with a centimetric, deformed mafic body indicating a shear zone. F) Characteristics of Domain III: tonalitic facies and a strong gneissic fabric, with some migmatitic structures, with a granulite mineral assemblage.

Table 03. Summary of U-Pb isotope analysis by LA-ICP-MS results on zircon and titanite grains from granulites and amphibolite of CUMC.

Domains	Sample	Cordinate	Age (Ma)	Internal texture and/or domains
Felsic Granulite Domain I	UC021	Lat: 18°27'48.18" S Long: 68°39'28.34" W	1742±53 Ma	magmatic and resorbed cores and relicts
			1190±9 Ma	oscillatory-zoned rim and convolute overgrowth
			1087±8 Ma	homogeneous rims, gray in CL

Felsic Granulite Domain II	UY1337	Lat: 18°28'41.91" S Long: 68°38'24.30" W	1767±22 Ma	well-developed oscillatory zoning and resorbed cores
			1190±14 Ma	fluid-induced recrystallization
			1046±20 Ma	homogeneous rims, gray in CL
Banded Granulite Domain III	UC016	Lat: 18°27'47.71" S Long: 68°39'56.02" W	1883±18 Ma	sectorial zoned core
			1802±21 Ma	magmatic and blurred cores
			1273±15 Ma	dark luminescent local recrystallized domain
			1170±13 Ma	oscillatory overgrowths, gray in CL
			1101±15 Ma	convolute texture
Amphibolite	UC032	Lat: 18° 26' 38.22" S Long: 68° 38' 30.01" O	1885±7 Ma	magmatic relict core
			1810±19 Ma	oscillatory-zoned, blurred, resorbed cores
			1674±53 Ma	oscillatory-zoned and blurry cores
			1190±17 Ma	partial concentric zoning, dark-gray in CL
			1007±9 Ma	weakly convolute zoned new zircon, dark-gray in CL
	UC010II	Lat: 18° 27' 58.11" S Long: 68° 39' 11.71" W	1173±23 Ma	unzoned and weakly concentrically zoned zircon
			1026±7 Ma	unzoned or concentric wide zonation internal textures
	UC001	Lat: 18°26'46.40" S Long: 68°38'18.40" W	985±10 Ma	zr - oval grain; internal homogeneous texture
			1045±7 Ma	ttn - round and flat plates; internal homogeneous texture

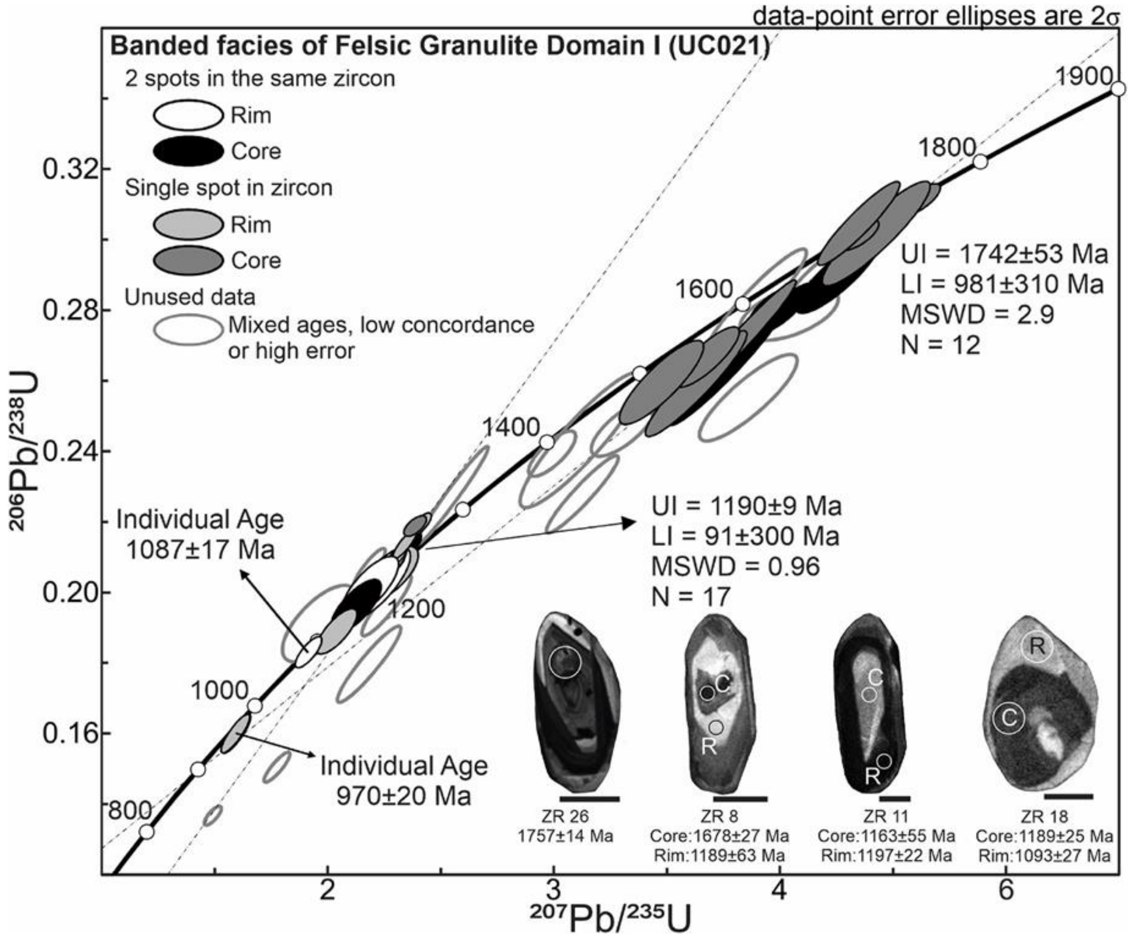

Figure 4. U–Pb concordia diagram for the felsic granulite from DI (sample UC021). On the basis of the upper intercept $^{207}Pb/^{206}Pb$ ages, two different populations of zircon were identified with ~1742 (mainly cores) and 1190 Ma (cores and rims) ages. The two youngest zircon rims have concordia ages of 1087 ± 17 and 970 ± 20 Ma. The four representative CL images of zircon included here show a Paleoproterozoic restitic core (ZR 8) and an oscillatory-zoned core (ZR 26), a Mesoproterozoic oscillatory-zoned zircon (ZR 8, ZR 11), and a homogeneous bright rim (ZR 18). Information for Figs. 4–9: Errors of individual data are stated at 2σ confidence limits. Analysis spots and obtained ages (apparent $^{207}Pb/^{206}Pb$ ages) are indicated below each zircon image. All scale bars on zircon grains are equivalent to 50 μm length. The blue ellipses, generated by Isoplot, represent the calculation of Concordia ages. UI: Upper Intercept; LI: Lower Intercept; C: Core; R: Rim; F.I.: Fluid Induced alteration.

Sample UY1337 - domain II

The zircon crystals, from the foliated facies of Felsic Granulite of DII, are 35–375 μm long, translucent, pink to brownish, subhedral, and slightly prismatic to subrounded. Many fractures and inclusions of magnetite and acicular apatite occur. The BSE and CL images show cores with oscillatory zoning and rims with altered domains and homogeneous overgrowth textures and with local recrystallization (Fig. 5). One hundred and three spots were analyzed on cores and rims.

Sixty-two analyses with concordance between 88 and 113% can be grouped into three populations. A Paleoproterozoic population with $^{207}Pb/^{206}Pb$ ages ranging from 1774 to 1537 Ma and two Mesoproterozoic population, one with $^{207}Pb/^{206}Pb$ ages between 1226 and 1152 Ma, and another with $^{207}Pb/^{206}Pb$ ages between 1069 and 976 Ma.

Forty-two analyses define an upper intercept age of 1767 ± 22 Ma for zircon with high Th/U ratios between 0.39 and 1.04. Cathodoluminescence images show cores with well-developed oscillatory zoning (ZR 4, Fig. 5 inset) and with resorption textures (ZR 18, Fig. 5 inset). For the oldest Mesoproterozoic age group, eleven data define an upper intercept age of 1190 ± 14 Ma. This includes data obtained on irregular low luminescence (CL) domains, cutting the zoning discordantly (ZR 4, and ZR 28), and homogeneous rims around old cores (ZR 18). Sometimes sector zoning in zircon cores is observed (ZR 39, Fig. 5 inset). A thin, irregular layer may separate cores from rims (ZR 4).

The youngest age population for this sample includes nine analyses on rims, with ages between 1069 and 976 Ma ($^{207}Pb/^{206}Pb$). CL images illustrate recrystallized rims with high luminescence and homogeneous texture around older cores (ZR 18, Fig. 5 inset). These zircon crystals have very variable Th/U ratios between 0.09 and 4.77. Five concordant results gave an age of 1048 ± 8 Ma. The two youngest concordant rim data gave a Concordia age of 969 ± 16 Ma.

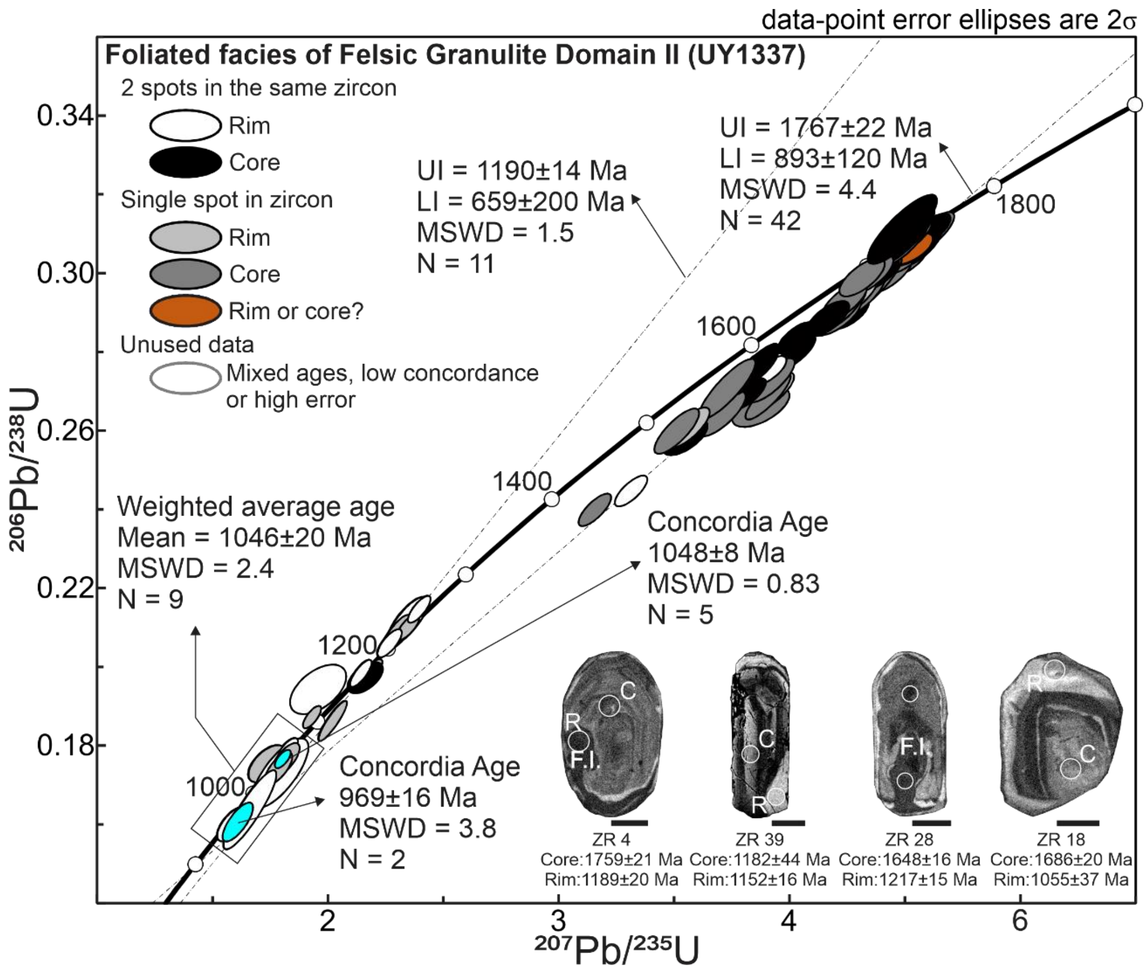

Figure 5. U–Pb concordia diagram for the felsic granulite from DII (sample UY1337). The upper intercept 207Pb/206Pb ages are ~1767 (mainly cores) and 1190 Ma (cores and rims), respectively. Five youngest zircon rims define a Concordia age of 1048 ± 8 Ma, and two concordant zircons yielded a Concordia age of 969 ± 16 Ma. This cloud of concordant zircon data relates to a weighted average of 1046 ± 20 Ma. The CL images show a Paleoproterozoic oscillatory-zoned core (ZR 4, ZR 18) with altered dark-luminescent domains (ZR 4 and ZR 28), a rare sectorial texture in the core (ZR 39), and a light-luminescent homogeneous rim (ZR 18) that is separated from the core by a dark margin

Sample UC016 - domain III

The zircon crystals from the leucocratic banded facies of the Banded Granulite of DIII are 80–350 μm long, transparent, and colorless, and have subhedral to anhedral, prismatic to ovoid shapes. A few fractures and some inclusions of opaque minerals were observed. BSE and CL images show well-preserved, diverse, oscillatory zonation. Both convolute and homogeneous rims can occur around cores (Fig. 6). The CL images show very thin, high-luminescent haloes (ZR 18, ZR 42 and ZR 4) between the cores and the low- to medium-luminescent oscillatory rims. Intermediate areas of dark luminescence are probably recrystallized (ZR 18 and ZR 42) (Fig. 6 inset). In other cases, an oscillatory-textured overgrowth (ZR18 - Fig. 6 inset) can be observed.

Sixty-six U–Pb data were obtained on cores and rims. Fifty-two analyses have concordance between 109 and 88% and allow to distinguish a Paleo- to Mesoproterozoic population with $^{207}Pb/^{206}Pb$ ages between 1831 and 1554 Ma, and a Mesoproterozoic population with $^{207}Pb/^{206}Pb$ ages between 1262 and 1157 Ma. The Paleoproterozoic zircon population defines an upper intercept age of 1802 ± 21 Ma (Th/U ratios between 0.31 and 1.35). The CL images show cores with well-developed zoning (ZR 18 and ZR 4, Fig. 6 inset), some of them surrounded by new domains (ZR42, Fig. 6 inset). The oldest age from sample UC016 corresponds to a concordant analysis of 1883 ± 37 Ma (Th/U of 0.49) obtained on a sector-zoned core.

For the Mesoproterozoic population, a few recrystallized rims of medium CL luminescence and with wide oscillatory overgrowths (ZR18, Fig. 6 inset) gave an upper intercept age of 1170 ± 13 Ma (four zircon crystals with Th/U ratios <0.73). A concordant age of 1273 ± 29 Ma was obtained on a local, CL dark luminescent, recrystallized area on a single grain of Th/U ratio of 0.05. Two zircon crystals gave the youngest concordant ages for this sample of 1101 ± 29 Ma (ZR 4R, Th/U = 0.1) and 961 ± 25 (Th/U = 1.38). These young ages were determined for a convolute rim with low CL luminescence (ZR 4) and a homogeneous overgrowth (ZR 17), respectively. There are several thin, light gray luminescent rims that were too thin to be analyzed (such as ZR 4, Fig. 6 inset).

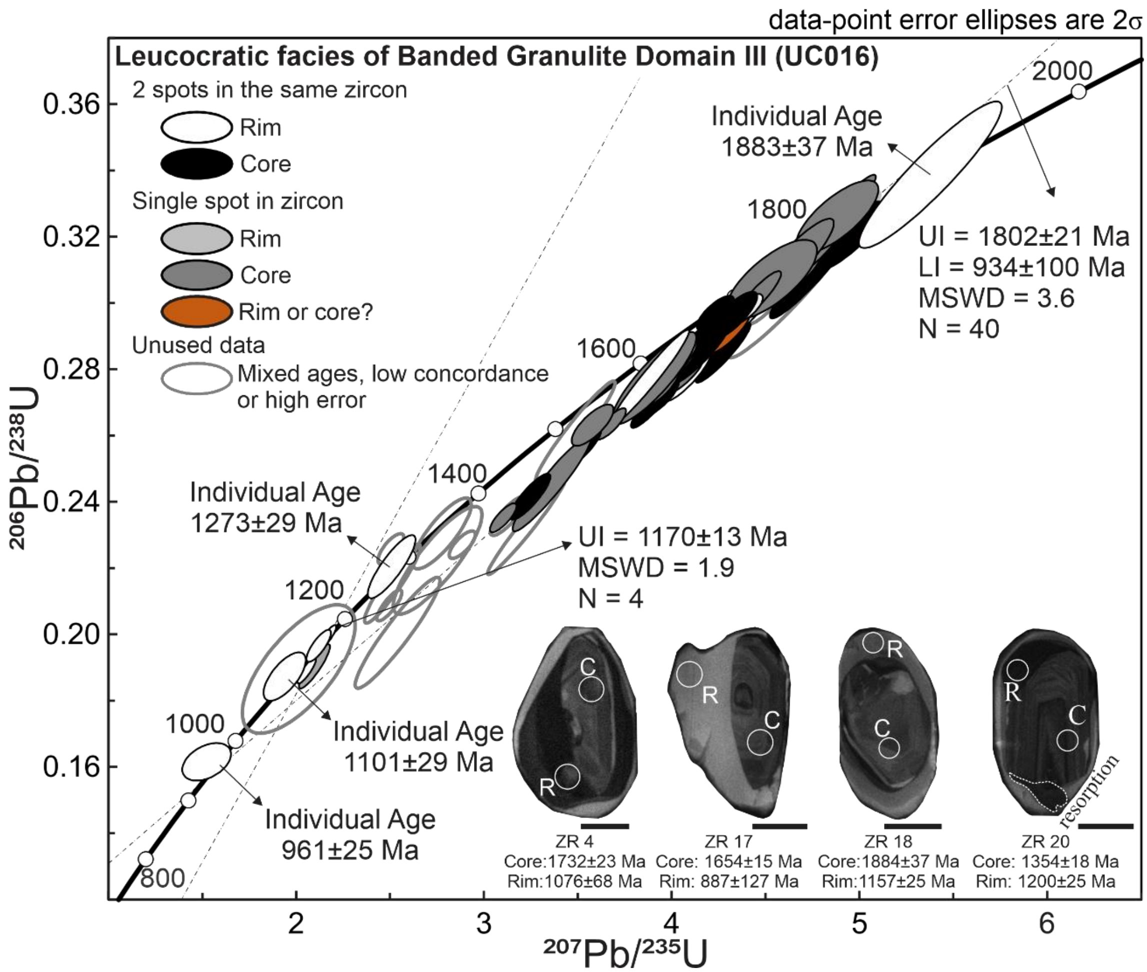

Figure 6. U–Pb concordia diagram for the mesocratic banded facies of granulite from DIII (sample UC16) The $^{207}Pb/^{206}Pb$ upper intercept Paleoproterozoic ages relate to a zircon population of ~1802 Ma, with ages mainly obtained in cores, with lower intercept age of ca. 934 Ma. Data for four younger zircon rims resulted in an upper intercept $^{207}Pb/^{206}Pb$ age of ~1170 Ma. The oldest age obtained is 1883 Ma from one concordant zircon core, and concordant zircon rims show individual ages of 1273, 1101 and 961 Ma. Four representative CL images exhibit well-preserved old cores with oscillatory (ZR 4, ZR 17, ZR 20) and sectorial (ZR 18) zonation. The CL images also show altered dark-luminescent domains (ZR 20, large oscillatory rims (ZR 18), convolute overgrowth (ZR 4), homogeneous, large, light-luminescent rims (ZR 17), and some evidence for resorption.

Sample UC032 – amphibolite from DI

Two populations of zircon grains were identified from this sample, a pinkish to brownish, subhedral, elongated and slightly pyramidal one that also contains a few ovoid crystals, and a second population of yellowish to light brownish, anhedral, ovoid and rounded crystals that displayed some fractures. CL and BSE imaging indicates that the elongated crystals have well-preserved internal oscillatory zonation, and the rounded ones have weakly-zoned, concentrically zoned, or diffuse zonation.

Sixty-nine U–Pb analyses were made on cores and rims. Forty-three analyses with concordance between 88 and 116% allow to differentiate two main populations of ages (Fig. 7): a rather heterogeneous Paleoproterozoic group with $^{207}Pb/^{206}Pb$ ages between 1839 and 1756 Ma as well as between 1761 and 1573 Ma, and a Mesoproterozoic group with $^{207}Pb/^{206}Pb$ ages between 1040 and 985 Ma (Fig. 7). For the Paleoproterozoic population, eleven grains define an upper intercept age of 1810 ± 19 Ma (Th/U ratios between 0.44 and 0.94). The CL images show domains of oscillatory zoning with local fracturing (ZR 2 and ZR 36, Fig. 7 inset). A few cores have partially blurry texture (ZR 2, Fig. 7 inset) surrounded by a homogeneous light-gray luminescent domain (ZR 2, Fig. 7 inset). A second upper intercept age of 1674 ± 53 Ma was obtained for ten zircon crystals with Th/U ratios between 0.34 and 0.67. The crystals are characterized by oscillatory internal zoning (ZR 36, Fig. 7) with low-luminescent (gray) and occasionally resorbed domains (ZR 2, Fig. 7).

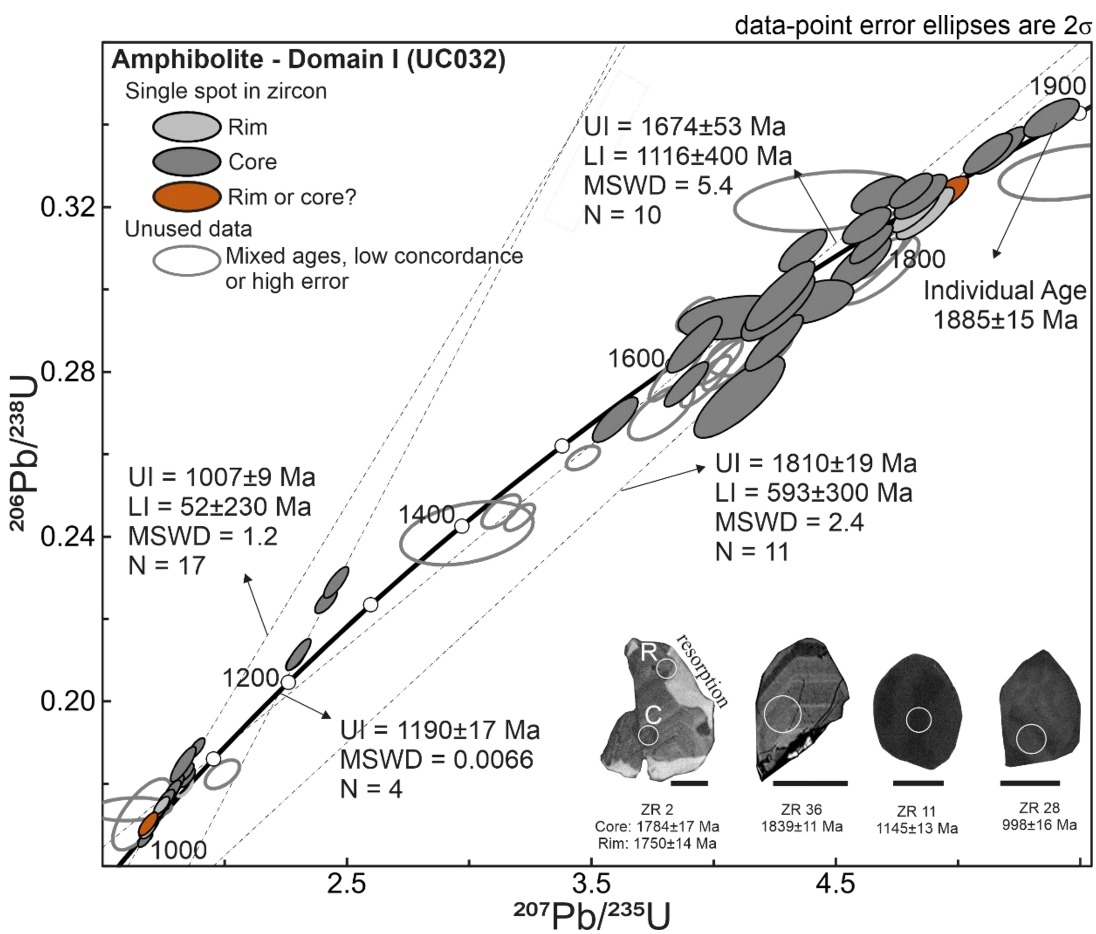

Figure 7. U–Pb concordia diagram for the amphibolite (UC032) hosted in felsic granulite D. The upper intercept $^{207}Pb/^{206}Pb$ ages are ~1810 Ma (cores and rims), ~1674 Ma (cores), ~1190 Ma for reverse discordant core data, and an ~1007 Ma age from cores and rims. The oldest concordant zircon core has a ~1810 Ma age, the same Paleoproterozoic inheritance analyzed for DIII (compare Fig. 6). Four CL images illustrate oscillatory-zoned cores (ZR 2 and ZR 36) and rounded zircon with dark-luminescent, weakly-zoned texture (ZR 11 and ZR 28).

Many analyses from these grains could not be considered, because they gave seemingly mixed ages derived from analysis of both rim and core material. One individual concordant zircon gave an age of 1885 ± 15 Ma (Th/U of 0.67) on a relic of an oscillatory-zoned core.

Some Mesoproterozoic data are concordant, and a few fall onto a discordia line or along a reverse discordia line. The analyses on ovoid to rounded, weakly convolutely zoned areas of 17 zircons (ZR 28, Fig. 7 inset) with dark-gray luminescence define the more prominent upper intercept age of 1007 ± 9 Ma (Th/U ratios between 0.14 and 0.82). A less prominent population forms a reverse discordia line of 1190 ± 17 Ma. The crystals have ovoid to rounded shapes and are characterized by Th/U ratios <0.12. CL images show dark luminescent, weakly convolute zonation (ZR 11, Fig. 7 inset), and some concentrically zoned overgrowths.

Sample UC010II - amphibolite from DI

The zircon crystals are translucent to opaque, brownish, have few fractures, and are almost devoid of inclusions. They are subhedral to anhedral, rounded or ovoid, and up to 120 μm long, but most crystals are <50 μm long. For this sample only BSE images are available, but they indicate that the crystals have weak zonation or a uniform internal texture. As the crystals are small and some of them have rims, most of the grains from this sample could not be analyzed. Twenty-five analyses on zircon with concordance between 98 and 113% define two Mesoproterozoic populations (Fig. 8). Five zircon grains, for which the majority of data lie along a reverse discordia line, yielded an upper intercept age of 1173 ± 23 Ma (Th/U ratios between 0.10 and 0.18). The zircons of this group are ovoid (ZR 15, Fig. 8 inset) and mostly uniform without zoned internal texture, with one exception of a weakly concentrically zoned zircon grain (Fig. 8 ZR 26). From the younger group of zircons with 207Pb/206Pb ages between 1055 and 1000 Ma, twenty age data resulted in an upper intercept age of 1026 ± 7 Ma (Th/U ratios between 0.30 and 0.53). The zircon grains of this group are elongate to rounded, and some are ovoid (ZR

26, ZR 25, Fig. 8 inset), and show homogeneous, unzoned or concentrically zoned (ZR 26) textures.

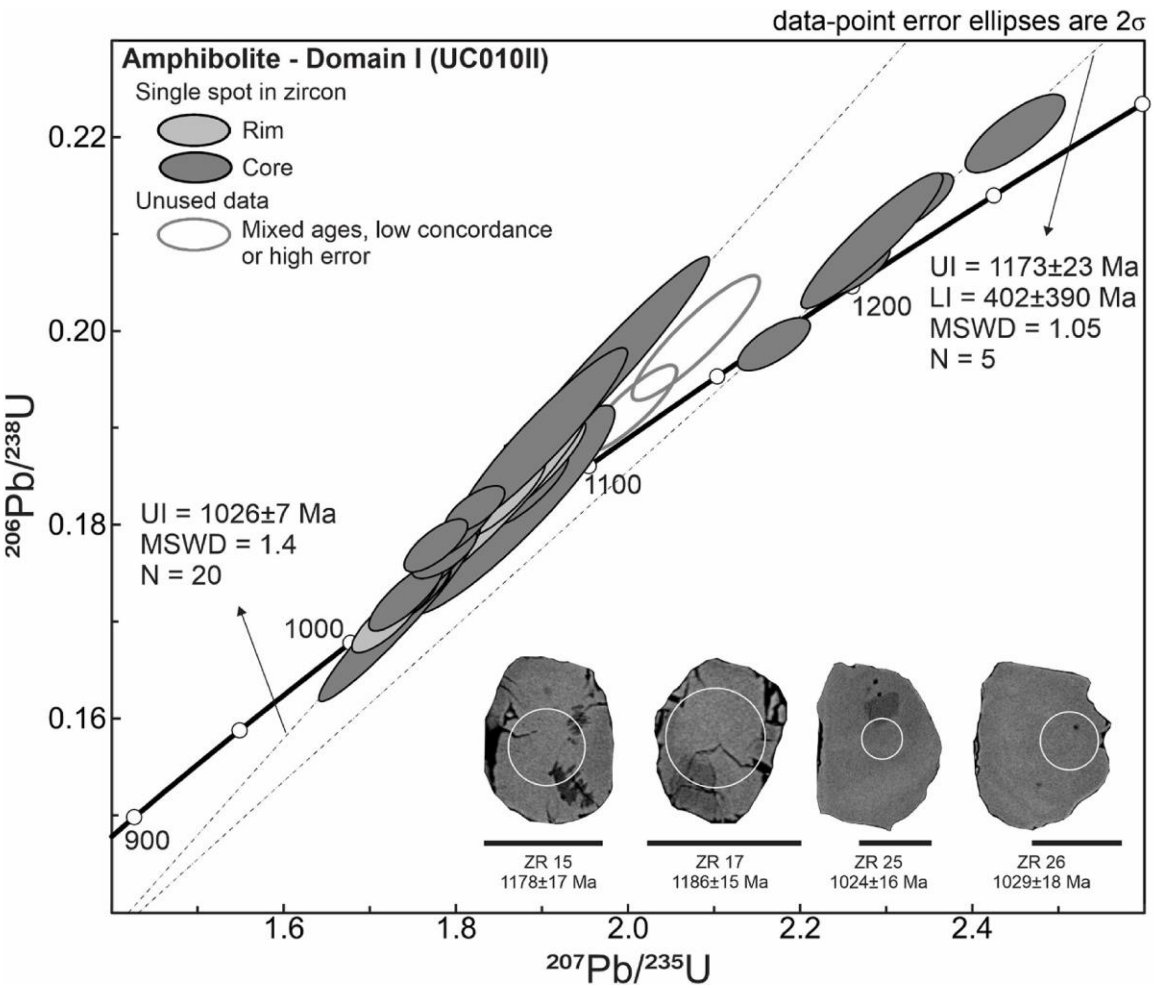

Figure 8. U–Pb concordia diagram for the amphibolite (UC010II) hosted in DI felsic granulite. The upper intercept $^{207}Pb/^{206}Pb$ ages identified an ~1173 Ma population from cores with reverse discordance, and an ~1026 Ma population of core and rim data. Four zircon BSE images show a rounded and fractured zircon (ZR 15 and ZR 17) with weakly-zoned textures (ZR 26 and ZR 25).

Sample UC 001 - amphibolite from domain I

The zircon crystals from this sample generally are up to 50 μm long fragments (Fig. 9), translucent and brownish, and euhedral to subhedral. Most are ovoid but a few have elongated shapes. BSE images reveal an almost homogeneous texture, with some fractures; no inclusions were observed. Twenty-three zircon crystals were dated, six of which with concordance between 90 and 106%. They gave $^{207}Pb/^{206}Pb$ ages between 1122 and 958 Ma. Three zircon crystals yielded a concordant age of 985 ± 20 Ma (Th/U ratios of 2.36–3.33).

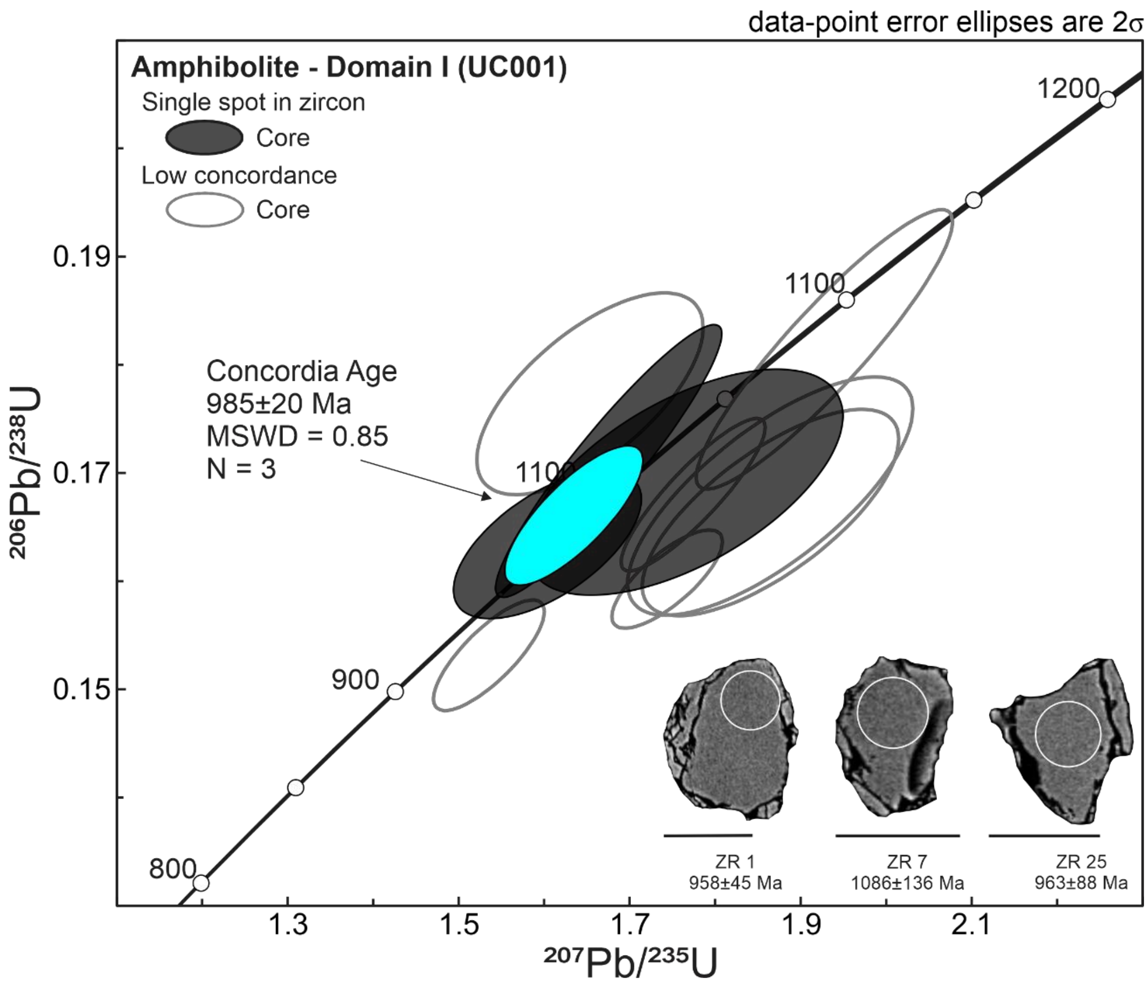

Figure 9. U–Pb concordia diagram for zircon from amphibolite sample UC001 hosted by felsic granulite from DI. A Concordia age was obtained at 985 ± 20 Ma, for three zircon crystals. It is not possible to identify any specific textures by BSE imaging. The zircon crystals are rounded and fragmented with some fractures.

2.5.2 Lu–Hf isotope analysis

Eleven zircon crystals from leucosomes generated at 1.2 Ga from domains DI and DII (felsic granulite samples UC021 and UY1337) were analyzed for Lu–Hf isotopes. Four Paleoproterozoic zircon grains yielded positive ϵHf_T between +2.7 (T = 1759 Ma) and +5.2 (T = 1736 Ma), with T_{DM} of ~2.2 to ~2.1 Ga. Seven Mesoproterozoic zircon rims yielded negative ϵHf_T values between − 9.2 (T = 1239 Ma) and − 2.6 (T = 1055), with T_{DM} of ~2.4 to ~1.9 Ga.

Five representative crystals from the partially preserved basement (paleosome) of DIII (granulite UC016) were analyzed. Three Paleoproterozoic grains yielded slightly negative to positive ϵHf_T values between – 0.2 (T = 1788 Ma) and +3.4 (T = 1789 Ma), with T_{DM} of ~2.4 to 2.2 Ga. Two Mesoproterozoic rims gave ϵHf_T values of − 6.8 (T = 1174 Ma) and − 15.1 (T = 1076 Ma), with T_{DM} of ~2.3 and ~2.6 Ga. Three zircon crystals from melanosome generated at 1.2 Ga were analyzed from amphibolite samples. One analysis resulted in a positive εHf_T value of +6.3 (T = 1799 Ma) with T_{DM} of 2.1 Ga (UC032). Two Mesoproterozoic zircon grains (UC010II) yielded negative ϵHf_T values of − 5.5 (T = 1021 Ma) and − 3.5 (T = 1030 Ma) and T_{DM} of 2.1 and 2.0 Ga, respectively.

2.6 Discussion

2.6.1 Timing of magmatism and metamorphism of the Cerro Uyarani metamorphic complex

Fig. 10 summarizes the different ages obtained for felsic and banded granulites (samples UC021, UY1337, and UC016) and amphibolites (samples UC032, UC010II, and UC001). The zircon textures for Paleoproterozoic, Mesoproterozoic, and Late Mesoproterozoic populations of CUMC are variable; they are summarized in Fig. 11.

These ages indicate two main events for the CUMC - Event 1 in the Paleoproterozoic and Event 2 at the end of the Mesoproterozoic (Fig. 12). The Mesoproterozoic event comprises two tectonic-magmatic- metamorphic cycles, probably as part of the same progressive orogenesis: Cycle 1, interpreted to respond to migmatization at ca. 1.19 Ga, and Cycle 2, which is related here to granulite metamorphism at ~1.0 Ga.

In order to shed some light onto the tectonic evolution of the CUMC and to discuss its possible affinity to other terranes, we provide a comparison of our U–Pb (Fig. 12) and Hf data with other data (Fig. 13) available for surrounding basement areas, such as the Rio Apa terrane (RAT, Ribeiro, et al., 2020), SW Amazon craton (SW AC and AC), Arequipa-Antofalla basement (AAB), Paragua ´ terrane (PT), eastern Bolivian basement (Redes et al., 2020), and Sunsas volcanic belt (Martin et al., 2020). All the εHf_T data (Fig. 13), except the ones from Redes et al. (2020) and Martin et al. (2020), were converted from εNd_T values by Ribeiro et al. (2020). Fig. 13 also shows the Grenville age data for the Sierra de Maz and Pie de Palo (Martin et al., 2019) related to a MARA craton (Casquet et al., 2012).

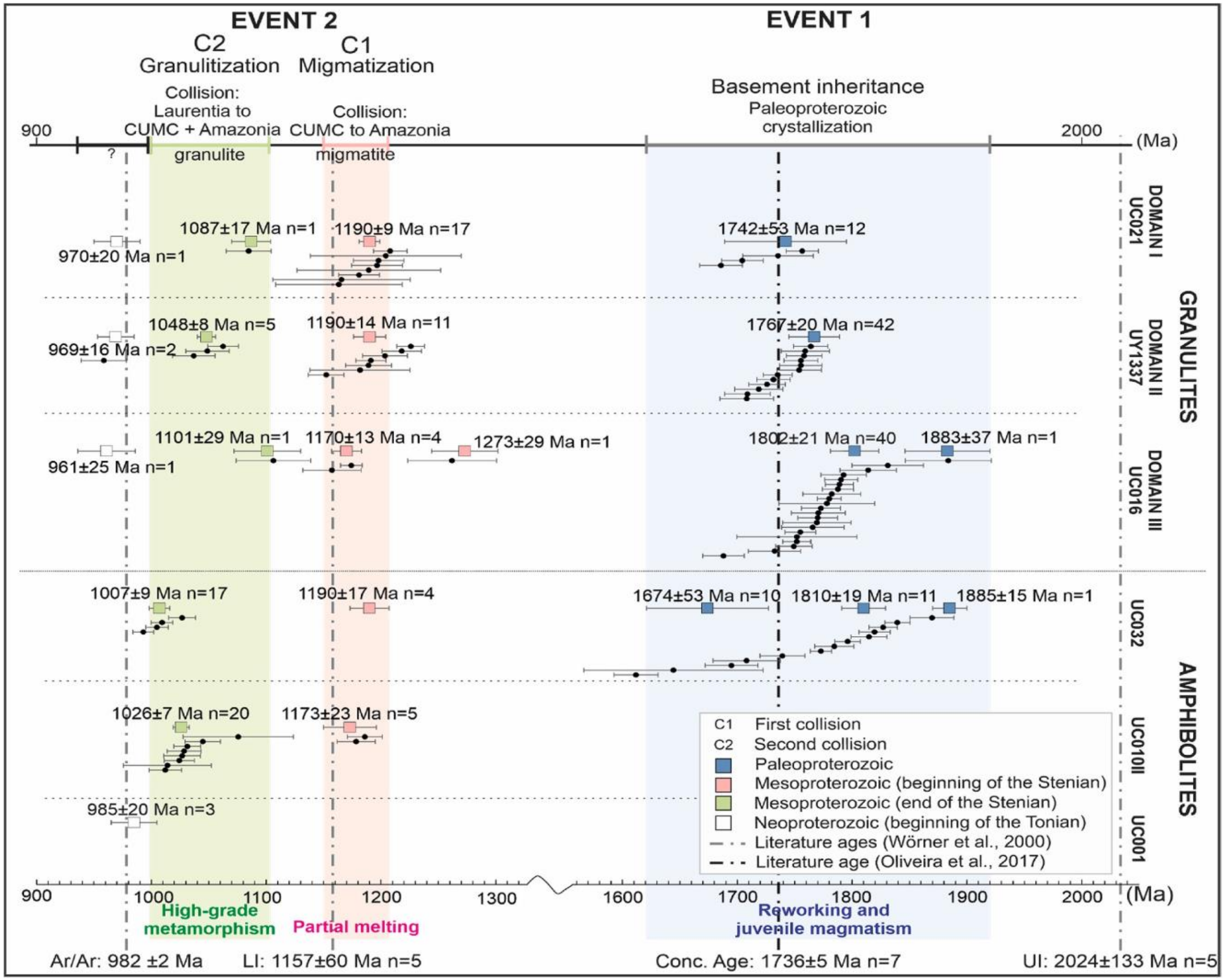

Figure 10. Compilation of U–Pb data obtained in this paper (data shown in Figs. 4–9) The U–Pb ages are marked by the colored squares with error bars. Apparent ages with concordance between 102 and 98% are shown with the black circles with error bars ($^{207}Pb/^{206}Pb$, in Ma). The vertical lines represent ages obtained by other methods and authors, as indicated in the figure.

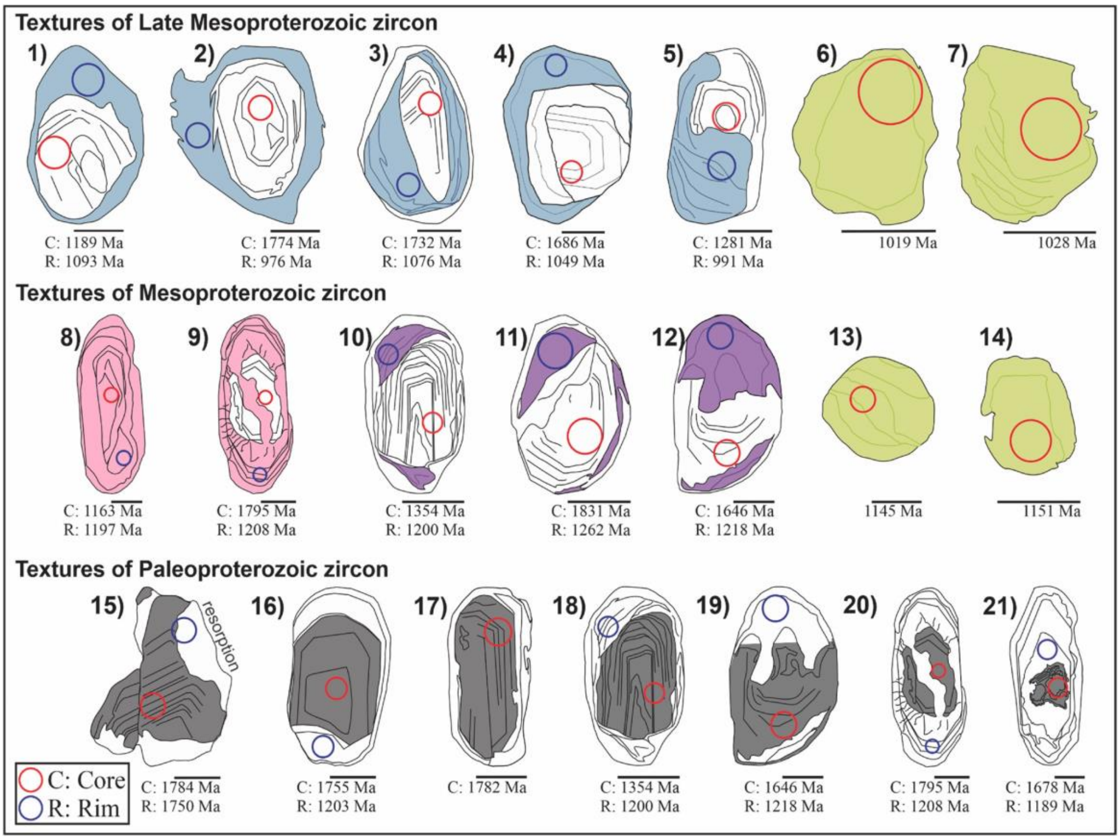

Figure 11. Textures of zircons found on CUMC granulites and amphibolites, based on CL and BSE images and compare with images from the literature1–5) Rounded- ovoid grains of high-grade metamorphism (compare with Figs. 10.1 and 10.2 of Rubatto, 2017) with homogeneous (1, 2) and concentric (3–5) rims cutting or overgrowing oscillatory-zoned older cores. 6–7) Rounded zircon grains with homogeneous, unzoned or weak-zoned textures, formed by high-grade metamorphism (Fig. 10. a and e in Kunz et al., 2018). 8, 9) Oscillatory zoning, forming new grains (8) or cutting oscillatory older cores (9) with radial fractures in the newly grown domain. 10–12) Localized zircon recrystallization associated to migmatization (see Fig. 6 of Kroner et al., 2014¨) showing convolute texture (10, see also Miller et al., 2007) or altered dark-luminescent domains (11 and 12; Kroner et al., 2014¨) penetrating oscillatory-zoned older cores. 13–14) Rounded zircon with homogeneous to weakly-zoned textures associated to high-grade metamorphism (P. Liu et al., 2014): (13) Weakly discernible, wide bands (Fig. 7.23–25 of Corfu et al., 2003); (13, 14) soccer ball zircon (Hoskin and Schaltegger, 2003). 15–21) Diverse oscillatory-zoned textures with resorption (15), cut by convolute younger overgrowth (16), sectorial zonation (17), partially obliterated and recrystallized by ~1.2 Ga domains (18 and 19), or restitic cores surrounded by well-developed Mesoproterozoic oscillatory-zoned rims (20 and 21). Scale bars always represent 50 μm length. The domains were colored according to: blue - metamorphic rims, green - new grains, gray – oscillatory-zoned zircon and lilac - alteration associated with migmatization..

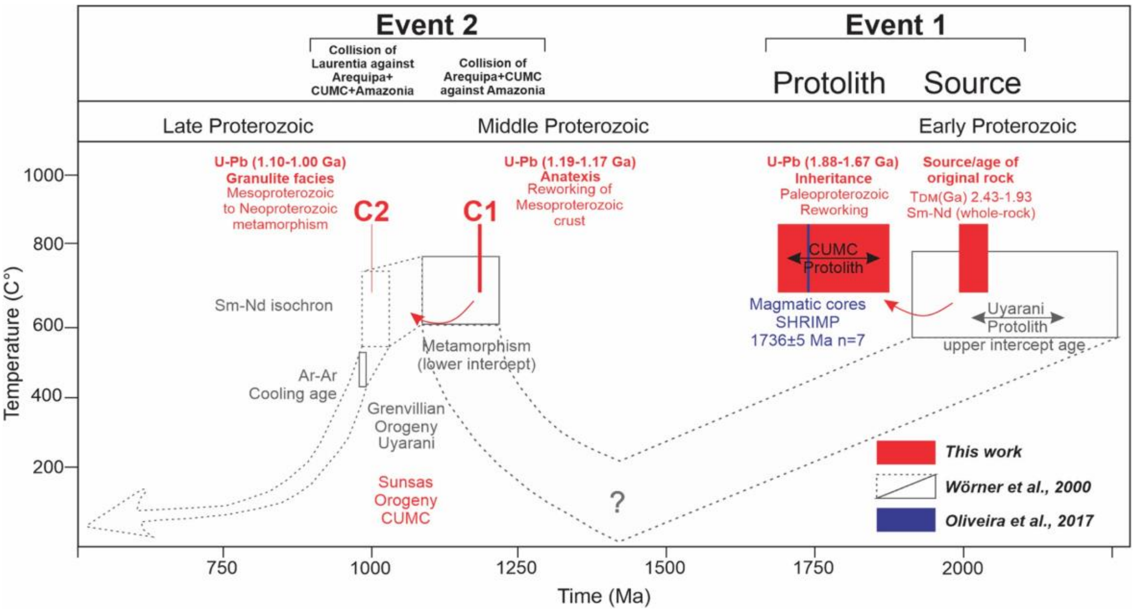

Figure 12. Comparison of our U–Pb zircon results for the CUMC with previously published data (Wörner et al., 2000; Oliveira et al., 2017). In summary, the original protolith has crystallization ages of 1.88–1.67 Ga and 2.40–1.90 Ga old probable sources. The 1.19–1.17 Ga age represents reworking by partial melting with migmatite (leucosomes) generation. The 1.10–1.00 Ga interval represents the last high-temperature event under granulite facies metamorphic conditions. The ~0.98 Ga (^{40}Ar-^{39}Ar plateau age, Wörner et al., 2000) age is interpreted as a cooling age related to amphibole generation (Wörner et al., 2000).

This comparison allows us to 1) discuss the possible affinity of the CUMC to Arequipa and other basement blocks; 2) indicate the probable paleogeographic position of the CUMC between ~1.8 and 1.0 Ga, by correlation (or not) with these other basements; and 3) investigate whether there is any relationship to the hypothetical MARA craton composed of the Maz, Arequipa and Rio Apa terranes postulated by Casquet et al. (2012).

2.6.2 The Paleoproterozoic event at CUMC (1.81–1.74 Ga)

The Paleoproterozoic event is mainly registered for the study area by the data for the felsic granulites of DI, DII, and banded granulite from DIII. Field, petrographic and geochronologic features indicate that DIII of tonalitic composition (Oliveira et al., 2017) is the domain that has best preserved protolith characteristics: strong gneiss banding, a distinctive NE-SW foliation trend (DI and DII with weak gneiss banding are mainly W-E foliated and banded) (compare Fig. 2), and the many Paleoproterozoic zircon cores, compared to zircon populations from the other domains. The effects of the 1.19 Ga magmatic event are more extensively found in the zircon populations of the DI and DII domains (Fig. 10) than in DIII, resulting in well-preserved cores for DIII zircon (Fig. 6). The zircon population from DIII of ~1.81 Ga age and the oldest single zircon of this study of ~1.88 Ga age are similar to the older zircon population found for amphibolite UC032 (see Fig. 10). This may indicate that amphibolite UC032 hosted by domain DI could have a genetic relationship with DIII.

The ϵHf_T values between − 0.19 and + 6.3 and the Paleoproterozoic Hf model ages (T_{DM}) between 2.42 and 2.05 Ga suggest that Event 1 could represent crustal reworking between 1.88 and 1.75 Ga in a magmatic arc setting, of a mainly juvenile Paleoproterozoic crust of tonalitic composition.

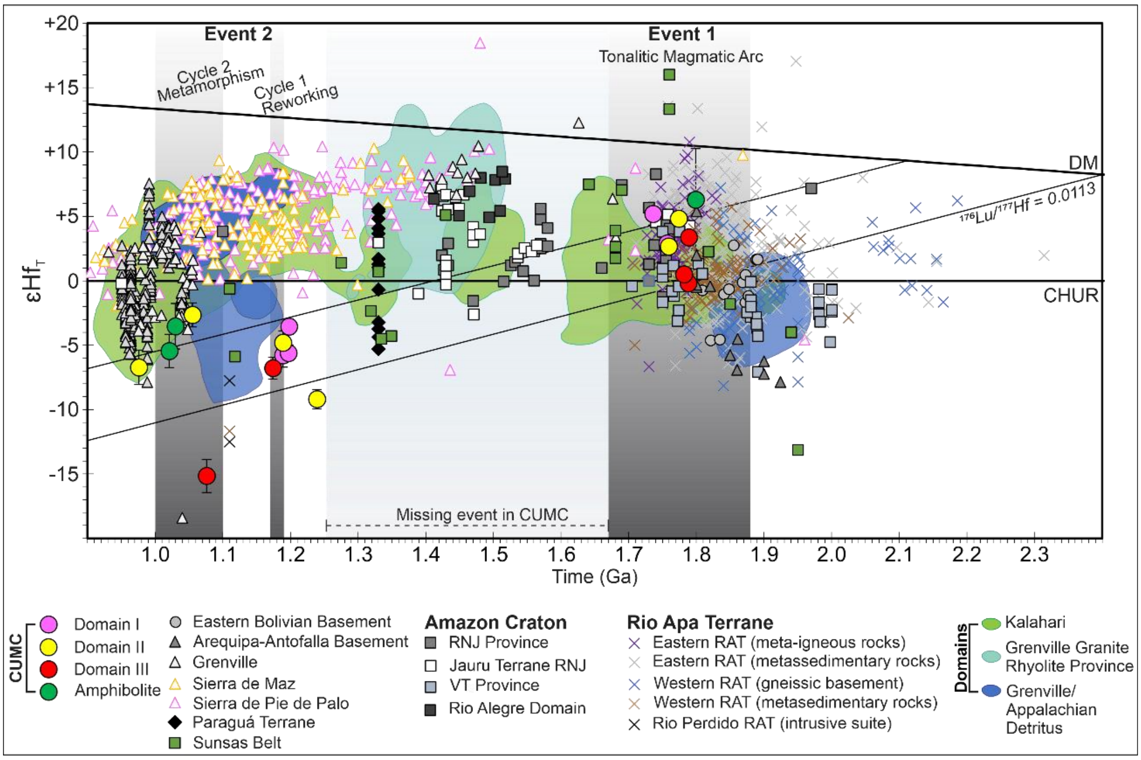

Figure 13. ϵHfT values versus Ages in Ga (for magmatic and metamorphic zircon) from the Cerro Uyarani Metamorphic Complex and other terranes. The squares, triangles, crosses, and the gray circle correspond to ϵHfT data calculated from ϵNd_T by Ribeiro et al. (2020). Data for the southwestern Amazon Craton (RNJ province, Jauru terrane RNJ, VT province and Rio Alegre Domain), Arequipa-Antofalla basement, Paraguá terrane, Rio Perdido RAT, eastern and western orthoderivated rocks RAT, eastern RAT (Alto Tererê Group), and western RAT (metasedimentary rocks) have been compiled from Ribeiro et al. (2020). The eastern Bolivian basement data are from Redes et al. (2020), and the Grenville and Sunsas data were compiled by Martin et al. (2020). The data from Sierras de Maz and Pie de Palo and fields for Kalahari and Grenville data were taken from Martin et al. (2019). Abbreviations: RAT: Rio Apa terrane and RNJ: Rio Negro Juruena province.

Hafnium and Nd T_{DM} of 2.19 and 2.03 Ga also endorse the hypothesis that the basement may be older than the ages found (so far) in CUMC zircons, which is further supported by the upper intercept age of Wörner et al. (2000, 2024 ± 130 Ma). Despite the large error of this 2.0 Ga age and only one metamorphosed zircon of 1.88 Ga having been observed here, we cannot exclude the possibility of more complex processes or even an older metamorphic basement that may have been involved in Paleoproterozoic crustal reworking.

2.6.3 Tracking the continental affinity of the CUMC

The CUMC records inherited ages of 1.88 Ga and younger ages of 1.81 Ga and 1.67 Ga interpreted here as the reworking of juvenile crust. Especially DIII, the migmatite part of the complex, is one that best preserves some characteristics of the tonalitic basement. DI and DII xenocrystic zircon indicates reworking at 1.77–1.74 Ga.

Wörner et al. (2000) , based on isotopic (Pb and Nd) and petrological analysis, related the CUMC with the Arequipa terrane, whereas Loewy et al. (2004) postulated that the CUMC terrane could have been part of the Northern Domain of the Arequipa-Antofalla basement (AAB), which corresponds to the extreme southern part of the Arequipa terrane. The few ϵHf_T data for the Arequipa-Antofalla basement found in the literature (Ribeiro et al., 2020) result from calculation from ϵNd_T (after Vervoort et al., 2011). Both CUMC and AAB show positive to slightly negative ϵHf_T, with CUMC having ϵHf (1.8–1.79 Ga) between +6.31 and − 0.19, and the AAB having ϵHf (1.82–1.8 Ga) between +5.39 and − 0.42. Unfortunately, for the 1.85–1.92 Ga zircon age range, we do not have Hf data for the CUMC to compare. However, the data in hand have practically the same Hf model ages that indicate reworking of a Paleoproterozoic crust of 2.3–2.4 Ga. Additionally, both CUMC and AAB do not show any reworking between 1.6 and 1.3 Ga.

The CUMC is somewhat similar in age to the Arequipa-Antofalla basement (Fig. 13), but with the distinction that the Arequipa basement in Peru exhibits inherited zircons with ages between 2.7 and 1.89 Ga, a magmatic event at 2.1–1.89 Ga, sedimentary sequences of 1.89–1.87 Ga, and UHT migmatite formed at ~1.87 Ga (Casquet et al., 2010). Based on the current U–Pb/Hf database, we postulate a substantial similarity between the CUMC and Arequipa terrane.

There are at least two hypotheses about the affinity of Arequipa terrane. Based on Pb isotopic data, Tosdal (1996) postulated that Arequipa originated in early Proterozoic time as part of Gondwana (Amazon craton), and based on geological, geometric, and age correlation, Wasteneys et al. (1995) and Casquet et al. (2008a,b) postulated that the Arequipa terrane derived from Laurentia and it was accreted to the western margin of Gondwana as an exotic terrane during the Grenvillian orogeny. However, the Pb isotopic character (Loewy et al., 2003) and chronology (Loewy et al., 2004) of the AAB are similar to the Namaqua margin of the Kalahari craton (as compiled by Martin et al., 2019). In terms of Hf data, the Kalahari field (Martin et al., 2019) is similar to the CUMC Hf data for Event 1 and Cycle 2 of Event 2 (Fig. 13).

We also compare our Hf data with several data from the Mesoproterozoic Grenville province (Fig. 13) collected by Thomas et al. (2017) and referred by Martin et al. (2020), besides other data, to investigate the hypothesis that AAB plus CUMC could have been part of Laurentia. The Grenville province has some older inliers of partially reworked crystalline rocks of various ages, like the Labrador province (1700–1600 Ma, reworked in Grenville times - Rivers et al., 2012), and the Mars Hill terrane (1800 Ma, reworked in the southern part of the Grenvillian Blue Ridge Massif - Ownby et al., 2004). Event 1 of the CUMC (1.88 and 1.75 Ga) is similar to these oldest events recognized in the Grenville province.

As we also see in Fig. 13, the CUMC juvenile Paleoproterozoic crust is also similar to meta-igneous rocks of the eastern Rio Apa terrane and partially similar to the metasedimentary rocks from the western (Amolar Group and Rio Naitaca formation) and the eastern (Alto Terere Group) ˆ Rio Apa terrane (Ribeiro et al., 2020), and from the SW Amazon craton - the Jauru terrane, the Ventuari-Tapajos and Rio Negro-Juruena prov´ inces, but not with data from the Maz terrane. For this reason, we postulate that AAB, CUMC, and RAT could have shared a similar history at least during the Paleoproterozoic.

Casquet et al. (2012) and Rapela et al. (2016) (amongst others) postulated that the Arequipa-Antofalla basement, the western Sierras Pampeanas (Maz terrane), and the Rio Apa terrane were part of a Paleoproterozoic block of Laurentian affinity, the so-called MARA block (M: Maz terrane, A: Arequipa terrane and RAT: Rio Apa terrane). They suggested that this block accreted to the margin of Gondwana during Paleozoic times (Casquet et al., 2012; Rapela et al., 2016). As compared in Fig. 13, neither CUMC nor AAB, nor Rio Apa terrane (Ribeiro et al., 2020) are similar to the Sierra de Maz or Sierra de Pie de Palo (Martin et al., 2019). The U–Pb/Hf data for the Maz terrane (Sierra de Maz and Sierra de Pie de Palo, in western Argentina) are derived from Cambrian and Ordovician metasedimentary rocks that have as main population Late Mesoproterozoic zircons with positive ϵHf_T (see Fig. 13). Few data, if any, relate to the Paleoproterozoic. Consequently, we do not find support for the possibility that CUMC, RAT and AAB were part of the MARA craton. We can conclude for the Paleoproterozoic that the CUMC has an affinity to the AAB and that maybe the CUMC represents an eastern part of the AAB. In addition, CUMC plus AAB are similar in U–Pb ages and Hf data with the Rio Apa terrane (Ribeiro et al., 2020; Redes et al., 2020) and with the southwestern part of the Amazon craton. Could the CUMC plus AAB, Rio Apa terrane, SW part of the Amazon craton, and the Grenville inliers have been part of a single province sharing a largely unified tectonic history during the Paleoproterozoic? Maybe. Further work is required.

2.6.4 The Mesoproterozoic event

The Mesoproterozoic event seen in the U–Pb data for CUMC zircon could be related to the Sunsas-Grenville Orogeny (Loewy et al., 2004; Teixeira et al., 2010; Ribeiro et al., 2020). However, this event can seemingly be divided into two successive cycles: a dominant Cycle 1 at ~1.19 Ga and a subordinate Cycle 2 at ~1.0 Ga.

Cycle 1 (~1.19 Ga): migmatization and zircon textures

Plotting the U–Pb results from DI, DII, and DIII and from amphibolites around 1.19 Ga, we obtain an upper intercept age of 1183 ± 8 Ma (MSWD = 2.9). The textures of zircons are contrasting between the different domains; from domains I and II, rims and cores show oscillatory zoning and irregular dark luminescence (altered) domains cutting Paleoproterozoic cores, and from Domain III, the typical textures are convoluted zoning. The amphibolites exhibit newly grown roundish or ovoid zircon crystals with almost homogeneous internal textures. These textures imply that the CUMC protolith was partially melted by anatexis at ~1190 Ma with the consequent generation of melanosomes (amphibolites), leucosomes (DI and DII), and paleosomes (DIII and mafic granulite), probably during progressive orogenesis.

The oscillatory zoning textures found in zircon rims and cores from DI (Figs. 4 and 11) are similar to textures already found in leucosomes (see, for example, Boger et al., 2005), which indicate zircon growth at 1.19–1.17 Ga. For the same age, DI and DII present altered domains with irregular dark luminescence (Figs. 5, 6 and 11) that cut the Paleoproterozoic cores. These features are similar to the fluid-induced alteration from charnockites (Kroner et al., 2014¨). Thus, we interpret the ages of ~1190 Ma due to the migmatization event that generated the leucosomes.

The negative ϵHf_T values obtained on rims of zircon from DI and DII and the Paleoproterozoic Hf model ages indicate that Cycle 1 of Event 2 reworked the tonalitic Paleoproterozoic crust (protolith) by anatexis, see for example ZR 4 from Domain II.

This anatexis could have happened in a magmatic arc setting, according to CUMC geochemistry (Oliveira et al., 2017). Nevertheless, the study of zircon textures (this work) correlates the anatexis to an orogenic setting through crustal thickening, exhumation, or post-collisional collapse (e.g., Brown, 2001; Sawyer, 2008). So, the age of ~1190 Ma indicates the time of partial melting of the CUMC protolith and generation of migmatites during progressive orogenesis.

Cycle 2 (~1.1–1.0 Ga): granulite metamorphism and Hf homogenization

The granulites from DI, DII and DIII exhibit youngest ages between 1101 and 1048 Ma (Fig. 10) that allow to obtain a weighted average age of 1056 ± 28 Ma (Fig. 14A) which is interpreted as the likely metamorphic peak that generated the granulite facies at CUMC. During this high temperature metamorphic event, new rounded zircon rims with homogeneous and convolute light-luminescence textures (CL) were crystallized onto the grains from felsic granulites. In contrast to granulites, amphibolites generated entirely new rounded and ovoid zircon crystals during this cycle.

The youngest U–Pb age of 1007 ± 9 Ma of the UC032 amphibolite and the weighted average age of 982 ± 4 Ma (Fig. 14A) obtained on samples UC021, UY1337, UC016, UC001 could be related to the cooling after granulite facies conditions or even to exhumation that exposed the CUMC basement. These youngest ages are similar with the ones obtained by Worner et al. (2000) ¨ of 1008 ± 16 Ma (Sm–Nd mineral isochron) and 982 ± 1.5 Ma (Ar–Ar age obtained for mafic granulites), respectively. The low-grade mineral assemblage with epidote and actinolite-tremolite in the granulites (Oliveira et al., 2017) indicates that after Cycle 2 a retrograde metamorphism was active. The similar ranges in $^{176}Hf/^{177}Hf_{(T)}$ ratios of zircon from the felsic granulite domains at ~1.19 Ga age - migmatization time - and from ~1.0 Ga - the time of high-grade metamorphism - suggests that the Hf isotopic composition of zircon was homogenized during high- grade metamorphism. Zircons from granulite facies of the Jiaobei terrane, eastern North China craton, show preservation of initial $^{176}Hf/^{177}Hf$ ratios in zircon recrystallized under fluid- or melt conditions (L. Zhao et al., 2002). Similar $^{176}Hf/^{177}Hf$ values of zircon from two subsequent processes were determined for pseudomorphic detrital zircon grains from the Shackleton Range (Zeh et al., 2010b) and metamorphic overgrowth from magmatic zircon crystals from the Limpopo Belt (e.g., Zeh et al., 2010a; Gerdes and Zeh (2009). These authors described a dissolution-Hf homogenization-reprecipitation process under sub-solidus high-grade metamorphic conditions in the presence of an aqueous fluid phase with the same Hf isotopic composition of pre-existing zircon and with the influence of syn-metamorphic deformation (Zeh et al., 2010a).

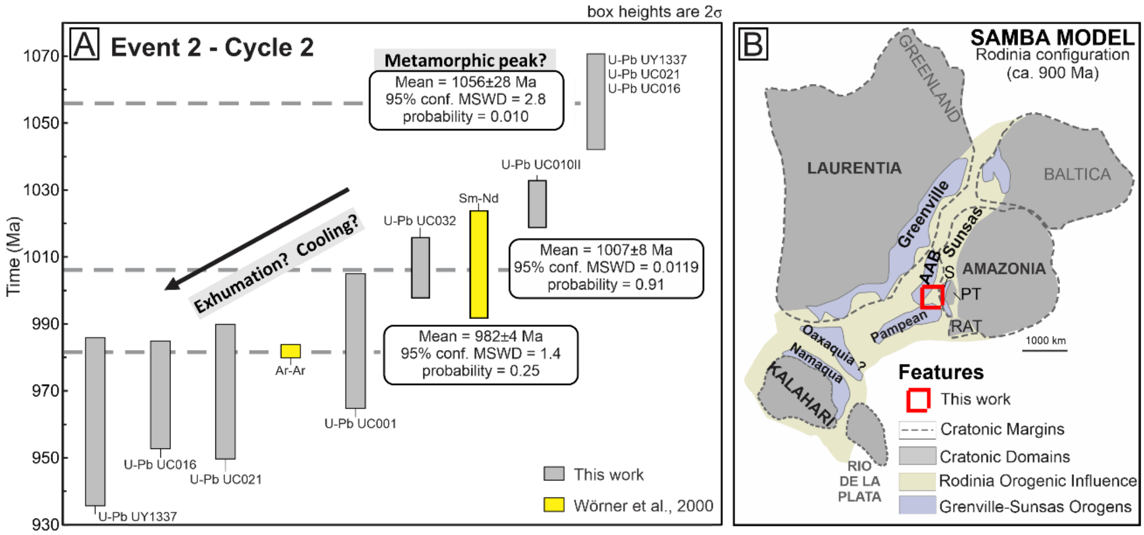

Figure 14. A) Ages obtained in this work and from Wörner et al. (2000) for Cycle 2 (C2) of Event 2 (compare text for discussion). B) Probable location of the CUMC in the Rodinia supercontinent tectonic context according to the SAMBA model (Johansson, 2014). The red square indicates the likely position of the Cerro Uyarani Metamorphic Complex in this model.

According to the SAMBA model (Johansson, 2009) and the recently published geochronological review of the Rodinia-forming Grenvillian orogeny (Johansson et al., 2022), we consider the Arequipa terrane (with the CUMC) as part of the smaller blocks situated in the intervening space between Amazonia and Laurentia Fig. 14B). Nevertheless, Johansson et al. (2022) in their compilation only considered the Laurentia, Baltica, Amazonia, Kalahari, and Australia cratons; our geochronological data also indicate two Mesoproterozoic cycles of 1.19 and 1.0 Ga with a quiescence between these them. Therefore, we linked the CUMC area (Arequipa terrane) with the "Proto-Rodinian" collisional orogens.

2.6.5 The tectonic evolution of the CUMC during the Mesoproterozoic: the Sunsas-Grenville orogeny

Before the reworking of the CUMC at ~1.19 Ga as part of the collision that caused the Sunsas-Grenville orogeny of the Rodinia assembly, there was a quiescence regarding geological events at the CUMC. The SW sector of the Amazon craton (Fig. 13) almost continuously experienced reworking from ~1.5 Ga until approximately 1.3 Ga, when the San Ignacio Orogeny occurred (Bettencourt et al., 2010; Ruiz et al., 2011). This orogeny is well represented in the Paragua terrane and the ´ SW part of the Amazon craton (e.g., Bettencourt et al., 2010; Couto de Nascimento et al., 2016). Curiously, the CUMC did not register any reworking process until 1.2 Ga, as we have shown here.

What happened with this terrane between 1.75 and 1.2 Ga remains unanswered. Several features that the CUMC shares with the Arequipa- Antofalla basement (AAB;

Worner et al., 2000¨ ; Tohver et al., 2004a,b; Mamani et al., 2010; Casquet et al., 2010; Ramos, 2018; this work) allow to think that the CUMC represented the margin of the AAB, which only became involved in the Sunsas-Grenville orogeny at the end of the Mesoproterozoic.

Possibly the CUMC was part of the southernmost portion of the Arequipa terrane from ~1.74 Ga, and it was then attached to the Paragua terrane and Amazon craton at 1.19 Ga. This collision generated ´ migmatites at CUMC and granites in the Sunsas-Aguapeí province. There are some similarities between the CUMC and the Sunsas-Aguapeí province in terms of ages (e.g., Teixeira et al., 2010; Condie et al., 2005). Santos et al. (2008) considered upper amphibolite facies conditions and even anatexis at 1.18–1.11 Ga in the Sunsas Orogen along the southeast Brazil–Bolivia border during the collision between Amazonia and the west-southwest parts of Laurentia. Between the three possibilities proposed by Boger et al. (2005) to explain the amalgamation of the Paragua ´ terrane and the Amazon craton, the one that involves the collision of the Paragua terrane and the AAB at the same time with the AC, forming the ´ Sunsas-Aguapeí belt, seems to be the more logical case. With the arrival of Laurentia passing through the Arequipa (with the CUMC at the Arequipa border) terrane front, the conditions of metamorphism were raised to granulite facies (Boger et al., 2005; Santos et al., 2008; Bettencourt et al., 2010; Ribeiro et al., 2020). Thus, the hypothetic magmatic arc would have been positioned at the Paragua ´ terrane front of the SW Amazon craton, today knows as Sunsas belt (Teixeira et al., 2010). Some authors (Hoffman, 1991; Sadowski and Bettencourt, 1996; Tohver et al., 2002, 2004) recognized that the effects of the Grenville collision were complex. They postulated two Late Mesoproterozoic deformation events: 1) an older, 1.2–1.12 Ga event recorded in the Paleo-to Mesoproterozoic basement rocks, interpreted as recording the Amazonia–Laurentia collision (Tohver et al., 2003), and 2) a younger, 1.1–0.95 Ga event mainly recorded in the metasedimentary Nova Brasilandia (ˆ Tohver et al., 2004a,b) and Sunsas-Aguapeí (Litherland et al., 1989; Teixeira et al., 2010) belts. These two events are similar in age with Cycles 1 and 2 defined here for the CUMC area.

2.6.6 The CUMC as a potential source area for younger basins

Fig. 15 highlights the position of the CUMC as a source of sediments for younger basins. The detrital zircon populations identified in younger basins such as those of NW Argentina or of the Arequipa basin, (see caption to Fig. 15), can be grouped into the two Mesoproterozoic cycles identified at CUMC, and some other events such as the San

Ignacio Orogeny at ~1.3 Ga (not identified at the CUMC). Fig. 13 also allows us to understand the CUMC as a source.

The more important points about Fig. 15 are: 1) The CUMC represents a potential source area for the Cerro Chilla (Bahlburg et al., 2020) or Puncoviscana (Adams, 2011; Hauser et al., 2011; Aparicio Gonzalez ´ et al., 2014) formations; 2) the CUMC could be a source area for the Arequipa basin; but as this basin is of Mesozoic age, the zircons related to these sedimentary strata could represent a second/third cycle of recycling from older sedimentary strata as well; and 3) in addition to cycles C1 and C2 identified for the CUMC with negative εHf characteristics, the diagram shows a contribution from juvenile crust that may not be exposed anymore.

The age distribution for crystalline basement inliers and detrital zircons from modern rivers from the Central Andes, which is compiled in Fig. 16, has significant maxima of zircon ages for events already known for the wider region. The Central Andes show small zircon age peaks from the Archean to the Paleoproterozoic, with a slightly more prominent peak around 2 Ga. The first significant peak is in the Paleoproterozoic (~1748 Ma), with age data found in magmatic and metamorphic cores. At this time, DI, DII, DIII granulites, and an amphibolite (UC032) from the CUMC registered magmatic and metamorphic Paleoproterozoic zircon cores. This peak probably reveals the primary Paleoproterozoic origin of the basement rocks of the Central Andes.

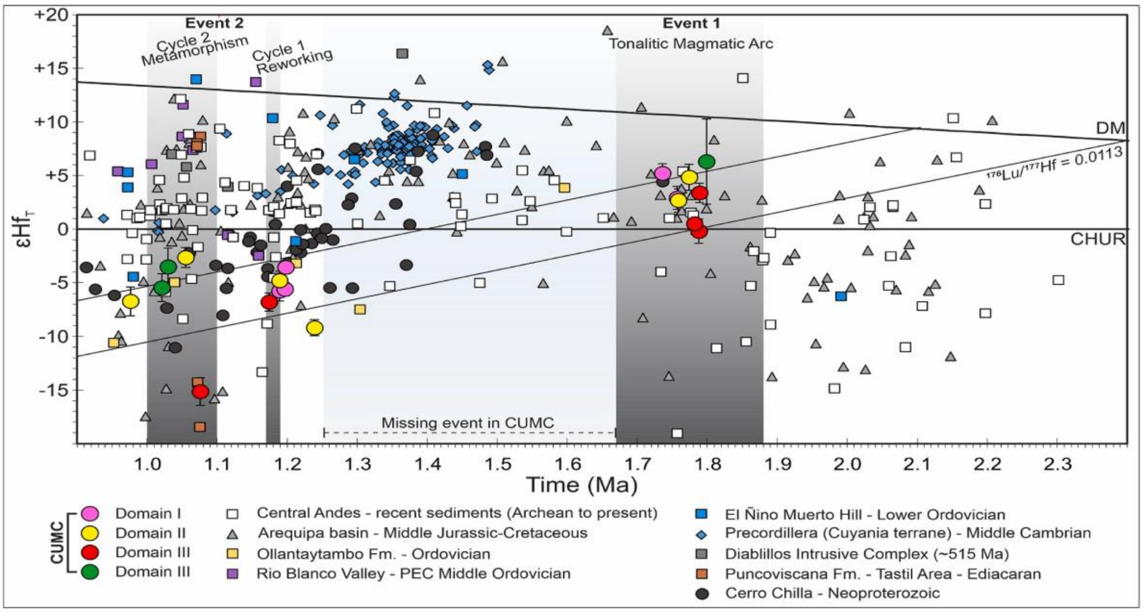

Figure 15. εHfT values versus magmatic and metamorphic zircon crystallization ages (Ga) for the Cerro Uyarani Metamorphic Complex compared to basin deposits, volcanic rocks, and recent sediments from the Central Andes (Pepper et al., 2016), Arequipa basin (Chavez et al., 2022), Ollantaytambo Fm. (Bahlburg et al., 2011), Rio Blanco Valley, El Nino ˜ Muerto Hill, Puncoviscana Fm. (Hauser et al., 2011), Diablillos Intrusive Complex (Ortiz et al., 2017), and Cerro Chilla volcano-sedimentary sequence (Bahlburg et al.,

2020). The squares, triangles and white circle correspond to ϵHf_T data converted from ϵNd_T data by Ribeiro et al. (2020). The CUMC data are also.

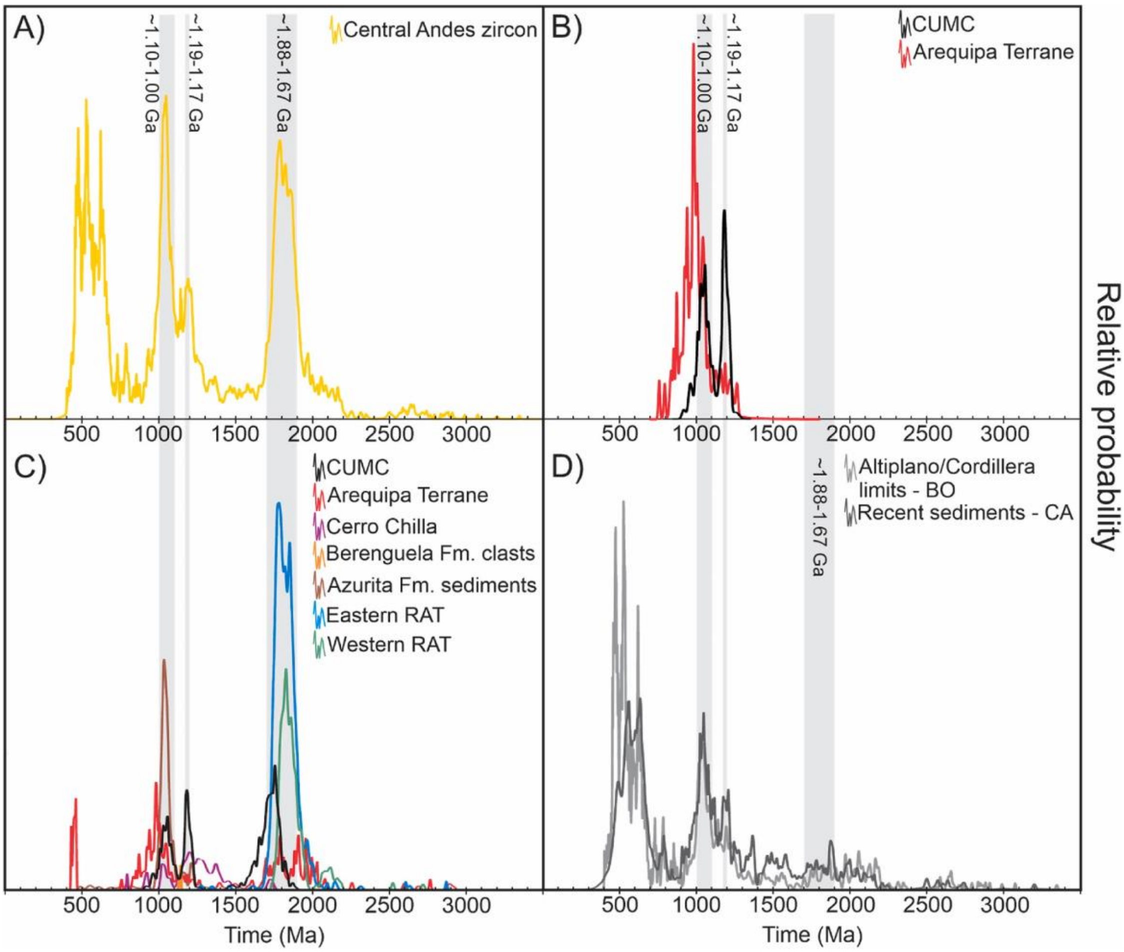

Figure 16. U–Pb probability density plots for the CUMC, Bolivia inliers, Arequipa terrane, Rio Apa terrane, SW Amazon craton, Paragua terrane, current sediments from ´ beaches and rivers in the Central Andes, and sediments from the boundary between the Altiplano and the Bolivian Cordillera. A) Overview of the main age peaks for the Central Andes. B) Comparison between age distributions for the CUMC and Arequipa terrane. C) Comparison of age distributions for each unit of crystalline rocks and detrital zircon data. D) Comparison of age distributions for current sediments from beaches and rivers and sediments from the region along the border between the Altiplano and Cordillera. All data have concordance between 90 and 110%.

A further significant peak at 1183 Ma for the CUMC rocks is emphasized in Fig. 16. This stage indicates a new zircon-forming and continental edge-forming event expressed by Paleoproterozoic zircons. Nevertheless, because of its lesser prominence, we interpret the age peak at ~1.18 Ga as linked to the first collision of the basement that included the CUMC with the basement that formed the ancient Amazon continent. Therefore, these ages are recorded mainly in rocks generated in magmatic belts, e.g., the Sunsas Belt, and at the orogenic edges of the entities involved in the collisions, e.g., the CUMC and Arequipa terrane. In addition, these zircons will be important in the units that had such terranes as source areas, such as the Cerro Chilla and Potoco Formations.

The most significant age peak for the Precambrian of the Central Andes is at 1050 Ma, which we interpret as the time of the major collisional event between Laurentia and Amazonia. The magnitude of the reworking at ~1.0 Ga explains this substantial stage of zircon generation, found in this study in the metamorphic rims of DI, DII, and DIII lithologies. Calculation of a weighted average for all these ages from granulite samples from the CUMC gives 1056 Ma and for new zircon grains generated in the amphibolite samples (UC032 and UC010II) ages of 1007 and 1026 Ma.

Our study of U–Pb/Hf isotopes for granulites and amphibolites from the Cerro Uyarani Metamorphic Complex detailed the tectonic events from 1.88 Ga to 0.9 Ga, which allowed to interpret a likely association with the Arequipa terrane and the comparison of the CUMC with several Precambrian basements in the surrounding Andean region. The interpretation of the acquired ages demonstrates the importance of studying zircon textures, a complex task but with significant results. The robust ages obtained for the CUMC contribute to future studies of the Precambrian evolution in the Andean region. At the same time this database contributes to understanding of provenance analyses in the regional basins.

2.7 CONCLUSION

The main conclusions regarding the geological evolution recorded by the CUMC, a strategic basement inlier of the Central Andes region, in the light of our new results, are:

1. The first event registered at the CUMC has analogous Hf isotopic character with most of the SW Amazon craton, eastern Rio Apa terrane, Alto Terere Group (ATG), Arequipa-Antofalla basement, and ´ Grenville inliers.
2. The CUMC, as part of the AAB, must have been detached from the Amazon craton and the Rio Apa terrane between 1.67 and ~1.2 Ga.
3. The ca. 1.3 Ga San Ignacio Orogeny, well represented in the Paragua ´ terrane and on the Amazon craton, is not represented at CUMC, which indicates that the CUMC only collided against the Amazon craton after this orogeny.
4. The CUMC collided at ~1.2 Ga with the Amazon craton and was later metamorphized to granulite grade at ~1 Ga, i.e., at the end of the Grenville Orogeny.
5. The migmatization and later granulite metamorphism seen at CUMC likely took place as two progressive stages of the same orogeny between 1.19 and 1.0 Ga.

6 The Hf data from the Cerro Chilla volcano-sedimentary sequence, Arequipa basin, Central Andes sediments, and Puncoviscana Formation indicate that the Cerro Uyarani Metamorphic Complex could have represented a potential source area for these deposits. However, data with less negative and positive εHf indicate that another provenance area was also involved or that we still do not have enough data to comprehensively describe the zircon populations in CUMC samples.

7 The CUMC has further potential to elucidate geological history of crustal growth for this wider terrane throughout the Paleo- and Mesoproterozoic. In particular, further detailed field analysis – geological and structural – would be useful.

8 No evidence to support that the CUMC could have been part of the alleged Mara craton has been found.

Credit authorship contribution statement

Juliana Rezende de Oliveira: Conceptualization, Data curation, Formal analysis, Investigation, Resources, Validation, Visualization, Writing – original draft, Writing – review & editing. **Natalia Hauser:** Writing – review & editing, Visualization, Validation, Supervision, Resources, Project administration, Methodology, Data curation, Conceptualization. **Wolf Uwe Reimold:** Validation, Visualization, Writing – review & editing. **Amarildo Salina Ruiz:** Writing – review & editing, Validation, Resources, Methodology, Investigation, Funding acquisition. **Ramiro Matos:** Investigation, Resources, Validation. **Thassio Werlang:** Writing – review & editing, Visualization, Validation, Investigation.

Declaration of competing interest

The authors declare that they have no known competing financial interests or personal relationships that could have appeared to influence the work reported in this paper.

Acknowledgements

Financial support was provided by the National Council for Scientific and Technological Development (CNPq) of Brazil under grant number 141387/2015–7 to N.H, A.S.R, and W.U.R. We thank CNPq of Brazil for the research productivity scholarship of the first author. The research of NH and WUR has been supported in part by CNPq fellowships (grants 309878/2019–5 and 305761/2019–6, respectively). We are also grateful for partial support of this study from the Coordenaçao de Aperfei˜ çoamento de Pessoal de Nível Superior – Brazil (CAPES) – under Finance Code 001. We thank Drs. Pedro Cordeiro and Elton Dantas for the comments on an early draft of this manuscript. We are grateful for the support of the Laboratory of Geochronology of the University of Brasilia technical team: Barbara Alcantara Ferreira Lima, ´ Erico Natal Pedro ´ Zacchi, Dr. Guilherme de Oliveira Gonçalves and Joseneusa Brilhante Rodrigues (Geological Survey of Brazi). The Editor Andres Folguera, the reviewer Fernando Corfu, and a second anonymous reviewer are thanked for editorial handling and constructive comments.

Appendix A. Supplementary data

Supplementary data to this article can be found online at

https://doi.org/10.1016/j.jsames.2022.103843.

2.8 REFERENCES

Adams, C.J., 2011. The Pacific Gondwana margin in the late Neoproterozoic-early Paleozoic: detrital zircon U-Pb ages from metasediments in northwest Argentina reveal their maximum age, provenance and tectonic setting. Gondwana Res. 19, 71–83. https://doi.org/10.1016/j.gr.2010.05.002.

Albarède, F., Telouk, P., Blichert-Toft, J., Boyet, M., Agranier, A., Nelson, B., 2004. Precise and accurate isotopic measurements using multiple collector ICPMS. Geochem. Cosmochim. Acta 68.

Aparicio Gonzalez, P., Pimentel, M., Hauser, N., Moya, M.C., 2014. U-Pb LA-ICP-MS geochronology of detrital zircon grains from low-grade metasedimentary rocks (Neoproterozoic-Cambrian) of the Mojotoro Range, northwest Argentina. J. S. Am. Earth Sci. 49, 39–50. https://doi.org/10.1016/j.jsames.2013.10.002.

Araujo, T.P., Mello, F.M., 2010. Processamento de imagens digitais - razão entre bandas. Geociências 29 (1), 121–131.

ASTER, 2018. Cerro Uyarani - Oruro Digital Elevation Model image from 2018 was retrieved on 2021_05_04 from https://search.earthdata.nasa.gov/search, maintained by the NASA EOSDIS Land Processes Distributed Active Archive Center (LP DAAC) at the USGS Earth Resources Observation and Science (EROS) Center, Sioux Falls. South Dakota.

Bahlburg, H., Hervé, F., 1997. Geodynamic evolution and tectonostratigraphic terranes of NW-Argentina and N-Chile. GSA Bull 109, 869–884. https://doi.org/10.1130/0016-7606(1997)109<0869:GEATTO>2.3.CO;2.

Bahlburg, H., Vervoort, J.D., DuFrane, S.A., Carlotto, V., Reimann, C., Cardenas, J., ´ 2011. The U-Pb and Hf isotope evidence of detrital zircons of the Ordovician Ollantaytambo Formation, southern Peru, and the Ordovician provenance and paleogeography of southern Peru and northern Bolivia. J. S. Am. Earth Sci. 32 https://doi.org/10.1016/j.jsames.2011.07.002, 0895-9811, 196-209.

Bahlburg, H., Zimmermann, U., Matos, R., Berndt, J., Jimenez, N., Gerdes, A., 2020. The Missing Link of Rodinia Breakup in Western South America: A Petrographical, Geochemical, and Zircon Pb-Hf Isotope Study of the Volcanosedimentary Chilla Beds (Altiplano, Bolivia). Geosph.

Bertotti, A.L., 2012. Lu-Hf em zircão por LA-MC-ICP-MS, Porto Alegre, PhD Thesis, 162pp. Universidade Federal do Rio Grande do Sul, Porto Alegre.

Bertotti, A.L., Chemale Jr., F., Kawashita, K., 2013. Lu-Hf em zircão por LA-ICP-MS: aplicação em Gabro do Ofiolito de Aburrá. Colômbia. Pesqui. Geoc. 40 (2), 117ˆ –127. https://doi.org/10.22456/1807-9806.43075.

Bettencourt, J.S., Leite Jr., W.B., Ruiz, A.S., Matos, R., Payolla, B.L., Tosdal, R.M., 2010. The rondonian-san Ignacio province in the SW amazonian craton: an overview. J. S. Am. Earth Sci. 29 (1), 28–46. https://doi.org/10.1016/j.jsames.2009.08.006.

Blichert-Toft, J., Albarède, F., 1997. The Lu-Hf isotope geochemistry of chondrites and the evolution of the mantle–crust system. Earth Planet Sci. Lett. 148, 243–258. https://doi.org/10.1016/s0012-821x(97)00040-x.

Boger, S.D., Raetz, M., Giles, D., Etchart, E., Fanning, M.C., 2005. U–Pb age data from the Sunsas region of Eastern Bolivia, evidence for the allochthonous origin of the Paraguá Block. Precambrian Res. 139, 121-146. https://doi.org/10.1016/j. precamres.2005.05.010.

Brown, M., 2001. Orogeny, migmatites and leucogranites: a review. J. Earth Syst. Sci. 110, 313–336. https://doi.org/10.1007/BF02702898.

Bühn, B.M., Pimentel, M.M., Matteini, M., Dantas, E.L., 2009. High spatial resolution analyses of Pb and U isotopes for geochronology by laser ablation multi-collector inductively coupled plasma mass spectrometry (LA-MC-ICP-MS). Ann. Acad. Bras. Ciências 81, 1–16. https://doi.org/10.1590/S0001-37652009000100011.

Casquet, C., Pankhurst, R.J., Fanning, C.M., Baldo, E., Galindo, C., Rapela, C.W., González-Casado, J.M., Dahlquist, J.A., 2006. U-Pb SHRIMP zircon dating of Grenvillian metamorphism in Western Sierras Pampeanas (Argentina): correlation with the Arequipa-Antofalla craton and constraints on the extent of the Precordillera Terrane. Gondwana Res. 9, 524–529. https://doi.org/10.1016/j.gr.2005.12.004.

Casquet, C., Pankhurst, R.J., Galindo, C., Rapela, C., Fanning, C.M., Baldo, E., Dahlquist, J., González Casado, J.M., Colombo, F., 2008a. A deformed alkaline igneous rock–carbonatite complex from the Western Sierras Pampeanas, Argentina: evidence for late Neoproterozoic opening of the Clymene Ocean? Precambrian Res.
165 (3–4), 205–220. https://doi.org/10.1016/j.precamres.2008.06.011.

Casquet, C., Pankhurst, R.J., Rapela, C., Galindo, C., Fanning, C.M., Chiaradia, M., Baldo, E., González-Casado, J.M., Dahlquist, J.A., 2008b. The Maz terrane: a mesoproterozoic domain in the western Sierras Pampeanas (Argentina) equivalent to the arequipa–antofalla block of southern Peru? Implications for western Gondwana margin evolution. Gondwana Res. 13, 163–175.

Casquet, C., Fanning, C.M., Galindo, C., Pankhurst, R.J., Rapela, C., Torres, P., 2010. The Arequipa Massif of Peru: new SHRIMP and isotope constraints on a Paleoproterozoic inlier in the Grenvillian orogen. J. S. Am. Earth Sci. 29 (1), 128–142. https://doi. org/10.1016/j.jsames.2009.08.009.

Casquet, C., Rapela, C.W., Pankhurst, R.J., Baldo, E.G., Galindo, C., Fanning, C.M., Dahlquist, J.A., Saavedra, J., 2012. A history of proterozoic terranes in southern south America: from Rodinia to Gondwana. Geosci. Front. 3, 137–145. https://doi. org/10.1016/j.gsf.2011.11.004.

Chauvel, C., Blichert-Toft, J., 2001. A hafnium isotope and trace element perspective on melting of the depleted mantle. Earth Planet Sci. Lett. 190 (3–4), 137–151. https:// doi.org/10.1016/S0012-821X(01)00379-X.

Chavez, C., Roddaz, M., Dantas, E.L., Ventura Santos, R., Alvan, A.A., 2022. Provenance ´ of the middle jurassic-cretaceous sedimentary rocks of the Arequipa basin (south Peru) and implications for the geodynamic evolution of the central Andes.
Gondwana Res. 101, 59–76. https://doi.org/10.1016/j.gr.2021.07.018, 1342-937X.

Chu, N.C., Taylor, R.N., Chavagnac, V., Nesbitt, R.W., Boella, R.M., Milton, J.A., German, C.R., Bayon, G., Burton, K., 2002. Hf isotope ratio analysis using multi- collector inductively coupled plasma mass spectrometry: an evaluation of isobaric interference corrections. J. Anal. At. Spectr. 17, 1567–1574. https://doi.org/ 10.1039/b206707b.

Cobbing, E.J., Pitcher, 1972. Plate tectonics and the Peruvian Andes. Nature 246, 51–53. https://doi.org/10.1038/physci240051a0.

Cobbing, E.J., Ozard, J.M., Snelling, N.J., 1977. Reconnaissance geochronology of the crystalline basement of the Coastal Cordillera of southern Peru. GSA Bull 88,
241–246. https://doi.org/10.1130/0016-7606.

Copernicus Sentinel Data, 2020. Cerro Uyarani - Oruro Sentinel-2A image from 2020 was retrieved on 2021_03_28, produced from European Space Agency - ESA remote sensing data, image processed by Copernicus Open Access Hub.

Condie, K.C., Beyer, E., Belousova, E., Griffin, W.L., O’Reilly, S.Y., 2005. U–Pb isotopic ages and Hf isotopic composition of single zircons: the search for juvenile Precambrian continental crust. Precambrian Res. 139, 1–2. https://doi.org/ 10.1016/j.precamres.2005.04.006, 42–100.

Cordani, U.G., Milani, E.J., Thomaz Filho, A., Campos, D.A., 2000. Tectonic evolution of south America. Rev. Geol. Chile 27 (2), 255. https://doi.org/10.4067/S0716- 02082000000200006.
Cordani, U.G., Teixeira, W., Tassinari, C.C.G., Coutinho, J.M.V., Ruiz, A.S., 2010. The Rio Apa craton in mato grosso do sul (Brazil) and northern Paraguay: geochronological evolution, correlations and tectonic implications for Rodinia and Gondwana. Am. J. Sci. 310, 981–1023. https://doi.org/10.2475/09.2010.09.
Corfu, F., Hanchar, J.M., Hoskin, P.W.O., Kinny, P., Hanchar, J.M., Hoskin, P.W.O., 2003. Atlas of zircon textures. In: Mineral, Zircon, Amer, Soc (Eds.), Rev. Mineral. Geochem. 53, 469–500. https://doi.org/10.2113/0530469.
Dalmayrac, B., Lancelot, J.R., Leyreloup, A., 1977. Two-billion-year granulites in the late Precambrian metamorphic basement along the southern Peruvian coast. Science 198, 49–51. https://doi.org/10.1126/science.198.4312.49.
Dorbath, C., Granet, M., Poupinet, G., Martínez, C., 1993. A teleseismic study of the Altiplano and the Eastern Cordillera and northern Bolivia: new constraints on a lithospheric model. J. Geophys. Res. 98, 9825–9844. https://doi.org/10.1029/ 92JB02406.
Drusch, M., Del Bello, U., Carlier, S., Colin, O., Fernandez, V., Gascon, F., Hoersch, B., Isola, C., Laberinti, P., Martimort, P., Meygret, A., Spoto, F., Sy, O., Marchese, F., Bargellini, P., 2012. Sentinel-2: ESA's optical high-resolution mission for GMES operational services. Rem. Sens. Environ. 120, 25–36. https://doi.org/10.1016/j. rse.2011.11.026.
Evernden, J.F., Kriz, S.J., Cherroni, M.C., 1977. Potassium-argon ages of some Bolivian rocks. Econ. Geol. 72 (6), 1042–1061. https://doi.org/10.2113/ gsecongeo.72.6.1042.
Fal, S., Maanan, M., Baidder, L., Rhinane, H., 2019. The Contribution of Sentinel-2 satellite images for geological mapping in the south of Tafilalet basin (Eastern Anti- Atlas, Morocco). Int. Arch. Photogram. Rem. Sens. Spatial Inf. Sci. XLII-4/W12, 75–82. https://doi.org/10.5194/isprs-archives-XLII-4-W12-75-2019.
Fuck, R.A., Brito Neves, B.B., Schobbenhaus, C., 2008. Rodinia descendants in south America. Precambrian Res. 160 (1–2), 108–126. https://doi.org/10.1016/j. precamres.2007.04.018.
Gerdes, A., Zeh, A., 2006. Combined U–Pb and Hf isotope LA-(MC-) ICP-MS analyses of detrital zircons: comparison with SHRIMP and new constraints for the provenance and age of an Armorican metasediment in Central Germany. Earth Planet Sci. Lett. 249, 47–61. https://doi.org/10.1016/j.epsl.2006.06.039.
Gerdes, A., Zeh, A., 2009. Zircon formation versus zircon alteration – new insights from combined U–Pb and Lu–Hf in situ LA-ICP-MS analyses, and consequences for the interpretation of Archean zircon from the Central Zone of the Limpopo Belt. Chem. Geol. 261, 230–243. https://doi.org/10.1016/j.chemgeo.2008.03.005.
Götze, H.J., Lahmeyer, B., Schmidt, S., Strunk, S., 1994. The lithospheric structure of the ̈ central Andes (20–26°S) as inferred from interpretation of regional gravity. In: Reutter, K.J., Scheuber, E., Wigger, P.J. (Eds.), Tectonics of the Southern Central Andes. Springer, Berlin-Heidelberg. https://doi.org/10.1007/978-3-642-77353-2_1.
Harmon, R.S., Barreiro, B.A., Moorbath, S., Hoefs, J., Francis, P.W., Thorpe, R.S., Déruelle, B., McHugh, J., Viglino, J.A., 1984. Regional O-, Sr-, and Pb-isotope relationships in late Cenozoic calc-alkaline lavas of the Andean Cordillera. J. Geol. Soc. 141 (5), 803–822. https://doi.org/10.1144/gsjgs.141.5.0803.
Hatcher Jr., R.D., Bream, B.R., Miller, C.L., Eckert Jr., J.O., Fullagar, P.D., Carrigan, C. W., 2004. Paleozoic structure of southern appalachian Blue Ridge grenvillian internal basement massifs. In: Bartholomew, M.J., Corriveau, L., McLelland, J., Tollo, R.P. (Eds.), Proterozoic Evolution of the Grenville Orogen in North America, vol. 197. Geol. Soc. of Amer. Memoirs, Boulder, CO, pp. 525–547. https://doi.org/ 10.1130/0-8137-1197-5.
Hauser, N., Matteini, M., Omarini, R., Pimentel, M.M., 2011. Combined U–Pb and Lu–Hf isotope data on turbidites of the Paleozoic basement of NW Argentina and petrology of associated igneous rocks: implications for the tectonic evolution of western Gondwana between 560 and 460 Ma. Gondwana Res. 19, 100–127. https://doi.org/ 10.1016/j.gr.2010.04.002.
Hoffman, P.F., 1991. Did the breakout of Laurentia turn Gondwana inside out? Science 252, 1409–1412. https://doi.org/10.1126/science.252.5011.1409.

Jackson, S.E., Pearson, N.J., Griffin, W.L., Belousova, E.A., 2004. The application of laser ablation-inductively coupled plasma-mass spectrometry to in situ U-Pb zircon geochronology. Chem. Geol. 211, 47–69. https://doi.org/10.1016/j. chemgeo.2004.06.017.

Johansson, Å., 2009. Baltica, Amazonia and the SAMBA connection—1000 million years of neighbourhood during the proterozoic? Precambrian Res. 175 (1–4), 221–234. https://doi.org/10.1016/j.precamres.2009.09.011

Johansson, Å., 2014. From Rodinia to Gondwana with the 'SAMBA' model—a distant view from Baltica towards Amazonia and beyond. Precambrian Res. 244, 226–235. https://doi.org/10.1016/j.precamres.2013.10.012.

Johansson, Å., Bingen, B., Huhma, H., Waight, T., Vestergaard, R., Soesoo, A., Skridlaite, G., Krzeminska, E., Shumlyanskyy, L., Holland, M.E., Holm-Denoma, C., Teixeira, W., Faleiros, F.M., Ribeiro, B.V., Jacobs, J., Wang, C., Thomas, R.J., Macey, P.H., Kirkland, C.L., Hartnady, M.I.H., Eglington, B.M., Puetz, S.J., Condie, K. C., 2022. A geochronological review of magmatism along the external margin of Columbia and in the Grenville-age orogens forming the core of Rodinia. Precambrian Res. 371, 1–43. https://doi.org/10.1016/j.precamres.2021.106463.

Karlstrom, K.E., Harlan, S.S., Williams, M.L., McClelland, J., Geissman, J.W., Åhäll, K.-I., 1999. Refining Rodinia: geologic evidence for the Australia–western US connection in the Proterozoic. GSA Today (Geol. Soc. Am.) 9 (10), 1–7. https://doi.org/ 10.1130/GSAT-1999-10-01-science.

Kroner, A., Wan, Y., Liu, X., Liu, D., 2014. Dating of zircon from high-grade rocks: which ¨ is the most reliable method? Geosci. Frontiers 5, 515–523. https://doi.org/10.1016/ j.gsf.2014.03.012.

Kunz, B.E., Regis, D., Engi, M., 2018. Zircon ages in granulite facies rocks: decoupling from geochemistry above 850 ◦C? Contrib. Mineral. Petrol. 173 (26), 1–21. https:// doi.org/10.1007/s00410-018-1454-5.

Lehmann, B., 1978. A Precambrian core sample from the Altiplano/Bolivia. Geol. Rundsch. 67, 270–278. https://doi.org/10.1007/BF01803266.

Litherland, M., Annells, R.N., Appleton, J.D., Berrangée, J.P., Bloomfield, K., Burton, C.C. I., Darbyshire, D.P.F., Fletcher, C.J.N., Hawkins, M.P., Klinck, B.A., Llanos, A., Mitchell, W.I., O'Connor, E.A., Pitfield, P.E.J., Power, G., Webb, B.C., Brit. Geol. S., London: H.M.S.O, 1986. The Geology and Mineral Resources of the Bolivian Precambrian Shield, vol. 153. Overseas Memoir, 9.

Litherland, M., Annels, R.N., Hawkins, M.P., Klinck, B.A., O'Connor, E.A., Pitfield, P.E.J., Power, G., Darbyshire, D.P.F., Fletcher, C.N.J., Mitchell, W.I., Webb, B.C., 1989. The Proterozoic of eastern Bolivia and its relationships to the Andean mobile belt. Precambrian Res. 43, 157–174. https://doi.org/10.1016/0301-9268(89)90054-5.

Loewy, S.L., Connelly, J.N., Dalziel, I.W.D., Gower, C.F., 2003. Eastern Laurentia in Rodinia: constraints from whole-rock Pb and U/Pb geochronology. Tectonophysics 375 (1–4), 169–197. https://doi.org/10.1016/S0040-1951(03)00338-X.

Loewy, S., Connelly, J.N., Dalziel, I.W., 2004. An orphaned basement block: the Arequipa-Antofalla Basement of the central Andean margin of South America. GSA Bull 116, 171–187. https://doi.org/10.1130/B25226.1.

Ludwig, K.R., Isoplot 3.75, 2012. A Geochronological Toolkit for Microsoft Excel, vol. 5. Berkeley Geochronology Center Spec. Publ., pp. 1–75.

Mamani, M., 2006. Variations in Magma Composition in Time and Space along the Central Andes (12◦S -28◦S). Ph. D. Dissertation, Universität ¨Göttingen, Göttingen, Germany, p. 123.

Mamani, M., Tassara, A., Wörner, G., 2008. Composition and structural control of crustal ¨ domains in the Central Andes. G-cubed 9 (3), Q03006. https://doi.org/10.1029/ 2007GC001925.

Mamani, M., Wörner, G., Sempere, T., 2010. Geochemical variations in igneous rocks of ¨ the Central Andean orocline (13◦S to 18◦S): tracing crustal thickening and magma generation through time. GSA Bull 122, 162–182. https://doi.org/10.1130/ B26538.1.

Martignole, J., Martelat, J.E., 2003. Regional-scale grenvillian-age UHT metamorphism in the mollendo–camana block (basement of the Peruvian Andes). J. Metamorph. Geol. 21, 99–120. https://doi.org/10.1046/j.1525-1314.2003.00417.x.

Martin, E.L., Collins, W.J., Spencer, C.J., 2019. Laurentian origin of the Cuyania suspect terrane, western Argentina, confirmed by Hf isotopes in zircon. Geol. Soc. Am. Bull. 132, 273–290. https://doi.org/10.1130/B35150.1.

Martin, E.L., Spencer, C.J., Collins, W.J., Thomas, R.J., Macey, P.H., Roberts, N.M.W., 2020. The core of Rodinia formed by the juxtaposition of opposed retreating and advancing accretionary orogens. Earth Sci. Rev. 211, 103413. https://doi.org/10.1016/j.earscirev.2020.103413, 0012-8252.

Matteini, M., Junges, S.L., Dantas, E.L., Pimentel, M.M., Bühn, B., 2010. In situ zircon U Pb and Lu Hf isotope systematic on magmatic rocks: insights on the crustal evolution of the Neoproterozoic Goiás Magmatic Arc, Brasília belt, Central Brazil. Gondwana ´ Res. 17, 1–12. https://doi.org/10.1016/j.gr.2009.05.008.

Morel, M.L.A., Nebel, O., Nebel-Jacobsen, Y.L., Miller, J.S., Vroon, P.Z., 2008. Hafnium isotope characterization of the GJ-1 zircon reference material by solution and laser ablation MC. ICPMS. Chem. Geol. 255, 231–235. https://doi.org/10.1016/j. chemgeo.2008.06.040.

Nascimento, N.D.C., Ruiz, A.S., Pierosan, R., Lima, G.A., Matos, J.B., Lafon, J.M., Moura, C.A.V., 2016. Petrogenesis, U-Pb and Sm-Nd geochronology of the furna azul migmatite: partial melting evidence during the san Ignacio orogeny, Paraguá terrane, SW Amazon craton. Brazilian J. Geol. 46 (2), 239–259. https://doi.org/ 10.1590/2317-4889201620160030.

Nebel, O., Nebel-Jacobsen, Y., Mezger, K., Berndt, J., 2007. Initial Hf isotope compositions in magmatic zircon from early Proterozoic rocks from the Gawler Craton, Australia: a test for zircon model ages. Chem. Geol. 241 (1–2), 23–37. https://doi.org/10.1016/j.chemgeo.2007.02.008.

Oliveira, F.V., 2015. Chronus: Um novo suplemento para a redução de dados U-Pb˜ obtidos por LA-MC-ICPMS. M.Sc. Diss. Inst. Geociencias, Universidade de Brasília, Brasilia, Brazil, p. 19559, 10.26512/2015.06.D.

Oliveira, J.R., Sousa, M. Z. A. de, Ruiz, A.S., Salinas, G.R.M., 2017. Granulito Uyarani – uma janela estrutural Pré-Cambriana no Altiplano Boliviano: petrogêenese e significado tectônico. Geol. Usp. Sˆérie Científica 17 (2), 223–245. https://doi.org/ 10.11606/issn.2316-9095.v17-385.

Omarini, R.H., Sureda, R.J., Götze, J.-H., Seilacher, A., Pflüger, F., 1999. Pucoviscana ¨ folded belt in northwestern Argentina: testimony of Late Proterozoic Rodinia fragmentation and pre-Gondwana collisional episodes. Int. J. Earth Sci. 88 (1), 76–97. https://doi.org/10.1007/s005310050247.

Ortiz, A., Hauser, N., Becchio, R., Suzaño, N., Nieves, A., Sola, A., Pimentel, M., Reimold, W., 2017. Zircon U-Pb ages and Hf isotopes for the Diablillos intrusive complex, southern Puna, Argentina: crustal evolution of the lower paleozoic orogen, southwestern Gondwana margin. J. S. Am. Earth Sci. 80, 316–339. https://doi.org/ 10.1016/j.jsames.2017.09.031.

Ownby, S.E., Miller, C.F., Berquist, P.J., Carrigan, C.W., Wooden, J.L., Fullagar, P.D., 2004. U–Pb geochronology and geochemistry of a portion of the Mars Hill Terrane, North Carolina-Tennessee: constraints on its origin, history and tectonic assembly. Geol. Soc. Am. Mem. 197, 609–632. https://doi.org/10.1130/0-8137-1197-5.609.

Pacci, D., Munizaga, F., Hervé, F., Kawashita, K., Cordani, U.G., 1980. Acerca de la edad Rb-Sr Precámbrica de rocas de la Formación Esquistos de Belén. Rev. Geol. Chile, Dept. de Parinacota, Chile 10. https://doi.org/10.5027/andgeoV7n3-a03.

Pankhurst, R.J., Hervé, F., Fanning, M.C., Calderon, M., Niemeyer, H., Griem-Klee, S., ´ Soto, F., 2016. The pre-Mesozoic rocks of northern Chile: U-Pb ages, and Hf and O isotopes. Earth Sci. Rev. 152, 88–105. https://doi.org/10.1016/j.earscirev.2015.11.009.

Patchett, P.J., 1983. Importance of the Lu–Hf isotopic system in studies of planetary chronology and chemical evolution. Geochem. Cosmochim. Acta 47, 81–91. https://doi.org/10.1016/0016-7037(83)90092-3.

Pepper, M., Gehrels, G., Pullen, A., Ibanez-Mejia, M., Ward, K.M., Kapp, P., 2016. Magmatic history and crustal genesis of western South America: constraints from U- Pb ages and Hf isotopes of detrital zircons in modern rivers. Geosphere. https://doi. org/10.1130/ges01315.1.
Quadros, M.L.E.S., Della Giustina, M.E.S., Rodrigues, J.B., Souza, V.S., 2021. A geochronological review of magmatism along the external margin of Columbia and in the Grenville-age orogens forming the core of Rodinia. J. S. Am. Earth Sci. 109, 103220. https://doi.org/10.1016/j.jsames.2021.103220, 2021 1-25.
Ramos, V.A., 1988. The tectonics of the Central Andes: 30° to 33°S latitude. In: Clark, S., Burchfiel, D. (Eds.), Processes in Continental Lithospheric Deformation. GSA Spec. https://doi.org/10.1130/SPE218-p31. Paper 218, 31–54.
Ramos, V.A., 2008a. The basement of the Central Andes: the Arequipa and related terranes. Annu. Rev. Earth Planet Sci. 36, 289–324. https://doi.org/10.1146/ annurev.earth.36.031207.124304.
Ramos, V.A., 2008b. Patagonia: a Paleozoic continent adrift? J. S. Am. Earth Sci. 26, 235–251. https://doi.org/10.1016/j.jsames.2008.06.002.
Ramos, V.A., 2018. Tectonic evolution of the central Andes: from terrane accretion to crustal delamination. In: Zamora, G., McClay, K.R. (Eds.), Petroleum Basins and Hydrocarbon Potential of the Andes of Peru and Bolivia. https://doi.org/10.1306/ 13622115M1172855.
Ramos, V.A., Vujovich, G.I., Dallmeyer, R.D., 1996. Los klippes y ventanas tectónicas de la estructura preándica de la Sierra de Pie de Palo (San Juan): edad e implicaciones tectónicas. In: Actas 13th Congreso Geológico Argentino and 3rd Congreso Exploración de Hidrocarburos, vol. 5, pp. 377–392. Buenos Aires.
Redes, L.A., Hauser, N., Ruiz, A.S., Matos, R., Reimold, W.U., Dantas, E.L., Schmitt, R.T., Lima, B.A.F., Zacchi, E.N.P., Chaves, J.G.S., Osorio, L.F.B., Pimentel, M.M., 2020. U–Pb and Hf isotopes in granitoids from the Eastern Bolivian basement: insights into the Paleoproterozoic evolution of the western part of South America. J. S. Am. Earth Sci. 104, 102806. https://doi.org/10.1016/j.jsames.2020.102806.
Ribeiro, B.V., Cawood, P.A., Faleiros, F.M., Mulder, J.A., Martin, E., Finch, M.A., Raveggi, M., Teixeira, W., Cordani, U.G., Pavan, M., 2020. A long-lived active margin revealed by zircon U–Pb–Hf data from the Rio Apa Terrane (Brazil): new insights into the Paleoproterozoic evolution of the Amazonian Craton. Precambrian Res. 350, 105919. https://doi.org/10.1016/j.precamres.2020.105919.
Rivers, T., Culshaw, N., Hynes, A., Indares, A., Jamieson, R., Martignole, J., 2012. The Grenville orogen—a post-LITHOPROBE perspective. In: Percival, J.A., Cook, F.A., Clowes, R.M. (Eds.), Tectonic Styles in Canada: the LITHOPROBE Perspective, vol. 49. Geol. Assoc. Canada Spec. Pap., pp. 97–236
Rizzotto, G.J., Hartmann, L.A., Santos, J.O.S., McNaughton, N.J., 2014. Tectonic evolution of the southern margin of the Amazonian craton in the late Mesoproterozoic based on field relationships and zircon U-Pb geochronology. An Acad. Bras Ciências 86, 57ˆ –84. https://doi.org/10.1590/0001-37652014104212.
Ruiz, A.S., Sousa, M.Z.A., Matos, J.B., Macambira, M.B., Lima, G.A., Faria, D.A., 2011. Cráton ou Terreno Paraguá? Uma discussão baseada em novos dados geológicos e geocronológicos do SW do Cráton Amazônico em território brasileiro. Simpósio Nacional de Estudos Tectônicos 13, 23ˆ9–242. Campinas. Short Paper.
Sadowski, G.R., Bettencourt, J.B., 1996. Mesoproterozoic tectonic correlations between eastern Laurentia and the western border of the Amazon Craton. Precambrian Res. 76, 213–227. https://doi.org/10.1016/0301-9268(95)00026-7.
Santos, J.O., Hartmann, L.A., Gaudette, H.E., Groves, D.I., Mcnaughton, N.J., Fletcher, I. R., 2000. A new understanding of the provinces of the Amazon Craton based on integration of field mapping and U-Pb and Sm-Nd geochronology. Gondwana Res. 3, 453–488. https://doi.org/10.1016/S1342-937X(05)70755-3.
Santos, J.O.S., Rizzotto, G.J., Chemale Jr., F., Hartmann, L.A., Quadros, M.L.E.S., McNaughton, N.J., 2003. Three distinctive collisional orogenies in the southwestern Amazon Craton: constraints from U–Pb geochronology. In: IV. South American Symposium. On Isotope Geology, Salvador, Brazil, Short Papers, vol. 1, pp. 282–285.

Santos, J.O.S., Rizzotto, G.J., Potter, P.E., McNaughton, N.J., Mato, R.S., Hartmann, L.A., Chemale Jr., F., Quadros, M.E.S., 2008. Age and autochthonous evolution of the sunsás orogen in the west Amazon craton based on mapping and U-Pb ´ geochronology. Precambrian Res. 165, 120–152. https://doi.org/10.1016/j.precamres.2008.06.009.

Sawyer, E.W., 2008. Working with migmatites: nomenclature for the constituent parts. In: Sawyer, E.W., Brown, M. (Eds.), Working with Migmatites. Mineral. Assoc. Can., Short Course Series, vol. 38, p. 28pp.

Scherer, E., Münker, C., Mezger, K., 2006. Calibration of the lutetium–hafnium clock. Science 293, 683–687. https://doi.org/10.1126/science.1061372.

Shackleton, R.M., Ries, A.C., Coward, M.P., Cobbold, P.R., 1979. Structure, metamorphism and geochronology of the Arequipa massif of Coastal Peru. J. Geol. Soc., London 136, 195–214. https://doi.org/10.1144/gsjgs.136.2.0195.

Sinha, A.K., McLelland, J.M., 1999. Lead isotope mapping of crustal reservoirs within the Grenville superterrane: II. Adirondack massif, New York. In: Sinha, A.K. (Ed.), Proc. Int. Conf. Basement Tect. 13, 297–312. https://doi.org/10.1007/978-94-011-4800- 9_17.

Tassinari, C.G.C., Macambira, M.J.B., 2004. A evolução tectônica do cráton ama zônico. In: Geol, Soc Brazilian (Ed.), Geologia do Continente Sul-Americano – Evolução da Obra de Fernando Flavio de Almeida, vol. XXVIII. Capítulo, 47 1–486, sbgeo.org.br/ home/pages/44.

Taylor, S.R., McLennan, S.M., 1985. The Continental Crust: its Composition and Evolution. Blackwell, Oxford, p. 312pp.

Teixeira, W., Geraldes, M.C., Matos, R., Ruiz, A.S., Saes, G., Vargas-Matto, G., 2010. A review of the tectonic evolution of the Sunsas belt, SW Amazonian Craton. J. S. ´ Am. Earth Sci. 29, 47–60. https://doi.org/10.1016/j.jsames.2009.09.007.

Teixeira, W., Cordani, U.G., Faleiros, F.M., Sato, K., Maurer, V.C., Ruiz, A.S., Azevedo, E. J.P., 2020. The Rio Apa Terrane reviewed: U-Pb zircon geochronology and provenance studies provide paleotectonic links with a growing Proterozoic Amazonia. Earth Sci. Rev. 202, 103089. https://doi.org/10.1016/j.earscirev.2020.103089.

Thomas, W.A., Gehrels, G.E., Greb, S.F., Nadon, G.C., Satkoski, A.M., Romero, M.C., 2017. Detrital zircons and sediment dispersal in the Appalachian foreland. Geosp 13 (6), 2206–2230. https://doi.org/10.1130/GES01525.1.

Tohver, E., van der Pluijm, B.A., Van der Voo, R., Rizzotto, G., Scandolara, J.E., 2002. Paleogeography of the Amazon craton at 1.2 Ga: early Grenville collision with the llano segment of Laurentia. Earth Planet Sci. Lett. 199, 185–200. https://doi.org/ 10.1016/S0012-821X(02)00561-7.

Tohver, E., van der Pluijm, B.A., Mezger, K., Essene, E.J., Scandolara, J., Rizzotto, G., 2003. Implications of a two-stage tectonic history of the SW Amazon craton: recognizing the Nova Brasilandia metasedimentary belt as a late Mesoproterozoic suture zone in Rodinia reconstructions. Geol. Soc. Amer. Abstr. with Programs 36, 301.

Tohver, E., Bettencourt, J.S., Tosdal, R., Mezger, K., Leite, W.B., Payolla, B.L., 2004a. Terrane transfer during the Grenville orogeny: tracing the Amazonian ancestry of southern Appalachian basement through Pb and Nd isotopes. Earth Planet Sci. Lett. 228 (1–2), 161–176. https://doi.org/10.1016/j.epsl.2004.09.029.

Tohver, E., Van Der Pluijm, B., Mezger, K., Essene, E., Scandolara, J., Rizzotto, G., 2004b. Significance of the Nova Brasilandia metasedimentary belt in western Brazil: ˆ redefining the mesoproterozoic boundary of the Amazon craton. Tectonics 23 (6), 5–20. https://doi.org/10.1029/2003TC001563.

Tosdal, R.M., 1996. The Amazon–Laurentian connection as viewed from Middle Proterozoic rocks in the central Andes, western Bolivia and northern Chile. Tectonics 15, 827–882. https://doi.org/10.1029/95TC03248.

Tröeng, B., Soria-Escalante, E., Claure, H., Mobarec, R., Murillo, F., 1994. Descubrimiento de basamento precambrico en la Cordillera Occidental Altiplano de los Andes Bolivianos, vol. XI. Memoria del Congresso de Geologica de Bolivia, pp. 231–237.

Vervoort, J.D., Plank, Terry, Prytulak, J., 2011. The Hf–Nd isotopic composition of marine sediments. Geochem. Cosmochim. Acta 75 (20), 5903–5926. https://doi.org/10.1016/j.gca.2011.07.046.

Walfort, B., Hammerschmidt, K., Worner, G., 1995. New Ar/Ar ages from tertiary¨ volcanics in the north Chilean Andes (18 S) : implication for tectonic and magmatic evolution. EUG-meeting strasburg. Terra Abstracts, Terra Nova 7, 354. April 1995. United States Geological Survey, 2013. Cerro Uyarani - Oruro Landsat-8 image from 2013 was retrieved on 2020-04-10 from https://earthexplorer.usgs.gov courtesy of the United States Geological Survey - USGS, maintained by Earth Explorer.

Wasteneys, A.H., Clark, A.H., Farrar, E., Langridge, R.J., 1995. Grenvillian granulite- facies metamorphism in the Arequipa massif, Peru: a Laurentia-Gondwana link. Earth Planet Sci. Lett. 132, 63–73. https://doi.org/10.1016/0012-821X(95)00055- H.

Wedepohl, K.H., 1995. The composition of the continental crust. Geochem. Cosmochim. Acta 59 (7), 1217–1232. https://doi.org/10.1016/0016-7037(95)00038-2.

Whitney, D.L., Evans, B.W., 2010. Abbreviations for names of rock-forming minerals. Am. Mineral. 95, 185–187. https://doi.org/10.2138/am.2010.3371.

Wiedenbeck, M., Allé, P., Corfu, F., Griffin, W.L., Meier, M., Oberli, F., Von Quadt, A., Roddick, J.C., Spiegel, W., 1995. Three natural zircon standards for U–Th–Pb, Lu–Hf, trace element and REE analyses. Geostand. Newsl. 19, 1–23. https://doi.org/ 10.1111/j.1751-908X.1995.tb00147.x.

Wiedenbeck, M., Hanchar, J.M., Peck, W.H., Sylvester, P., Valley, J., Whitehouse, M., Kronz, A., Morishita, Y., Nasdala, L., Fiebig, J., Franchi, I., Girard, J.P., Greenwood, R.C., Hinton, R., Kita, N., Mason, P.R.D., Norman, M., Ogasawara, M., Piccoli, P.M., Rhede, D., Satoh, H., Schulz-Dobrick, B., Skår, O., Spicuzza, M.J., Terada, K., Tindle, A., Togashi, S., Vennemann, T., Xie, Q., Zheng, Y.F., 2004. Further characterization of the 91500-zircon crystal. Geostand. Geoanal. Res. 28, 9–39. https://doi.org/10.1111/j.1751-908X.2004.tb01041.x.

Wilson, P., 1975. Potassium-argon Age Studies in Peru with Special Reference to the Emplacement of the Coastal Batholith. Ph.D. Thesis. University of Liverpool, England, p. 299.

Wörner, G., Lezaun, J., Beck, A., Heber, V., Lucassen, F., Zinngrebe, E., Rössling, R., Wilke, H.G., 2000. Precambrian and early paleozoic evolution of the andean basement at belen (northern Chile) and Cerro Uyarani (western Bolivia Altiplano). J. S. Am. Earth Sci. 13, 717–737. https://doi.org/10.1016/S0895-9811(00)00056-0.

Zeh, A., Gerdes, A., Barton Jr., J., Klemd, R., 2010a. U-Th-Pb and Lu-Hf systematics of zircon from TTG's, leucosomes, meta-anorthosites and quartzites of the Limpopo
Belt (South Africa): constraints for the formation, recycling and metamorphism of Palaeoarchaean crust. Precambrian Res. 179, 50–68. https://doi.org/10.1016/j.precamres.2010.02.012.

Zeh, A., Gerdes Will, T.M., Frimmel, H.E., 2010b. Hafnium isotope homogenization during metamorphic zircon growth in amphibolite-facies rocks: examples from the Shackleton Range (Antarctica). Geochem. Cosmochim. Acta 74, 4740–4758. https://doi.org/10.1016/j.gca.2010.05.016.

Zhao, G., Cawood, P.A., Wilde, S.A., Sun, M., 2002. Review of global 2.1–1.8 Ga orogens: implications for a pre-Rodinia supercontinent. Earth Sci. Rev. 59, 125–162. https://doi.org/10.1016/S0012-8252(02)00073-9.

2.9 SUPPLEMENTARY MATERIAL

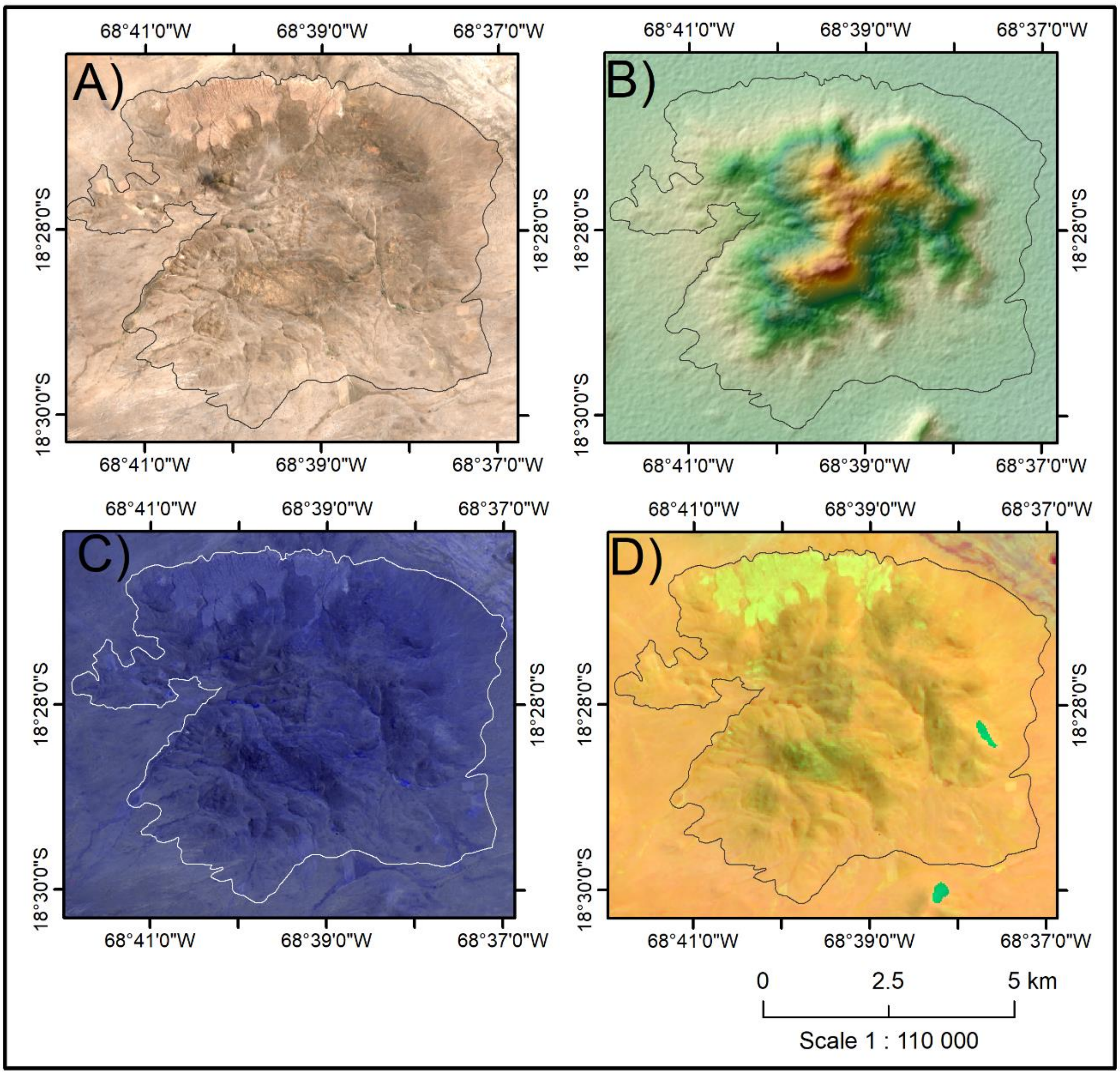

Figure 1. Domain characterization with remote sensing images. A) Spatial and spectral characteristics of Sentinel-2A band 10m data (https://sentinel.esa.int). B) ASTER Global Digital Elevation model (https://earthdata.nasa.gov/) based on Shuttle Radar Topography Mission data (https://earthexplorer.usgs.gov), using the Hillshade tool C) Landsat-8 image (https:// earthexplorer.usgs.gov) with combined bands: R1/G2/B5 and D) Landsat-8 image (https:// earthexplorer.usgs.gov) with combined bands: R10/G7/B3.

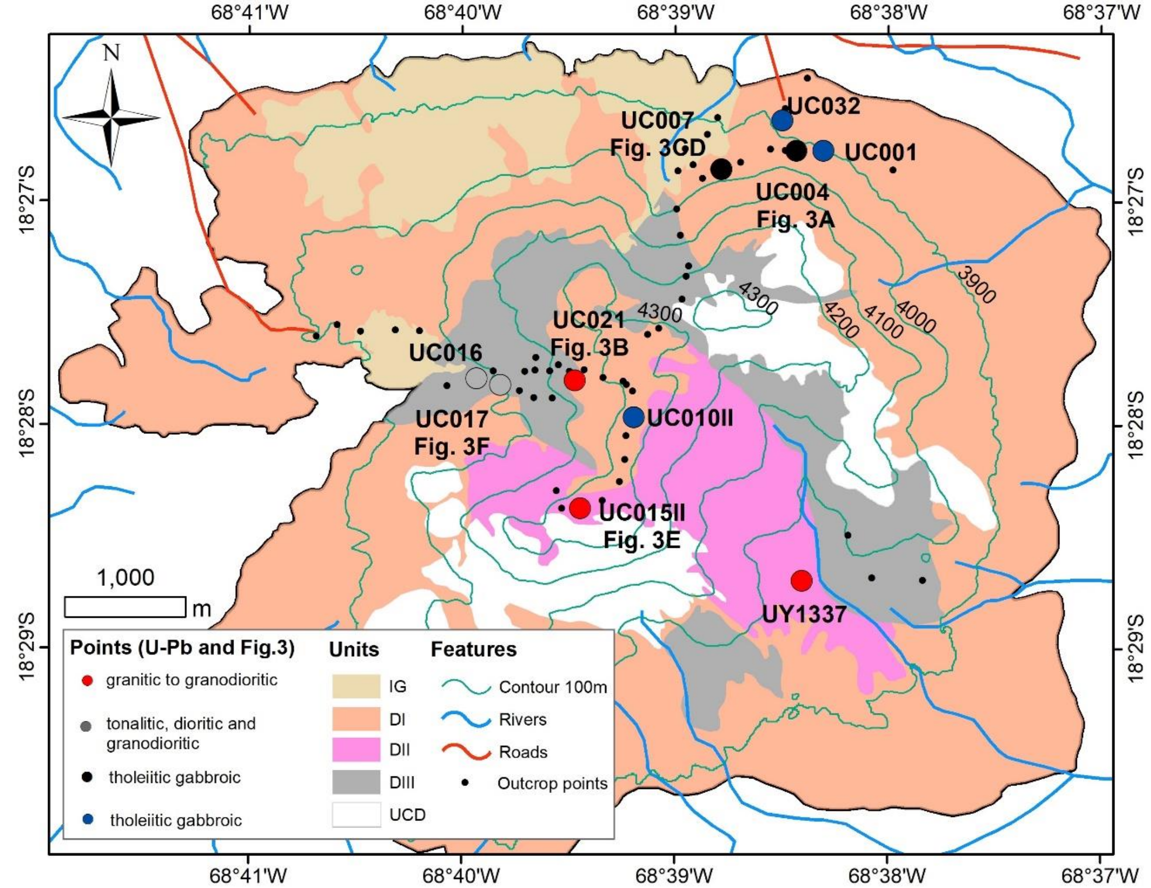

Figure 2. Outcrop map of the study area. Outcrop points indicate field observations from different CUMC domains. Points (U-Pb and Fig. 3) indicate selected places for U-Pb sampling (UC021, UY1337, UC016, UC032, UC10II, and UC001) and outcrops illustrated in figure 3 for the CUMC domains I, II, III, and mafic bodies. The colored circles (red, gray, black, and blue) indicate the chemical composition for U-Pb selected samples.

Supplementary Table 01: Characterization of the domains of the CUMC on the basis of remote sensing observations (Sentinel-2, Landsat-8 yellow and Landsat-8 blue data). These characteristcis allow us to define 5 domains.

Unit name	Colors and tones	Shape	Texture	Limit	Area (ha)
Ignimbrite Domain (IG)	Sentinel-2: orange beige. Yellow Landsat-8: vibrant light yellow. Landsat-8 blue: light gray.	Irregular ovoid form. The weathering causes large open grooves in the ignimbrite, which exposes the basement. Discordant contact with the basement.	Medium roughness, with grooves caused by weathering.	Sinuous and well-defined.	377 (9%)
Felsic Granulite Domain I (DI)	Sentinel-2: light orange interspersed with dark gray. Yellow Landsat-8: thin yellow band followed by gray and salmon colored, thick bands, trending NE to SW. Landsat-8 blue: dark blue and grayish blue.	Ovoid shape with concentric subdomains. Three bands with a variety of shades that follow the occurrence of felsic and mafic granulite. Envelopes the other domains as DIII, or is cut off by them.	Medium to high roughness.	Sinuous boundaries.	2594 (62%)
Felsic Granulite Domain II (DII)	Sentinel-2: light beige interspersed with gray. Yellow Landsat-8: orange with round bodies in light gray color. Landsat-8 blue: intercalated with light gray and light blue bands.	Roundish shape, resembling a pluton.	Medium roughness and locally higher roughness.	Limits are variably curved or straight.	323 (8%)

Granulite Domain (DIII)	Sentinel-2: grayish brown sometimes intercalated with beige bands. Yellow Landsat-8: dark mustard. This domain is darker than DI and DII and much lighter than DIII. Landsat-8 blue: bluish-purple band and light gray band.	Tabular. NE-SW at central-northern region of the complex and NW-SE in the central-eastern. A small occurrence in the southern region just south of DII.	Smooth texture.	Irregular. Locally defined by color and eslewhere by faults.	453.5 (11%)
Plutonic Domain (DIV)	Sentinel-2: yellowish beige and light brown. Yellow Landsat-8: green and gray. Landsat-8 blue: dark blue.	Mainly ovoid bodies of variable size, and a comparatively longer, elongated body trending NW-SE, parallel to DIII.	High roughness	Well marked, mainly by the texture that stands out from the others.	420.3 (10%)

List of images used in the processing of geological map data:

Sentinel-2 10m (R:4, G:3, B:2) - Natural color

Landsat-8 (R:10, G:7, B:3) – Yellow

Landsat-8 (R:1, G:3, B:5) – Blue

SRTM Hillshade

Supplementary Table 02: Results of U-Pb isotope analysis by LA-ICP-MS on zircon from granulites and amphibolite samples of CUMC.

				Radiogenic ratios							Apparent Ages (Ma)						
Sample	Spots	Th/U	^{206}Pb mV[1]	$^{207}Pb/^{206}Pb$	1σ %	$^{207}Pb/^{235}U$	1σ %	$^{206}Pb/^{238}U$	1σ %	Rho	$^{207}Pb/^{206}Pb$	2σ abs	$^{207}Pb/^{235}U$	2σ abs	$^{206}Pb/^{238}U$	2σ abs	Conc (%)
UC021	ZR26	0.83	0.0112	0.11	0.4	4.62	0.8	0.31	0.6	0.75	1757	14	1752	13	1748	18	100
UC021	ZR20C	0.77	0.0163	0.11	0.8	4.26	1.8	0.29	1.5	0.86	1737	31	1685	29	1643	45	95
UC021	ZR21	0.85	0.0163	0.11	0.8	4.42	2.2	0.30	2.0	0.91	1736	31	1717	36	1701	60	98
UC021	ZR24	0.65	0.0150	0.10	0.5	4.34	0.9	0.30	0.6	0.69	1704	18	1702	14	1699	18	100
UC021	ZR04C	0.67	0.0182	0.10	0.4	4.03	1.1	0.28	1.0	0.87	1697	16	1641	19	1597	28	94
UC021	ZR05C	0.86	0.0162	0.10	0.5	4.35	1.7	0.30	1.6	0.93	1686	19	1702	28	1715	48	102
UC021	ZR08C	1.05	0.0138	0.10	0.7	3.76	2.8	0.26	2.7	0.96	1678	27	1585	44	1515	72	90
UC021	ZR03C	0.62	0.0030	0.10	0.6	3.97	1.1	0.28	0.8	0.75	1666	23	1628	18	1598	23	96
UC021	ZR06C	1.01	0.0349	0.10	0.4	3.84	2.5	0.27	2.4	0.97	1661	16	1600	40	1554	67	94
UC021	ZR15	0.35	0.0034	0.10	0.8	3.63	2.5	0.26	2.4	0.93	1650	30	1555	40	1487	63	90
UC021	ZR30	0.67	0.0070	0.10	0.8	3.68	1.6	0.27	1.3	0.83	1622	29	1566	25	1525	35	94
UC021	ZR07	0.49	0.0071	0.10	1.1	3.47	2.2	0.26	1.9	0.86	1567	40	1521	34	1489	50	95
UC021	ZR03R	0.19	0.0149	0.08	0.4	2.36	1.0	0.21	0.8	0.81	1209	16	1231	14	1244	18	103
UC021	ZR02R	0.04	0.0102	0.08	0.4	2.24	0.9	0.20	0.8	0.83	1208	15	1192	13	1184	17	98
UC021	ZR17C	0.17	0.0319	0.08	0.5	2.37	0.8	0.21	0.6	0.68	1207	19	1233	12	1248	13	103
UC021	ZR14	0.51	0.0112	0.08	1.7	2.27	2.3	0.21	1.6	0.67	1204	66	1204	33	1204	35	100
UC021	ZR17R	0.18	0.0111	0.08	0.6	2.25	0.9	0.20	0.6	0.68	1198	22	1197	13	1196	14	100
UC021	ZR11R	0.04	0.0126	0.08	0.6	2.29	1.0	0.21	0.8	0.76	1197	22	1210	15	1218	18	102
UC021	ZR13R	0.15	0.0446	0.08	0.4	2.41	0.8	0.22	0.6	0.76	1191	16	1246	12	1278	15	107
UC021	ZR08R	0.24	0.0008	0.08	1.6	2.23	2.6	0.20	2.0	0.78	1189	63	1189	36	1189	44	100
UC021	ZR18C	0.11	0.0153	0.08	0.6	2.29	1.0	0.21	0.7	0.70	1189	25	1209	15	1220	16	103
UC021	ZR16R	0.13	0.0149	0.08	0.6	2.29	1.1	0.21	0.9	0.78	1189	23	1209	16	1220	19	103
UC021	ZR20R	0.10	0.0169	0.08	0.4	2.31	0.8	0.21	0.6	0.74	1187	15	1215	11	1232	13	104
UC021	ZR01R	0.22	0.0105	0.08	0.3	2.34	0.9	0.21	0.8	0.86	1184	12	1226	13	1250	18	106
UC021	ZR22R	0.15	0.0177	0.08	0.5	2.19	0.8	0.20	0.6	0.70	1181	18	1179	11	1177	12	100

UC021	ZR12C	0.19	0.0290	0.08	0.5	2.39	0.9	0.22	0.5	0.64	1176	21	1240	12	1277	13	109
UC021	ZR04R	0.09	0.0124	0.08	1.5	2.19	2.3	0.20	1.7	0.74	1166	60	1178	32	1185	38	102
UC021	ZR11C	0.18	0.0016	0.08	1.4	2.13	2.1	0.20	1.6	0.74	1163	55	1158	29	1155	33	99
UC021	ZR10R	0.34	0.0080	0.08	1.1	2.04	1.8	0.19	1.4	0.76	1154	44	1130	25	1117	28	97
UC021	ZR18R	0.36	0.0066	0.08	0.7	1.92	1.3	0.18	1.0	0.78	1093	27	1087	17	1085	20	99
UC021	ZR09R	0.37	0.0084	0.07	0.7	1.59	1.6	0.16	1.4	0.86	991	30	968	20	958	25	97
UC021	*ZR13C*	*0.69*	*0.0032*	*0.20*	*6.2*	*7.96*	*6.7*	*0.29*	*2.5*	*0.37*	*2845*	*196*	*2227*	*118*	*1619*	*72*	*57*
UC021	*ZR02C*	*0.57*	*0.0033*	*0.11*	*1.1*	*3.86*	*2.3*	*0.26*	*2.0*	*0.86*	*1795*	*40*	*1605*	*37*	*1465*	*51*	*82*
UC021	*ZR22C*	*0.69*	*0.0132*	*0.10*	*1.8*	*4.04*	*2.2*	*0.28*	*1.1*	*0.52*	*1713*	*67*	*1642*	*36*	*1587*	*32*	*93*
UC021	*ZR27*	*0.80*	*0.0058*	*0.10*	*0.5*	*4.16*	*1.4*	*0.29*	*1.3*	*0.88*	*1705*	*20*	*1666*	*23*	*1636*	*36*	*96*
UC021	*ZR25C*	*0.67*	*0.0174*	*0.10*	*0.5*	*3.78*	*0.9*	*0.27*	*0.7*	*0.74*	*1652*	*18*	*1589*	*14*	*1541*	*18*	*93*
UC021	*ZR23C*	*0.82*	*0.0053*	*0.10*	*0.5*	*3.51*	*0.9*	*0.25*	*0.6*	*0.69*	*1626*	*20*	*1528*	*14*	*1459*	*16*	*90*
UC021	*ZR05R*	*0.26*	*0.0047*	*0.10*	*0.8*	*3.89*	*2.3*	*0.28*	*2.2*	*0.93*	*1625*	*28*	*1612*	*38*	*1602*	*62*	*99*
UC021	*ZR28*	*0.55*	*0.0173*	*0.10*	*0.6*	*3.13*	*2.1*	*0.23*	*2.0*	*0.94*	*1615*	*21*	*1439*	*32*	*1323*	*47*	*82*
UC021	*ZR29*	*0.55*	*0.0025*	*0.10*	*1.1*	*3.31*	*1.8*	*0.25*	*1.3*	*0.74*	*1574*	*41*	*1483*	*27*	*1420*	*33*	*90*
UC021	*ZR25R*	*0.43*	*0.0034*	*0.09*	*1.5*	*3.12*	*3.6*	*0.24*	*3.2*	*0.91*	*1490*	*54*	*1438*	*54*	*1404*	*81*	*94*
UC021	*ZR01C*	*0.20*	*0.0342*	*0.09*	*0.8*	*2.99*	*1.4*	*0.24*	*1.1*	*0.77*	*1440*	*31*	*1406*	*22*	*1383*	*27*	*96*
UC021	*ZR23R*	*0.49*	*0.0068*	*0.09*	*0.9*	*2.18*	*2.6*	*0.18*	*2.5*	*0.93*	*1385*	*33*	*1176*	*36*	*1065*	*48*	*77*
UC021	*ZR10C*	*0.41*	*0.0139*	*0.09*	*0.5*	*1.78*	*1.3*	*0.15*	*1.2*	*0.87*	*1329*	*20*	*1037*	*17*	*903*	*19*	*68*
UC021	*ZR09C*	*0.51*	*0.0189*	*0.08*	*0.7*	*2.26*	*2.0*	*0.20*	*1.8*	*0.91*	*1281*	*28*	*1200*	*28*	*1156*	*38*	*90*
UC021	*ZR16C*	*0.01*	*0.0329*	*0.08*	*0.4*	*2.55*	*2.6*	*0.23*	*2.5*	*0.98*	*1229*	*15*	*1286*	*37*	*1321*	*60*	*107*
UC021	*ZR06R*	*0.01*	*0.0379*	*0.08*	*0.5*	*1.49*	*1.0*	*0.14*	*0.8*	*0.77*	*1175*	*21*	*927*	*13*	*826*	*12*	*70*
UC021	*ZR12R*	*0.23*	*0.0198*	*0.08*	*0.5*	*2.18*	*1.4*	*0.21*	*1.2*	*0.88*	*1113*	*21*	*1175*	*19*	*1209*	*27*	*109*
UC021	*ZR19*	*0.18*	*0.0188*	*0.07*	*2.5*	*1.96*	*3.4*	*0.19*	*2.3*	*0.68*	*1055*	*98*	*1103*	*45*	*1128*	*48*	*107*
UY1337	ZR08C	0.56	0.0111	0.11	0.4	4.80	0.9	0.32	0.7	0.78	1774	15	1784	15	1793	21	101
UY1337	ZR42	1.04	0.0201	0.11	0.3	4.52	0.7	0.30	0.5	0.73	1768	11	1735	11	1708	15	97
UY1337	ZR06	0.48	0.0098	0.11	0.4	4.62	0.9	0.31	0.7	0.79	1764	15	1752	15	1742	22	99

UY1337	ZR04C	0.90	0.0165	0.11	0.6	4.55	1.0	0.31	0.7	0.72	1759	21	1740	16	1724	22	98
UY1337	ZR38	0.51	0.0072	0.11	0.3	4.45	0.8	0.30	0.6	0.78	1758	13	1722	13	1691	19	96
UY1337	ZR33C	0.52	0.0071	0.11	0.4	4.61	0.8	0.31	0.6	0.72	1758	16	1751	14	1745	18	99
UY1337	ZR41C	0.44	0.0066	0.11	0.4	4.50	0.8	0.30	0.6	0.71	1755	15	1732	13	1712	17	98
UY1337	ZR45	0.74	0.0093	0.11	0.5	4.53	0.8	0.31	0.5	0.65	1755	18	1737	14	1721	16	98
UY1337	ZR27	0.44	0.0085	0.11	0.5	4.53	0.8	0.31	0.5	0.63	1754	20	1737	14	1723	16	98
UY1337	ZR36C	0.70	0.0083	0.11	0.4	4.37	1.1	0.30	1.0	0.89	1742	13	1706	19	1677	30	96
UY1337	ZR46C	0.70	0.0122	0.11	0.6	4.25	0.9	0.29	0.6	0.65	1739	20	1685	14	1641	17	94
UY1337	ZR02C	0.47	0.0104	0.11	0.4	4.32	0.9	0.29	0.8	0.82	1739	14	1697	15	1663	22	96
UY1337	ZR58C	0.53	0.0073	0.11	0.4	4.39	0.8	0.30	0.6	0.72	1736	14	1711	13	1691	17	97
UY1337	ZR22	0.49	0.0102	0.11	0.3	4.54	0.8	0.31	0.6	0.76	1735	13	1737	13	1739	18	100
UY1337	ZR53C	0.51	0.0084	0.11	0.4	4.50	1.0	0.31	0.8	0.83	1732	14	1731	16	1730	24	100
UY1337	ZR47C	0.48	0.0044	0.11	1.0	3.88	1.3	0.27	0.8	0.59	1726	36	1609	21	1521	21	88
UY1337	ZR54	0.58	0.0075	0.11	0.4	4.29	1.0	0.29	0.8	0.81	1726	16	1691	16	1663	23	96
UY1337	ZR31C	0.70	0.0075	0.11	0.4	4.51	1.1	0.31	0.9	0.86	1726	16	1733	18	1738	29	101
UY1337	ZR34R	0.56	0.0055	0.11	0.5	3.93	0.9	0.27	0.7	0.77	1724	17	1620	15	1542	20	89
UY1337	ZR37C	0.59	0.0058	0.11	0.4	3.91	1.0	0.27	0.9	0.87	1723	13	1616	17	1535	24	89
UY1337	ZR10	0.46	0.0063	0.11	0.4	4.24	0.9	0.29	0.7	0.79	1722	16	1681	15	1649	21	96
UY1337	ZR23	0.41	0.0098	0.11	0.7	4.20	1.1	0.29	0.7	0.68	1721	25	1675	17	1638	21	95
UY1337	ZR52C	0.60	0.0102	0.11	0.5	4.22	1.0	0.29	0.7	0.77	1719	18	1678	16	1645	21	96
UY1337	ZR15C	0.45	0.0113	0.11	0.6	4.35	1.0	0.30	0.7	0.71	1719	21	1703	16	1690	20	98
UY1337	ZR25	0.50	0.0100	0.10	0.5	4.24	0.9	0.29	0.7	0.72	1714	20	1682	15	1657	20	97
UY1337	ZR49C	0.50	0.0061	0.10	0.5	4.17	0.9	0.29	0.6	0.69	1710	20	1668	15	1634	18	96
UY1337	ZR16C	0.39	0.0084	0.10	0.5	4.32	0.9	0.30	0.7	0.71	1709	20	1697	15	1687	20	99
UY1337	ZR59C	0.63	0.0098	0.10	0.6	4.49	1.4	0.31	1.2	0.84	1708	23	1730	23	1747	35	102
UY1337	ZR32C	0.52	0.0075	0.10	0.4	4.03	0.8	0.28	0.6	0.76	1704	14	1641	13	1592	18	93
UY1337	ZR48C	0.68	0.0062	0.10	0.5	3.92	1.1	0.27	0.8	0.79	1701	19	1619	17	1556	23	91
UY1337	ZR49R	0.60	0.0177	0.10	0.4	3.92	0.8	0.28	0.5	0.70	1681	15	1617	12	1569	15	93
UY1337	ZR30C	0.42	0.0073	0.10	0.4	4.03	0.8	0.28	0.6	0.73	1679	15	1640	13	1610	16	96
UY1337	ZR51C	0.58	0.0102	0.10	0.4	3.82	0.8	0.27	0.6	0.74	1677	15	1598	13	1538	16	92

UY1337	ZR43C	0.58	0.0076	0.10	0.6	3.71	1.1	0.26	0.9	0.77	1656	23	1573	18	1512	24	91
UY1337	ZR50C	0.71	0.0056	0.10	0.5	3.86	1.0	0.28	0.7	0.75	1648	20	1606	16	1573	20	95
UY1337	ZR28C	0.44	0.0114	0.10	0.4	3.85	1.1	0.28	1.0	0.86	1648	16	1603	18	1569	27	95
UY1337	ZR55C	0.72	0.0076	0.10	0.6	3.73	1.3	0.27	1.2	0.86	1624	21	1578	21	1544	32	95
UY1337	ZR56C	0.53	0.0071	0.10	0.8	3.55	1.1	0.26	0.7	0.64	1617	29	1538	18	1482	19	92
UY1337	ZR01R	0.39	0.0353	0.10	0.5	3.57	1.0	0.26	0.8	0.77	1607	20	1542	16	1495	21	93
UY1337	ZR51R1	0.57	0.0075	0.10	0.4	3.32	0.9	0.24	0.7	0.75	1591	16	1485	14	1412	17	89
UY1337	ZR12	0.40	0.0258	0.10	0.6	3.51	1.1	0.26	0.9	0.80	1587	21	1530	18	1490	24	94
UY1337	ZR11C	0.89	0.0125	0.10	0.5	3.16	0.9	0.24	0.7	0.77	1537	17	1447	14	1387	18	90
UY1337	ZR33R	0.04	0.0210	0.08	0.3	2.37	0.8	0.21	0.7	0.81	1226	12	1235	12	1240	15	101
UY1337	ZR13R	0.02	0.0261	0.08	0.4	2.35	0.9	0.21	0.6	0.74	1218	17	1226	12	1231	14	101
UY1337	ZR28R	0.03	0.0221	0.08	0.4	2.39	0.8	0.21	0.6	0.77	1217	15	1241	12	1255	15	103
UY1337	ZR59R	0.07	0.0260	0.08	0.5	2.31	1.0	0.21	0.7	0.76	1203	20	1215	13	1221	16	101
UY1337	ZR58R	0.31	0.0129	0.08	0.9	2.34	1.5	0.21	1.2	0.78	1203	34	1226	21	1239	26	103
UY1337	ZR57R	0.05	0.0214	0.08	0.3	2.20	0.7	0.20	0.5	0.71	1191	13	1180	10	1174	11	99
UY1337	ZR04R	0.06	0.0248	0.08	0.5	2.27	0.9	0.21	0.7	0.74	1189	20	1202	13	1209	15	102
UY1337	ZR44R	0.11	0.0383	0.08	0.4	2.29	1.1	0.21	0.9	0.85	1188	17	1209	16	1222	21	103
UY1337	ZR39C	0.04	0.0208	0.08	1.1	2.16	1.4	0.20	0.8	0.57	1182	44	1169	20	1162	17	98
UY1337	ZR35R	0.07	0.0289	0.08	0.4	2.02	1.2	0.19	1.1	0.90	1161	16	1122	17	1103	23	95
UY1337	ZR39R	0.07	0.0314	0.08	0.4	2.14	0.9	0.20	0.7	0.79	1152	16	1162	12	1168	15	101
UY1337	ZR30R	4.77	0.0008	0.08	1.8	1.79	2.8	0.17	2.1	0.74	1069	72	1043	36	1030	39	96
UY1337	ZR18R	2.80	0.0010	0.07	0.9	1.81	1.4	0.18	1.0	0.70	1055	37	1051	18	1049	19	99
UY1337	ZR03R	2.01	0.0021	0.07	0.9	1.79	1.4	0.17	1.0	0.71	1047	36	1040	18	1037	18	99
UY1337	ZR46R	0.11	0.0212	0.07	0.6	1.83	1.0	0.18	0.7	0.69	1039	25	1055	13	1062	13	102
UY1337	ZR08R	2.06	0.0016	0.07	1.5	1.74	1.9	0.18	1.1	0.58	976	60	1022	24	1043	21	107
UY1337	ZR56R	0.13	0.0135	0.07	1.2	1.66	2.8	0.16	2.5	0.89	1028	49	994	35	979	45	95
UY1337	ZR31R	0.40	0.0080	0.07	1.2	1.59	1.7	0.16	1.1	0.67	978	48	964	21	959	20	98

UY1337	*ZR40C*	*0.87*	*0.0065*	*0.11*	*2.5*	*4.04*	*2.86*	*0.26*	*1.3*	*0.45*	*1825*	*90*	*1643*	*46*	*1505*	*34*	*82*
UY1337	*ZR29*	*0.54*	*0.0080*	*0.11*	*0.4*	*4.53*	*0.84*	*0.31*	*0.6*	*0.74*	*1759*	*15*	*1736*	*14*	*1717*	*19*	*98*
UY1337	*ZR05C*	*0.43*	*0.0074*	*0.11*	*0.5*	*4.64*	*1.08*	*0.31*	*0.9*	*0.8*	*1755*	*21*	*1703*	*16*	*1690*	*20*	*96*
UY1337	*ZR17*	*0.41*	*0.0078*	*0.11*	*0.4*	*4.74*	*0.82*	*0.32*	*0.6*	*0.78*	*1747*	*23*	*1730*	*23*	*1747*	*35*	*100*
UY1337	*ZR03C*	*0.25*	*0.0211*	*0.11*	*0.8*	*4.02*	*1.74*	*0.27*	*1.5*	*0.85*	*1746*	*31*	*1639*	*28*	*1557*	*41*	*89*
UY1337	*ZR36R*	*0.56*	*0.0110*	*0.11*	*0.3*	*4.38*	*0.77*	*0.30*	*0.6*	*0.79*	*1742*	*11*	*1709*	*13*	*1681*	*18*	*97*
UY1337	*ZR09*	*0.77*	*0.0065*	*0.11*	*0.4*	*4.44*	*0.93*	*0.30*	*0.8*	*0.83*	*1728*	*21*	*1740*	*16*	*1724*	*22*	*100*
UY1337	*ZR18C*	*0.51*	*0.0079*	*0.10*	*0.6*	*4.17*	*0.99*	*0.29*	*0.7*	*0.74*	*1686*	*20*	*1737*	*14*	*1723*	*16*	*102*
UY1337	*ZR32R1*	*0.47*	*0.0058*	*0.10*	*0.5*	*4.52*	*1*	*0.32*	*0.8*	*0.79*	*1680*	*18*	*1734*	*16*	*1779*	*24*	*106*
UY1337	*ZR52R*	*0.30*	*0.0094*	*0.10*	*0.5*	*4.05*	*1.11*	*0.29*	*0.9*	*0.81*	*1679*	*20*	*1645*	*18*	*1618*	*26*	*96*
UY1337	*ZR19C*	*0.46*	*0.0092*	*0.10*	*0.5*	*4.13*	*1.08*	*0.29*	*0.9*	*0.8*	*1664*	*19*	*1660*	*18*	*1656*	*25*	*100*
UY1337	*ZR21*	*0.55*	*0.0138*	*0.10*	*0.6*	*3.83*	*1.46*	*0.27*	*1.3*	*0.87*	*1661*	*23*	*1599*	*23*	*1552*	*35*	*93*
UY1337	*ZR20C*	*0.55*	*0.0121*	*0.10*	*0.6*	*3.95*	*1.21*	*0.28*	*1.0*	*0.83*	*1655*	*21*	*1624*	*19*	*1600*	*28*	*97*
UY1337	*ZR24*	*0.58*	*0.0146*	*0.10*	*0.7*	*3.73*	*1.01*	*0.27*	*0.6*	*0.64*	*1655*	*25*	*1579*	*16*	*1522*	*17*	*92*
UY1337	*ZR13C*	*0.33*	*0.0055*	*0.10*	*0.5*	*3.91*	*1.16*	*0.28*	*1.0*	*0.82*	*1646*	*20*	*1615*	*19*	*1591*	*27*	*97*
UY1337	*ZR14*	*0.45*	*0.0068*	*0.10*	*0.6*	*3.82*	*1*	*0.27*	*0.7*	*0.73*	*1646*	*21*	*1597*	*16*	*1560*	*20*	*95*
UY1337	*ZR41R*	*0.57*	*0.0145*	*0.10*	*0.7*	*3.99*	*1.22*	*0.29*	*1.0*	*0.78*	*1633*	*24*	*1633*	*20*	*1633*	*28*	*100*
UY1337	*ZR07C*	*0.40*	*0.0070*	*0.10*	*0.4*	*3.67*	*1.02*	*0.27*	*0.8*	*0.82*	*1616*	*16*	*1565*	*16*	*1527*	*23*	*95*
UY1337	*ZR53R*	*0.60*	*0.0187*	*0.10*	*0.7*	*3.59*	*1.68*	*0.26*	*1.5*	*0.89*	*1611*	*25*	*1547*	*27*	*1500*	*40*	*93*
UY1337	*ZR26*	*0.24*	*0.0181*	*0.10*	*1.2*	*3.65*	*1.39*	*0.27*	*0.7*	*0.48*	*1558*	*43*	*1559*	*22*	*1561*	*19*	*100*
UY1337	*ZR40R*	*0.50*	*0.0077*	*0.10*	*0.5*	*3.34*	*1.13*	*0.25*	*1.0*	*0.84*	*1552*	*18*	*1489*	*18*	*1446*	*25*	*93*
UY1337	*ZR57C*	*0.47*	*0.0117*	*0.09*	*0.8*	*3.02*	*1.34*	*0.23*	*1.0*	*0.72*	*1524*	*32*	*1412*	*20*	*1339*	*23*	*88*
UY1337	*ZR37R*	*0.13*	*0.0171*	*0.09*	*0.4*	*2.79*	*0.79*	*0.22*	*0.6*	*0.75*	*1460*	*14*	*1352*	*12*	*1284*	*14*	*88*
UY1337	*ZR50R*	*0.38*	*0.0099*	*0.09*	*0.5*	*2.83*	*0.8*	*0.23*	*0.5*	*0.65*	*1448*	*18*	*1364*	*12*	*1311*	*12*	*91*
UY1337	*ZR51R2*	*0.23*	*0.0119*	*0.09*	*0.8*	*2.55*	*1.92*	*0.22*	*1.7*	*0.89*	*1340*	*30*	*1288*	*28*	*1257*	*39*	*94*
UY1337	*ZR35C*	*0.23*	*0.0117*	*0.09*	*0.7*	*2.19*	*1.32*	*0.19*	*1.1*	*0.82*	*1327*	*26*	*1178*	*18*	*1099*	*22*	*83*
UY1337	*ZR47R*	*0.33*	*0.0303*	*0.09*	*0.8*	*2.55*	*1.29*	*0.22*	*1.0*	*0.76*	*1324*	*29*	*1287*	*19*	*1265*	*23*	*95*
UY1337	*ZR44C*	*0.08*	*0.0161*	*0.08*	*0.8*	*3.13*	*1.65*	*0.27*	*1.4*	*0.85*	*1265*	*31*	*1440*	*25*	*1561*	*39*	*123*
UY1337	*ZR48R*	*0.01*	*0.0112*	*0.08*	*1.1*	*2.33*	*1.47*	*0.21*	*1.0*	*0.65*	*1241*	*41*	*1220*	*21*	*1209*	*21*	*97*

UY1337	*ZR02R*	*0.15*	*0.0346*	*0.08*	*0.5*	*2.40*	*0.88*	*0.21*	*0.6*	*0.68*	*1239*	*20*	*1244*	*13*	*1246*	*14*	*101*
UY1337	*ZR05R*	*0.05*	*0.0070*	*0.08*	*0.4*	*2.27*	*0.77*	*0.21*	*0.6*	*0.72*	*1203*	*15*	*1204*	*11*	*1204*	*12*	*100*
UY1337	*ZR43R*	*0.35*	*0.0275*	*0.08*	*0.7*	*2.01*	*0.99*	*0.18*	*0.6*	*0.64*	*1200*	*26*	*1120*	*13*	*1080*	*13*	*90*
UY1337	*ZR20R*	*0.03*	*0.0071*	*0.08*	*0.6*	*2.27*	*1.01*	*0.21*	*0.7*	*0.71*	*1190*	*24*	*1202*	*14*	*1208*	*16*	*101*
UY1337	*ZR34C*	*0.39*	*0.0434*	*0.08*	*0.9*	*1.75*	*1.66*	*0.16*	*1.3*	*0.79*	*1181*	*37*	*1028*	*21*	*958*	*23*	*81*
UY1337	*ZR19R*	*0.07*	*0.0661*	*0.08*	*0.4*	*2.25*	*0.8*	*0.21*	*0.6*	*0.73*	*1180*	*16*	*1197*	*11*	*1206*	*13*	*102*
UY1337	*ZR15R*	*0.06*	*0.0729*	*0.08*	*0.5*	*2.35*	*0.9*	*0.22*	*0.7*	*0.72*	*1178*	*20*	*1228*	*13*	*1257*	*15*	*107*
UY1337	*ZR11R*	*0.04*	*0.0168*	*0.08*	*0.4*	*2.49*	*0.85*	*0.23*	*0.7*	*0.79*	*1177*	*15*	*1270*	*12*	*1325*	*16*	*113*
UY1337	*ZR55R*	*0.10*	*0.0204*	*0.08*	*0.8*	*2.07*	*1.26*	*0.19*	*0.9*	*0.72*	*1143*	*32*	*1139*	*17*	*1136*	*19*	*99*
UY1337	*ZR07R*	*0.09*	*0.0124*	*0.07*	*0.4*	*1.93*	*0.84*	*0.19*	*0.6*	*0.74*	*1063*	*17*	*1093*	*11*	*1108*	*13*	*104*
UY1337	*ZR16R*	*0.21*	*0.0135*	*0.07*	*0.4*	*1.94*	*0.88*	*0.19*	*0.7*	*0.8*	*1048*	*15*	*1094*	*12*	*1118*	*14*	*107*
UY1337	*ZR56R*	*0.13*	*0.0195*	*0.07*	*1.2*	*1.66*	*2.8*	*0.16*	*2.5*	*0.89*	*1028*	*49*	*994*	*35*	*979*	*45*	*95*
UY1337	*ZR32R2*	*0.26*	*0.0080*	*0.07*	*2.1*	*1.96*	*2.54*	*0.19*	*1.3*	*0.52*	*1016*	*85*	*1102*	*34*	*1146*	*28*	*113*
UY1337	*ZR01C*	*0.10*	*0.0158*	*0.07*	*3.8*	*1.65*	*4.18*	*0.17*	*1.8*	*0.43*	*911*	*151*	*990*	*52*	*1025*	*34*	*113*
UC016	ZR18C	0.49	0.0093	0.12	1.0	5.39	2.9	0.34	2.7	0.92	1884	37	1882	49	1881	87	100
UC016	ZR10C	0.54	0.0070	0.11	0.9	4.94	1.6	0.32	1.3	0.82	1831	31	1810	28	1791	42	98
UC016	ZR23C	1.01	0.0082	0.11	0.5	4.75	1.9	0.31	1.8	0.94	1824	18	1776	31	1736	54	95
UC016	ZR5	0.41	0.0035	0.11	0.7	4.74	1.1	0.31	0.8	0.74	1814	25	1775	19	1742	26	96
UC016	ZR22C	0.55	0.0055	0.11	0.5	4.68	1.3	0.31	1.1	0.87	1793	20	1763	22	1738	35	97
UC016	ZR26R	0.55	0.0070	0.11	0.4	4.65	1.1	0.31	0.9	0.86	1790	14	1758	18	1731	28	97
UC016	ZR37C	0.48	0.0097	0.11	0.3	4.92	1.0	0.33	0.8	0.86	1789	12	1806	16	1821	26	102
UC016	ZR38	0.92	0.0074	0.11	0.4	4.83	0.9	0.32	0.7	0.81	1788	14	1790	15	1793	23	100
UC016	ZR42	0.52	0.0041	0.11	0.7	4.76	1.5	0.32	1.3	0.85	1782	25	1778	25	1775	40	100
UC016	ZR36	0.81	0.0083	0.11	0.4	4.28	1.4	0.29	1.3	0.93	1780	13	1690	23	1618	37	91
UC016	ZR35	0.89	0.0098	0.11	0.3	4.94	1.3	0.33	1.2	0.94	1780	10	1808	22	1833	40	103
UC016	ZR7	0.33	0.0028	0.11	1.2	4.89	1.8	0.33	1.4	0.75	1778	42	1801	31	1820	43	102
UC016	ZR3	0.66	0.0044	0.11	0.5	4.55	0.9	0.30	0.7	0.75	1773	17	1739	15	1712	20	97
UC016	ZR2	0.53	0.0041	0.11	0.6	4.50	1.0	0.30	0.7	0.69	1771	23	1732	17	1700	21	96

UC016	ZR44	0.49	0.0045	0.11	0.5	4.61	1.1	0.31	0.9	0.83	1770	17	1751	18	1736	27	98
UC016	ZR9R	0.51	0.0043	0.11	0.8	4.58	1.7	0.31	1.4	0.85	1769	30	1745	28	1725	44	98
UC016	ZR12	0.43	0.0037	0.11	0.8	4.66	1.8	0.31	1.6	0.89	1766	27	1761	30	1757	50	99
UC016	ZR8R	0.61	0.0057	0.11	0.5	4.40	0.9	0.30	0.7	0.77	1758	17	1712	15	1675	21	95
UC016	ZR19R2	0.31	0.0091	0.11	0.4	4.49	1.6	0.30	1.5	0.94	1755	14	1729	26	1708	45	97
UC016	ZR40	1.35	0.0076	0.11	0.4	4.32	1.1	0.29	0.9	0.85	1754	16	1696	18	1650	27	94
UC016	ZR14	0.49	0.0050	0.11	1.4	4.54	2.2	0.31	1.6	0.73	1752	52	1739	36	1727	48	99
UC016	ZR32C	1.17	0.0063	0.11	0.3	4.47	1.1	0.30	1.0	0.90	1752	12	1725	19	1703	30	97
UC016	ZR24R	0.55	0.0052	0.11	0.4	4.40	0.8	0.30	0.6	0.74	1749	16	1713	14	1683	19	96
UC016	ZR23R	0.95	0.0066	0.11	0.4	4.09	1.2	0.28	1.1	0.88	1744	16	1652	20	1581	31	91
UC016	ZR4C	0.43	0.0039	0.11	0.6	4.33	1.2	0.30	1.0	0.81	1732	23	1700	20	1673	30	97
UC016	ZR6C	0.41	0.0047	0.11	0.8	4.04	1.4	0.28	1.0	0.75	1717	31	1643	22	1586	29	92
UC016	ZR21C	0.34	0.0096	0.11	0.6	3.93	1.2	0.27	0.9	0.78	1715	23	1621	19	1549	25	90
UC016	ZR30R	0.65	0.0121	0.11	0.8	4.15	1.9	0.29	1.6	0.87	1715	31	1664	30	1623	46	95
UC016	ZR33C	0.73	0.0101	0.11	0.4	3.91	1.3	0.27	1.2	0.91	1715	14	1616	20	1542	32	90
UC016	ZR27	1.02	0.0064	0.10	0.4	3.95	1.0	0.27	0.8	0.82	1702	16	1624	16	1564	23	92
UC016	ZR15C	0.64	0.0110	0.10	0.4	4.04	0.8	0.28	0.6	0.71	1698	15	1643	13	1601	16	94
UC016	ZR29	0.62	0.0062	0.10	0.5	4.01	1.3	0.28	1.2	0.88	1689	19	1637	21	1597	33	95
UC016	ZR19C	0.71	0.0055	0.10	0.5	4.24	1.0	0.30	0.7	0.76	1688	18	1682	16	1677	21	99
UC016	ZR34	0.98	0.0084	0.10	1.1	3.92	2.3	0.28	2.1	0.88	1666	39	1617	38	1579	57	95
UC016	ZR17C	0.51	0.0076	0.10	0.4	3.89	2.2	0.28	2.1	0.97	1654	15	1612	35	1579	60	95
UC016	ZR43	0.75	0.0075	0.10	0.3	3.69	0.9	0.26	0.7	0.83	1649	12	1568	14	1509	20	92
UC016	ZR41	0.65	0.0303	0.10	0.3	3.55	1.0	0.26	0.9	0.87	1626	12	1538	16	1474	23	91
UC016	ZR25	0.90	0.0087	0.10	0.7	3.37	2.5	0.25	2.4	0.95	1614	27	1497	39	1416	61	88
UC016	ZR11C	0.57	0.0043	0.10	0.7	3.59	1.3	0.26	1.0	0.76	1601	28	1547	20	1507	26	94
UC016	ZR16C	0.82	0.0084	0.10	0.6	3.25	1.4	0.24	1.2	0.86	1579	22	1470	21	1396	29	88
UC016	ZR28	0.54	0.0069	0.10	0.4	3.11	0.9	0.24	0.8	0.81	1544	15	1435	14	1363	19	88
UC016	ZR10R	0.05	0.0140	0.08	1.0	2.51	2.1	0.22	1.8	0.86	1262	39	1276	30	1284	41	102

UC016	ZR20R	0.61	0.0130	0.08	0.6	2.10	1.6	0.19	1.4	0.89	1200	25	1149	22	1123	30	94
UC016	ZR33R	0.27	0.0205	0.08	0.2	2.17	0.8	0.20	0.7	0.85	1174	9	1172	12	1172	15	100
UC016	ZR21R	0.02	0.0192	0.08	0.3	2.06	1.0	0.19	0.9	0.87	1173	13	1136	13	1116	17	95
UC016	ZR18R	0.73	0.0051	0.08	0.6	2.12	1.2	0.20	1.0	0.81	1157	25	1157	17	1157	21	100
UC016	ZR4R	0.10	0.0166	0.08	1.7	1.94	2.4	0.19	1.6	0.68	1076	68	1096	31	1106	32	103
UC016	ZR17R	1.38	0.0011	0.07	3.1	1.53	3.5	0.16	1.4	0.41	887	127	941	42	965	26	109
UC016	*ZR30C*	*0.52*	*0.0071*	*0.11*	*0.4*	*5.01*	*0.8*	*0.33*	*0.6*	*0.75*	*1806*	*13*	*1821*	*13*	*1835*	*19*	*102*
UC016	*ZR16R*	*0.12*	*0.0252*	*0.11*	*0.9*	*4.67*	*3.2*	*0.31*	*3.1*	*0.95*	*1804*	*33*	*1761*	*54*	*1725*	*93*	*96*
UC016	*ZR24C*	*0.78*	*0.0095*	*0.11*	*0.4*	*4.49*	*1.0*	*0.30*	*0.8*	*0.85*	*1779*	*13*	*1730*	*16*	*1689*	*25*	*95*
UC016	*ZR13*	*0.51*	*0.0045*	*0.11*	*0.4*	*4.55*	*0.9*	*0.30*	*0.8*	*0.81*	*1777*	*15*	*1740*	*16*	*1709*	*23*	*96*
UC016	*ZR26C*	*0.66*	*0.0091*	*0.11*	*0.3*	*4.24*	*1.0*	*0.29*	*0.9*	*0.87*	*1742*	*12*	*1682*	*16*	*1635*	*25*	*94*
UC016	*ZR8C*	*0.37*	*0.0084*	*0.11*	*0.7*	*4.40*	*1.3*	*0.30*	*1.1*	*0.81*	*1730*	*25*	*1712*	*22*	*1697*	*32*	*98*
UC016	*ZR32R*	*0.15*	*0.0277*	*0.11*	*0.7*	*4.38*	*2.3*	*0.30*	*2.1*	*0.94*	*1726*	*25*	*1709*	*37*	*1695*	*63*	*98*
UC016	*ZR37R*	*0.25*	*0.0210*	*0.10*	*0.4*	*3.23*	*2.6*	*0.23*	*2.5*	*0.98*	*1635*	*16*	*1463*	*40*	*1348*	*62*	*82*
UC016	*ZR19R*	*0.54*	*0.0045*	*0.10*	*0.6*	*3.49*	*2.5*	*0.26*	*2.4*	*0.96*	*1563*	*21*	*1524*	*39*	*1496*	*64*	*96*
UC016	*ZR15R*	*0.48*	*0.0057*	*0.10*	*0.5*	*3.13*	*1.2*	*0.24*	*1.0*	*0.84*	*1552*	*20*	*1439*	*18*	*1364*	*25*	*88*
UC016	*ZR9C*	*0.53*	*0.0053*	*0.09*	*0.5*	*2.88*	*1.0*	*0.23*	*0.7*	*0.75*	*1469*	*20*	*1378*	*15*	*1319*	*18*	*90*
UC016	*ZR31*	*0.90*	*0.0062*	*0.09*	*1.2*	*2.54*	*3.6*	*0.20*	*3.4*	*0.94*	*1464*	*46*	*1283*	*52*	*1178*	*73*	*80*
UC016	*ZR39*	*0.27*	*0.0072*	*0.09*	*1.8*	*2.75*	*3.5*	*0.22*	*3.0*	*0.85*	*1421*	*69*	*1343*	*52*	*1294*	*70*	*91*
UC016	*ZR22R*	*0.37*	*0.0030*	*0.09*	*1.3*	*2.78*	*2.3*	*0.23*	*1.9*	*0.82*	*1368*	*48*	*1349*	*34*	*1337*	*46*	*98*
UC016	*ZR20C*	*0.57*	*0.0124*	*0.09*	*0.5*	*2.50*	*1.1*	*0.21*	*0.9*	*0.84*	*1354*	*18*	*1271*	*16*	*1222*	*20*	*90*
UC016	*ZR1*	*0.28*	*0.0193*	*0.08*	*0.8*	*2.51*	*2.4*	*0.22*	*2.3*	*0.93*	*1306*	*30*	*1276*	*35*	*1257*	*52*	*96*
UC016	*ZR11R*	*0.05*	*0.0202*	*0.08*	*0.7*	*2.50*	*1.1*	*0.23*	*0.8*	*0.74*	*1207*	*26*	*1273*	*16*	*1313*	*20*	*109*
UC016	*ZR6R*	*0.79*	*0.0003*	*0.08*	*4.4*	*2.01*	*6.1*	*0.19*	*4.2*	*0.68*	*1121*	*172*	*1120*	*81*	*1119*	*86*	*100*
UC032	ZR51	0.67	0.0227	0.11	0.5	5.39	0.9	0.34	0.6	0.66	1870	19	1883	15	1895	19	101
UC032	ZR36	0.77	0.0268	0.11	0.3	5.18	0.8	0.33	0.7	0.83	1839	11	1849	14	1857	23	101

UC032	ZR10	0.94	0.0168	0.11	0.3	5.13	0.8	0.33	0.6	0.77	1827	12	1841	13	1853	20	101
UC032	ZR30	0.59	0.0208	0.11	0.4	4.96	0.8	0.32	0.6	0.72	1820	14	1812	13	1805	17	99
UC032	ZR17	0.60	0.0116	0.11	0.4	4.87	1.0	0.32	0.8	0.82	1815	16	1798	17	1783	25	98
UC032	ZR47	0.71	0.0194	0.11	0.3	4.83	0.8	0.32	0.7	0.81	1796	11	1791	14	1786	21	99
UC032	ZR02N	0.51	0.0108	0.11	0.5	4.85	0.9	0.32	0.7	0.75	1784	17	1794	15	1803	22	101
UC032	ZR58B	0.46	0.0090	0.11	0.6	4.61	1.1	0.31	0.9	0.78	1783	21	1751	18	1724	26	97
UC032	ZR59N	0.44	0.0476	0.11	1.0	4.11	1.8	0.27	1.5	0.80	1780	38	1657	30	1561	41	88
UC032	ZR53N	0.57	0.0232	0.11	0.3	4.65	0.8	0.31	0.6	0.81	1773	9	1759	13	1747	19	99
UC032	ZR33B	0.59	0.0243	0.11	1.3	4.41	1.5	0.30	0.7	0.48	1761	48	1715	25	1677	22	95
UC032	ZR08	0.52	0.0150	0.11	0.5	4.25	1.1	0.29	1.0	0.85	1756	18	1684	19	1627	28	93
UC032	ZR03	0.45	0.0334	0.11	0.4	4.81	0.7	0.32	0.5	0.72	1761	13	1787	12	1810	17	103
UC032	ZR56N	0.67	0.0189	0.11	0.5	4.63	0.9	0.32	0.6	0.67	1739	20	1755	15	1768	18	102
UC032	ZR22	0.59	0.0179	0.11	0.7	4.68	1.0	0.32	0.6	0.60	1715	25	1764	16	1804	18	105
UC032	ZR09	0.34	0.0125	0.10	0.8	4.27	1.4	0.30	1.1	0.79	1708	29	1687	24	1670	33	98
UC032	ZR23	0.58	0.0693	0.10	0.6	4.28	1.4	0.30	1.2	0.85	1695	23	1689	22	1684	34	99
UC032	ZR19	0.31	0.0486	0.10	0.5	4.37	0.9	0.31	0.7	0.74	1668	18	1707	15	1738	21	104
UC032	ZR40N	0.40	0.0383	0.10	0.3	3.89	0.9	0.28	0.8	0.85	1659	12	1612	15	1576	22	95
UC032	ZR38	0.68	0.1087	0.10	2.1	4.09	2.3	0.29	0.7	0.32	1644	78	1652	37	1658	22	101
UC032	ZR20	0.25	0.0547	0.10	0.5	3.93	1.2	0.29	1.0	0.84	1612	19	1619	19	1625	28	101
UC032	ZR29	0.37	0.0699	0.10	0.5	3.60	1.1	0.27	0.8	0.79	1573	20	1550	17	1533	23	97
UC032	ZR45	0.12	0.0712	0.08	0.4	2.29	0.7	0.21	0.5	0.69	1175	14	1210	10	1229	11	105
UC032	ZR44	0.11	0.0904	0.08	0.3	2.30	0.9	0.21	0.7	0.84	1175	12	1214	13	1236	17	105
UC032	ZR25	0.10	0.0634	0.08	0.4	2.42	0.8	0.22	0.5	0.70	1151	16	1248	11	1304	13	113
UC032	ZR11	0.07	0.1059	0.08	0.3	2.46	0.8	0.23	0.7	0.80	1145	13	1260	12	1329	16	116
UC032	ZR32	0.82	0.0154	0.07	0.4	1.85	0.7	0.18	0.5	0.70	1040	15	1063	10	1074	10	103
UC032	ZR12	0.49	0.0196	0.07	0.4	1.84	0.8	0.18	0.5	0.67	1016	18	1060	10	1082	10	107
UC032	ZR55	0.47	0.0298	0.07	0.3	1.68	0.7	0.17	0.5	0.70	1014	14	1000	9	993	9	98

UC032	ZR34	0.42	0.0358	0.07	0.3	1.76	0.8	0.18	0.6	0.81	1013	10	1032	10	1041	12	103
UC032	ZR31	0.36	0.0133	0.07	0.3	1.80	0.7	0.18	0.5	0.74	1012	11	1044	9	1059	10	105
UC032	ZR37	0.19	0.0764	0.07	0.3	1.79	0.8	0.18	0.7	0.83	1012	12	1040	11	1054	14	104
UC032	ZR50	0.18	0.0532	0.07	0.2	1.81	0.7	0.18	0.5	0.76	1010	10	1048	9	1066	10	106
UC032	ZR41	0.16	0.0668	0.07	0.3	1.70	0.7	0.17	0.5	0.71	1009	14	1009	9	1009	9	100
UC032	ZR48	0.61	0.0172	0.07	0.3	1.73	0.8	0.17	0.6	0.80	1009	11	1021	10	1027	12	102
UC032	ZR16	0.44	0.0239	0.07	0.4	1.79	0.7	0.18	0.5	0.71	1007	15	1042	10	1059	10	105
UC032	ZR60	0.29	0.0395	0.07	0.4	1.69	0.8	0.17	0.5	0.69	1004	17	1005	10	1005	10	100
UC032	ZR27	0.14	0.0368	0.07	0.4	1.89	0.7	0.19	0.5	0.72	1002	14	1077	10	1114	11	111
UC032	ZR05	0.31	0.0181	0.07	0.5	1.76	0.8	0.18	0.5	0.68	1001	18	1032	10	1046	10	104
UC032	ZR54	0.36	0.0197	0.07	0.3	1.73	0.7	0.17	0.5	0.71	1000	14	1020	9	1029	10	103
UC032	ZR28	0.20	0.0143	0.07	0.4	1.74	0.7	0.17	0.5	0.67	998	16	1025	10	1038	9	104
UC032	ZR26	0.24	0.0295	0.07	0.6	1.69	0.9	0.17	0.7	0.71	986	22	1004	12	1013	13	103
UC032	ZR52	0.22	0.0451	0.07	0.5	1.83	1.1	0.18	0.9	0.83	985	22	1057	15	1093	19	111
UC032	*ZR42N*	*0.78*	*0.0572*	*0.12*	*2.1*	*5.48*	*2.3*	*0.33*	*0.8*	*0.36*	*1970*	*74*	*1897*	*39*	*1831*	*26*	*93*
UC032	*ZR33N*	*0.28*	*0.0184*	*0.11*	*4.0*	*6.31*	*4.2*	*0.40*	*1.0*	*0.25*	*1877*	*142*	*2020*	*72*	*2161*	*38*	*115*
UC032	*ZR13*	*0.30*	*0.0025*	*0.11*	*0.9*	*4.67*	*1.5*	*0.30*	*1.1*	*0.74*	*1818*	*34*	*1762*	*25*	*1714*	*33*	*94*
UC032	*ZR56B*	*0.68*	*0.0180*	*0.11*	*0.4*	*4.71*	*1.1*	*0.31*	*0.9*	*0.87*	*1803*	*14*	*1769*	*18*	*1740*	*29*	*97*
UC032	*ZR14*	*0.30*	*0.0194*	*0.11*	*0.5*	*4.65*	*1.2*	*0.31*	*1.1*	*0.87*	*1799*	*18*	*1757*	*21*	*1722*	*32*	*96*
UC032	*ZR24*	*0.11*	*0.0215*	*0.11*	*0.4*	*4.68*	*0.8*	*0.31*	*0.5*	*0.68*	*1764*	*16*	*1764*	*13*	*1763*	*17*	*100*
UC032	*ZR15*	*0.56*	*0.0386*	*0.11*	*0.5*	*5.38*	*1.0*	*0.36*	*0.7*	*0.76*	*1757*	*19*	*1882*	*17*	*1997*	*26*	*114*
UC032	*ZR02B*	*0.42*	*0.0077*	*0.11*	*0.4*	*4.27*	*0.7*	*0.29*	*0.5*	*0.66*	*1750*	*14*	*1687*	*12*	*1637*	*14*	*94*
UC032	*ZR35*	*0.18*	*0.0586*	*0.11*	*1.4*	*4.15*	*1.7*	*0.29*	*0.9*	*0.52*	*1722*	*51*	*1664*	*28*	*1618*	*26*	*94*
UC032	*ZR06*	*0.69*	*0.0605*	*0.10*	*0.5*	*4.08*	*1.2*	*0.28*	*1.0*	*0.84*	*1708*	*19*	*1649*	*19*	*1604*	*28*	*94*
UC032	*ZR43B*	*0.47*	*0.0272*	*0.10*	*0.5*	*4.29*	*1.0*	*0.30*	*0.8*	*0.79*	*1700*	*18*	*1691*	*16*	*1685*	*23*	*99*
UC032	*ZR43N*	*0.76*	*0.0702*	*0.10*	*0.4*	*3.97*	*1.1*	*0.28*	*0.9*	*0.86*	*1690*	*14*	*1628*	*17*	*1580*	*26*	*93*
UC032	*ZR01*	*0.61*	*0.0893*	*0.10*	*0.4*	*4.02*	*1.0*	*0.28*	*0.8*	*0.81*	*1684*	*16*	*1639*	*16*	*1603*	*22*	*95*
UC032	*ZR53B*	*0.52*	*0.0036*	*0.10*	*1.0*	*3.79*	*1.4*	*0.27*	*1.0*	*0.71*	*1654*	*35*	*1590*	*23*	*1542*	*28*	*93*
UC032	*ZR57*	*0.09*	*0.0115*	*0.10*	*3.2*	*4.46*	*3.4*	*0.32*	*0.9*	*0.27*	*1635*	*118*	*1723*	*56*	*1797*	*29*	*110*

UC032	*ZR18*	*0.35*	*0.1018*	*0.10*	*0.4*	*3.85*	*1.2*	*0.28*	*1.1*	*0.89*	*1617*	*15*	*1604*	*20*	*1594*	*31*	*99*
UC032	*ZR49*	*0.60*	*0.0102*	*0.10*	*0.6*	*3.47*	*0.8*	*0.26*	*0.4*	*0.56*	*1567*	*21*	*1519*	*13*	*1485*	*12*	*95*
UC032	*ZR07*	*0.58*	*0.1348*	*0.10*	*0.5*	*3.93*	*0.8*	*0.29*	*0.6*	*0.69*	*1566*	*17*	*1619*	*13*	*1661*	*16*	*106*
UC032	*ZR58N*	*0.12*	*0.0535*	*0.10*	*0.4*	*3.21*	*0.8*	*0.24*	*0.5*	*0.69*	*1529*	*16*	*1459*	*12*	*1411*	*14*	*92*
UC032	*ZR04*	*0.25*	*0.0111*	*0.09*	*0.7*	*3.13*	*1.0*	*0.25*	*0.7*	*0.65*	*1472*	*26*	*1440*	*16*	*1418*	*17*	*96*
UC032	*ZR42B*	*0.11*	*0.0035*	*0.09*	*9.2*	*6.21*	*10.6*	*0.49*	*5.3*	*0.49*	*1467*	*332*	*2006*	*178*	*2570*	*221*	*175*
UC032	*ZR21*	*0.42*	*0.0119*	*0.09*	*3.4*	*2.99*	*3.7*	*0.24*	*1.3*	*0.35*	*1427*	*129*	*1405*	*56*	*1391*	*33*	*97*
UC032	*ZR40B*	*0.19*	*0.0493*	*0.08*	*1.2*	*1.99*	*1.4*	*0.18*	*0.8*	*0.54*	*1176*	*45*	*1112*	*19*	*1080*	*15*	*92*
UC032	*ZR46*	*0.08*	*0.0465*	*0.07*	*0.3*	*1.84*	*0.7*	*0.18*	*0.5*	*0.69*	*1050*	*13*	*1058*	*9*	*1062*	*9*	*101*
UC032	*ZR59B*	*0.11*	*0.0090*	*0.07*	*2.1*	*1.66*	*2.9*	*0.17*	*2.0*	*0.70*	*922*	*84*	*994*	*37*	*1026*	*39*	*111*
UC032	*ZR39*	*0.40*	*0.0274*	*0.07*	*4.1*	*1.62*	*4.1*	*0.17*	*0.7*	*0.16*	*853*	*165*	*977*	*51*	*1033*	*12*	*121*
UC010II	ZR22	0.10	0.0260	0.08	0.5	2.45	1.0	0.22	0.7	0.78	1213	19	1258	14	1284	17	106
UC010II	ZR17	0.14	0.0292	0.08	0.4	2.26	0.8	0.21	0.5	0.72	1186	15	1201	11	1209	12	102
UC010II	ZR14	0.18	0.0267	0.08	0.3	2.34	0.8	0.21	0.6	0.76	1183	13	1223	11	1246	13	105
UC010II	ZR15	0.16	0.0329	0.08	0.4	2.17	0.8	0.20	0.6	0.71	1178	17	1172	11	1168	12	99
UC010II	ZR4	0.12	0.0314	0.08	0.4	2.29	1.5	0.21	1.4	0.93	1176	16	1208	21	1225	30	104
UC010II	ZR12	0.34	0.0108	0.07	1.0	1.87	2.6	0.18	2.4	0.92	1055	39	1069	35	1076	48	102
UC010II	ZR20	0.30	0.0104	0.07	0.4	1.89	1.0	0.18	0.8	0.84	1053	16	1076	13	1087	17	103
UC010II	ZR13	0.33	0.0221	0.07	0.4	1.90	1.2	0.19	1.1	0.90	1042	16	1080	16	1099	22	105
UC010II	ZR6	0.45	0.0121	0.07	0.4	1.86	2.0	0.18	2.0	0.96	1037	16	1067	27	1082	39	104
UC010II	ZR5	0.43	0.0146	0.07	0.4	1.73	2.1	0.17	2.0	0.96	1035	18	1021	27	1014	38	98
UC010II	ZR11	0.37	0.0156	0.07	0.4	1.86	1.1	0.18	0.9	0.86	1032	16	1066	14	1083	18	105
UC010II	ZR24	0.42	0.0121	0.07	0.4	1.76	0.8	0.17	0.6	0.73	1030	17	1031	11	1031	12	100
UC010II	ZR26	0.34	0.0110	0.07	0.4	1.75	1.0	0.17	0.8	0.81	1029	18	1029	12	1028	15	100
UC010II	ZR8	0.37	0.0155	0.07	0.4	1.74	0.9	0.17	0.7	0.78	1025	17	1025	12	1024	13	100
UC010II	ZR2	0.53	0.0145	0.07	0.3	1.78	0.9	0.18	0.8	0.86	1025	12	1038	12	1045	15	102
UC010II	ZR25	0.38	0.0116	0.07	0.4	1.72	0.9	0.17	0.8	0.81	1024	16	1016	12	1012	14	99
UC010II	ZR10	0.30	0.0165	0.07	0.3	1.80	0.7	0.18	0.5	0.74	1023	13	1045	9	1055	10	103

UC010II	ZR3	0.32	0.0210	0.07	0.4	1.74	1.0	0.17	0.8	0.83	1021	18	1025	13	1027	16	101
UC010II	ZR21	0.44	0.0099	0.07	0.5	1.79	0.9	0.18	0.6	0.70	1020	20	1041	11	1051	12	103
UC010II	ZR1	0.38	0.0140	0.07	0.4	1.93	2.3	0.19	2.2	0.97	1017	16	1092	30	1130	45	111
UC010II	ZR19	0.31	0.0053	0.07	0.5	1.96	2.8	0.19	2.7	0.97	1016	22	1102	37	1147	57	113
UC010II	ZR9	0.35	0.0040	0.07	0.6	1.90	2.1	0.19	2.0	0.94	1013	25	1082	28	1116	41	110
UC010II	ZR27	0.42	0.0156	0.07	0.4	1.81	0.9	0.18	0.8	0.82	1011	16	1048	12	1066	15	105
UC010II	ZR16	0.32	0.0107	0.07	0.4	1.82	0.8	0.18	0.5	0.70	1009	17	1054	10	1076	11	107
UC010II	ZR29	0.32	0.0114	0.07	0.4	1.78	0.8	0.18	0.6	0.74	1000	17	1038	11	1056	12	106
UC010II	*ZR23*	*0.15*	*0.0007*	*0.08*	*5.0*	*1.37*	*11.5*	*0.13*	*10.4*	*0.90*	*1096*	*193*	*877*	*131*	*793*	*154*	*72*
UC010II	*ZR28*	*0.33*	*0.0085*	*0.08*	*0.4*	*2.00*	*1.1*	*0.19*	*1.0*	*0.87*	*1086*	*16*	*1117*	*15*	*1132*	*20*	*104*
UC010II	*ZR18*	*0.17*	*0.0082*	*0.08*	*0.5*	*2.08*	*1.5*	*0.20*	*1.3*	*0.91*	*1086*	*20*	*1142*	*20*	*1171*	*28*	*108*
UC001	ZR7	3.33	0.0027	0.08	3.5	1.76	4.3	0.17	2.5	0.59	1086	136	1033	55	1008	47	93
UC001	ZR25	2.72	0.0052	0.07	2.2	1.60	2.8	0.16	1.7	0.61	963	88	972	35	976	31	101
UC001	ZR1	2.36	0.0082	0.07	1.1	1.68	3.2	0.17	3.0	0.93	958	45	1000	41	1019	57	106
UC001	*ZR24*	*4.76*	*0.0076*	*0.20*	*5.4*	*5.03*	*5.7*	*0.18*	*1.8*	*0.32*	*2856*	*171*	*1825*	*95*	*1062*	*36*	*37*
UC001	*ZR13*	*5.25*	*0.0086*	*0.19*	*2.9*	*5.10*	*3.6*	*0.19*	*2.2*	*0.60*	*2761*	*92*	*1835*	*60*	*1134*	*45*	*41*
UC001	*ZR6*	*5.50*	*0.0079*	*0.18*	*5.0*	*5.36*	*6.4*	*0.22*	*3.9*	*0.62*	*2631*	*161*	*1879*	*106*	*1276*	*91*	*49*
UC001	*ZR18*	*7.37*	*0.0056*	*0.12*	*4.5*	*3.27*	*5.3*	*0.20*	*2.7*	*0.52*	*1896*	*158*	*1475*	*80*	*1200*	*60*	*63*
UC001	*ZR26*	*8.28*	*0.0048*	*0.11*	*4.5*	*2.34*	*4.8*	*0.16*	*1.7*	*0.35*	*1736*	*161*	*1226*	*68*	*957*	*30*	*55*
UC001	*ZR10*	*2.28*	*0.0026*	*0.10*	*2.6*	*2.05*	*3.8*	*0.15*	*2.7*	*0.71*	*1609*	*97*	*1131*	*51*	*899*	*45*	*56*
UC001	*ZR9*	*4.76*	*0.0059*	*0.10*	*5.4*	*2.40*	*6.0*	*0.18*	*2.5*	*0.41*	*1559*	*197*	*1242*	*84*	*1067*	*49*	*68*
UC001	*ZR19*	*6.90*	*0.0058*	*0.09*	*3.2*	*2.37*	*3.7*	*0.18*	*1.8*	*0.49*	*1514*	*120*	*1234*	*53*	*1081*	*36*	*71*
UC001	*ZR3*	*3.58*	*0.0072*	*0.09*	*1.2*	*2.21*	*3.1*	*0.17*	*2.8*	*0.91*	*1486*	*46*	*1185*	*43*	*1026*	*54*	*69*
UC001	*ZR17*	*4.73*	*0.0075*	*0.09*	*11.4*	*2.25*	*12.0*	*0.19*	*3.8*	*0.32*	*1384*	*408*	*1196*	*162*	*1095*	*77*	*79*
UC001	*ZR2*	*2.49*	*0.0056*	*0.08*	*2.1*	*1.83*	*3.0*	*0.16*	*2.1*	*0.71*	*1310*	*79*	*1057*	*39*	*938*	*37*	*72*
UC001	*ZR11*	*3.16*	*0.0052*	*0.08*	*2.3*	*1.86*	*3.3*	*0.17*	*2.3*	*0.71*	*1228*	*88*	*1069*	*43*	*992*	*43*	*81*
UC001	*ZR14*	*2.94*	*0.0020*	*0.08*	*2.5*	*1.86*	*3.7*	*0.17*	*2.7*	*0.73*	*1210*	*95*	*1069*	*48*	*1000*	*50*	*83*

UC001	*ZR22*	*2.30*	*0.0029*	*0.08*	*0.9*	*1.74*	*1.5*	*0.16*	*1.2*	*0.76*	*1171*	*36*	*1025*	*19*	*958*	*21*	*82*
UC001	*ZR20*	*2.75*	*0.0062*	*0.08*	*1.2*	*1.93*	*3.2*	*0.18*	*2.9*	*0.91*	*1122*	*49*	*1091*	*42*	*1075*	*57*	*96*
UC001	*ZR21*	*2.44*	*0.0036*	*0.08*	*0.8*	*1.77*	*1.9*	*0.17*	*1.7*	*0.88*	*1110*	*33*	*1036*	*25*	*1001*	*32*	*90*
UC001	*ZR15*	*2.24*	*0.0069*	*0.07*	*1.0*	*1.54*	*1.7*	*0.15*	*1.4*	*0.79*	*1005*	*40*	*945*	*21*	*919*	*23*	*91*
UC001	*ZR8*	*5.79*	*0.0085*	*0.07*	*8.0*	*1.73*	*8.9*	*0.18*	*3.9*	*0.43*	*944*	*313*	*1020*	*112*	*1056*	*75*	*112*
UC001	*ZR4*	*2.81*	*0.0075*	*0.07*	*2.4*	*1.65*	*3.3*	*0.18*	*2.1*	*0.66*	*857*	*100*	*991*	*41*	*1052*	*42*	*123*
UC001	*ZR27*	*3.25*	*0.0080*	*0.06*	*4.7*	*1.27*	*4.9*	*0.15*	*1.2*	*0.25*	*627*	*196*	*832*	*54*	*911*	*21*	*145*

Data report template (with modifications) from http://www.plasmage.org/recommendations

Notes: Convertion factor from mV to CPS is 62500000

Concentration uncertainty c.20%

Data not corrected for common-Pb

Concordance calculated as ($^{206}Pb/^{238}U$ age / $^{207}Pb/^{206}Pb$ age) * 100

Decay constants of Jaffey et al 1971 used

Abreviations: C - core; R - rim and ZR - zircon.

Data not used to calculate ages are at the end in italics for each sample.

Supplementary Table 03: LA-ICP-MS Lu-Hf isotope data of zircon from CUMC.

Sample	***Measured***				***$^{207}Pb/^{206}Pb$***	***Calculated***				***Average***
	$^{176}Lu/^{177}Hf$	**±2σ**	**$^{176}Hf/^{177}Hf$**	**±2σ**	**Ma**	**$(^{176}Hf/^{177}Hf)_T$**	**±2σ**	**εHf_0**	**εHf_T**	**T_{DM} Ga**
UC021 DI										
ZR26	0.002617	0.001266	0.281842	0.000030	1757	0.000030	0.000030	-33.4	2.9	2.2
ZR21	0.000881	0.000732	0.281860	0.000025	1736	0.000025	0.000025	-32.7	5.2	2.1
ZR17R	0.001051	0.002065	0.281953	0.000017	1198	0.000017	0.000017	-29.4	-3.6	2.1
ZR16R	0.000657	0.000041	0.281887	0.000026	1189	0.000026	0.000026	-31.8	-5.8	2.2
ZR11R	0.000748	0.000332	0.281889	0.000017	1197	0.000017	0.000017	-31.7	-5.6	2.2
UY1337 DII										
ZR2R	0.001413	0.000236	0.281778	0.000021	1239	0.281744	0.000021	-35.7	-9.2	2.4
ZR4C	0.001926	0.001148	0.281811	0.000030	1759	0.281744	0.000030	-34.5	2.7	2.2
ZR4R	0.000695	0.000137	0.281915	0.000025	1189	0.281899	0.000025	-30.8	-4.8	2.2
ZR8C	0.001939	0.002155	0.281863	0.000034	1774	0.281795	0.000034	-32.7	4.8	2.1
ZR8R	0.001272	0.001957	0.282005	0.000038	976	0.281981	0.000038	-27.6	-6.7	2.1
ZR18R	0.000929	0.000124	0.282065	0.000026	1055	0.282046	0.000026	-25.5	-2.6	1.9
UC016 DIII										
ZR4R	0.001072	0.000793	0.281702	0.000036	1076	0.281679	0.000036	-38.3	-15.1	2.6
ZR33R	0.000703	0.000373	0.281869	0.000024	1174	0.281853	0.000024	-32.4	-6.8	2.3
ZR37C	0.000652	0.000703	0.281768	0.000025	1789	0.281745	0.000025	-36.0	3.4	2.2
ZR38	0.001457	0.002152	0.281696	0.000032	1788	0.281645	0.000032	-38.6	-0.2	2.4
ZR42	0.000559	0.000569	0.281687	0.000028	1782	0.281668	0.000028	-38.8	0.5	2.4
UC032 - Amphibolite										
ZR14	0.001802	0.001579	0.281884	0.000112	1799	0.281820	0.000112	-31.9	6.3	2.1
ZR16	0.001701	0.001435	0.282839	0.000184	1007	0.282806	0.000184	1.9	23.2	0.4
UC010II - Amphibolite										
ZR3	0.000413	0.000104	0.281996	0.000036	1021	0.281988	0.000036	-27.9	-5.5	2.1
ZR24	0.000653	0.001059	0.282050	0.000050	1030	0.282037	0.000050	-26.0	-3.5	2.0

3 CAPÍTULO 3 – PAPER 2

U-Pb/Hf isotopic composition of the Belén Metamorphic Complex, northern Chile: new constrains on the Ordovician Famatinian Magmatic arc

Juliana Rezende de Oliveira [a], Natalia Hauser [a], Pedro Cordeiro [b], Carlos Marquadt [b], Wolf Uwe Reimold[a]

[a]*Instituto de Geociências, Universidade de Brasília (UnB), 70910-900 Brasília, DF, Brazil*
[b]*Department of Mining Engineering, Pontifical Catholic University of Chile, 7820436 Santiago, Chile*

Abstract

The geological history of Famatinian magmatism is a complex event along the proto-Andean margin of Gondwana, involving several distinct episodes. The Famatinian magmatism developed across contrasting crustal domains that reflect in the genesis and ages of Famatinian magmas. U-Pb zircon ages constrain Famatinian magmatism range from Late Cambrian to Late Ordovician. This work sticks to determine the rock groups that belong to the Belén Metamorphic Complex Ordovician orthoderivated rocks, establish the magmatic age range, and suggest the origin and tectonic history of the Belén Metamorphic Complex. We also highlight the differences and similarities of the BMC concerning the regional Famatinian magmatism. The plutonic rocks of the Famatinian magmatism in the Belén Metamorphic Complex were deformed and metamorphized into gneisses, schists, and migmatized rocks by a shear system. The U-Pb analysis in zircon grains (LA-ICP-MS) defines the intrusion age between ~482 to 456 Ma, with a flare-up phase in 470 to 464 Ma. The strongly negative to less slightly positive εHfT data define a significant degree of crustal assimilation from a Precambrian source in the subduction zone with minor involvement of juvenile components from the mantle.

Keyword
Famatinian magmatism, Belén Metamorphic Complex, U-Pb zircon ages, Lu-Hf isotopes, Ordovician.

3.1 INTRODUCTION

The Arequipa-Antofalla Basement is a Proterozoic terrane that outcrops along the western margin of South America, between the Andean Cordillera and present-day Peru–Chile trench. It was reworked during the Paleozoic Famatinian Magmatic cycle (Tosdal, 1996; Wörner et al., 2000; Loewy et al., 2004; Casquet et al., 2010; Pankhurst et al., 2016). For that reason, it is really important peace to understand the evolution of the western margin of South America (Fig. 1).

The Belén Metamorphic Complex (BMC; García, 1996; Basei et al., 1996;), composed by orthoderived rocks and exposed at the north extreme of Chile, represents a classical area of basement outcrops. Until today, there are few U-Pb geochronological data, that does not cover the entire magmatic sequence (e.g., Wörner et al., 2000; Loewy et al., 2004; Pankhurst et al., 2016). The magmatic sequence groups orthoderived mafic, intermediate, and felsic rocks in smaller volumes that previously were considered as pre-Cambrian basement (e.g., Pacci et al., 1980; Tosdal, 1996). However, Basei et al. (1996) and U-Pb in zircon, K-Ar on minerals and Rb-Sr whole rock data, posteriorly, Wörner et al. (2000), Loewy et al. (2004) and Pankhurst et al. (2016) indicate that this basement represents mainly a reworking of a Paleoproterozoic terrane during Ordovician times.

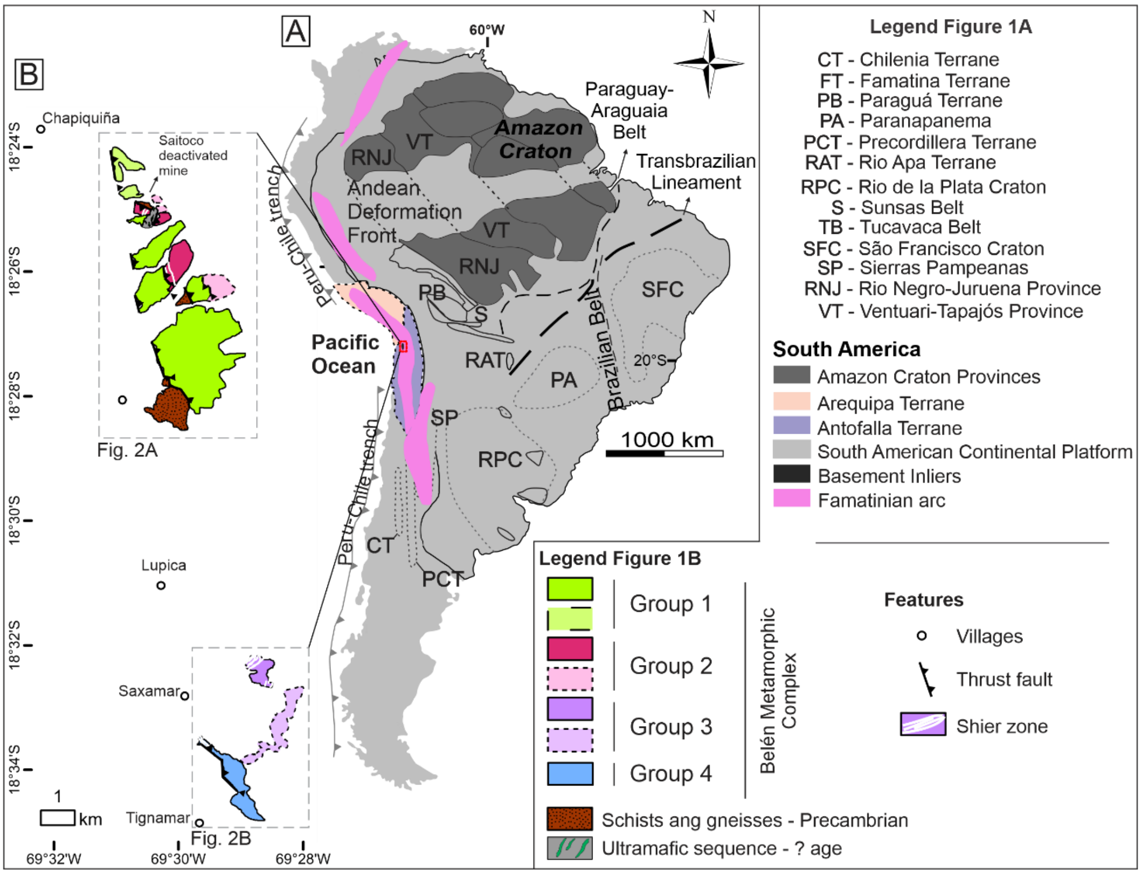

Fig. 1. A) Schematic map of South America showing the Arequipa and Antofalla terranes after Ramos (2009), the geological provinces of the Amazon craton after Cordani et al. (2009) and the Famatinian Ordovician magmatic arc between Venezuela and Argentina (Ramos, 2018). B) Belen Metamorphic Complex exposures, the boxes indicate the northern BMC (Fig. 2A) and southern BMC (Fig. 2 B) areas, which are detailed in the figure 2.

As the geochronological data of the BMC are few and not cover the entire lithologies recognized, like quartz monzodiorite, mylonitic amphibole gneiss with tonalitic composition, mylonitic biotite gneiss with granodioritic composition, and schists. We performed a U-Pb (LA-ICPMS) dating and pioneer Hf isotopic data on typical (amphibole gneiss and biotite gneiss) and less-studied lithotypes of the complex. Our results improve the knowledge on the Famatinian magmatism of the BMC and together with Hf isotopic composition we can better understand the evolution of the Famatinian arc, in terms of lull or flare-up events in a regional scale.

3.2 Geological Setting

The Famatinian orogeny, Famatinian cycle, and Famatinian magmatism are terms that sometimes are used as synonymous, nevertheless there are some differences between them. The Famatinian orogeny represent the first orogenic event after the final assembly (e.g., Pankhurst et al., 2006, 2016; Chew et al., 2007, 2008, 2016; Alasino et al., 2016, 2020; Van der Lelij et al., 2016; García-Ramírez et al., 2017) of SW Gondwana supercontinent. It happened between 552–520 Ma and was known as the early Cambrian Pampean orogeny (Casquet et al., 2018). “Famatinian Cycle” is term that was apply to Early Ordovician granites and metasedimentary rocks that crops out in the 6000 m high Sierra de Famatina in northwest Argentina (Aceñolaza and Toselli, 1976) and the term Famatinian magmatism is referred specifically to the igneous activity, related with the Famatinian orogeny.

So, the Famatinian orogeny is a term that includes the Early–Middle Ordovician magmatic rocks that at the time were deformed, metamorphosed and sheared (Rapela et al., 2018) and that now outcrops as the Famatinian arc, recognized from Venezuela to northeast Patagonia (e.g., Pankhurst et al., 2006; Chew et al., 2007; Alasino et al., 2016; Van der Lelij et al., 2016; García-Ramírez et al., 2017; Otamendi et al., 2020; Alasino et al., 2020). The Famatinian arc is strongly diverse in rock types (Rapela et al., 2018), involve metasedimentary rocks, carbonate and siliciclastic rocks from the platform, K-bentonite intersperse with limestones, and orthoderivated rocks (e.g., Rapela et al., 2016; Astini et al., 1995; Fanning et al., 2004; Niemeyer et al., 2014). The orthoderivated rock types developed across different crustal domains that reflect in the Famatinian magmas genesis and magmatism position, sedimentary record, metamorphic P/T conditions, mineralogy, and volume of orthoderived and igneous rocks. The orthoderived rocks were identified in Venezuela, Colombia, Ecuador, Peru, Bolivia, Chile, and northwestern Argentina, extending into northern and central Andes, sub-parallel to the modern Andean chain, and continues since Rio de la Plata craton to northeast Patagonia, westernmost inliers in the Andean belt (Rapela et al., 2007).

3.2.1 Main stages of the Famatinian magmatism

The first studies about the Famatinian magmatic rocks (e.g., Haller and Ramos, 1984; Astini and Benedetto, 1996; Astini et al., 1995; Pankhurst et al., 1998; Chernicoff and Ramos, 2004) recognized a peak of magmatic activity around 470 Ma with a later deformation around 460 Ma. Since then, diverse ranges of ages between Late Cambrian to Ordovician were identified. For example, in Peru, the San Juan, Mollendo, and Ocoña gneiss and granites range between 468 and 464 Ma. In Chile, the Belén foliated granodiorites and felsic dike, and Quebrada Choja orthogneiss, granite, and tonalite, exhibit ages between 497 and 444 Ma (Loewy et al., 2004). The first age was interpreted as magmatism followed by metamorphism at ca. 440 Ma.

Other authors considered older ages for the Famatinian arc starting from 485 to 465 Ma for the emplacement of the Famatinian arc, where mantle-derived mafic magma with island arcs signature were generated at the same time that intermediate to felsic calc-alkaline magmas (Ducea et al., 2010). Magmatism around 510 Ma until the earliest Silurian (Reitsma et al., 2012) with a magmatic peak between 480 and 460 Ma, like the Machu Picchu Inlier with ages between 480 Ma and 472 Ma and final Famatinian phase around 447 Ma (age from Miskovic et al., 2009). Granitoid plutons in the Norte Grande area from Argentina and more mafic rocks at Belén and andesite and dacite at Cordón de Lila from Chile defined an igneous event between 490 and 465 Ma, synchronous with the Famatinian magmatic arc (Pankhurst et al., 2016). U-Pb ages between 540 and 490 Ma as a possible intrusion emplacement age of Diablillos Intrusive Complex in Puna Argentina (Ortiz et al., 2017). A long-lived magmatism with low and high volume of magmatic episodes between ∼540 Ma and ∼440 Ma (Ortiz et al., 2019a; Ortiz et al., 2019b).

Sato et al. (2003) recognized at the Sierra de San Luis of eastern Sierras Pampeanas a main Famatinian phase, between 507 and 454 Ma, related with intense magmatic activities of more than ~30 Ma with deformation and regional metamorphism (480 a 445 Ma), followed by late and post-orogenic Devonian events. Chew et al. (2016), for the Famatinian rocks exposed in Peru, interpreted two phases of contemporaneous metamorphism and magmatism first at ~480 Ma and then at ~435 Ma followed by metamorphism and minor magmatism at ca. 420 to 350 Ma and finally metamorphism at ~315 Ma. For the northwestern part of Argentina near Bolivia and Chile boundaries, Bahlburg et al. (2016) recognized a protracted magmatism in a first phase among 480 and 460 Ma, and in a second phase between 453 and 444 Ma. A recent review of Famatinian magmatism for an extensive portion of Argentina and Chile also resulted in the identification of two stages (Rapela et al., 2018), a roll-back stage between 486 and 474 Ma, followed by a slab break-off stage between 472 and 468 Ma, considered as a flare-up phase.

3.2.2 The Belén Metamorphic Complex

The metamorphic rocks that outcrop near Belén village, in the extreme north of Chile, were initially defined as the Belén Shales (Montocino, 1963) and later as Belén Schist Formation (Salas et al., 1966; Pacci et al., 1980). Finally, on the basis of metamorphic and magmatic units with complex evolution, it was defined as the Belén Metamorphic Complex (García, 1996; Basei et al., 1996).

In the Arica map (Garcia et al, 2004) three main areas with a general N-S orientation are recognized. In terms of volume of outcrops, the main area is Belén sector, and the other two areas are in Quebrada Achacagua sector (northern BMC, Fig. 1B) and Quebrada Saxamar or Tignámar sector (southern BMC, Fig. 1B). Garcia et al. (2004) defined two lithotype groups, one composed mainly by schists, amphibolites, and gneisses and few phyllites, serpentinites, mafic and felsic dikes, quartzites and migmatites of Upper Proterozoic ages and a second one of orthogneisses of Lower Paleozoic ages. During this work, we defined two main areas (Fig. 2), northern BMC and southern BMC, the first one to the east and north of Belén village, encompass Belén and Quebrada Achacagua sectors being the most voluminous in terms of outcrops and best known (e.g., Wörner et al., 2000; Loewy et al., 2004). The second one ~5 kilometers south of the northern BMC, comprise Quebrada Saxamar sector.

The first geochronology data for the complex, Rb-Sr whole rock isochron age of ~1.0 Ga (Pacci et al., 1990), and U-Pb in zircon of ~1.2 Ga (Damm et al., 1990), indicated Mesoproterozoic ages. Later, a Rb-Sr whole-rock isochron age, two K-Ar ages on minerals (mineral type not mentioned), and two U-Pb ages in zircon (Basei et al., 1996) performed on schists, orthogneisses, and granitic veins of the Belén Metamorphic Complex, redefined the ages of the Complex. The obtained ages indicate U-Pb crystallization ages in zircon between 507±48 Ma and 475±31 Ma and regional metamorphism at ~516 Ma.

A biotite gneiss and an amphibole gneiss from northern BCM obtained U-Pb ages (ID-TIMS) on zircon crystals (Wörner et al., 2000) with upper intercepts at 1877±139/131 Ma and 1745±27 Ma, and lower intercept ages of 366±3 Ma and 456±4 Ma, respectively. The authors interpret Proterozoic protolith ages associated to Arequipa terrane and a regional metamorphism along the western margin of South America for the younger ages. However, when compiling the ages obtained by U-Pb (Wörner et al., 2000) with K-Ar ages from Lucassen et al. (2000) and Basei et al. (1996), the authors identified two main age groups associable with regional metamorphism of 536–460 Ma and 390–360 Ma, considered as unclear to interpret as these results would indicate two separate parts of the crust under similar metamorphic conditions in different ages later juxtaposed, but there is no tectonic evidence in the field work to support this hypothesis (Wörner et al., 2000).

Two foliated granodiorites from northern and southern BMC exhibit ages of ~ 473 Ma interpret as crystallization age. A felsic dike from northern BMC hosted by garnet mica schist revealed upper intercept age of 1866 ± 2 Ma, suggesting a Paleoproterozoic source as southern Peru granitic gneiss (Arequipa terrane) and lower intercept age of 227±17 Ma interpreted as Pb-loss with geological meaningless (Loewy et al., 2004).

The most recent dating for the Belén Metamorphic Complex was a U–Pb SHRIMP zircon age obtained on amphibole orthogneiss that brought an age of 472±2 Ma. This age is considered synchronous with the Famatinian magmatic arc of Argentina (Pankhurst et al., 2016).

3.3 METHODOLOGY

3.3.1 Separation and preparation of zircon crystals

The zircon samples preparation and concentration were performed at the Laboratory of Geochronology of the University of Brasilia. Nearly 30 kg per eleven samples were mashed in a jaw crusher, crushed in a vibratory cup mill, separated by different grain sizes (< 250 µm) and separated by density. For the concentration of zircon, we use a Frantz isodynamic separator. We select around 70 to 130 zircon grains from quartz monzodiorite, ortho- gneisses and shist and 13 to 65 zircon crystals from amphibolite samples by handpicking. The zircon grains were settled into an epoxy mount, polished into half thickness, and analyzed by FEI QUANTA 450 scanning electron microscope (SEM) to obtain backscattered electron (BSE) and cathodoluminescence (CL) images.

3.3.2 U-Pb isotope analysis

The zircon grains U-Pb isotope analysis were produced by LA-ICP-MS at the Laboratory of Geochronology of the University of Brasilia (Supplementary Table 1_U-Pb) with a Thermo-Fisher Neptune HR-MC-ICP-MS equipment, with Nd: YAG UP213 New Wave laser-ablation coupled. The analyses method were based on the standard-sample bracketing (Albarède et al., 2004) utilizing the GJ-1 standard (Jackson et al., 2004) to control fractionation. The standard 91500 zircon (Wiedenbeck et al., 1995, 2004) was also analyzed during analytical sessions as an unknown pattern, with tuned masses of 238, 232, 208, 207, 206, 204 and 202. The ablation time was 40 seconds with 1 second of integration time. Spot size was 25 to 30 µm by a laser adjustment of 10 Hz and 2.5-5.5 J / cm^2. Ratios ^{207}Pb/^{206}Pb and ^{206}Pb/^{238}U were time-corrected. An UnB Geochronology Laboratory in-house Chronus software was used to data reduction the (Oliveira, 2015).

Common ^{204}Pb was checked based on the ^{202}Hg and (^{204}Hg + ^{204}Pb) masses. The correction of common Pb contribution (^{204}Pb) was not necessary. The analytical errors were disseminated by the quadratic addition [(2SD ^ 2 + 2SE ^ 2) 1/2] (SD = standard deviation; SE = standard error) of external reproducibility and performance accuracy. The standard deviation generated from repeated analyses (n = 20, ~ 1.1 % for $^{207}Pb/^{206}Pb$ and up to ~ 2 % for $^{206}Pb/^{238}U$) of the GJ-1 zircon standard during the analytical sessions represented the external reproducibility. The performance accuracy was taken as the standard error calculated for each analysis. The weighted mean ages and Tera–Wasserburg diagrams are shown with 2σ error ellipses and were calculated by Isoplot-3/Ex. software (Ludwig, 2012). We adopted a geological time scale updated version by Cohen et al. (2013). For more details about the U-Pb methodology on zircon at Laboratory of Geochronology of the University of Brasilia see Bühn et al. (2008).

3.3.3 Lu-Hf isotope analysis

For Lu-Hf isotopes (Supplementary Table 2_Lu-Hf) the same instrument for U-Pb isotope analysis were used. The crystals selection was based on parameters of concordant U-Pb data (6/8 and 7/6 ages concordance) and crystal size. The Lu-Hf isotope data ablation time were over 40–50 seconds of, applying a 40 µm spot size, and 85% of energy. The Lu-Hf spot was placed as close as possible to the U-Pb previous spots in order to analyze same U and Pb isotopic characteristics portions of the zircon grain. The isotopes ^{171}Yb, ^{173}Yb and ^{175}Lu signals were monitored for interference-free during the analysis to correct the isobaric interferences of ^{176}Yb and ^{176}Lu on the ^{176}Hf signal. The isotopic abundances of Lu and Hf was used to calculate the ^{176}Yb and ^{176}Lu contribution and the contemporaneous measurements of ^{171}Yb and ^{173}Yb offer a method to correct for mass-bias of Yb by $^{173}Yb/^{171}Yb$ normalization factor of 1.132685 (Chu et al., 2002). The $^{179}Hf/^{177}Hf$ value of 0.7325 was used to Hafnium isotope normalization (Patchett, 1983). To more detailed method description see Matteini et al. (2010).

The εHf_T values calculation use the decay constant λ=1.865∗10^{-11} after Scherer et al. (2006), and the $^{176}Lu/^{177}Hf$ = 0.0332 and $^{176}Hf/^{177}Hf$ = 0.282772 CHUR values after Blichert-Toft and Albarède (1997). The average crustal Lu-Hf ratio permits two-stage T_{DM} ages calculation from the initial Hf isotopic composition (Gerdes and Zeh, 2006, 2009; Nebel et al., 2007) and the $^{176}Lu/^{177}Hf$ value of 0.0113 were used for the average crust (Taylor and McLennan, 1985; Wedepohl, 1995). The $^{176}Lu/^{177}Hf$ value of 0.0384 were used to depleted mantle Hf model ages (T_{DM} Hf) and $^{176}Hf/^{177}Hf$ = 0.28325 were used for the depleted mantle (Chauvel and Blichert-Toft, 2001). Replicate analyses of the GJ-1 reference zircon were done during the analytical phase which yielded an average $^{176}Hf/^{177}Hf$ ratio of 0.282006±16 (2σ, for n = 25), and a replicate analyses of a 200 ppb Hf JMC 475 standard solution doped with Yb (Yb/Hf = 0.02) were obtained

($^{176}Hf/^{177}Hf$ = 0.282162±13 2σ, n = 4) before Hf isotope measurements on zircon, according to reference value for the GJ standard zircon (Morel et al., 2008).

3.4 RESULTS

3.4.1 Field relationships and petrography

The Belén Metamorphic Complex (BMC) Ordovician rocks are sectored in northern and southern BMC (Fig. 2).

We grouped the lithotypes of the Belén Metamorphic Complex into five compositional groups, the first and second group outcropping in the northern sector of the complex, the second and third group occurring in the southern sector of the complex, and the fifth group in the entire complex, northern and southern BMC. These being the focus of the U-Pb geochronology and Hf isotopes of this work.

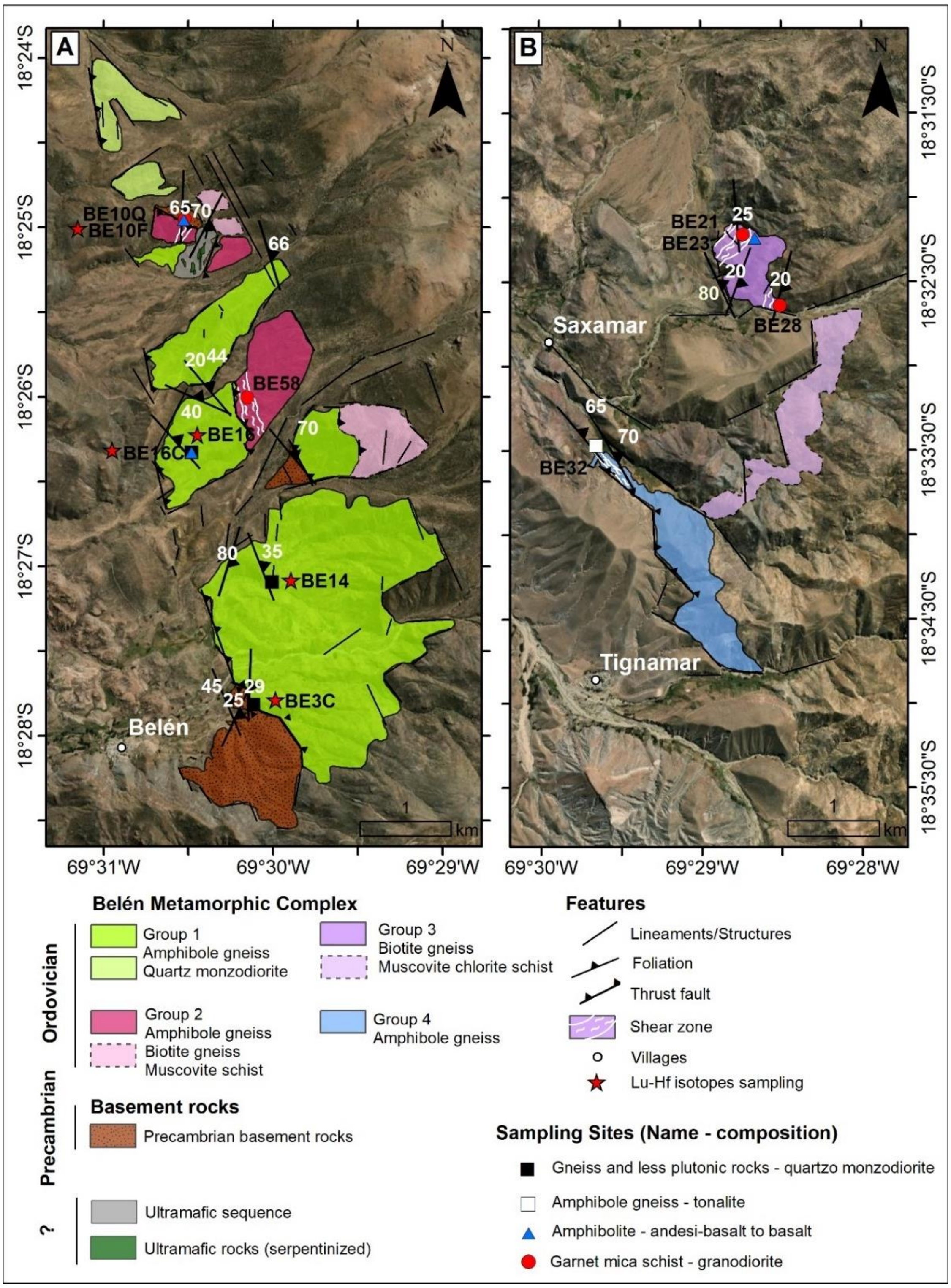

Fig. 2. Geological map and main geological structures of the BMC of northern Chile (1:50,000 scale). Contacts according to fieldwork, inferred limits using satellite imagery and descriptions Wörner et al. (2000) and Loewy et al. (2004) sample location. The white lines indicate shear zones. The map indicates the sampling sites for U-Pb and Lu-Hf analysis. Due to the scale, amphibolite outcrops are not shown on the map. A) Northern BMC groups BMC groups 1 and 2, Precambrian schists and gneisses, and ultramafic rocks. B) Southern BMC includes groups 3 and 4.

The first group comprises gneisses (Fig. 3A) and igneous rocks (Fig. 3C), with quartz monzodioritic composition. The second group is less voluminous than the first, consists of gneisses, schists, and mylonitic rocks with granodiorite composition (Fig. 3B), with garnet (<2%). The third group represents the most characteristic rocks of the southern area, includes gneisses and schists with granodioritic composition (perhaps be associated with group two of the northern area). The fourth group consisting of amphibole gneiss chloritized of tonalitic composition (Fig. 3D). The fifth group is amphibolites boudin hosted (Fig. 3E-F) in the rocks from groups 1 to 4.

The first and second groups from northern sector of BMC shows main foliation of 343/30, except for the vertical foliation of the shist from the Saitoco mine. Oldest metasedimentary rocks outcrops only at northern BMC, by tectonic contact with first group stocks at NW northern sector, at central BMC, and to the south of northern BMC. A sequence of ultramafic rocks (BE11) occurs near the Saitoco mine, and minor occurrences occur in the central (BE59) and south (B42) of northern BMC, usually in contact with Precambrian rocks. The third and fourth groups exhibit main foliation of 340/50, only the schists present horizontal foliation.

The BMC lithologies outcrops in hills of deformed stocks. Eight mapped stocks and five inferred stocks in northern BMC exhibit approximate dimension of 0.3 km x 0.5 km up to 3.0 km x 2.5 km. Southern BMC present two mapped elongated (0.7 km x 3 km) and rounded (0.8 km x 1 km) stocks and one inferred elongated stock around 0.5 km x 2.8 km.

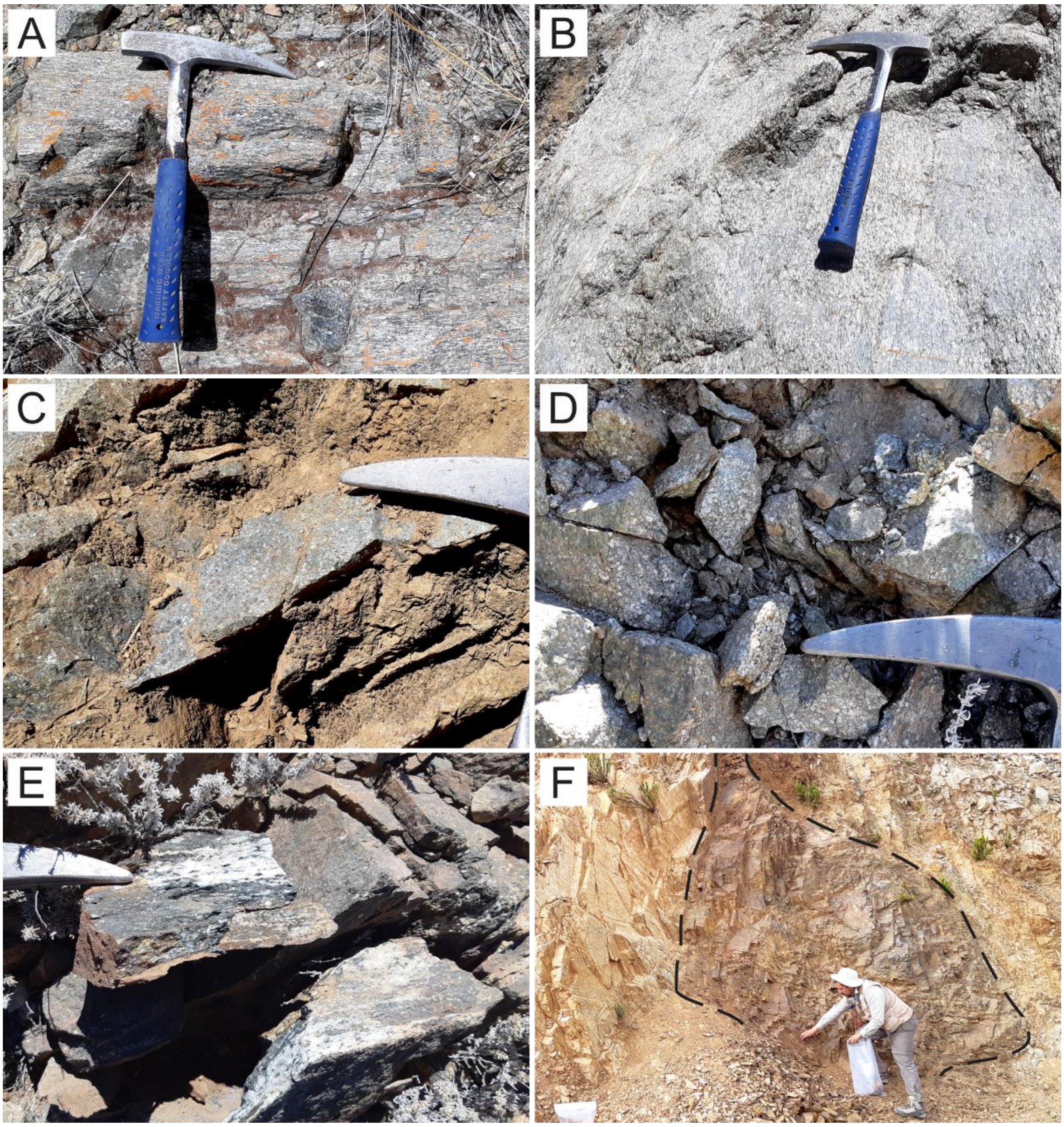

Fig. 3. Field photographs from the Belén Metamorphic Complex, highlighting the structural features: A) Amphibole gneiss (BE60) from the NE part of the northern BMC. The gneissic structure (343/66) is denoted by layers of mafic minerals or felsic minerals. This outcrop marks the contact to the east end of the mafic pluton exposure with younger sedimentary rocks, by a sedimentary breccia with amphibole gneiss clasts. B) Biotite gneiss outcrop (BE24) from N part of southern BMC. The outcrops of points BE21 to BE24 track in the NW side and the points BE27 to BE21 track in the SE side of the same hill with granodioritic chemical composition rocks, evidence the differentiation by alteration and deformation for the same rocks. C) Quartz monzodiorite (BE49) from south central portion of southern BMC. Outcrop of medium-grained massive gabbro. D-E) Rocks outcrops in a hill next to road cut, as extensive and very fractured small blocks: D) Coarse-grained amphibole gneiss (sample BE32), with banding orientation of 320/65. E) Amphibolite (sample BE33) of an elongated metric body emplaced in granodioritic gneiss. The hammer indicates a felsic level parallel to the main foliation of the rock. F) This outcrop is in the NW part in the north end of northern BMC, in trenches of an ended mine. The outcrop exhibits deformed amphibolite boudin emplaced in a muscovite biotite schist, all rocks show vertically dip at this point (9/60-72).

Group 1

This group includes quartz-monzodiorite plutonic rocks (Fig. 3C) and amphibole gneiss with quartz-monzodiorite composition (BE3C and BE14). The outcrops are large extensive expositions mainly on the side of the hills, in dry rivers (named regionally as

Quebrada) and in road-cuts with approximate dimension of ~10 meters until 350 m. The outcrop of quartz-monzodiorite (sample BE16) hosts a small amphibolite boudin (BE16C). The group 1 rocks are partially covered by the Tertiary volcaniclastic Lupica formation rocks to the east and in tectonic contact to Precambrian rocks or covered by younger formations to the west.

Quartz-monzodiorite (sample BE16)

A massive, coarse-grained, and dark-gray rock composed by plagioclase (~40 %, Andesine), poikilitic amphibole (~25 %), alkali feldspar (~15 %), and quartz (~7 %) porphyroclasts (Fig. 4A), occur in the central part of northern BMC at a road cut (Fig. 2). Biotite (~8 %) partially chloritized and associated with muscovite (~2 %) occur among amphibole and feldspar porphyroclasts. The feldspars are intensely sericitized. The matrix is composed of the same primary mineralogy. The poikilitic amphibole show inclusions of acicular tourmaline (Fig. 4B), in the planes of cleavage. Large zircon (included in amphibole, plagioclase, biotite and quartz), titanite, apatite, and epidote (in smaller volumes) compose the accessory minerals (~3 %). Opaque minerals (~2 %) are disseminated.

Amphibole gneiss (samples BE3C and BE14)

Medium-grained and dark-gray amphibole gneisses (samples BE3C and BE14 and Fig. 4E) occurs as the most voluminous lithotype in the northern sector of the BMC. The amphibole gneiss shown the porphyroclasts of plagioclase (30-40 %, Andesine), amphibole (20-30 %), alkali feldspar (10-15 %) and quartz (10-12 %) that indicate a quartz monzodiorite as the probable protolith. Biotite (~15 %), levels surround the porphyroclasts defining the rock foliation. The feldspars occur with sericitization. Accessory phases are allanite (BE14), zircon, apatite, epidote, and Fe-Ti oxides (~3 %). Opaque minerals are rare. Matrix exhibit locally quartz ribbon (Fig. 4E), minor biotite, amphibole, and feldspars.

Group 2

The northern sector group 2 has granodioritic composition and outcrops as schists and mylonitic rocks associated to shear zones. The muscovite chlorite gneiss (sample BE58) is located in the shear zone that deform garnet amphibole gneiss in contact to amphibole gneiss of group 1. The garnet mica schist (sample BE10Q) outcrops in a cut on the side of the hill, with an extension of ~25m and vertical foliation (33/80) and make contact with the Precambrian rocks of the Saitoco mine. This schist host 2 large metric boudins of amphibolite (Fig. 3C) and contacting the metasedimentary Precambrian basement to the north, amphibole gneiss to the south and mafic and ultramafic sequence unit to the east.

Muscovite chlorite gneiss (sample BE58)

A medium-grained and dark-gray muscovite chlorite gneiss (sample BE58) is located in the shear zone, in the contact between amphibole gneiss with amphibole gneiss with garnet, in the northern sector. The muscovite chlorite gneiss shows porphyroclasts of feldspars strongly sericitized (~55 %) and quartz (~20 %). Chlorite (15 %) associated to muscovite (10 %) and clay minerals surround the porphyroclasts, alteration minerals caused by shear zone. Accessory phases are zircon and apatite (~2 %). Opaque minerals are associated with biotite. The deformation microstructures are quartz ribbons, mineral fish of chlorite, interlobate contacts and localized granoblastic texture.

Garnet mica schist (sample BE10Q)

A fine-grained, light gray to medium gray garnet mica schist (sample BE10Q, Fig. 4G) with well-marked bands outcrops at the abandoned Saitoco mine, located on the northern BMC. It is composed of quartz (~40%), feldspar (~25%), chlorite (~20 %), muscovite (~15 %), biotite (~5 %), and opaque minerals (~3 %). Garnet makes up less than 2 % of the rock minerals. The feldspars are intensely sericitized. Zircon and apatite represent ±2 % of the rock composition. The quartz forms ribbons, interlobate contacts due to grain boundary migration and some development of granoblastic textures. Micas levels parallel to quartz ribbons, denoting the main foliation of the rock.

Group 3

They are metamorphic and deformed rocks of granodioritic composition, as Group 2, but outcropping in the southern sector of the BMC. Different from the northern area the deformation is widespread generating the mylonization of gneisses and punctual schistosity. Among the three stocks that occur in the southern sector, one is smaller and rounded, mostly outcropping biotite gneiss (BE21, Fig. 3D) and host amphibolite with pinch-and-swell structure. The muscovite chlorite schist (sample BE28) occurs in contact with biotite gneiss, in the SE side of the same stock, for 180 m, with horizontal foliation

(15/18). Muscovite chlorite schist makes contact with garnet mica shist and a few amphibolite boudin occur between these two schists.

Biotite gneiss (sample BE21)

A medium-grained and light-gray biotite gneiss (BE21, Fig. 4D) is the characteristic lithotype of the southern sector of the BMC. The biotite gneiss exhibits porphyroclasts of quartz (~35 %), plagioclase (~20 %, Albite-Andesine) and alkali feldspar (10 %) that indicate that the protolith was probably a granodiorite. Levels of biotite (~25 %, partially chloritized) associated to epidotes (~8 %) are interspersed with levels of quartz and levels of feldspars. Locally, quartz ribbons and grain boundary migration are observed. Accessory minerals are mainly zircon and apatite. The feldspars are sericitized.

Muscovite chlorite schist (sample BE28)

The muscovite chlorite schist (sample BE28, Fig. 4H) outcrops only in southeastern contact with biotite gneiss stock (BE21-BE25 and BE31) in the southern sector of the complex. This lithotype is very fine-grained, light brown and banded composed by quartz (~45%), feldspar (~40%), chlorite (~10 %), and muscovite (~5 %). Zircon, opaque minerals, and Fe-Ti oxides constitute less than 2 % of the rock minerals. Quartz crystals forms ribbons, interlobate contacts due to grain boundary migration, and some straight contacts among quartz grains that tend to make angles of about 120°. The biotite and chlorite occur parallel to quartz ribbons, evidencing the rock foliation. The feldspar is intensely sericitized.

Group 4

It occurs in a second stock from the southern area of the BMC, elongated in the NNW-SSE direction. The amphibole gneiss (sample BE32) exposed on the side of the hill is intensely mylonitized and chloritized and with several amphibolite boudins.

Amphibole gneiss (sample BE32)

The amphibole gneiss chloritized (sample BE32) are coarse-grained (Fig. 4C) and light-gray banded rocks. Porphyroclasts of plagioclase (~43 %, Andesine), quartz (~20 %), and alkali feldspar (~7 %) indicate that the protolith was a tonalite. The texture is granoblastic (Fig. 4C). Pseudomorphic amphibole porphyroclasts are entirely replaced by a set of chlorite, muscovite, opaque minerals, and Fe-Ti oxides (~25 %). Biotite (~3 %)

heavily altered and replaced by opaque and Fe-Ti oxides (~2 %) also occur interstitial to quartz and feldspars from matrix. The feldspars show sericitization. Accessory phases are zircon, epidote, and apatite (~2 %).

Group 5

Amphibolite

Samples BE10F (BE67), BE16C, and BE23 correspond to amphibolite (Fig. 3E) boudinaged (Fig. 3F), and pinch-and-swell structures hosted by orthogneisses and orthoshists in northern and southern BMC. Few outcrops present quartzofeldspathic layers (Fig. 3E).

They are homogeneous, fine-grained to medium-grained, and dark gray rocks with gabbroic composition composed of amphibole (25-45 %), plagioclase (Labradorite in sample BE10F, Labradorite in sample BE16C and Albite/Oligoclase in sample BE23) representing 35-45 %, quartz (5-10 %), biotite (7-10 %), and hematite (5-10 %). Scarce alkali-feldspar show Carlsbad twinning (BE23, Fig. 4F). Zircon, apatite, and epidote aggregates are under 3 % of the rock composition, plus Fe-Ti oxides. Amphibole and biotite bands mark lepidoblastic and nematoblastic textures that alternate with the quartzfeldspathic minerals of granoblastic texture and the quartzfeldspathic minerals set the localized granoblastic texture. Quartz, zircon, apatite, and titanite aggregates occurs included in amphibole. Acicular tourmaline occurs on amphibole cleavages. The plagioclase is strongly sericitized, with rare myrmekite intergrowth (BE16C). Some amphibolite own disseminated malachite, chalcocite, and chalcopyrite.

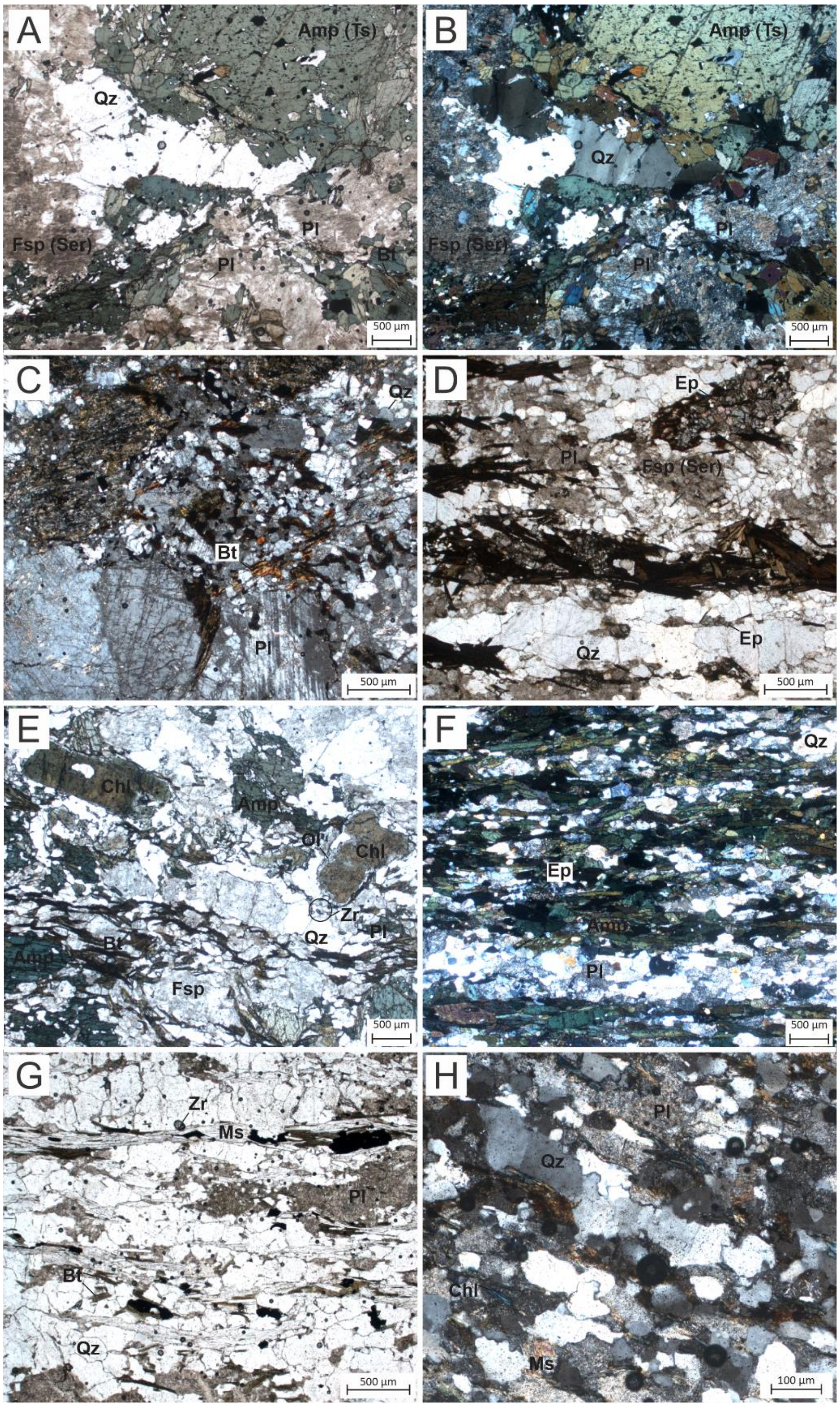

Fig. 4. Photomicrographs of different BMC rock types: A) Coarse-grained quartz monzodiorite (sample BE16) showing porphyroclasts of amphibole with opaque and tourmaline inclusion. Some biotite is associated to amphibole of matrix (Plane-polarized light). B) Quartz monzodiorite (sample BE16) showing porphyroclasts of sericitized feldspars and quartz. Matrix of minor amphibole, feldspar, quartz, and biotite between the main minerals (Crossed-nicols). C) Andesine and pseudomorphic amphibole porphyroclasts of coarse-grained amphibole gneiss (sample BE32). The matrix is composed of feldspar, quartz, biotite, and opaque minerals, showing granoblastic texture (Crossed-nicols). D) Medium-grained biotite gneiss (sample BE21) showing foliation evidence by layer of biotite and epidote. The quartz ribbon is parallel to mafic layers and the feldspar are strongly sericitized (Plane-polarized light). E) The amphibole gneiss (sample BE14) exhibit foliation mark by biotite, amphibole, and quartz ribbon. The olivine is chloritized, with preserved borders (Plane-polarized light). F) Amphibolite showing amphibole and epidote levels

interlayed with quartzofeldspathic levels (Crossed-nicols). G) Garnet mica schist (sample BE10Q) showing muscovite, opaque minerals and biotite associated and parallel to quartz ribbons levels denoting the rock foliation. Plagioclase is intensely sericitized (Plane-polarized light). H) Muscovite chlorite schist (sample BE28) with quartz ribbon parallel to micas orientation (Crossed-nicols).

3.4.2 U-Pb data

The U-Pb data obtained define the ages of five groups of crystalline rocks from the Belén Metamorphic Complex described in the previous topic. The Supplementary Table 01_U-Pb compiled all isotopic results.

Group 1

Quartz monzodiorite (sample BE16)

Zircon crystals from the coarse-grained quartz monzodiorite gabbro (sample BE16) are 65–300 μm long, translucent to slightly metamict, with few fractures. They have some inclusions of apatite, opaque minerals, and unidentified minerals. The crystals are euhedral to subhedral prismatic long and short shapes. According to the BSE images, the zircon internal textures are mainly oscillatory zoning (ZR27) with oscillatory zoned overgrowth (ZR1), and few parallel zonings (ZR22).

From thirty-one U–Pb analyses, obtained mainly in cores twenty-seven show concordance between 102 and 80 % with $^{206}Pb/^{238}U$ ages between 485 and 443 Ma. The 469±4 Ma (MSWD=2.6) from lower intercept age of Tera-Wasserburg diagram (Concordance = 102-80 %) was obtained from twenty spots with Th/U ratios between 0.48 and 1.28 (Fig. 5C).

Amphibole gneiss (sample BE3C)

Zircon crystals are 80–300 μm long, transparent, colorless to light brown, and slightly fractured. They have inclusions of apatite and opaque minerals. The crystals are mostly euhedral to subhedral, with slightly rounded prismatic shapes. According to the CL images, the zircon cores are large, with a well-marked oscillatory zonation (ZR5C and ZR7). There are also recrystallized domains (ZR5R and ZR18), and oscillatory-zoning truncated by subsequent oscillatory zoning.

Thirty-three U–Pb analyses were obtained on cores and few recrystallized domains. Twenty-eight analysis show concordance between 109 and 89 % with $^{206}Pb/^{238}U$ ages between 499 and 443 Ma. Nineteen analyses with $^{206}Pb/^{238}U$ ages between 499 and 464

Ma exhibit a Tera-Wasserburg concordia age of 482±3 Ma (MSWD=0.35) obtained on cores and few recrystallized domains with Th/U ratios between 0.32 and 0.82 (Fig. 5A).

A translucent, colorless, 110 µm long, prismatic, and flattened zircon crystal with no inclusions represents the single Paleoproterozoic zircon dated in 1952±25 Ma (MSWD=0.0016), with Th/U ratios of 0.16. The CL image shows a round, low-luminescence core followed by a thick, high-luminescence rim, similar to a convoluted texture.

Amphibole gneiss (sample BE14)

Zircon crystals are 75–300 µm long, slightly opaque, and slightly metamict, with few fractures. They have some inclusions of apatite, opaque minerals and unidentified minerals. The crystals are mostly euhedral with prismatic shapes and few crystals are rounded. According to the BSE images, the zircon cores are large, with a well-marked oscillatory from the core (ZR19) to the rim (ZR4 and ZR9). BSE images also indicates parallel internal textures and few crystals with light colored spots and streaks.

Thirty crystals were selected and analyzed on cores and on recrystallized domains of the crystals for U–Pb data. Twenty-four analyses show concordance between 106 and 90 %. A Middle Ordovician population with $^{206}Pb/^{238}U$ ages between 472 and 454 Ma can be identified from fifteen concordant data. A concordant age of 464±2 Ma (MSWD=1.6) was obtained on cores and few rims with Th/U ratios between 0.68 and 1.29 (Fig. 5B).

Group 2

Muscovite biotite gneiss (sample BE58)

Zircon crystals are 100–325 µm long, translucent to slightly opaque, with few fractures and fragmented zircon crystals. They have some inclusions of acicular apatite and opaque minerals. The crystals are euhedral with prismatic shapes. According to the BSE images, the zircon cores exhibit well-developed oscillatory zoning (ZR6, ZR14 and ZR21).

Thirty-five U-Pb spots were analyzed from the core to the border. Twenty-six analyses show concordance between 110 and 90 % with $^{206}Pb/^{238}U$ ages between 492 and 433 Ma. From them twenty-one analyses obtained a concordant age of 467±2 Ma (MSWD=0.45) showed in a tera-Wasserburg diagram, with Th/U ratios between 0.51 and 1.26 (Fig. 5D).

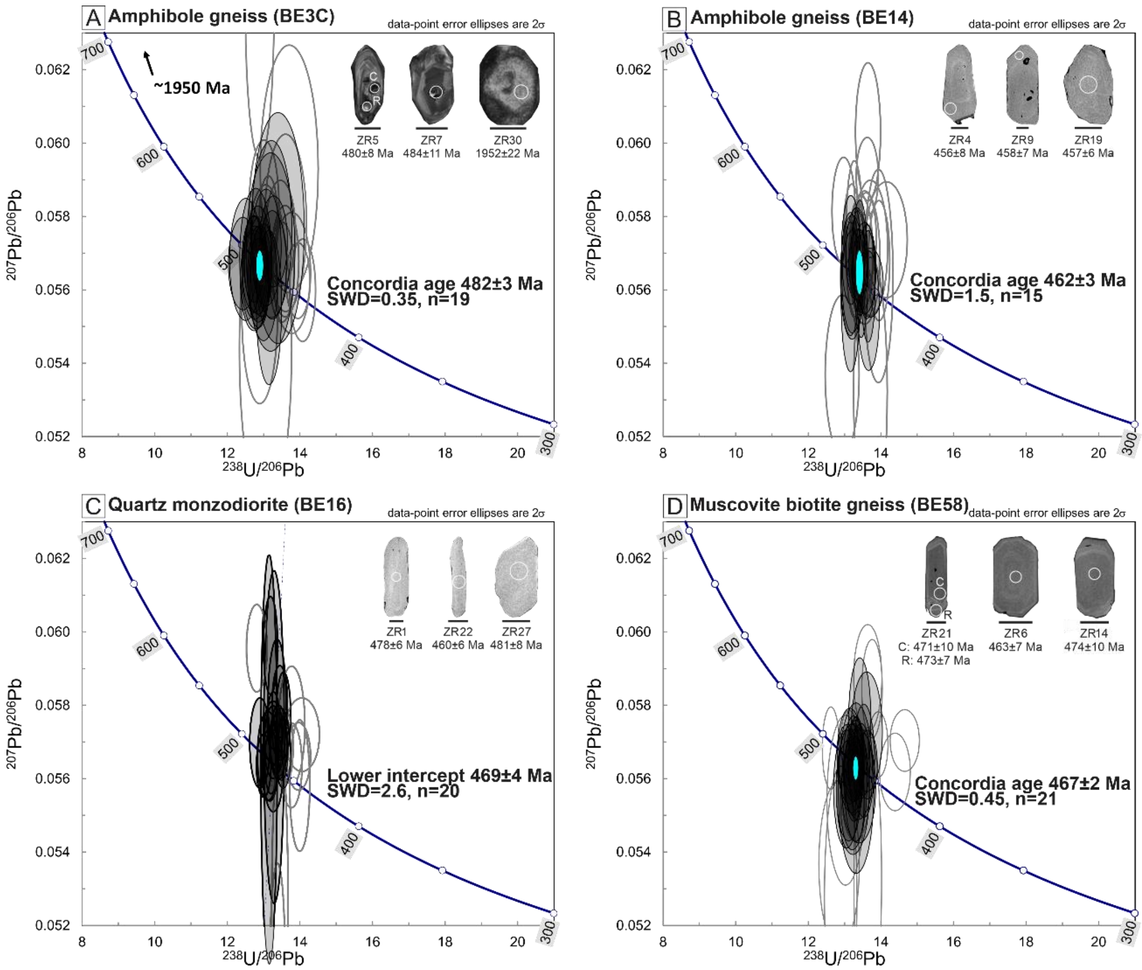

Fig. 5. Tera-Wasserburg diagrams for the Belén Metamorphic Complex group 1 rocks (A-C) and group 2 rock (D) from northern BMC. A) Amphibole gneiss (BE3C) with 482±3 Ma concordia age and one inherited zircon with ~1950 Ma. The CL images of Lower Ordovician zircon crystals show oscillatory zoning at core (ZR5 and ZR 7) and rim (ZR5) and a Paleoproterozoic zircon with convolute internal texture (ZR 30). B) Amphibole gneiss (BE14) with concordia age of 464±3 Ma. The CL images of zircon grains show oscillatory zoning at core (ZR19) and rim (ZR4 and ZR9). C) Quartz monzodiorite (BE16) lower intercept age of 469±4 Ma. The BSE images show oscillatory zoning truncated by oscillatory overgrowth (ZR1), parallel (ZR22), and weakly oscillatory zoning at core (ZR27). D) Muscovite biotite gneiss (BE58) with concordia age of 467±2 Ma. The CL images show oscillatory zoning from the core to the rim (ZR21, ZR6, ZR14). Information for Figures 4-6: Errors of individual data are stated at 2σ confidence limits. Analysis spots and obtained ages (apparent $^{206}Pb/^{238}U$ ages < 1.0 Ga and $^{207}Pb/^{206}Pb$ ages > 1.0 Ga) are indicated below each zircon image. All scale bars on zircon grains are equivalent to 50 μm length. The blue-colored ellipses were generated by Isoplot calculating the Concordia Age. C: Core, and R: Rim.

Garnet mica schist (sample BE10Q)

Zircon crystals are 110–300 μm long, transparent, colorless, and slightly fractured. They have unidentified included minerals. The zircon present subhedral prismatic shapes, somewhat rounded. The CL images shows oscillatory-zoned textures from the (ZR1) to the border of crystal (ZR26), oscillatory-zoned overgrowth (ZR25), parallel textures, and recrystallized burred domains (ZR1).

Ninety-three spots were analyzed for U–Pb data. Eighty-three analyses show concordance between 110 and 81 % with $^{206}Pb/^{238}U$ ages between 489 and 428 Ma. The

Tera-Wasserburg lower intercept age of 465±3 Ma (MSWD=1.9) was obtained on cores and recrystallized domains with Th/U ratios between 0.24 and 1.58 (Fig. 6D).

Group 3

Biotite gneiss (sample BE21)

Zircon crystals are 80–330 μm long, transparent colorless to translucent, and few fractures. They have some inclusions of acicular apatite, opaque minerals and unidentified minerals. The zircon crystals are euhedral with prismatic shapes. On the BSE images, the zircon shows well-developed oscillatory zoning from core to rims (ZR2, ZR23, and ZR27).

Forty-eight U-Pb analyses were obtained on cores and rims. Forty-four analyses show concordance between 108 and 84 %, with $^{206}Pb/^{238}U$ ages between 501 and 429 Ma. From them, seventeen analyses (Conc = 108-84 %) show a concordant age of 467±2 Ma (MSWD=1.5) was obtained on cores and rims with Th/U ratios between 0.45 and 1.09 (Fig. 6A).

Group 4

Amphibole gneiss (Sample BE32)

Zircon crystals are 80–410 μm long, transparent, colorless and some of them are fractured. They have few inclusions of opaque minerals and apatite. The zircon crystals are euhedral with prismatic shapes. The BSE images did not show any internal textures.

Thirty crystals were selected and analyzed for U–Pb data. Seventeen analyses show concordance between 109 and 76 %, with $^{206}Pb/^{238}U$ ages between 471 and 445 Ma. The weighted age give 456±4 Ma (MSWD=1.4) obtained on cores with Th/U ratios between 1.13 and 1.48 (Fig. 6B).

Muscovite chlorite schist (sample BE28)

Zircon crystals are 50–160 μm long, translucent brown to metamictic, fragmented and fractured. They have opaque and unidentified included minerals. The zircon crystals are subhedral to anhedral with prismatic to rounded shapes. The BSE images, shows few oscillatory zoned and parallel textures.

A hundred zircon crystals were selected and analyzed for U–Pb data. Sixty-seven analyses show concordance between 106 and 90 %, and thirty-two data from them show $^{206}Pb/^{238}U$ ages between 480 and 452 Ma (concordance between 104-93 %). These thirty-two analyses exhibit weighted age of 467±3 Ma (MSWD=3.7) obtained on cores with Th/U ratios between 0.33 and 1.16 (Fig. 6C).

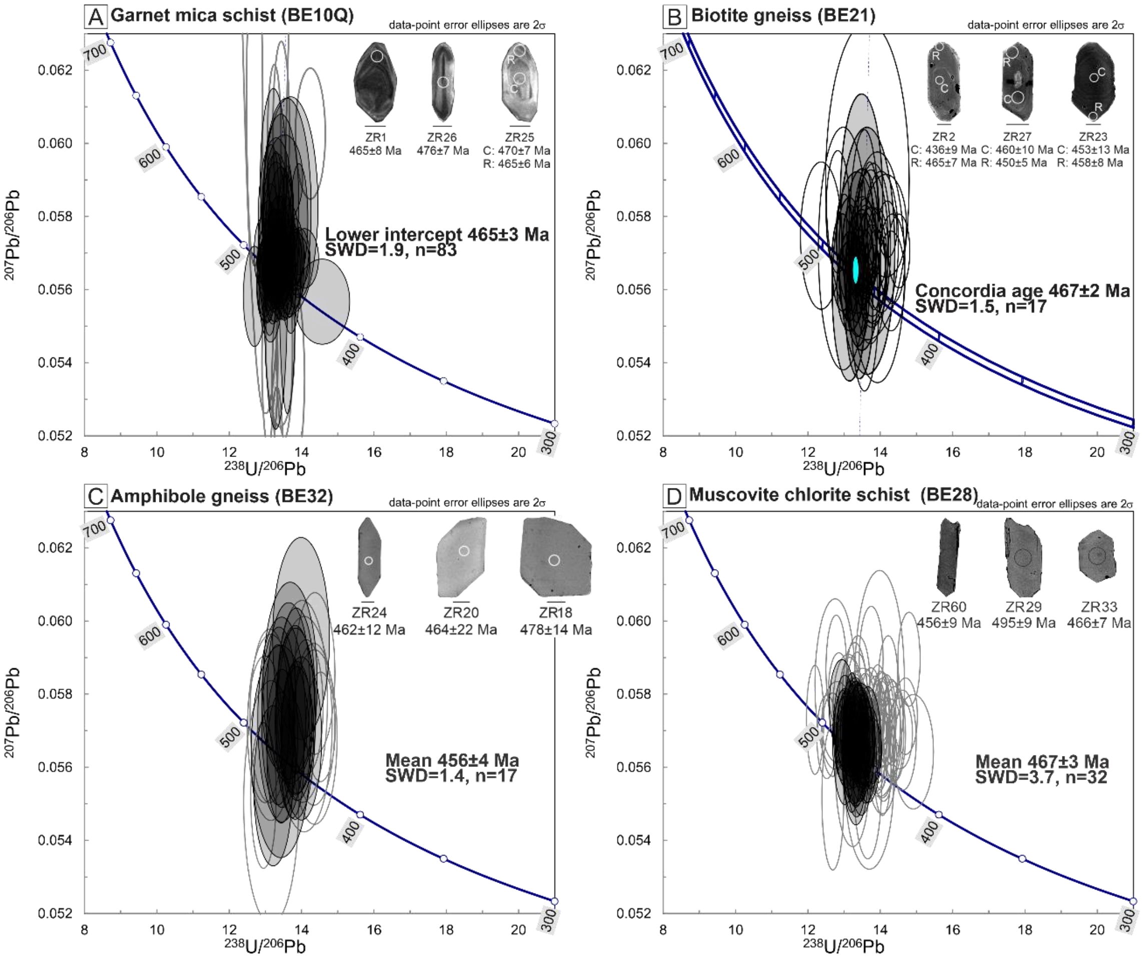

Fig. 6. Tera-Wasserburg diagrams for the Belén Metamorphic Complex group 2 rock (A) from northern BMC, group 3 rocks (B and D) from southern BMC and group 4 rock (C) from southern BMC. A) garnet mica schist (BE10Q) with lower intercept age of 465±3 Ma. The CL images show oscillatory zoned core and rim (ZR1 and ZR25) and parallel zircon core with oscillatory zoned rim (ZR26). B) Biotite gneiss (BE21) with concordia age of 467±2 Ma. The CL images show oscillatory zoning from the core to the rim (ZR2, ZR27, ZR23). C) Amphibole gneiss (BE32) with mean age of 456±4 Ma. The BSE images show prismatic shape of the crystals, but the internal textures are unrecognizable (ZR24, ZR20, ZR18). D) Muscovite chlorite schist (BE28) with mean age of 467±3 Ma. The BSE images show the prismatic short and elongated shapes, but internal textures are difficult to identify (ZR60, ZR29, ZR33).

Group 5

Amphibolite (Sample BE10F)

Sample BE10F provides few zircon crystals 75–170 μm long, transparent, colorless, slightly fractured, and fragmented. They have opaque and unidentified included minerals. The zircon present subhedral to anhedral prismatic and rounded shapes. The BSE images exhibit slightly oscillatory-zoned texture (ZR10) and core with parallel texture (ZR2).

Thirteen zircons were analyzed for U–Pb data. Five analyses show concordance between 103 and 89 %, with $^{206}Pb/^{238}U$ ages between 491 and 481 Ma. These analyses display a concordia age of 485±3 Ma (MSWD=3.1), obtained on cores with Th/U ratios between 0.46 and 1.16 (Fig. 7A).

Amphibolite (Sample BE16C)

Euhedral to subhedral zircon crystals with prismatic rounded shapes are 30–220 μm long, translucent to opaque, fractured, and fragmented. They have opaque and unidentified included minerals. The BSE images exhibit oscillatory-zoned textures (ZR6), parallel textures, and recrystallized domains, but the image does not show much of the textures.

Thirteen zircons were selected and analyzed for U–Pb data. Nineteen analyses show concordance between 104 and 93 %, with $^{206}Pb/^{238}U$ ages between 499 and 449 Ma. Fifteen analyses (concordance of 104-94 %) from them reveals a concordia age of 469±3 Ma (MSWD=1.07) from core and rim with Th/U ratios between 0.38 and 1.55 (Fig. 7B).

Amphibolite (Sample BE23)

Zircon crystals are 50–200 μm long opaque, metamict, few of them are translucent, fractured, and fragmented. They have opaque and unidentified included minerals. The crystals are euhedral to anhedral with prismatic to rounded shapes. The BSE images exhibit mainly oscillatory-zoned textures (ZR6 and ZR20) and rare parallel texture.

Thirty-two crystals were analyzed for U–Pb data. Seventeen analyses show concordance between 108 and 89 %, with $^{206}Pb/^{238}U$ ages between 497 and 451 Ma. Among these, six analyzes on cores (Conc = 104-97 %) yielded a concordia age of 470±4 Ma (MSWD=0.51), with Th/U ratios values of 0.59-1.35.

Two Paleoproterozoic zircon crystals show $^{207}Pb/^{206}Pb$ ages of 1975 and 1881 Ma, with concordance of 105-98 %, and Th/U ratio values of 0.43 and 0.87 respectively. The BSE images evidence rounded zircon grains with complex internal texture like sector zoning or convolute texture (ZR18) and slightly oscillatory-zoned texture.

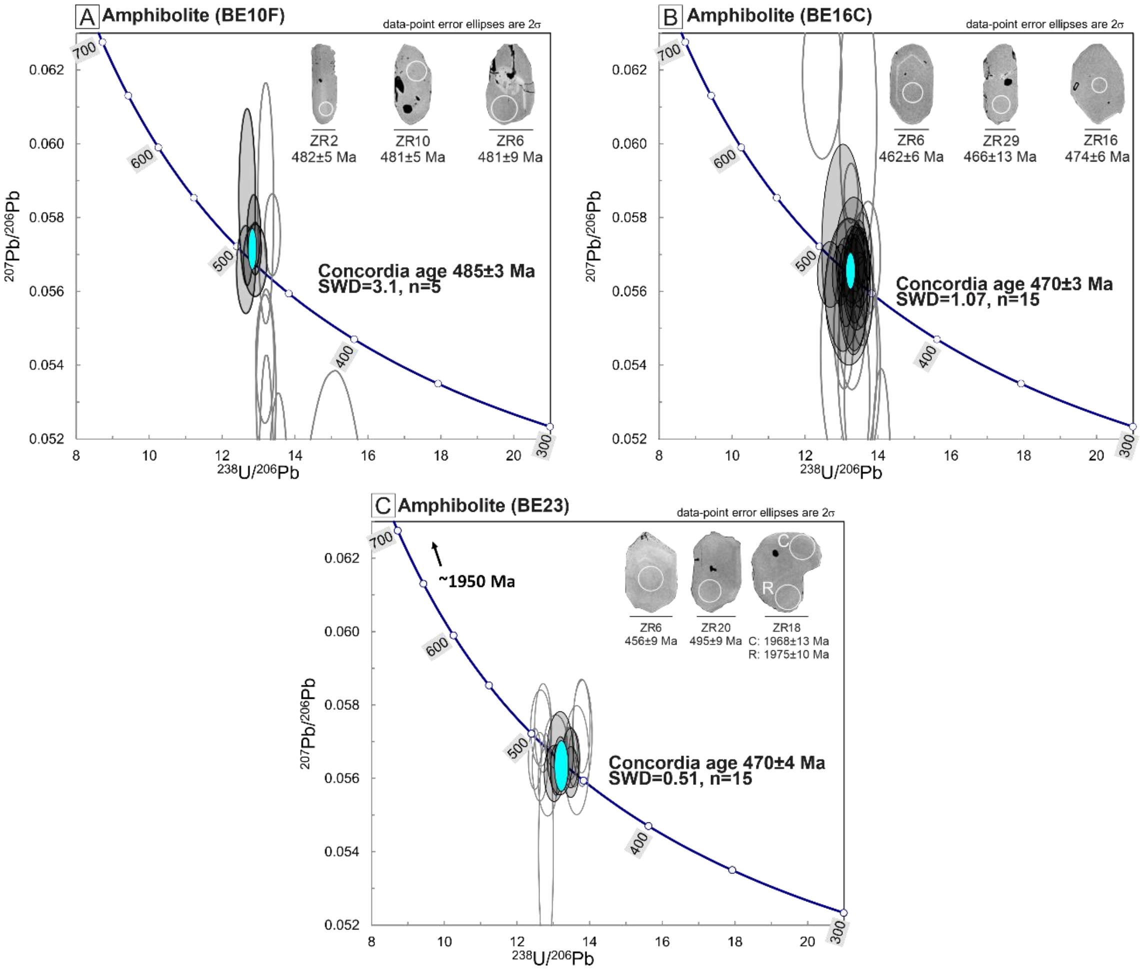

Fig. 7. Tera-Wasserburg diagrams from Belén Metamorphic Complex amphibolites (group 5) from northern (BE10F and BE16C) and southern BMC (BE23). A) Amphibolite (BE10F) with concordia age of 485±3 Ma. The BSE images show weak parallel zoning (ZR2), weak oscillatory zoning (ZR10), and rim with unidentifiable texture (ZR6). B) Amphibolite (BE16C) with concordia age of 470±3 Ma. The BSE images show weak oscillatory zoning (ZR6), but mostly without textures (ZR29 and ZR16). C) Amphibolite (BE23) with inheritance $^{207}Pb/^{206}Pb$ apparent age of 1.97-1.9 Ga from two zircon crystals and concordia age from Ordovician zircon grains of 470±4 Ma. The BSE images show oscillatory zoning at core (ZR6) and rim (ZR20). The BSE images of the Paleoproterozoic zircon show chaotic internal texture (ZR 18).

3.4.3 Lu-Hf data

Twenty-three zircon crystals from Groups 1 and 5 from Belén Metamorphic Complex (BMC) rocks were analyzed for Lu–Hf isotopes. Five zircon crystals from the quartz monzodiorite (sample BE16) yielded negative εHf_T values between -12.5 (T = 474 Ma) and -8.6 (T = 471), with Paleoproterozoic T_{DM} values ranging from ~2.0 to ~1.8 Ga. Nine zircon grains from amphibole gneiss samples (BE3C and BE14) revealed also negative εHf_T values between −12.4 (T = 471 Ma) and -6.8 (T = 487), with Paleoproterozoic T_{DM} values ranging from ~2.0 to ~1.7 Ga. Nine zircon crystals from amphibolite samples BE10F and BE16C exhibited negative to positive εHf_T values between -13.1 (T = 474 Ma) and +3.5 (T = 466 Ma), with Paleoproterozoic to Mesoproterozoic T_{DM} values between ∼2.0 to 1.1 Ga.

3.5 DISCUSSION

3.5.1 Belén Metamorphic Complex faults and shear zones

The Precambrian metasedimentary rocks, ultramafic sequence, and the Ordovician orthoderived rocks are defined as Belén Metamorphic Complex (BMC, e.g., Salas et al., 1966; Basei et al., 1996; Garcia et al., 2004). However, we interpret it as a complex subject only of the Ordovician rocks generated by Famatinian magmatism, already suggested by Wörner et al. (2000) and Lower et al. (2004).

Based on the fieldwork and petrography data we individualize BMC rocks in 5 groups by composition: group 1 – quartz monzodiorite, gneissic majority; group 2 – gneisses and schists of granodiorite composition; group 3 – granodioritic gneiss and schist; group 4 – tonalitic gneiss mylonitized; and group 5 – represented by amphibolite boudins emplaced in group 1 to 4 rocks. Groups 1 and 2 are located in the northern part of the BMC while groups 3 and 4 at southern part. The contact relationship between the rocks from these groups was not possible to established. Regardless of, we identified a relationship of less evolved rocks (group 1 and 3) juxtaposed at -west to more evolved rocks (group 2 and 3) at northeast.

Plutonic rocks show gradual deformation. In the northern sector, the shear zones deformed granodioritic gneiss into schist. Most northern outcrops are gneissic, with few preserved magmatic outcrops. The southern area deformation is widespread, as seen by the mylonitization of the gneisses, except in the SE portion of the easternmost stock, where intense shear generates schists with high-grade deformation microstructures. These differences indicate that the northern and southern BMC areas were affected by different phases of deformation or responded differently to the same deformation process.

Mega thrust faults (e.g., Pacci et al., 1980; Basei et al., 1996; Garcia et al., 2004; Zentilli et al., 2018) set the contact between the BMC rocks and the metasedimentary Precambrian rocks or younger volcanic formations to the west. In addition to the known major structures, we recognized several smaller NNW-trending structures from satellite imagery in the northern BMC, interpreted as minor faults.

The schistosity, gneissic foliation, and mylonitic structures depict the shearing of the BMC magmatic rocks. These shearing evidences are parallel to minor and major faults

(Fig. 2). This pattern of structures occurs in the Sierra de Valle Fértil, Argentina, as compressional ductile shear zone overprinted by brittle faults (Cristofolini et al., 2014), on Guacha Corral shear zone in the Sierras Pampeanas, Argentina that brittle fault (ENE) zones overprinted sub-parallel mylonitic foliation (460-450 Ma) (Semenov & Weimberg, 2017). Having said that, we postulate that BMC shear zones and fault system are related to Famatinian Orogeny.

Characterization and age of the Belén Metamorphic Complex

The Famatinian flare-up magmatism in the Belén Metamorphic Complex occurred in a restricted age range of voluminous magmatism between 470 to 464 Ma (Fig. 8). Interpreted as crystallization ages of quartz monzodioritic and granodioritic protoliths, subsequently deformed. The zircon shows oscillatory and recrystallized domains. Despite that, it was impossible to individualize magmatic and metamorphic ages according to different zircon domains. The data overlap in time due to the superposition of analytical error between the analysis.

This magmatic peak is within the 472-468 Ma flare-up period recognized in the Sierras Pampeanas (Rapela et al., 2018) associated to slab break-off. Older age of 482 Ma (sample BE3C) in northern BMC and younger age of 456 Ma (sample BE32) in southern BMC, indicate minor magmatism before and after the magmatic peak.

Foliated granodiorite rocks dated by Loewy et al., (2004) exhibit 473±2 Ma in northern and 473±3 Ma in southern BMC, considering the error these ages are within the flare-up age established in this work. Younger age of 456 Ma interpreted as metamorphic age was obtained by Wörner et al. (2000) in an intermediate amphibole gneiss, in northern BMC, whereas we reinterpret as magmatic age. At less than 1 km NW in northern BMC an amphibole gneiss outcrop dated an igneous crystallization age of 472 Ma (Pankhurst et al., 2016).

The compilation of geochronological and compositional data for the BMC rocks suggests early quartz monzodioritic magmatism at 482 Ma only in the northern area, followed by quartz monzodioritic and granodioritic magmatic activity between 470-464 Ma concomitant in north and south sectors of the BMC, and a late magmatism under 456 Ma with quartz monzodioritic composition in northern BMC and tonalitic magmatism in southern BMC.

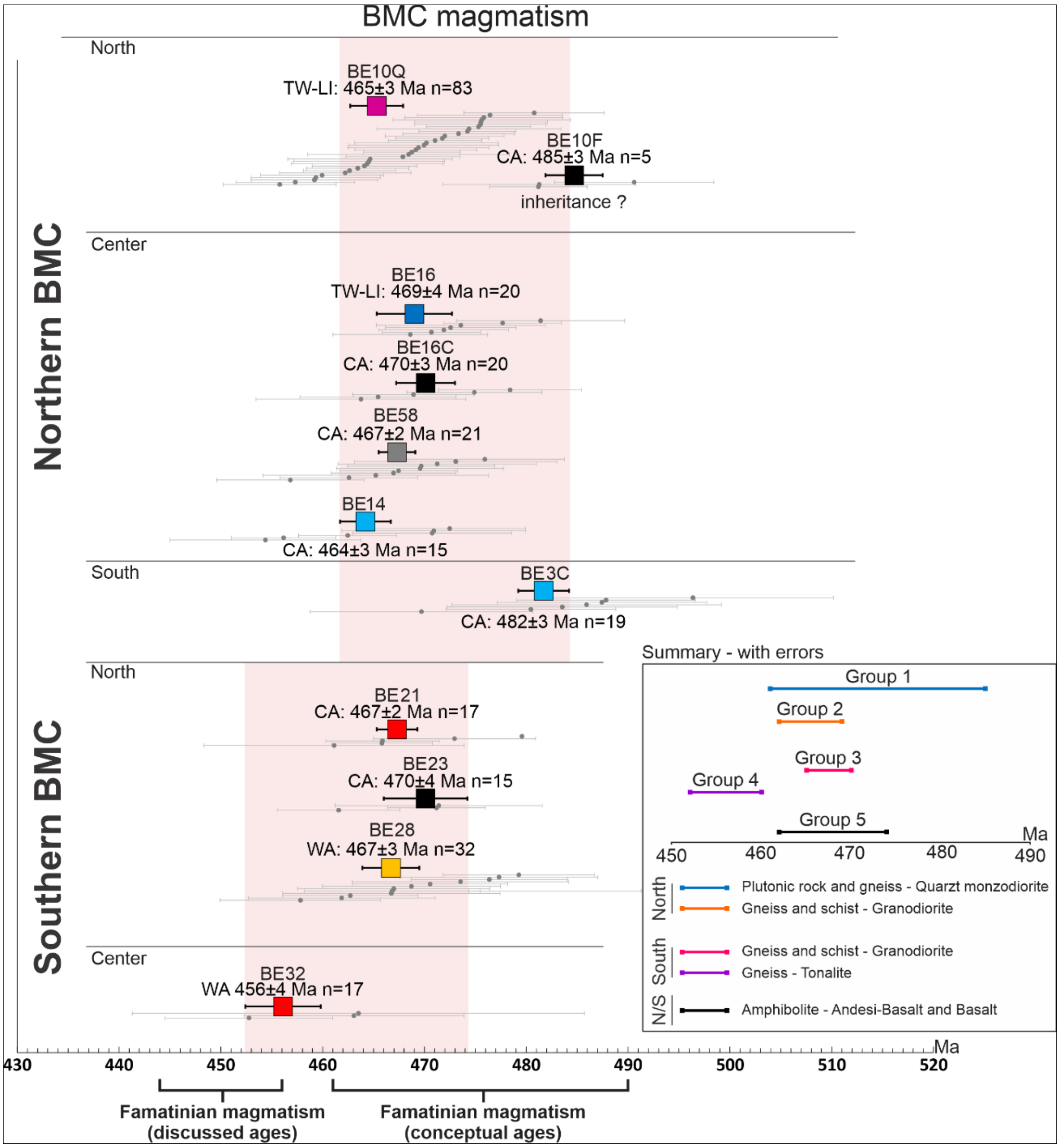

Fig. 8. Compilation of U–Pb data obtained in this paper (data shown in Figs. 4-6). The U–Pb ages are marked by the colored squares with error bars. Apparent ages with concordance between 102 and 98% are shown with the gray circles with error bars ($^{206}Pb/^{238}U$, in Ma). The vertical light pink contrast the different range of ages from northern and southern BMC. A box with compiled ages is presented to the right of the image, according to the 5 rock groups established in this study.

In relation to the amphibolite zircon grains, the few crystals have typological variety, sizes, shapes, and internal textures that may indicate inheritance from relatively older sources in the case of the sample BE10F or contaminated from the host rock (BE16C and BE23). An amphibolite of 485 Ma (sample BE10F) hosted in garnet mica schist (BE10Q) of 465 Ma. The older age was probably inherited zircons captured during the mafic magma rise. Considering field work and geochronology we interpret that all three amphibolite outcrops (BE10F, BE16C, and BE23) represents disrupted syn-plutonic mafic dikes as composite enclaves filling early fractures (Kumar, 2020) of the host rocks (samples BE10Q, BE16, and BE21).

All BMC dated samples present older and younger concordant ages (Fig. 8) than the postulated as the “best crystallization age”. The zircon $^{206}Pb/^{238}U$ general ages show an extensive concordant age distribution (Conc=2%) varies from 496 (sample BE3C) to 453 Ma (sample BE32). Therefore, we could not rule out the possibility of older ages to the Belén Metamorphic Complex magmatism.

Our new geochronological set of U-Pb in zircon (eleven samples from northern and southern BMC, Fig. 8) improve the previously known robust age range from 472 ± 3 Ma to 456±4 Ma (Wörner et al., 2000; Loewy et al., 2004; Pankhurst et al., 2016) to 482±3 Ma to 456±4 Ma. Therefore, Famatinian magmatic activity in the Belén Metamorphic Complex area stand for at least 26 Ma.

The relative probability curve with apse at 469 Ma (Fig. 9A) and Quantile-Quantile (QQ) plots diagram and proportion diagram (Fig. 9B) shows a substantial similarity in the distribution of apparent ages $^{206}Pb/^{238}U$ of ~450-465 Ma between the data compiled from the regional Famatinian magmatism (e.g., Lork and Bahlburg, 1993; Astini et al., 1995; Pankhurst et al., 1998; Saavedra et al., 1998; Quenardelle and Ramos, 1999; Pankhurst et al., 2000; Wörner et al., 2000; Loewy et al., 2004; Hauser et al., 2011; Niemeyer et al., 2014; Pankhurst et al., 2016; Rapela et al., 2018; Ortiz et al., 2019b) and the data obtained in this work for the Belén Metamorphic Complex rocks (Fig. 9C). This similarity may indicate a period of significant zircon generation over the entire length of the arc. For ages above 465 Ma, we identified a minor variance for BMC concerning the regional data. This higher variance for the regional Famatinian ages highlights the heterogeneity magmatism in which the BMC represents a single part of the whole.

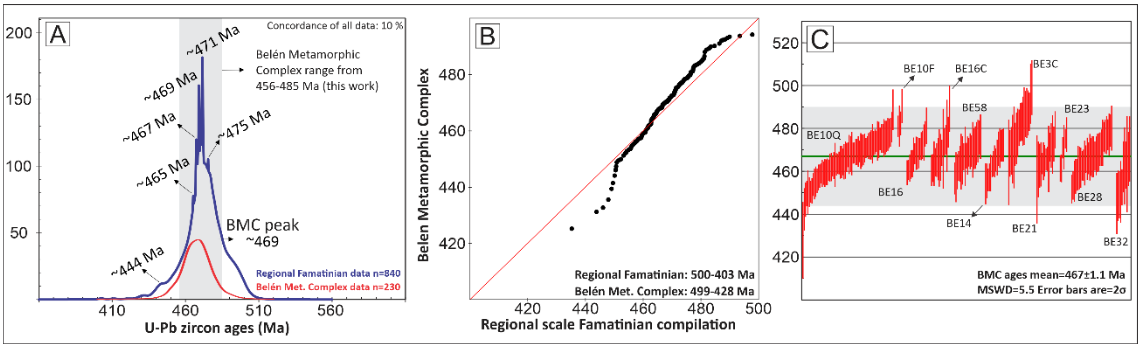

Fig. 9. *Age distribution of BMC and Famatinian magmatism on a regional scale. A) Comparison of relative probability curves. B) QQ plot and proportion diagram. C) Average age obtained for the BMC.*

The Famatinian magmatism is part of an Famatinian orogenic event caused by accretion of terranes in the development of the proto-Gondwana margin (Ramos, 1999; Varela et al., 2011; Casquet et al., 2012; Romero et al., 2013; Bahlburg et al., 2016). In the case of the BMC, the Famatinian magmatism reflect the reaccretion between Arequipa and Antofalla terrane through proto-Gondwana continental margin (Bahlburg & Hervé 1997; Rapalini 2005; Ramos 2008).

Evolution of the Belén Metamorphic Complex

The absence of pre-arc crust and the predominance of subduction-related rocks with continental isotopic signatures are two main issues discussed for the Famatinian arc (Otamendi et al., 2020). The new data constrain the isotopic characteristics of the continental crust beneath the BMC at 469±6 Ma (average of the obtained ages) that in order have tectonic and geodynamic implications on the evolution of the Famatinian Arc.

The negative εHf_T values and the T_{DM} of ~2.04 Ga for the BMC could be explained by three main petrogenetic processes: 1) the reworking of a Paleoproterozoic crust by partial melting during the Ordovician (Rapela et al., 2018); 2) mantle source contaminated by subducted sediments (Cornet et al., 2022); or 3) juvenile magmas highly contaminated by installation of the magmatic arc in an accretionary prism (Jiang et al., 2016). As the Hf isotopic data showed (Fig. 10, yellow circle 1), the sediments source could be a Paleoproterozoic crust, the same Cerro Uyarani Metamorphic Complex (CUMC, T_{DM}=2.63-1.81 Ga, Oliveira et al., 2022) or still an older one (Peruvian Arequipa-Antofalla Basement ?). As only few inherited zircon (three crystals) with ages around 1.97-1.95 Ga were identified in the BMC, the first possibility is not so likely. Alternatively, and probably better, is that the negative εHf_T zircon values from the BMC are explained by the second or third possibility, the juvenile magmas highly contaminated by subducted sediments or accretionary wedge (Fig. 10, yellow circle 2).

Belén Metamorphic Complex show mainly negative εHf_T values similar with the values obtained for amphibole gneiss from Belén and granitoids from Cordón de Lila in Chile (compiled by Pankhurst et al., 2016). Also, negative εHf_T values also occur for peraluminous and metaluminous granitoids, k-bentonites, and a gabbroic rock from Sierras Pampeanas in Argentina (Rapela et al., 2018). The Belén Metamorphic Complex pattern is somewhat similar to granitic vein from Sierra de Maz in Argentina (Martin et al., 2019). The amphibolite (BE16C) from northern part of the BMC (470 Ma) shows negative εHf_T values similar with a metadacite of 483 Ma (Hauser et al., 2011) from NW

Argentina. Despite similarities, the εHf$_T$ values of the BMC are strongly negative in relation to the bulk data compiled in Figure 10, also suggesting that Famatinian magmatism in BMC area was installed in an accretionary wedge (for example Peixoto et al., 2015), which is consistent with the tectonics established for the region due to the separation of the Arequipa and Antofalla terranes, development of a back-arc basin in an attenuated crust, and the reaccretion of the Antofalla through Arequipa terrane in the Ordovician (Ramos, 2008). Precambrian metasedimentary rocks (Pankhurst et al., 2016) and ultramafic rocks (Garcia et al., 2004; Wörner et al., 2000) juxtaposed to BMC rocks (Fig. 2) may be part of the accretionary wedge intruded by BMC Famatinian magmatism.

Paleoproterozoic Sm-Nd T$_{DM}$ (whole rock) ages for BMC rocks, inherited ~1.87 Ga zircon in felsic dike at Belén, and the overlap of Pb isotopic composition between Arequipa terrane and Belén Metamorphic Complex also imply significant contamination of Paleoproterozoic crust (1.9–1.8 Ga) or entirely derivation from Arequipa Terrane (Loewy et al., 2004).

The Hf zircon isotopes from amphibolite, representing the most primitive magma so far observed in the area, show highly variable positive to negative εHf$_T$ data produced by the contamination reinforce the second hypothesis.

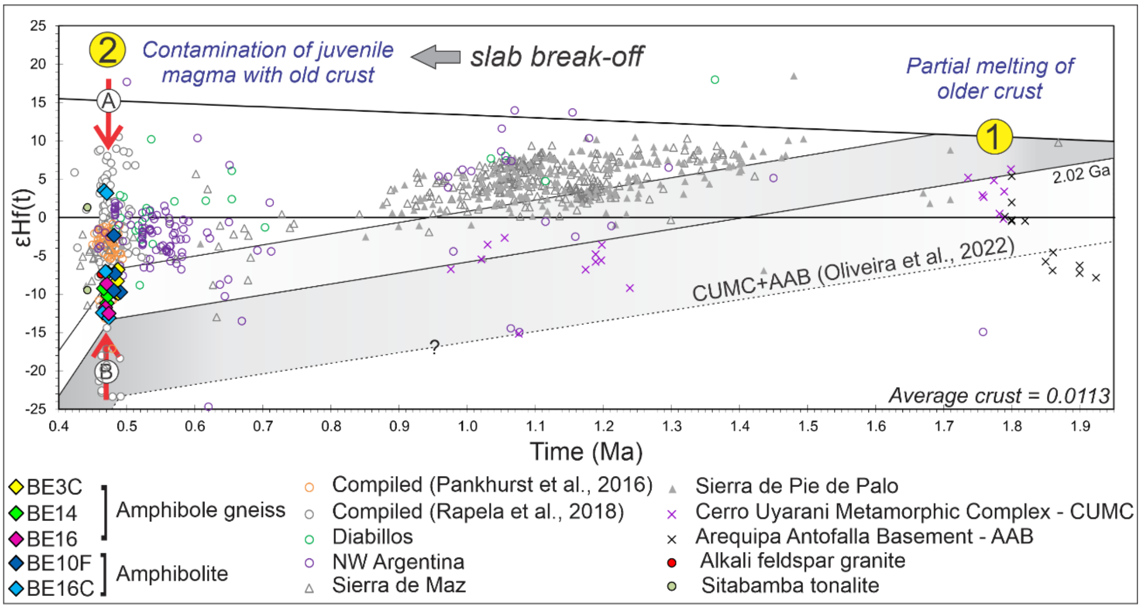

Fig. 10. εHfT values versus Ages in Ga for zircon from the Belén Metamorphic Complex rocks (square, circle, and diamond symbols) compared with εHfT values from the Famatinian and other units. . Igneous Famatinian compiled data from Pankhurst et al. (2016) in grey circles and from Rapela et al. (2018) in orange circles. The green circles correspond to Diablillos Intrusive Complex (Ortiz et al., 2017), purple circle from Ordovician plutonic rocks from NW Argentina (Hauser et al., 2011), the grey triangles represent εHfT data from Maz terrane (Martin et al., 2019), the crosses (purple and black) are data from Arequipa Antofalla Basement (Ribeiro et al., 2020), and the northern extension CUMC (Oliveira et al., 2022). The

light green (Chew, 2007) and red (Mišković and Schaltegger, 2009) filled circles are from Famatinian magmatism exposed in Peru.

Several authors recognized the importance of the juvenile component in the construction of the Famatinian arc. Stern and Bloomer (1992) and Otamendi et al. (2020) postulated a proto Famatinian crust dominated by a lithosphere formed during the infant Famatinian magmatic arc. The young slab sinking into the upper mantle could carried a rapidly assimilated craton-derived sediments, resulting in plutonic batholiths with subduction geochemical characteristics but with continental isotopic signatures. O–Sr–Nd isotopic composition of the Famatinian arc magmas (Alasino et al., 2020) show varied results. The authors suggest a binary mixing model with a crustal contribution, as shown by the Hf data. The percentage of metasedimentary rocks assimilation was rated 5% to 40% for gabbro, migmatites, and hybrid granitoids, although the rhyolite composition does not show bulk assimilation of supracrustal rocks.

The incorporation of a juvenile magma at ~469 Ma is consistent with the interpretation of Casquet et al. (2012). He postulated that part of the dominant Famatinian magmatism originated in depleted mantle was heavily contaminated by crustal components. The Precordillera terrane continental collision produced the roll-back of the slab with the consequent slab break-off stage and input of mantellic magmas between 472-468 Ma (Rapela et al., 2018). This slab break-off produced a voluminous metaluminous magmatism, and the flare-up episode in the Argentina NW region. Further south, at Belén Metamorphic Complex in Chile, during the slab break-off stage (Rapela et al., 2018), were produced quartz monzodiorite, granodiorite and tonalite plutonic rocks, hardly deformed and metamorphized, mainly between 470-464 Ma (this work), a synchronous flare-up period between Famatinian magmatism in the Sierras Pampeanas.

3.6 CONCLUSION

1- The plutonic rocks of the Famatinian magmatism in the Belén Metamorphic Complex were transformed into gneisses, schists, and migmatized rocks by shear deformation and related metamorphism.
2- The Belén Metamorphic Complex protolith rocks are emplaced between ~482 to 456 Ma, whilst the flare-up phase is limited between 470 to 464 Ma.
3- The BMC magmatism own a significant degree of crustal assimilation in the subduction zone with minor involvement of juvenile component from the mantle, supported by U-Pb Paleoproterozoic inheritances and hardly negative εHf_T data.

3.7 ACKNOWLEDGEMENTS

This work was carried out with the financial support of the Coordination for the Improvement of Higher Education Personnel - Brazil CAPES - Financing Code 001, responsible for the student's doctoral scholarship. I also thank the National Council for Scientific and Technological Development (CNPq) for supporting the research of N.H and W.U.R through research grants n◦ 309878/2019–5 and 305761/2019–6, respectively.

3.8 REFERENCES

Aceñolaza, F. G., & Toselli, A. J., 1976. Consideraciones estratigráficas y tectónicas sobre el Paleozoico Inferior del noroeste argentino. Memorias 2° Congreso Latinoamericano de Geología, 755–764.

Alasino, P., Casquet, C., Galindo, C., Pankhurst, R., Rapela, C., Dahlquist, J., Recio, C., Baldo, E., Larrovere, M., & Ramacciotti, C., 2020. O–H–Sr–Nd isotope constraints on the origin of the Famatinian magmatic arc, NW Argentina. Geological Magazine, 157(12), 2067–2080. https://doi.org/10.1017/S0016756820000321

Alasino, P. H., Casquet, C., Pankhurst, R. J., Rapela, C. W., Dahlquist, J. A., Galindo, C., Larrovere, M. A., Recio, C., Paterson, S. R., Colombo, F., & Baldo, E. G., 2016. Mafic rocks of the Ordovician Famatinian magmatic arc (NW Argentina): New insights into the mantle contribution. Geological Society of America Bulletin, 128(7–8), 1105–1120. https://doi.org/10.1130/B31417.1

Albarède, F., Telouk, P., Blichert-Toft, J., Boyet, M., Agranier, A., & Nelson, B., 2004. Precise and accurate isotopic measurements using multiple-collector ICPMS. Geochimica et Cosmochimica Acta, 68(12), 2725–2744. https://doi.org/10.1016/j.gca.2003.11.024

Astini, R. A., Benedetto, J. L., & Vaccari, N. E., 1995. The early Paleozoic evolution of the Argentine Precordillera as a Laurentian rifted, drifted, and collided terrane: A geodynamic model. Geological Society of America Bulletin, 107(3), 253–273. https://doi.org/10.1130/0016-7606(1995)107<0253:TEPEOT>2.3.CO;2

Astini, R. A., & Benedetto, J. L., 1996. Tectonostratigraphic development and history of an allochthonous terrane in the Pre-Andean Gondwana margin: the Argentine Precordillera. 3rd International Symposium on Andean Geodynamics, 759–762.

Bahlburg, H., Berndt, J., & Gerdes, A., 2016. The ages and tectonic setting of the Faja Eruptiva de la Puna Oriental, Ordovician, NW Argentina. Lithos, 256–257, 41–54. https://doi.org/10.1016/j.lithos.2016.03.018

Bahlburg, H., & Hervé, F., 1997. Geodynamic evolution and tectonostratigraphic terranes of northwestern Argentina and northern Chile. Geological Society of America Bulletin, 109(7), 869–884. https://doi.org/10.1130/0016-7606(1997)109<0869:GEATTO>2.3.CO;2

Basei, M. A., Charrier, R., & Herve, F. 1996. New ages (U-Pb, Rb-Sr, K-Ar) from supposed pre-cambrian units in Northern Chile : some geotectonic implications. 3rd International Symposium on Andean Geodynamics, 763–766.

Bertotti, A. L., 2012. Lu-Hf em zircão por LA-MC-ICP-MS [Universidade Federal do Rio Grande do Sul]. http://www.bibliotecadigital.ufrgs.br/da.php?nrb=000860173&loc=2012&l=69fef4c265f28528

Bertotti, A. L., Chemale Jr., F., & Kawashita, K., 2013. Lu-Hf em zircão por LA-MC-ICP-MS: aplicação em gabro do Ofiolito Aburrá, Colômbia. Pesquisas Em Geociências, 40(2), 117–127. https://doi.org/10.22456/1807-9806.43075

Blichert-Toft, J., & Albarède, F., 1997. The Lu-Hf isotope geochemistry of chondrites and the evolution of the mantle-crust system. Earth and Planetary Science Letters, 148(1–2), 243–258. https://doi.org/10.1016/S0012-821X(97)00040-X

Bühn, B., Pimentel, M. M., Matteini, M., & Dantas, E. L., 2009. High spatial resolution analysis of Pb and U isotopes for geochronology by laser ablation multi-collector inductively coupled plasma mass spectrometry (LA-MC-ICP-MS). Anais Da Academia Brasileira de Ciências, 81(1), 99–114. https://doi.org/10.1590/S0001-37652009000100011

Casquet, C., Fanning, C. M., Galindo, C., Pankhurst, R. J., Rapela, C. W., & Torres, P., 2010. The Arequipa Massif of Peru: New SHRIMP and isotope constraints on a Paleoproterozoic inlier in the Grenvillian orogen. Journal of South American Earth Sciences, 29(1), 128–142. https://doi.org/10.1016/j.jsames.2009.08.009

Casquet, C., Dahlquist, J. A., Verdecchia, S. O., Baldo, E. G., Galindo, C., Rapela, C. W., Pankhurst, R. J., Morales, M. M., Murra, J. A., & Mark Fanning, C., 2018. Review of the Cambrian Pampean orogeny of Argentina; a displaced orogen formerly attached to the Saldania Belt of South Africa? Earth-Science Reviews, 177, 209–225. https://doi.org/10.1016/j.earscirev.2017.11.013

Casquet, C., Rapela, C. W., Pankhurst, R. J., Baldo, E., Galindo, C., Fanning, C. M., & Dahlquist, J., 2012. Fast sediment underplating and essentially coeval juvenile magmatism in the Ordovician margin of Gondwana, Western Sierras Pampeanas, Argentina. Gondwana Research, 22(2), 664–673. https://doi.org/10.1016/j.gr.2012.05.001

Chauvel, C., & Blichert-Toft, J., 2001. A hafnium isotope and trace element perspective on melting of the depleted mantle. Earth and Planetary Science Letters, 190(3–4), 137–151. https://doi.org/10.1016/S0012-821X(01)00379-X

Chernicoff, C. J., & Ramos, V. A., 2003. El basamento de la sierra de San Luis: Nuevas evidencias magnéticas y sus implicancias tectónicas. Revista de La Asociación Geológica Argentina, 58(4), 511–524.

Chew, D. M., Magna, T., Kirkland, C. L., Miskovic, A., Cardona, A., Spikings, R., & Schaltegger, U. 2008. Detrital zircon fingerprint of the Proto-Andes: Evidence for a Neoproterozoic active margin? Precambrian Research, 167(1–2), 186–200. https://doi.org/10.1016/j.precamres.2008.08.002

Chew, D. M., Pedemonte, G., & Corbett, E., 2016. Proto-Andean evolution of the Eastern Cordillera of Peru. Gondwana Research, 35, 59–78. https://doi.org/10.1016/j.gr.2016.03.016

Chew, D. M., Schaltegger, U., Košler, J., Whitehouse, M. J., Gutjahr, M., Spikings, R. A., & Miskovic, A. 2007. U-Pb geochronologic evidence for the evolution of the Gondwanan margin of the north-central Andes. Geological Society of America Bulletin, 119(5–6), 697–711. https://doi.org/10.1130/B26080.1

Christiansen, R., Morosini, A., Enriquez, E., Muñoz, B., Lince Klinger, F., Martinez, M. P., Ortiz Suárez, A., & Kostadinoff, J. 2019. 3D litho-constrained inversion model of southern Sierra Grande de San Luis: New insights into the Famatinian tectonic setting. Tectonophysics, 756, 1–24. https://doi.org/10.1016/j.tecto.2019.02.015.

Chu, X. L., Huo, W. G., & Zhang, X. 2002. S, C, and Pb isotopes and sources of metallogenetic elements of the Dajing Cu-polymetallic deposit in Linxi County, Inner Mongolia, China. Acta Petrologica Sinica, 18(4), 566–574.

Cohen, K. M., Finney, S. C., Gibbard, P. L., & Fan, J.-X. 2013. The ICS International Chronostratigraphic Chart. Episodes, 36(3), 199–204. https://doi.org/10.18814/epiiugs/2013/v36i3/002.

Cornet, J., Laurent, O., Wotzlaw, J.-F. , Antonelli, M.A., Otamendi, J., Bergantz, G.W., Bachmann, O. 2022. Reworking subducted sediments in arc magmas and the isotopic diversity of the continental crust: The case of the Ordovician Famatinian crustal section, Argentina, Earth and Planetary Science Letters, 595, 117706.

Cristofolini, E. A., Otamendi, J. E., Walker, B. A., Tibaldi, A. M., Armas, P., Bergantz, G. W., & Martino, R. D., 2014. A Middle Paleozoic shear zone in the Sierra de Valle Fértil, Argentina: Records of a continent-arc collision in the Famatinian margin of Gondwana. Journal of South American Earth Sciences, 56, 170–185. https://doi.org/10.1016/j.jsames.2014.09.010

Damm, K.-W., Pichowiak, S., Harmon, R. S., Todt, W., Kelley, S., Omarini, R., & Niemeyer, H., 1990. Pre-Mesozoic evolution of the central Andes; The basement revisited. In Plutonism from Antarctica to Alaska (pp. 101–126). https://doi.org/10.1130/SPE241-p101

Ducea, M. N., Otamendi, J. E., Bergantz, G., Stair, K. M., Valencia, V. A., & Gehrels, G. E., 2010. Timing constraints on building an intermediate plutonic arc crustal section: U- Pb zircon geochronology of the Sierra Valle Fértil-La Huerta, Famatinian arc, Argentina. Tectonics, 29(4), TC4002. https://doi.org/10.1029/2009TC002615

Fanning, C. M., Pankhurst, R. J., Rapela, C. W., Baldo, E. G., Casquet, C., & Galindo, C., 2004. K-bentonites in the Argentine Precordillera contemporaneous with rhyolite volcanism in the Famatinian Arc. Journal of the Geological Society, 161(5), 747–756. https://doi.org/10.1144/0016-764903-130

García, M., Gardeweg, M., Clavero, J., & Hérail, G., 2004. Hoja Arica, Región de Tarapacá. Servicio Nacional de Geología y Minería, Carta Geológica de Chile, Serie Geología Básica (Issue 84).

García, M., Herail, G., & Charrier, R., 1996. The cenozoic forearc evolution in northern Chile: The western border of the altiplano of Belen (Chile). 3rd International Symposium on Andean Geodynamics, 359–362.

García-Ramírez, C. A., Rey León, V., & Valencia, V. A., 2017. Ortoneises en la Franja Silos-Babega, Macizo de Santander, Colombia: evidencias de la orogenia famatiniana en los Andes del norte. Andean Geology, 44(3), 307–327. https://doi.org/10.5027/andgeoV44n3-a04

Gerdes, A., & Zeh, A., 2009. Zircon formation versus zircon alteration — New insights from combined U–Pb and Lu–Hf in-situ LA-ICP-MS analyses, and consequences for the interpretation of Archean zircon from the Central Zone of the Limpopo Belt. Chemical Geology, 261(3–4), 230–243. https://doi.org/10.1016/j.chemgeo.2008.03.005

Gerdes, A., & Zeh, A., 2006. Combined U–Pb and Hf isotope LA-(MC-)ICP-MS analyses of detrital zircons: Comparison with SHRIMP and new constraints for the provenance and age of an Armorican metasediment in Central Germany. Earth and Planetary Science Letters, 249(1–2), 47–61. https://doi.org/10.1016/j.epsl.2006.06.039

Haller, M. A., & Ramos, V. A., 1984. Las ofilotas famatinianas de las provincias de San Juan y Mendoza. 9° Congreso Geológico Argentino, 66–83.

Hauser, N., Matteini, M., Omarini, R. H., & Pimentel, M. M., 2011. Combined U–Pb and Lu–Hf isotope data on turbidites of the Paleozoic basement of NW Argentina and petrology of associated igneous rocks: Implications for the tectonic evolution of western Gondwana between 560 and 460 Ma. Gondwana Research, 19(1), 100–127. https://doi.org/10.1016/j.gr.2010.04.002

Jackson, S. E., Pearson, N. J., Griffin, W. L., & Belousova, E. A., 2004. The application of laser ablation-inductively coupled plasma-mass spectrometry to in situ U–Pb zircon geochronology. Chemical Geology, 211(1–2), 47–69. https://doi.org/10.1016/j.chemgeo.2004.06.017

Jiang, Y. D., K. Schulmann, M. Sun, P. Štípská, A. Guy, V. Janoušek, O. Lexa, and C. Yuan, 2016. Anatexis of accretionary wedge, Pacific - type magmatism, and formation of vertically stratified continental crust in the Altai Orogenic Belt, Tectonics, 35, 3095–3118, doi:10.1002/2016TC004271.

Kumar, S., 2020. Schedule of Mafic to Hybrid Magma Injections Into Crystallizing Felsic Magma Chambers and Resultant Geometry of Enclaves in Granites: New Field and Petrographic Observations From Ladakh Batholith, Trans-Himalaya, India. Frontiers in Earth Science, 8, 551097. https://doi.org/10.3389/feart.2020.551097

Larrovere, M. A., de los Hoyos, C. R., Willner, A. P., Verdecchia, S. O., Baldo, E. G., Casquet, C., Basei, M. A., Hollanda, M. H., Rocher, S., Alasino, P. H., & Moreno, G. G., 2019. Mid-crustal deformation in a continental margin orogen: structural evolution and timing of the Famatinian Orogeny, NW Argentina. Journal of the Geological Society, 177(2), 233–257. https://doi.org/10.1144/jgs2018-230

Loewy, S. L., Connelly, J. N., & Dalziel, I. W. D., 2004. An orphaned basement block: The Arequipa-Antofalla Basement of the central Andean margin of South America. Geological Society of America Bulletin, 116(1–2), 171–187. https://doi.org/10.1130/B25226.1

Lucassen, F., Becchio, R., Wilke, H. G., Franz, G., Thirlwall, M. F., Viramonte, J., & Wemmer, K., 2000. Proterozoic–Paleozoic development of the basement of the Central Andes (18–26°S) — a mobile belt of the South American craton. Journal of South American Earth Sciences, 13(8), 697–715. https://doi.org/10.1016/S0895-9811(00)00057-2

Ludwig, K. R., 2012. Isoplot 3.75. A Geochronological Toolkit for Microsoft Excel. In Berkeley Geochronology Center, Special Publication (Vol. 5, p. 75).

Martin, E. L., Collins, W. J., & Spencer, C. J. 2020. Laurentian origin of the Cuyania suspect terrane, western Argentina, confirmed by Hf isotopes in zircon. GSA Bulletin, 132(1–2), 273–290. https://doi.org/10.1130/B35150.1

Matteini, M., Junges, S. L., Dantas, E. L., Pimentel, M. M., & Bühn, B., 2010. In situ zircon U–Pb and Lu–Hf isotope systematic on magmatic rocks: Insights on the crustal evolution of the Neoproterozoic Goiás Magmatic Arc, Brasília belt, Central Brazil. Gondwana Research, 17(1), 1–12. https://doi.org/10.1016/j.gr.2009.05.008

Mišković, A., Spikings, R. A., Chew, D. M., Košler, J., Ulianov, A., & Schaltegger, U., 2009. Tectonomagmatic evolution of Western Amazonia: Geochemical characterization and zircon U-Pb geochronologic constraints from the Peruvian Eastern Cordilleran granitoids. Geological Society of America Bulletin, 121(9–10), 1298–1324. https://doi.org/10.1130/B26488.1

Montecinos, P., 1963. Observaciones de Geología en el Cuadrángulo de Campanani, Departamento de Arica, Provincia de Tarapacá. Universidad de Chile. 109.

Morel, M. L. A., Nebel, O., Nebel-Jacobsen, Y. J., Miller, J. S., & Vroon, P. Z. 2008. Hafnium isotope characterization of the GJ-1 zircon reference material by solution and laser-ablation MC-ICPMS. Chemical Geology, 255(1–2), 231–235. https://doi.org/10.1016/j.chemgeo.2008.06.040

Nebel, O., Nebel-Jacobsen, Y., Mezger, K., & Berndt, J., 2007. Initial Hf isotope compositions in magmatic zircon from early Proterozoic rocks from the Gawler Craton, Australia: A test for zircon model ages. Chemical Geology, 241(1–2), 23–37. https://doi.org/10.1016/j.chemgeo.2007.02.008

Niemeyer, H., Meffre, S., & Guerrero, R., 2014. Zircon U–Pb geochronology of granitic rocks of the Cordón de Lila and Sierra de Almeida ranges, northern Chile: 30 m.y. of Ordovician plutonism on the western border of Gondwana. Journal of South American Earth Sciences, 56, 228–241. https://doi.org/10.1016/j.jsames.2014.09.011

Oliveira, F. V., 2016. Chronus: Um novo suplemento para a redução de dados U-Pb obtidos por LA-MC-ICPMS.

Ortiz, A., Hauser, N., Becchio, R., Suzaño, N., Nieves, A., Sola, A., Pimentel, M., & Reimold, W., 2017. Zircon U-Pb ages and Hf isotopes for the Diablillos Intrusive Complex, Southern Puna, Argentina: Crustal evolution of the Lower Paleozoic Orogen, Southwestern Gondwana margin. Journal of South American Earth Sciences, 80, 316–339. https://doi.org/10.1016/j.jsames.2017.09.031

Ortiz, A., Quiroga, M., Becchio, R., Hauser, N., & Monteros, E., 2019. The Lower Paleozoic Plutonic-Volcanic connection in the Eastern Magmatic Belt, SW Gondwana, northern Puna Argentina. Journal of South American Earth Sciences, 95, 102306. https://doi.org/10.1016/j.jsames.2019.102306

Ortiz, A., Suzaño, N., Hauser, N., Becchio, R., & Nieves, A., 2019. New hints on the evolution of the Eastern Magmatic Belt, Puna Argentina. SW Gondwana margin: Zircon U-Pb ages and Hf isotopes in the Pachamama Igneous-Metamorphic Complex. Journal of South American Earth Sciences, 94, 102246. https://doi.org/10.1016/j.jsames.2019.102246

Otamendi, J. E., Cristofolini, E. A., Morosini, A., Armas, P., Tibaldi, A. M., & Camilletti, G. C., 2020. The geodynamic history of the Famatinian arc, Argentina: A record of exposed geology over the type section (latitudes 27°- 33° south). Journal of South American Earth Sciences, 100, 102558. https://doi.org/10.1016/j.jsames.2020.102558

Pacci, D., Hervé, F., Munizaga, F., Kawashita, K., & Cordani, U., 1980. Acerca de la edad Rb-Sr Precámbrica de rocas de la Formación Esquistos de Belén, Departamento de Parinacota, Chile. Revista Geológica de Chile, 11, 43–50.

Pankhurst, R. J., Rapela, C. W., & Fanning, C. M., 2000. Age and origin of coeval TTG, I- and S-type granites in the Famatinian belt of NW Argentina. Earth and Environmental Science

Transactions of the Royal Society of Edinburgh, 91(1–2), 151–168. https://doi.org/10.1017/S0263593300007343

Pankhurst, R. J., Leat, P. T., Sruoga, P., Rapela, C. W., Márquez, M., Storey, B. C., & Riley, T. R., 1998. The Chon Aike province of Patagonia and related rocks in West Antarctica: A silicic large igneous province. Journal of Volcanology and Geothermal Research, 81(1–2), 113–136. https://doi.org/10.1016/S0377-0273(97)00070-X

Pankhurst, R. J., Rapela, C. W., Fanning, C. M., & Márquez, M., 2006. Gondwanide continental collision and the origin of Patagonia. Earth-Science Reviews, 76(3–4), 235–257. https://doi.org/10.1016/j.earscirev.2006.02.001

Pankhurst, R. J., Hervé, F., Fanning, C. M., Calderón, M., Niemeyer, H., Griem-Klee, S., & Soto, F., 2016. The pre-Mesozoic rocks of northern Chile: U–Pb ages, and Hf and O isotopes. Earth-Science Reviews, 152, 88–105. https://doi.org/10.1016/j.earscirev.2015.11.009

Patchett, P. J., 1983. Importance of the Lu-Hf isotopic system in studies of planetary chronology and chemical evolution. Geochimica et Cosmochimica Acta, 47(1), 81–91. https://doi.org/10.1016/0016-7037(83)90092-3

Quenardelle, S. M., & Ramos, V. A., 1999. Ordovician western Sierras Pampeanas magmatic belt: Record of Precordillera accretion in Argentina. In V. A. Ramos & J. D. Keppie (Eds.), Laurentia-Gondwana connections before Pangea (Vol. 336, pp. 63–86). Geological Society of America. https://doi.org/10.1130/0-8137-2336-1.63

Ramos, V. A., 2008. The Basement of the Central Andes: The Arequipa and Related Terranes. Annual Review of Earth and Planetary Sciences, 36(1), 289–324. https://doi.org/10.1146/annurev.earth.36.031207.124304

Ramos, V. A., 1999. Rasgos estructurales del territorio argentino. In R. Caminos (Ed.), Geología Argentina (Vol. 29, Issue 24, pp. 715–784). Instituto de Geología y Recursos Minerales.

Ramos, V.A., 2018. The Famatinian Orogen Along the Protomargin of Western Gondwana: Evidence for a Nearly Continuous Ordovician Magmatic Arc Between Venezuela and Argentina. In: , et al. The Evolution of the Chilean-Argentinean Andes. Springer Earth System Sciences. Springer, Cham. https://doi.org/10.1007/978-3-319-67774-3_6

Rapalini, A. E., 2005. The accretionary history of southern South America from the latest Proterozoic to the Late Palaeozoic: some palaeomagnetic constraints. Geological Society, London, Special Publications, 246(1), 305–328. https://doi.org/10.1144/GSL.SP.2005.246.01.12

Rapela, C. W., Pankhurst, R. J., Casquet, C., Fanning, C. M., Baldo, E. G., González-Casado, J. M., Galindo, C., & Dahlquist, J., 2007. The Río de la Plata craton and the assembly of SW Gondwana. Earth-Science Reviews, 83(1–2), 49–82. https://doi.org/10.1016/j.earscirev.2007.03.004

Rapela, C. W., Pankhurst, R. J., Casquet, C., Dahlquist, J. A., Fanning, C. M., Baldo, E. G., Galindo, C., Alasino, P. H., Ramacciotti, C. D., Verdecchia, S. O., Murra, J. A., & Basei, M. A. S., 2018. A review of the Famatinian Ordovician magmatism in southern South America: evidence of lithosphere reworking and continental subduction in the early proto-Andean margin of Gondwana. Earth-Science Reviews, 187, 259–285. https://doi.org/10.1016/j.earscirev.2018.10.006

Rapela, C. W., Verdecchia, S. O., Casquet, C., Pankhurst, R. J., Baldo, E. G., Galindo, C., Murra, J. A., Dahlquist, J. A., & Fanning, C. M., 2016. Identifying Laurentian and SW Gondwana sources in the Neoproterozoic to Early Paleozoic metasedimentary rocks of the Sierras Pampeanas: Paleogeographic and tectonic implications. Gondwana Research, 32, 193–212. https://doi.org/10.1016/j.gr.2015.02.010

Reitsma, M. J. 2012. Reconstructing the Late Paleozoic: Early Mesozoic plutonic and sedimentary record of south-east Peru: Orphaned back-arcs along the western margin of Gondwana [University of Geneva]. https://doi.org/10.13097/archive-ouverte/unige:23095

Romero, D., Valencia, K., Alarcón, P., Peña, D., & Ramos, V. A., 2013. The offshore basement of Perú: Evidence for different igneous and metamorphic domains in the forearc. Journal of South American Earth Sciences, 42, 47–60. https://doi.org/10.1016/j.jsames.2012.11.003

Saavedra, J., Toselli, A., Rossi, J., Pellitero, E., & Durand, F., 1998. The Early Palaeozoic magmatic record of the Famatina System: a review. Geological Society, London, Special Publications, 142(1), 283–295. https://doi.org/10.1144/GSL.SP.1998.142.01.14

Salas, R. O., Kast, R. F., Montecinos, F. P., & Salas, I. Y., 1966. Geología y recursos minerales del departamento de Arica. Provincia de Tarapa. Instituto de Investigaciones Geológicas Chile, 21, 114.

Sato, A. M., & González, P. D., 2003. Evolución del orógeno Famatiniano en la Sierra de San Luis: magmatismo de arco, deformación y metamorfismo de bajo a alto grado. Revista de La Asociación Geológica Argentina, 58(4), 487–504.

Scherer, H. H., Snow, C. A., & Ernst, W. G., 2006. Geologic-petrochemical comparison of early Mesozoic mafic arc terranes: Western Paleozoic and Triassic belt, Klamath Mountains, and Jura–Triassic arc belt, Sierran Foothills. In A. W. Snoke & C. G. Barnes (Eds.), Geological Studies in the Klamath Mountains Province, California and Oregon: A volume in honor of William P. Irwin (Vol. 410, Issue 18, pp. 377–392). Geological Society of America. https://doi.org/10.1130/2006.2410(18)

Stern, R. J., & Bloomer, S. H., 1992. Subduction zone infancy: Examples from the Eocene Izu-Bonin-Mariana and Jurassic California arcs. Geological Society of America Bulletin, 104(12), 1621–1636. https://doi.org/10.1130/0016-7606(1992)104<1621:SZIEFT>2.3.CO;2

Taylor, S., & McLennan, S., 1985. The Continental Crust: Its Composition and Evolution: An Examination of the Geochemical Record Preserved in Sedimentary Rocks. Taylor, S.R., McLennan, S.M., 312.

Tosdal, R. M., 1996. The Amazon-Laurentian connection as viewed from the Middle Proterozoic rocks in the central Andes, western Bolivia and northern Chile. Tectonics, 15(4), 827–842. https://doi.org/10.1029/95TC03248

Van der Lelij, R., Spikings, R., Ulianov, A., Chiaradia, M., & Mora, A., 2016. Palaeozoic to Early Jurassic history of the northwestern corner of Gondwana, and implications for the evolution of the Iapetus, Rheic and Pacific Oceans. Gondwana Research, 31, 271–294. https://doi.org/10.1016/j.gr.2015.01.011

Varela, R., Basei, M. A. S., González, P. D., Sato, A. M., Naipauer, M., Campos Neto, M., Cingolani, C. A., & Meira, V. T., 2011. Accretion of Grenvillian terranes to the southwestern border of the Río de la Plata craton, western Argentina. International Journal of Earth Sciences, 100(2–3), 243–272. https://doi.org/10.1007/s00531-010-0614-2

Wedepohl, H. K., 1995. The composition of the continental crust. Geochimica et Cosmochimica Acta, 59(7), 1217–1232. https://doi.org/10.1016/0016-7037(95)00038-2

Wiedenbeck, M., Allé, P., Corfu, F., Griffin, W. L., Meier, M., Oberli, F., von Quadt, A., Roddick, J. C., & Spiegel, W., 1995. Three natural zircon standards for U-Th-Pb, Lu-Hf, trace elements and REE analyses. Geostandards Newsletter, 19(1), 1–23. https://doi.org/10.1111/j.1751-908X.1995.tb00147.x

Wiedenbeck, M., Hanchar, J. M., Peck, W. H., Sylvester, P., Valley, J., Whitehouse, M., Kronz, A., Morishita, Y., Nasdala, L., Fiebig, J., Franchi, I., Girard, J.-P., Greenwood, R. C., Hinton, R., Kita, N., Mason, P. R. D., Norman, M., Ogasawara, M., Piccoli, P. M., Zheng, Y.-F., 2004. Further Characterization of the 91500 Zircon Crystal. Geostandards and Geoanalytical Research, 28(1), 9–39. https://doi.org/10.1111/j.1751-908X.2004.tb01041.x

Wörner, G., Lezaun, J., Beck, A., Heber, V., Lucassen, F., Zinngrebe, E., Rössling, R., & Wilke, H., 2000. Precambrian and Early Paleozoic evolution of the Andean basement at Belen (northern Chile) and Cerro Uyarani (western Bolivia Altiplano). Journal of South American Earth Sciences, 13(8), 717–737. https://doi.org/10.1016/S0895-9811(00)00056-0

Zentilli, M., Salas-Olivares, R. A., & Graves, M. C., 2018. A unique Sn-bearing Bi-Ag-Sb, polymetallic, epithermal district in the Chilean Andes: Capitana Mine, Tignamar, Arica-relation to the Proterozoic-Paleozoic Belén Metamorphic Complex. XV Congreso Geológico Chileno.

3.9 SUPPLEMENTARY MATERIAL

Supplementary Table 01: Results of U-Pb isotope analysis by LA-ICP-MS on zircon from orthogneiss, orthoschist and amphibolite samples of BMC.

					Radiogenic ratios					Apparent Ages (Ma)						
Spots	Th/U	^{206}Pb mV[1]	^{207}Pb/^{206}Pb	1σ %	^{207}Pb/^{235}U	1σ %	^{206}Pb/^{238}U	1σ %	Rho	^{207}Pb/^{206}Pb	2σ abs	^{207}Pb/^{235}U	2σ abs	^{206}Pb/^{238}U	2σ abs	Conc (%)
Group 1: Quartz monzodiorite - sample BE16																
ZR22	0.48	0.0014	0.06	0.8	0.61	1.3	0.08	0.9	0.71	490	35	483	10	481	8	98
ZR1	1.05	0.0054	0.06	0.5	0.60	0.9	0.08	0.6	0.71	466	22	476	7	478	6	102
ZR18	0.66	0.0016	0.06	0.8	0.60	1.3	0.08	0.9	0.72	477	35	474	10	474	8	99
ZR2	0.83	0.0044	0.06	4.0	0.59	4.1	0.08	0.7	0.17	473	173	473	31	473	6	100
ZR10	0.72	0.0030	0.06	0.6	0.59	1.0	0.08	0.7	0.70	467	27	471	8	472	6	101
ZR21	0.99	0.0036	0.06	0.8	0.62	1.1	0.08	0.6	0.55	590	36	492	9	471	5	80
ZR13	1.21	0.0047	0.06	0.5	0.59	0.8	0.08	0.5	0.65	470	22	471	6	471	5	100
ZR11	1.00	0.0048	0.06	0.6	0.59	1.0	0.08	0.8	0.73	491	27	473	8	469	7	95
ZR30	1.14	0.0037	0.06	0.5	0.60	1.0	0.08	0.8	0.80	501	22	474	8	469	7	94
ZR7	0.61	0.0018	0.06	0.7	0.58	1.2	0.08	0.8	0.72	461	32	467	9	469	8	102
ZR19	1.04	0.0060	0.06	0.4	0.60	0.8	0.08	0.5	0.69	514	18	476	6	468	5	91
ZR9	0.90	0.0032	0.06	3.2	0.59	3.4	0.08	0.9	0.26	497	139	473	25	468	8	94
ZR14	0.86	0.0039	0.06	1.2	0.60	1.5	0.07	0.8	0.51	529	54	476	11	465	7	88
ZR20	0.65	0.0040	0.06	0.6	0.59	1.0	0.07	0.7	0.69	491	27	468	8	464	6	94
ZR5	1.04	0.0041	0.06	0.5	0.59	1.0	0.07	0.7	0.76	489	22	468	7	463	7	95
ZR15C	0.63	0.0036	0.06	0.6	0.60	0.9	0.07	0.6	0.68	534	25	475	7	462	6	87
ZR29	1.28	0.0090	0.06	0.3	0.59	0.9	0.07	0.7	0.81	500	15	468	6	462	6	92
ZR8	0.62	0.0046	0.06	0.5	0.58	0.8	0.07	0.5	0.65	483	21	465	6	461	5	95
ZR27	0.85	0.0026	0.06	0.6	0.58	0.9	0.07	0.6	0.68	479	25	463	7	460	6	96
ZR25	0.94	0.0047	0.06	0.7	0.59	1.0	0.07	0.6	0.58	519	32	469	8	459	5	88
ZR24	1.06	0.0046	0.12	29.4	1.40	29.9	0.08	5.4	0.18	2014	892	889	326	508	52	25
ZR3	0.82	0.0026	0.06	0.7	0.64	1.2	0.08	0.9	0.74	587	31	503	10	485	8	83
ZR4	0.68	0.0026	0.05	2.4	0.52	2.6	0.07	0.7	0.26	224	111	426	18	465	6	207
ZR12	1.02	0.0035	0.05	3.6	0.54	3.7	0.07	0.7	0.19	298	160	436	26	462	6	155
ZR6	0.68	0.0030	0.06	0.6	0.58	1.0	0.07	0.7	0.68	485	27	463	7	458	6	94

ZR16	0.66	0.0025	0.06	0.8	0.56	1.2	0.07	0.9	0.72	467	33	455	9	452	8	97
ZR15R	0.39	0.0012	0.06	1.1	0.58	1.6	0.07	1.1	0.69	509	47	461	12	452	9	89
ZR28	0.78	0.0021	0.06	0.6	0.56	1.2	0.07	1.0	0.82	476	24	451	9	446	8	94
ZR23	0.84	0.0023	0.06	1.3	0.55	1.5	0.07	0.8	0.52	445	55	445	11	445	7	100
ZR17	0.79	0.0032	0.06	0.6	0.56	1.6	0.07	1.4	0.89	499	27	452	11	443	12	89

					Radiogenic ratios					Apparent Ages (Ma)						
Spots	Th/U	^{206}Pb mV[1]	^{207}Pb/^{206}Pb	1σ %	^{207}Pb/^{235}U	1σ %	^{206}Pb/^{238}U	1σ %	Rho	^{207}Pb/^{206}Pb	2σ abs	^{207}Pb/^{235}U	2σ abs	^{206}Pb/^{238}U	2σ abs	Conc (%)
Group 1: Amphibole gneiss - sample BE3C																
ZR30	0.16	0.0100	0.12	0.6	5.83	2.3	0.35	2.2	0.95	1952	22	1951	39	1951	73	100
ZR13	0.82	0.0035	0.06	0.8	0.63	1.6	0.08	1.3	0.82	480	37	496	12	499	13	104
ZR26	0.75	0.0028	0.06	1.1	0.63	1.9	0.08	1.4	0.77	485	50	494	15	496	14	102
ZR9	0.43	0.0021	0.06	0.8	0.62	1.3	0.08	0.9	0.74	485	33	487	10	488	9	101
ZR29	0.58	0.0029	0.06	0.9	0.61	1.5	0.08	1.1	0.76	480	38	486	11	487	10	102
ZR16	0.78	0.0024	0.06	0.9	0.61	1.6	0.08	1.2	0.78	462	41	483	12	487	12	105
ZR6	0.53	0.0031	0.06	0.8	0.61	1.5	0.08	1.1	0.77	471	37	484	11	487	11	103
ZR5C	0.64	0.0018	0.06	1.3	0.61	2.0	0.08	1.4	0.72	486	58	486	15	486	13	100
ZR7	0.32	0.0025	0.06	1.0	0.61	1.6	0.08	1.2	0.75	484	44	484	12	484	11	100
ZR23	0.69	0.0029	0.06	0.9	0.61	1.3	0.08	0.9	0.71	469	38	481	10	483	9	103
ZR22	0.58	0.0027	0.06	0.8	0.60	1.3	0.08	0.9	0.73	460	35	479	10	483	9	105
ZR18	0.72	0.0024	0.06	0.8	0.60	1.3	0.08	0.9	0.71	472	36	479	10	480	8	102
ZR12	0.43	0.0018	0.06	1.1	0.60	1.7	0.08	1.2	0.72	460	48	475	13	478	11	104
ZR19	0.54	0.0017	0.06	1.1	0.60	1.7	0.08	1.3	0.75	497	47	479	13	476	12	96
ZR28	0.51	0.0024	0.06	1.5	0.58	1.9	0.08	1.1	0.57	433	66	466	14	473	10	109
ZR4C	0.52	0.0008	0.06	1.9	0.60	2.8	0.08	2.1	0.73	493	83	475	21	471	19	96
ZR27	0.61	0.0010	0.06	1.7	0.60	2.4	0.08	1.7	0.71	517	73	478	19	471	16	91
ZR8	0.58	0.0029	0.06	1.0	0.59	1.6	0.08	1.2	0.75	479	44	471	12	470	11	98
ZR10	0.70	0.0021	0.06	0.8	0.60	1.5	0.08	1.2	0.80	504	35	475	11	468	11	93
ZR11	0.73	0.0007	0.06	2.2	0.59	3.1	0.07	2.2	0.70	518	95	473	24	464	20	90
ZR15	*0.92*	*0.0012*	*0.06*	*1.8*	*0.59*	*2.4*	*0.08*	*1.6*	*0.64*	*430*	*81*	*473*	*18*	*482*	*15*	*112*
ZR24	*0.77*	*0.0018*	*0.06*	*2.5*	*0.68*	*2.8*	*0.08*	*1.2*	*0.44*	*726*	*105*	*527*	*23*	*482*	*11*	*66*
ZR5R	*0.75*	*0.0033*	*0.06*	*1.2*	*0.62*	*1.8*	*0.08*	*1.3*	*0.70*	*538*	*54*	*488*	*14*	*477*	*12*	*89*
ZR4R	*0.60*	*0.0012*	*0.05*	*3.3*	*0.57*	*4.0*	*0.08*	*2.2*	*0.56*	*387*	*147*	*461*	*30*	*476*	*21*	*123*
ZR20	*0.51*	*0.0037*	*0.06*	*0.6*	*0.61*	*1.1*	*0.08*	*0.8*	*0.72*	*532*	*28*	*483*	*8*	*473*	*7*	*89*

ZR17	*0.61*	*0.0023*	*0.06*	*1.0*	*0.59*	*1.6*	*0.07*	*1.3*	*0.78*	*512*	*42*	*470*	*12*	*462*	*11*	*90*
ZR21	*0.53*	*0.0018*	*0.06*	*0.9*	*0.58*	*1.4*	*0.07*	*1.0*	*0.72*	*471*	*40*	*463*	*11*	*461*	*9*	*98*
ZR3	*0.39*	*0.0023*	*0.06*	*1.0*	*0.58*	*1.6*	*0.07*	*1.1*	*0.72*	*483*	*45*	*462*	*12*	*458*	*10*	*95*
ZR14	*0.63*	*0.0010*	*0.06*	*1.7*	*0.59*	*2.4*	*0.07*	*1.7*	*0.71*	*523*	*72*	*468*	*18*	*457*	*15*	*87*
ZR25	*0.51*	*0.0009*	*0.06*	*2.3*	*0.60*	*3.3*	*0.07*	*2.4*	*0.71*	*578*	*98*	*475*	*25*	*454*	*21*	*79*
ZR1R	*0.54*	*0.0024*	*0.06*	*1.1*	*0.57*	*1.9*	*0.07*	*1.5*	*0.79*	*470*	*50*	*455*	*14*	*452*	*13*	*96*
ZR2	*0.53*	*0.0027*	*0.06*	*0.7*	*0.56*	*1.2*	*0.07*	*1.0*	*0.79*	*462*	*29*	*449*	*9*	*446*	*8*	*97*
ZR1C	*0.85*	*0.0039*	*0.06*	*0.9*	*0.55*	*1.5*	*0.07*	*1.0*	*0.71*	*452*	*42*	*444*	*10*	*443*	*9*	*98*

					Radiogenic ratios					Apparent Ages (Ma)						
Spots	Th/U	^{206}Pb mV[1]	^{207}Pb/^{206}Pb	1σ %	^{207}Pb/^{235}U	1σ %	^{206}Pb/^{238}U	1σ %	Rho	^{207}Pb/^{206}Pb	2σ abs	^{207}Pb/^{235}U	2σ abs	^{206}Pb/^{238}U	2σ abs	Conc (%)
Group 1: Amphibole gneiss - sample BE14																
ZR16	0.87	0.0043	0.06	1.2	0.59	1.5	0.08	0.8	0.56	470	51	472	11	472	7	101
ZR30	0.88	0.0032	0.06	1.4	0.59	1.7	0.08	0.8	0.48	445	64	468	13	472	7	106
ZR20	1.04	0.0027	0.06	1.0	0.60	1.3	0.08	0.8	0.60	495	44	476	10	472	7	95
ZR15	0.69	0.0023	0.06	1.2	0.59	1.6	0.08	1.0	0.63	466	51	470	12	471	9	101
ZR1	0.68	0.0020	0.06	0.9	0.59	1.3	0.08	0.9	0.65	462	42	469	10	471	8	102
ZR12	0.81	0.0023	0.06	0.8	0.59	1.3	0.08	0.9	0.71	491	36	471	10	467	8	95
ZR21	0.69	0.0038	0.06	0.8	0.59	1.0	0.07	0.6	0.56	490	35	470	8	466	5	95
ZR10	0.75	0.0045	0.06	0.6	0.58	1.1	0.07	0.8	0.76	480	26	467	8	465	7	97
ZR23	1.29	0.0057	0.06	1.1	0.59	1.3	0.07	0.6	0.50	487	47	468	10	464	6	95
ZR26	1.22	0.0052	0.06	1.0	0.58	1.2	0.07	0.5	0.46	458	43	462	9	462	5	101
ZR13	0.71	0.0031	0.06	0.8	0.58	1.3	0.07	1.0	0.73	476	36	462	10	459	8	97
ZR19	1.03	0.0031	0.06	0.8	0.57	1.2	0.07	0.7	0.61	472	37	460	9	457	6	97
ZR29	0.77	0.0038	0.06	1.0	0.57	1.3	0.07	0.6	0.47	456	46	456	9	456	5	100
ZR4	0.72	0.0026	0.06	1.1	0.56	1.5	0.07	0.9	0.60	430	50	452	11	456	8	106
ZR5	0.82	0.0042	0.06	0.6	0.57	1.3	0.07	1.1	0.84	460	25	455	9	454	9	99
ZR3	*0.59*	*0.0023*	*0.05*	*1.6*	*0.57*	*2.2*	*0.08*	*1.5*	*0.67*	*358*	*72*	*460*	*16*	*480*	*14*	*134*
ZR22	*0.19*	*0.0036*	*0.06*	*1.0*	*0.62*	*1.4*	*0.08*	*1.0*	*0.70*	*535*	*42*	*489*	*11*	*479*	*9*	*89*
ZR17	*0.73*	*0.0064*	*0.06*	*0.8*	*0.60*	*1.1*	*0.08*	*0.7*	*0.59*	*514*	*37*	*478*	*9*	*471*	*6*	*92*
ZR25	*0.86*	*0.0036*	*0.06*	*1.5*	*0.60*	*1.7*	*0.08*	*0.7*	*0.43*	*506*	*64*	*475*	*13*	*468*	*7*	*93*
ZR18	*0.69*	*0.0049*	*0.06*	*0.8*	*0.59*	*1.1*	*0.07*	*0.7*	*0.59*	*499*	*36*	*471*	*8*	*466*	*6*	*93*
ZR14	*0.78*	*0.0019*	*0.06*	*1.1*	*0.58*	*1.5*	*0.07*	*1.0*	*0.65*	*490*	*47*	*467*	*11*	*462*	*9*	*94*
ZR27	*0.67*	*0.0018*	*0.06*	*1.2*	*0.58*	*1.8*	*0.07*	*1.3*	*0.70*	*487*	*55*	*464*	*14*	*459*	*11*	*94*

ZR9	*0.47*	*0.0037*	*0.06*	*0.8*	*0.58*	*1.2*	*0.07*	*0.8*	*0.69*	*507*	*35*	*466*	*9*	*458*	*7*	*90*
ZR11	*1.00*	*0.0049*	*0.06*	*0.6*	*0.60*	*1.2*	*0.07*	*0.9*	*0.78*	*570*	*28*	*476*	*9*	*457*	*8*	*80*
ZR7	*0.71*	*0.0016*	*0.06*	*1.2*	*0.61*	*1.6*	*0.07*	*1.0*	*0.63*	*615*	*52*	*483*	*13*	*456*	*9*	*74*
ZR8	*0.90*	*0.0024*	*0.06*	*1.3*	*0.57*	*1.9*	*0.07*	*1.4*	*0.73*	*497*	*55*	*461*	*14*	*454*	*12*	*91*
ZR2	*0.78*	*0.0022*	*0.05*	*2.8*	*0.54*	*3.1*	*0.07*	*1.4*	*0.44*	*338*	*124*	*435*	*22*	*454*	*12*	*134*
ZR28	*0.67*	*0.0018*	*0.06*	*2.1*	*0.56*	*2.4*	*0.07*	*1.2*	*0.49*	*467*	*90*	*450*	*17*	*447*	*10*	*96*
ZR24	*0.71*	*0.0031*	*0.06*	*1.1*	*0.56*	*1.5*	*0.07*	*0.9*	*0.59*	*484*	*49*	*453*	*11*	*446*	*7*	*92*
ZR6	*0.72*	*0.0046*	*0.06*	*1.1*	*0.56*	*2.0*	*0.07*	*1.6*	*0.83*	*505*	*46*	*451*	*14*	*440*	*14*	*87*

					Radiogenic ratios					Apparent Ages (Ma)						
Spots	Th/U	^{206}Pb mV[1]	^{207}Pb/^{206}Pb	1σ %	^{207}Pb/^{235}U	1σ %	^{206}Pb/^{238}U	1σ %	Rho	^{207}Pb/^{206}Pb	2σ abs	^{207}Pb/^{235}U	2σ abs	^{206}Pb/^{238}U	2σ abs	Conc (%)
Group 2: Muscovite biotite gneiss - sample BE58																
ZR11	0.70	0.0013	0.06	1.1	0.59	1.6	0.08	1.1	0.68	441	49	470	12	476	10	108
ZR27C	1.22	0.0044	0.06	0.5	0.60	1.0	0.08	0.9	0.82	478	21	476	8	476	8	100
ZR14	0.56	0.0008	0.06	0.9	0.59	1.5	0.08	1.1	0.73	440	41	468	11	474	10	108
ZR1	1.01	0.0031	0.06	0.9	0.59	1.4	0.08	1.1	0.76	477	38	474	11	473	10	99
ZR21C	0.54	0.0020	0.06	0.8	0.59	1.4	0.08	1.1	0.78	463	35	470	10	471	10	102
ZR29	0.52	0.0021	0.06	0.9	0.58	1.4	0.08	1.0	0.71	429	41	464	11	471	9	110
ZR9	0.72	0.0006	0.06	1.3	0.58	1.9	0.08	1.4	0.73	441	55	465	14	470	13	107
ZR24	0.70	0.0029	0.06	0.5	0.59	1.0	0.08	0.8	0.77	463	24	469	8	470	7	101
ZR4	0.64	0.0014	0.06	0.9	0.59	1.3	0.08	0.9	0.68	467	40	469	10	470	8	101
ZR8	0.84	0.0018	0.06	0.6	0.58	1.0	0.08	0.7	0.70	446	28	465	8	469	6	105
ZR26	0.70	0.0012	0.06	1.2	0.58	1.5	0.08	1.0	0.623	450	51	465	11	468	9	104
ZR28	0.51	0.0027	0.06	0.5	0.58	0.9	0.08	0.6	0.707	464	23	467	7	467	6	101
ZR15	0.80	0.0009	0.06	1.7	0.58	2.3	0.08	1.5	0.664	442	73	463	17	467	14	106
ZR19	0.70	0.0016	0.06	0.7	0.59	1.1	0.08	0.7	0.643	475	32	468	8	467	6	98
ZR2	0.83	0.0022	0.06	0.8	0.58	1.5	0.07	1.2	0.804	458	37	464	11	465	11	102
ZR25	0.52	0.0023	0.06	1.1	0.57	1.8	0.07	1.4	0.785	444	47	461	13	465	13	105
ZR22	0.77	0.0015	0.06	1.1	0.59	1.5	0.07	0.9	0.618	516	49	473	11	464	8	90
ZR6	0.61	0.0025	0.06	0.6	0.58	1.1	0.07	0.8	0.713	472	28	464	8	463	7	98
ZR20	0.66	0.0015	0.06	1.1	0.58	1.4	0.07	0.9	0.628	472	46	462	11	460	8	97
ZR12	1.26	0.0024	0.06	1.1	0.58	1.7	0.07	1.3	0.745	502	48	465	13	457	11	91
ZR7	0.63	0.0024	0.06	0.6	0.57	1.1	0.07	0.8	0.77	468	25	459	8	457	7	98

ZR27R	0.57	0.0021	0.06	0.7	0.62	1.1	0.08	0.8	0.686	485	31	490	9	492	7	101
ZR17	0.50	0.0008	0.08	1.9	0.91	2.3	0.08	1.2	0.542	1272	72	655	22	491	12	39
ZR18	0.75	0.0007	0.05	1.7	0.58	2.5	0.08	1.8	0.715	357	76	462	18	483	16	135
ZR30	0.66	0.0011	0.05	2.7	0.56	3.1	0.08	1.4	0.456	319	122	454	23	482	13	151
ZR16	0.55	0.0008	0.06	1.7	0.59	2.3	0.08	1.6	0.686	429	73	469	18	477	15	111
ZR21R	0.64	0.0083	0.06	0.5	0.60	0.9	0.08	0.7	0.766	492	21	477	7	473	7	96
ZR10	0.62	0.0011	0.06	0.9	0.58	1.5	0.08	1.2	0.764	438	41	463	11	468	11	107
ZR3	0.99	0.0025	0.06	0.9	0.59	1.5	0.07	1.2	0.752	557	41	473	12	456	10	82
ZR31C	0.75	0.0047	0.05	3.2	0.54	3.4	0.07	1.1	0.338	340	140	437	24	456	10	134
ZR23R	0.46	0.0025	0.06	0.9	0.59	1.3	0.07	0.8	0.667	547	37	468	9	452	7	83
ZR13	0.66	0.0026	0.06	0.5	0.56	1.0	0.07	0.8	0.776	489	23	454	7	447	7	92
ZR31R	0.57	0.0028	0.06	0.7	0.54	1.4	0.07	1.2	0.842	459	30	437	10	433	10	94
ZR23C	0.34	0.0072	0.06	0.5	0.54	1.3	0.07	1.1	0.881	493	21	436	9	426	9	86
ZR5	0.53	0.0065	0.08	2.3	0.42	8.9	0.04	8.6	0.964	1087	93	356	53	254	43	23

					Radiogenic ratios					Apparent Ages (Ma)						
Spots	Th/U	^{206}Pb mV[1]	$^{207}Pb/^{206}Pb$	1σ %	$^{207}Pb/^{235}U$	1σ %	$^{206}Pb/^{238}U$	1σ %	Rho	$^{207}Pb/^{206}Pb$	2σ abs	$^{207}Pb/^{235}U$	2σ abs	$^{206}Pb/^{238}U$	2σ abs	Conc (%)
Group 2: Biotite muscovite schist - sample BE10Q																
ZR11	1.20	0.0016	0.06	0.934	0.61	1.4	0.08	1.0	0.701	445	41	481	11	489	9	110
ZR22	0.65	0.0030	0.06	0.587	0.61	1.0	0.08	0.7	0.731	492	26	483	8	481	7	98
ZR12	0.80	0.0026	0.06	0.599	0.60	1.0	0.08	0.7	0.711	461	26	475	8	478	7	104
ZR8	0.63	0.0039	0.06	0.595	0.60	1.0	0.08	0.7	0.721	456	26	474	8	478	7	105
ZR9	0.45	0.0019	0.06	0.641	0.59	1.1	0.08	0.8	0.738	456	28	474	8	477	7	105
ZR36	0.84	0.0073	0.06	0.31	0.60	0.9	0.08	0.8	0.849	483	14	478	7	476	7	99
ZR61	0.83	0.0042	0.06	0.478	0.60	1.0	0.08	0.8	0.813	473	21	475	8	476	8	101
ZR89	0.73	0.0054	0.06	0.331	0.60	1.1	0.08	0.9	0.886	481	15	477	8	476	9	99
ZR26	0.71	0.0031	0.06	0.848	0.60	1.2	0.08	0.7	0.61	467	37	474	9	476	7	102
ZR65	0.81	0.0040	0.06	0.531	0.60	1.0	0.08	0.7	0.736	481	23	476	7	475	6	99
ZR90	0.47	0.0036	0.06	0.497	0.60	0.8	0.08	0.6	0.669	479	22	476	6	475	5	99

ZR10	0.41	0.0016	0.06	0.844	0.60	1.3	0.08	0.9	0.699	497	37	479	10	475	8	95
ZR23	0.53	0.0014	0.06	0.817	0.60	1.3	0.08	1.0	0.741	479	36	475	10	474	9	99
ZR35	0.24	0.0073	0.06	0.3	0.59	0.7	0.08	0.5	0.73	469	14	473	5	474	5	101
ZR39	0.53	0.0039	0.06	0.7	0.59	1.0	0.08	0.6	0.61	446	32	469	8	474	6	106
ZR63	0.64	0.0046	0.06	0.4	0.59	0.8	0.08	0.6	0.75	470	16	473	6	473	5	101
ZR2	0.51	0.0016	0.06	1.0	0.59	1.5	0.08	1.0	0.69	453	44	470	11	473	9	104
ZR92	0.49	0.0041	0.06	0.7	0.62	1.0	0.08	0.6	0.62	561	31	488	8	472	6	84
ZR.85	0.99	0.0029	0.06	0.7	0.61	1.1	0.08	0.7	0.67	521	31	481	8	472	7	91
ZR84	0.48	0.0028	0.06	0.7	0.60	1.0	0.08	0.7	0.67	499	29	477	8	472	6	95
ZR31	0.68	0.0034	0.06	0.6	0.59	0.9	0.08	0.6	0.68	468	25	471	7	472	6	101
ZR32	0.69	0.0068	0.06	0.4	0.59	0.7	0.08	0.5	0.70	478	16	473	5	472	5	99
ZR67	0.71	0.0086	0.06	0.3	0.59	0.7	0.08	0.5	0.72	470	14	471	5	471	5	100
ZR7	0.65	0.0029	0.06	0.7	0.59	1.1	0.08	0.7	0.67	458	31	469	8	471	7	103
ZR14	0.85	0.0019	0.06	1.7	0.62	2.1	0.08	1.1	0.54	568	72	487	16	470	10	83
ZR33	0.81	0.0028	0.06	0.6	0.59	1.0	0.08	0.8	0.75	481	25	472	8	470	7	98
ZR60	0.53	0.0031	0.06	0.6	0.59	1.1	0.08	0.8	0.76	466	26	469	8	470	7	101
ZR19	0.51	0.0016	0.06	0.9	0.59	1.3	0.08	0.9	0.69	488	38	473	10	470	8	96
ZR87	0.53	0.0051	0.06	0.5	0.60	0.8	0.08	0.5	0.65	505	22	476	6	470	5	93
ZR50	0.68	0.0044	0.06	0.5	0.59	1.0	0.08	0.8	0.79	470	20	470	7	469	7	100
ZR18	0.52	0.0024	0.06	0.6	0.60	1.0	0.08	0.7	0.68	498	27	474	7	469	6	94
ZR64	0.52	0.0068	0.06	0.3	0.59	0.8	0.08	0.7	0.80	473	14	470	6	469	6	99
ZR40	0.52	0.0068	0.06	0.3	0.59	0.7	0.08	0.5	0.74	478	13	470	5	469	5	98
ZR71	0.48	0.0062	0.06	0.3	0.59	0.7	0.08	0.5	0.72	496	15	473	5	469	5	95
ZR13	0.43	0.0013	0.06	1.1	0.59	1.6	0.08	1.1	0.70	478	46	470	12	468	10	98
ZR15	0.53	0.0024	0.06	0.8	0.59	1.3	0.08	0.9	0.71	480	36	470	10	468	8	98
ZR21	0.71	0.0023	0.06	2.7	0.58	2.9	0.08	1.0	0.34	452	120	465	22	468	9	104
ZR66	0.77	0.0040	0.06	0.5	0.59	0.9	0.08	0.6	0.70	473	22	469	7	468	6	99
ZR28	0.72	0.0012	0.06	1.0	0.60	1.6	0.08	1.2	0.75	528	45	478	12	468	11	89
ZR17	0.50	0.0012	0.06	1.5	0.60	2.1	0.08	1.5	0.71	530	63	478	16	468	14	88
ZR16	0.49	0.0016	0.06	1.0	0.60	1.5	0.08	1.1	0.71	539	43	480	11	467	10	87
ZR52	1.10	0.0021	0.06	0.8	0.59	1.1	0.08	0.7	0.65	505	33	473	8	467	7	92
ZR27	0.67	0.0020	0.06	0.7	0.59	1.3	0.07	0.9	0.75	507	32	473	9	465	9	92
ZR1	0.53	0.0042	0.06	0.5	0.58	1.1	0.07	0.9	0.81	467	24	465	8	465	8	99
ZR34	0.47	0.0028	0.06	0.6	0.59	1.0	0.07	0.7	0.70	490	26	469	7	465	6	95
ZR6	0.65	0.0027	0.06	0.8	0.58	1.2	0.07	0.8	0.70	466	33	465	9	465	7	100

ZR37	0.54	0.0044	0.06	0.5	0.58	1.0	0.07	0.8	0.82	466	20	465	8	464	7	100
ZR62	0.65	0.0038	0.06	0.5	0.58	0.8	0.07	0.6	0.70	475	20	466	6	464	5	98
ZR56	0.54	0.0065	0.06	0.4	0.58	0.7	0.07	0.5	0.70	480	16	466	5	464	5	97
ZR88	0.66	0.0060	0.06	0.3	0.58	0.8	0.07	0.6	0.74	471	15	465	6	463	5	98
ZR29	0.63	0.0011	0.06	1.6	0.60	2.2	0.07	1.5	0.68	546	70	478	17	463	13	85
ZR4	0.46	0.0013	0.06	1.3	0.59	1.8	0.07	1.1	0.64	509	57	471	13	463	10	91
ZR82	0.49	0.0035	0.06	0.4	0.57	0.9	0.07	0.7	0.79	448	16	460	6	463	6	103
ZR81	0.27	0.0064	0.06	0.3	0.58	0.7	0.07	0.5	0.71	472	15	464	5	463	5	98
ZR42	1.01	0.0044	0.06	0.4	0.58	0.9	0.07	0.7	0.78	470	19	464	7	462	6	98
ZR68	0.62	0.0018	0.06	0.6	0.59	1.0	0.07	0.7	0.69	499	28	468	8	462	6	93
ZR44	0.66	0.0080	0.06	0.3	0.58	0.7	0.07	0.5	0.77	477	11	463	5	461	5	97
ZR47	1.03	0.0044	0.06	0.5	0.59	0.9	0.07	0.6	0.72	519	22	470	7	460	6	89
ZR79	0.66	0.0028	0.06	0.9	0.58	1.2	0.07	0.7	0.58	471	38	462	9	460	6	98
ZR78	0.56	0.0036	0.06	0.4	0.58	0.8	0.07	0.7	0.78	486	17	464	6	460	6	95
ZR41	1.58	0.0054	0.06	0.7	0.60	1.7	0.07	1.5	0.88	569	32	478	13	460	13	81
ZR75	0.55	0.0026	0.06	0.6	0.57	1.0	0.07	0.7	0.70	462	28	460	8	459	6	100
ZR69	0.55	0.0042	0.06	0.4	0.58	0.8	0.07	0.6	0.74	471	17	461	6	459	5	97
ZR73	0.57	0.0041	0.06	0.5	0.57	0.9	0.07	0.7	0.76	468	21	461	7	459	6	98
ZR46	0.26	0.0044	0.06	0.4	0.58	0.8	0.07	0.5	0.69	480	18	463	6	459	5	96
ZR48	0.37	0.0058	0.06	0.8	0.59	1.0	0.07	0.6	0.57	531	33	471	8	459	5	86
ZR45	0.68	0.0052	0.06	0.4	0.58	0.8	0.07	0.6	0.73	498	18	465	6	458	5	92
ZR30	0.62	0.0008	0.06	2.1	0.59	2.9	0.07	2.0	0.69	539	90	472	22	458	18	85
ZR83	0.69	0.0032	0.06	2.4	0.57	2.6	0.07	0.7	0.26	452	107	456	19	457	6	101
ZR77	0.55	0.0029	0.06	0.6	0.57	1.0	0.07	0.6	0.66	462	27	457	7	456	6	99
ZR3	0.92	0.0028	0.06	0.6	0.58	1.1	0.07	0.8	0.74	504	27	463	8	455	7	90
ZR20	0.85	0.0006	0.06	2.1	0.59	3.1	0.07	2.3	0.73	541	88	469	23	454	20	84
ZR80	0.65	0.0052	0.06	1.1	0.57	1.4	0.07	0.8	0.58	467	47	456	10	454	7	97
ZR43	0.94	0.0069	0.06	0.4	0.57	0.8	0.07	0.6	0.74	484	17	459	6	454	5	94
ZR57	0.92	0.0045	0.06	0.4	0.57	0.8	0.07	0.7	0.78	486	16	457	6	451	6	93
ZR55	0.91	0.0035	0.06	0.7	0.57	1.0	0.07	0.6	0.58	476	32	455	7	451	5	95
ZR51	0.81	0.0051	0.06	0.4	0.57	1.0	0.07	0.8	0.82	487	18	457	7	450	7	92
ZR59	0.71	0.0032	0.06	0.4	0.57	1.3	0.07	1.1	0.90	483	19	456	9	450	10	93
ZR53	1.00	0.0036	0.06	0.8	0.57	1.1	0.07	0.7	0.61	482	34	455	8	450	6	93
ZR76	0.78	0.0054	0.06	1.0	0.57	1.3	0.07	0.7	0.55	527	44	460	9	447	6	85
ZR54	1.07	0.0058	0.06	0.6	0.56	1.1	0.07	0.9	0.80	481	26	453	8	447	8	93

ZR58	0.96	0.0031	0.06	0.5	0.56	1.3	0.07	1.1	0.89	486	20	450	9	442	10	91
ZR24	0.45	0.0030	0.06	0.8	0.53	2.3	0.07	2.1	0.93	439	34	430	16	428	18	97
ZR49	*0.65*	*0.0064*	*0.06*	*3.0*	*0.66*	*3.1*	*0.08*	*0.7*	*0.23*	*644*	*126*	*517*	*25*	*489*	*7*	*76*
ZR86	*0.75*	*0.0029*	*0.09*	*15.8*	*0.91*	*16.1*	*0.08*	*2.8*	*0.17*	*1334*	*558*	*657*	*150*	*478*	*25*	*36*
ZR91	*1.49*	*0.0035*	*0.05*	*1.8*	*0.57*	*2.0*	*0.08*	*0.7*	*0.34*	*372*	*81*	*456*	*14*	*473*	*6*	*127*
ZR70	*0.52*	*0.0044*	*0.06*	*1.4*	*0.62*	*1.6*	*0.08*	*0.6*	*0.37*	*605*	*60*	*493*	*12*	*469*	*5*	*78*
ZR93	*0.47*	*0.0044*	*0.05*	*4.0*	*0.50*	*4.1*	*0.08*	*0.7*	*0.17*	*128*	*182*	*414*	*27*	*467*	*6*	*364*
ZR38	*0.62*	*0.0048*	*0.05*	*1.7*	*0.56*	*2.2*	*0.07*	*1.2*	*0.57*	*396*	*77*	*453*	*16*	*464*	*11*	*117*
ZR74	*1.21*	*0.0029*	*0.06*	*1.5*	*0.62*	*1.7*	*0.07*	*0.7*	*0.40*	*619*	*66*	*490*	*13*	*463*	*6*	*75*
ZR72	*0.48*	*0.0035*	*0.05*	*1.8*	*0.55*	*2.0*	*0.07*	*0.7*	*0.34*	*388*	*80*	*448*	*14*	*460*	*6*	*119*
ZR5	*0.69*	*0.0014*	*0.05*	*2.3*	*0.54*	*2.7*	*0.07*	*1.3*	*0.50*	*354*	*101*	*440*	*19*	*456*	*12*	*129*
ZR25	*0.67*	*0.0011*	*0.06*	*1.2*	*0.58*	*1.7*	*0.07*	*1.2*	*0.70*	*613*	*50*	*467*	*13*	*437*	*10*	*71*

					Radiogenic ratios					Apparent Ages (Ma)						
Spots	Th/U	^{206}Pb mV[1]	$^{207}Pb/^{206}Pb$	1σ %	$^{207}Pb/^{235}U$	1σ %	$^{206}Pb/^{238}U$	1σ %	Rho	$^{207}Pb/^{206}Pb$	2σ abs	$^{207}Pb/^{235}U$	2σ abs	$^{206}Pb/^{238}U$	2σ abs	Conc (%)
Group 3: Biotite gneiss - sample BE21																
ZR18	0.59	0.0012	0.06	0.9	0.60	1.3	0.08	0.9	0.69	482	39	480	10	480	8	100
ZR28R	0.45	0.0019	0.06	0.8	0.59	1.2	0.08	0.9	0.70	466	36	472	9	473	8	101
ZR14C	0.94	0.0007	0.06	1.8	0.59	2.4	0.08	1.5	0.63	453	79	469	18	473	14	104
ZR22R	0.73	0.0016	0.06	0.8	0.59	1.4	0.08	1.1	0.78	456	36	470	11	472	10	103
ZR32R	0.97	0.0026	0.06	0.8	0.60	1.1	0.08	0.7	0.63	495	35	476	9	472	6	95
ZR21	0.97	0.0009	0.06	1.3	0.59	2.2	0.07	1.7	0.78	503	58	472	16	466	15	93
ZR33R	0.82	0.0028	0.06	0.8	0.58	1.1	0.07	0.6	0.58	464	34	466	8	466	6	100
ZR13R	0.47	0.0059	0.06	0.4	0.58	0.8	0.07	0.6	0.69	476	20	468	6	466	5	98
ZR2R	0.51	0.0017	0.06	0.5	0.57	1.0	0.07	0.8	0.77	437	24	460	8	465	7	106
ZR20	0.91	0.0011	0.06	1.0	0.58	1.5	0.07	1.0	0.66	451	46	463	11	465	9	103
ZR4R	0.54	0.0055	0.06	0.4	0.59	0.8	0.07	0.5	0.69	487	19	468	6	464	5	95
ZR1	0.47	0.0014	0.06	1.3	0.57	1.8	0.07	1.1	0.64	429	58	458	13	463	10	108
ZR32C	0.79	0.0019	0.06	0.7	0.58	1.4	0.07	1.1	0.81	490	31	467	10	463	10	94
ZR16R	0.59	0.0007	0.06	2.0	0.60	2.7	0.07	1.8	0.66	547	85	476	20	461	16	84
ZR26	1.09	0.0010	0.06	1.3	0.58	2.0	0.07	1.4	0.72	463	59	461	15	461	13	100
ZR19	1.01	0.0008	0.06	1.0	0.59	1.7	0.07	1.3	0.78	522	44	471	13	461	12	88
ZR24C	0.59	0.0004	0.06	2.4	0.58	3.3	0.07	2.3	0.69	494	104	463	25	456	20	92

Spots	Th/U	^{206}Pb mV[1]	^{207}Pb/^{206}Pb	1σ %	^{207}Pb/^{235}U	1σ %	^{206}Pb/^{238}U	1σ %	Rho	^{207}Pb/^{206}Pb	2σ abs	^{207}Pb/^{235}U	2σ abs	^{206}Pb/^{238}U	2σ abs	Conc (%)
					Radiogenic ratios					Apparent Ages (Ma)						
Group 3: Chlorite schist - sample BE28																
ZR15C	*0.65*	*0.0003*	*0.06*	*3.7*	*0.71*	*5.5*	*0.09*	*4.0*	*0.73*	*445*	*162*	*544*	*45*	*567*	*43*	*128*
ZR24R	*0.53*	*0.0011*	*0.06*	*1.4*	*0.64*	*2.4*	*0.08*	*1.9*	*0.80*	*510*	*60*	*503*	*19*	*501*	*18*	*98*
ZR9C	*0.45*	*0.0018*	*0.06*	*1.1*	*0.62*	*1.6*	*0.08*	*1.0*	*0.66*	*534*	*48*	*493*	*12*	*484*	*10*	*91*
ZR22C	*0.59*	*0.0005*	*0.06*	*2.3*	*0.61*	*3.2*	*0.08*	*2.2*	*0.67*	*496*	*102*	*482*	*24*	*479*	*20*	*96*
ZR12R	*0.59*	*0.0023*	*0.06*	*0.7*	*0.61*	*1.0*	*0.08*	*0.7*	*0.69*	*513*	*29*	*484*	*8*	*477*	*7*	*93*
ZR14R	*0.55*	*0.0046*	*0.06*	*0.5*	*0.59*	*0.8*	*0.08*	*0.5*	*0.62*	*462*	*24*	*469*	*6*	*471*	*5*	*102*
ZR27C	*0.67*	*0.0021*	*0.06*	*0.9*	*0.58*	*1.5*	*0.07*	*1.1*	*0.77*	*500*	*37*	*467*	*11*	*460*	*10*	*92*
ZR13C	*0.65*	*0.0009*	*0.06*	*2.5*	*0.58*	*2.9*	*0.07*	*1.3*	*0.46*	*484*	*110*	*463*	*21*	*459*	*12*	*95*
ZR10	*0.70*	*0.0024*	*0.06*	*0.8*	*0.59*	*1.1*	*0.07*	*0.6*	*0.58*	*531*	*35*	*470*	*8*	*458*	*6*	*86*
ZR33C	*0.79*	*0.0016*	*0.06*	*0.8*	*0.58*	*1.3*	*0.07*	*1.0*	*0.73*	*493*	*36*	*464*	*10*	*458*	*9*	*93*
ZR23R	*0.47*	*0.0018*	*0.06*	*0.9*	*0.58*	*1.4*	*0.07*	*0.9*	*0.69*	*496*	*40*	*464*	*10*	*458*	*8*	*92*
ZR4C	*0.78*	*0.0039*	*0.06*	*0.5*	*0.58*	*0.9*	*0.07*	*0.6*	*0.71*	*481*	*24*	*462*	*7*	*458*	*6*	*95*
ZR17	*0.69*	*0.0004*	*0.06*	*3.0*	*0.60*	*4.6*	*0.07*	*3.5*	*0.75*	*566*	*128*	*475*	*34*	*456*	*30*	*81*
ZR29	*0.98*	*0.0017*	*0.06*	*0.9*	*0.58*	*1.2*	*0.07*	*0.7*	*0.58*	*533*	*40*	*467*	*9*	*454*	*6*	*85*
ZR25	*1.16*	*0.0013*	*0.06*	*1.3*	*0.57*	*1.9*	*0.07*	*1.3*	*0.68*	*467*	*57*	*456*	*14*	*453*	*11*	*97*
ZR23C	*0.80*	*0.0007*	*0.06*	*1.4*	*0.57*	*2.1*	*0.07*	*1.4*	*0.69*	*499*	*63*	*461*	*15*	*453*	*13*	*91*
ZR31	*1.02*	*0.0010*	*0.06*	*1.1*	*0.57*	*1.8*	*0.07*	*1.3*	*0.74*	*476*	*49*	*456*	*13*	*452*	*11*	*95*
ZR11	*0.77*	*0.0017*	*0.06*	*0.8*	*0.57*	*1.4*	*0.07*	*1.1*	*0.77*	*473*	*36*	*455*	*10*	*452*	*9*	*96*
ZR16C	*0.55*	*0.0007*	*0.06*	*1.5*	*0.57*	*2.1*	*0.07*	*1.4*	*0.67*	*501*	*66*	*459*	*16*	*451*	*12*	*90*
ZR27R	*0.56*	*0.0041*	*0.06*	*0.5*	*0.56*	*0.8*	*0.07*	*0.5*	*0.64*	*465*	*23*	*453*	*6*	*450*	*5*	*97*
ZR9R	*0.77*	*0.0040*	*0.06*	*0.4*	*0.56*	*0.9*	*0.07*	*0.7*	*0.79*	*486*	*19*	*454*	*7*	*448*	*6*	*92*
ZR6	*0.56*	*0.0026*	*0.06*	*0.8*	*0.57*	*1.3*	*0.07*	*0.9*	*0.72*	*492*	*35*	*455*	*9*	*448*	*8*	*91*
ZR30	*1.06*	*0.0007*	*0.06*	*2.2*	*0.56*	*3.2*	*0.07*	*2.2*	*0.70*	*476*	*98*	*452*	*23*	*447*	*19*	*94*
ZR28C	*0.68*	*0.0012*	*0.06*	*1.3*	*0.56*	*2.0*	*0.07*	*1.4*	*0.71*	*503*	*58*	*454*	*14*	*444*	*12*	*88*
ZR8	*1.51*	*0.0042*	*0.06*	*0.9*	*0.56*	*1.9*	*0.07*	*1.6*	*0.86*	*520*	*40*	*453*	*14*	*440*	*14*	*85*
ZR7	*1.22*	*0.0060*	*0.06*	*0.4*	*0.56*	*0.9*	*0.07*	*0.7*	*0.81*	*516*	*18*	*451*	*7*	*439*	*6*	*85*
ZR2C	*1.08*	*0.0012*	*0.06*	*0.9*	*0.54*	*1.5*	*0.07*	*1.1*	*0.74*	*462*	*41*	*440*	*11*	*436*	*9*	*94*
ZR5	*0.95*	*0.0017*	*0.06*	*0.8*	*0.55*	*1.3*	*0.07*	*1.0*	*0.75*	*485*	*35*	*443*	*10*	*435*	*8*	*90*
ZR12C	*0.77*	*0.0023*	*0.06*	*0.6*	*0.54*	*1.1*	*0.07*	*0.8*	*0.76*	*494*	*27*	*440*	*8*	*429*	*7*	*87*
ZR3	*0.87*	*0.0085*	*0.06*	*9.4*	*0.58*	*26.6*	*0.07*	*24.9*	*0.94*	*743*	*376*	*463*	*189*	*408*	*196*	*55*
ZR15R	*0.41*	*0.0113*	*0.05*	*2.9*	*0.29*	*4.0*	*0.04*	*2.8*	*0.68*	*191*	*134*	*262*	*19*	*270*	*15*	*142*

ZR72	0.52	0.0030	0.06	0.8	0.62	1.4	0.08	1.1	0.78	518	36	487	11	480	10	93
ZR40	0.68	0.0032	0.06	0.8	0.61	1.2	0.08	0.8	0.67	487	35	481	9	479	7	98
ZR32	0.90	0.0015	0.06	1.2	0.60	1.7	0.08	1.1	0.64	482	53	478	13	477	10	99
ZR58	0.88	0.0042	0.06	0.6	0.60	1.0	0.08	0.8	0.73	490	27	479	8	477	7	97
ZR2	0.85	0.0029	0.06	0.7	0.60	1.2	0.08	0.9	0.76	492	32	480	10	477	9	97
ZR30	0.65	0.0037	0.06	0.7	0.60	1.2	0.08	0.8	0.72	476	32	476	9	476	8	100
ZR67	0.70	0.0034	0.06	0.7	0.60	1.1	0.08	0.7	0.68	491	31	479	8	476	7	97
ZR12	0.58	0.0032	0.06	0.8	0.59	1.4	0.08	1.2	0.81	475	33	474	11	474	11	100
ZR78	0.45	0.0024	0.06	0.9	0.60	1.3	0.08	0.9	0.69	494	38	475	10	471	8	95
ZR34	0.70	0.0027	0.06	1.3	0.59	1.6	0.08	0.8	0.52	479	58	472	12	471	8	98
ZR98	0.69	0.0031	0.06	0.9	0.59	1.4	0.08	1.0	0.68	486	41	472	10	469	9	97
ZR16	0.48	0.0014	0.06	0.8	0.59	1.3	0.08	1.0	0.73	463	37	468	10	469	9	101
ZR26	0.59	0.0026	0.06	0.8	0.59	1.3	0.08	1.0	0.73	494	37	472	10	467	9	95
ZR61	0.65	0.0037	0.06	0.7	0.59	1.1	0.08	0.7	0.68	481	31	470	8	467	7	97
ZR66	0.61	0.0015	0.06	1.2	0.59	1.6	0.08	1.0	0.64	482	52	470	12	467	9	97
ZR62	0.59	0.0060	0.06	0.8	0.58	1.3	0.08	1.0	0.78	457	33	465	10	467	9	102
ZR15	0.85	0.0024	0.06	1.1	0.59	1.5	0.08	1.0	0.64	473	48	468	11	467	9	99
ZR39	0.33	0.0022	0.06	1.4	0.58	1.9	0.08	1.2	0.64	468	60	467	14	467	11	100
ZR19	0.48	0.0028	0.06	0.9	0.58	1.2	0.08	0.8	0.66	449	38	463	9	466	7	104
ZR59	0.59	0.0041	0.06	0.9	0.59	1.4	0.07	1.1	0.75	490	38	470	11	466	10	95
ZR51	0.57	0.0030	0.06	0.7	0.59	1.0	0.07	0.7	0.68	488	29	470	8	466	6	95
ZR46	0.52	0.0032	0.06	0.8	0.59	1.5	0.07	1.2	0.78	490	37	468	11	464	10	95
ZR3	0.62	0.0032	0.06	0.8	0.58	1.2	0.07	0.8	0.68	477	33	465	9	463	7	97
ZR23	0.49	0.0035	0.06	0.7	0.58	1.1	0.07	0.7	0.70	457	29	462	8	463	7	101
ZR25	0.78	0.0017	0.06	1.2	0.58	1.6	0.07	1.0	0.64	468	52	463	12	462	9	99
ZR1	0.58	0.0038	0.06	0.7	0.58	1.4	0.07	1.1	0.80	485	32	466	10	462	10	95
ZR44	1.16	0.0028	0.06	0.9	0.58	1.5	0.07	1.1	0.75	488	40	466	11	462	10	95
ZR27	0.58	0.0025	0.06	0.8	0.58	1.2	0.07	0.8	0.67	476	37	462	9	459	7	96
ZR55	0.62	0.0029	0.06	0.8	0.57	1.3	0.07	0.9	0.71	462	35	459	9	458	8	99
ZR60	0.57	0.0021	0.06	1.1	0.57	1.6	0.07	1.1	0.68	477	47	459	12	456	9	96
ZR18	0.97	0.0055	0.06	0.7	0.57	1.1	0.07	0.7	0.68	473	32	457	8	454	6	96
ZR14	0.49	0.0025	0.06	0.5	0.57	1.0	0.07	0.8	0.76	470	23	455	7	452	7	96
ZR64	*0.48*	*0.0014*	*0.06*	*1.0*	*0.65*	*1.3*	*0.08*	*0.8*	*0.60*	*503*	*44*	*507*	*11*	*508*	*8*	*101*
ZR29	*0.57*	*0.0033*	*0.06*	*0.7*	*0.63*	*1.2*	*0.08*	*0.9*	*0.74*	*485*	*32*	*493*	*10*	*495*	*9*	*102*

ZR24	*0.61*	*0.0044*	*0.06*	*0.7*	*0.62*	*1.3*	*0.08*	*1.0*	*0.77*	*487*	*32*	*489*	*10*	*489*	*9*	*100*
ZR10	*0.65*	*0.0028*	*0.06*	*1.4*	*0.60*	*1.8*	*0.08*	*1.0*	*0.55*	*419*	*63*	*477*	*13*	*489*	*9*	*117*
ZR21	*0.58*	*0.0019*	*0.06*	*1.6*	*0.63*	*2.4*	*0.08*	*1.8*	*0.74*	*540*	*69*	*496*	*19*	*487*	*17*	*90*
ZR70	*0.75*	*0.0019*	*0.06*	*1.0*	*0.63*	*1.4*	*0.08*	*0.9*	*0.66*	*555*	*41*	*498*	*11*	*486*	*9*	*87*
ZR71	*0.83*	*0.0069*	*0.06*	*0.7*	*0.62*	*1.6*	*0.08*	*1.4*	*0.87*	*501*	*30*	*487*	*12*	*485*	*13*	*97*
ZR28	*0.67*	*0.0040*	*0.06*	*0.6*	*0.62*	*1.2*	*0.08*	*0.9*	*0.79*	*534*	*26*	*492*	*9*	*483*	*8*	*90*
ZR6	*0.53*	*0.0031*	*0.06*	*0.9*	*0.61*	*1.6*	*0.08*	*1.3*	*0.79*	*518*	*40*	*482*	*12*	*474*	*12*	*92*
ZR42	*0.53*	*0.0022*	*0.06*	*1.1*	*0.60*	*1.5*	*0.08*	*1.0*	*0.66*	*506*	*48*	*478*	*12*	*472*	*9*	*93*
ZR92	*0.74*	*0.0029*	*0.06*	*1.4*	*0.58*	*2.1*	*0.08*	*1.4*	*0.71*	*445*	*62*	*465*	*15*	*470*	*13*	*106*
ZR45	*0.89*	*0.0061*	*0.06*	*0.4*	*0.59*	*0.9*	*0.08*	*0.7*	*0.76*	*497*	*19*	*474*	*7*	*469*	*6*	*94*
ZR75	*0.67*	*0.0029*	*0.06*	*0.8*	*0.59*	*1.3*	*0.08*	*0.9*	*0.74*	*501*	*34*	*474*	*10*	*468*	*9*	*94*
ZR68	*0.53*	*0.0029*	*0.06*	*1.1*	*0.60*	*1.5*	*0.08*	*1.1*	*0.69*	*523*	*46*	*477*	*12*	*468*	*10*	*89*
ZR33	*0.60*	*0.0026*	*0.06*	*0.6*	*0.59*	*1.1*	*0.07*	*0.8*	*0.74*	*510*	*28*	*474*	*8*	*466*	*7*	*91*
ZR76	*0.35*	*0.0029*	*0.06*	*0.9*	*0.59*	*1.4*	*0.07*	*0.9*	*0.68*	*500*	*41*	*472*	*10*	*466*	*8*	*93*
ZR65	*0.53*	*0.0020*	*0.06*	*0.8*	*0.60*	*1.2*	*0.07*	*0.9*	*0.72*	*527*	*34*	*476*	*9*	*465*	*8*	*88*
ZR74	*0.76*	*0.0017*	*0.06*	*0.8*	*0.60*	*1.3*	*0.07*	*1.0*	*0.76*	*543*	*34*	*478*	*10*	*465*	*9*	*86*
ZR31	*0.72*	*0.0046*	*0.06*	*0.6*	*0.59*	*0.9*	*0.07*	*0.6*	*0.68*	*506*	*26*	*470*	*7*	*463*	*6*	*91*
ZR54	*0.57*	*0.0019*	*0.06*	*0.8*	*0.58*	*1.3*	*0.07*	*0.9*	*0.72*	*489*	*36*	*466*	*10*	*461*	*8*	*94*
ZR94	*0.50*	*0.0031*	*0.06*	*0.7*	*0.59*	*1.6*	*0.07*	*1.4*	*0.86*	*513*	*32*	*469*	*12*	*460*	*12*	*90*
ZR20	*0.73*	*0.0024*	*0.06*	*0.8*	*0.58*	*1.2*	*0.07*	*0.8*	*0.67*	*480*	*34*	*462*	*9*	*458*	*7*	*95*
ZR41	*0.47*	*0.0026*	*0.06*	*1.0*	*0.58*	*1.5*	*0.07*	*1.0*	*0.66*	*492*	*46*	*464*	*11*	*458*	*9*	*93*
ZR36	*0.67*	*0.0029*	*0.06*	*0.6*	*0.58*	*1.0*	*0.07*	*0.7*	*0.73*	*484*	*25*	*462*	*7*	*457*	*6*	*95*
ZR43	*0.59*	*0.0028*	*0.06*	*0.6*	*0.58*	*1.0*	*0.07*	*0.7*	*0.70*	*491*	*25*	*462*	*7*	*456*	*6*	*93*
ZR56	*0.57*	*0.0025*	*0.06*	*1.5*	*0.56*	*2.0*	*0.07*	*1.2*	*0.59*	*438*	*67*	*453*	*14*	*456*	*10*	*104*
ZR35	*0.43*	*0.0015*	*0.06*	*1.7*	*0.56*	*2.7*	*0.07*	*2.0*	*0.75*	*438*	*77*	*452*	*19*	*454*	*18*	*104*
ZR86	*1.02*	*0.0078*	*0.06*	*0.5*	*0.57*	*0.9*	*0.07*	*0.6*	*0.69*	*489*	*22*	*459*	*6*	*453*	*5*	*93*
ZR38	*0.43*	*0.0046*	*0.06*	*0.7*	*0.57*	*1.2*	*0.07*	*0.9*	*0.75*	*480*	*32*	*458*	*9*	*453*	*8*	*94*
ZR22	*1.04*	*0.0024*	*0.06*	*0.6*	*0.57*	*1.1*	*0.07*	*0.8*	*0.75*	*496*	*27*	*460*	*8*	*453*	*7*	*91*
ZR47	*0.66*	*0.0020*	*0.06*	*0.6*	*0.58*	*1.1*	*0.07*	*0.9*	*0.77*	*519*	*27*	*464*	*8*	*453*	*7*	*87*
ZR48	*0.23*	*0.0024*	*0.06*	*0.9*	*0.59*	*1.4*	*0.07*	*1.0*	*0.70*	*566*	*40*	*472*	*10*	*453*	*9*	*80*
ZR81	*0.85*	*0.0026*	*0.06*	*0.8*	*0.57*	*1.1*	*0.07*	*0.7*	*0.65*	*503*	*34*	*458*	*8*	*449*	*6*	*89*
ZR17	*0.65*	*0.0026*	*0.06*	*0.9*	*0.56*	*1.3*	*0.07*	*0.9*	*0.67*	*478*	*39*	*454*	*10*	*449*	*8*	*94*
ZR49	*0.50*	*0.0017*	*0.06*	*1.2*	*0.56*	*1.6*	*0.07*	*1.0*	*0.60*	*493*	*53*	*455*	*12*	*447*	*8*	*91*
ZR50	*0.38*	*0.0023*	*0.06*	*0.9*	*0.56*	*1.2*	*0.07*	*0.7*	*0.57*	*491*	*41*	*454*	*9*	*446*	*6*	*91*
ZR8	*0.50*	*0.0024*	*0.06*	*2.1*	*0.57*	*3.0*	*0.07*	*2.0*	*0.68*	*541*	*92*	*461*	*22*	*445*	*17*	*82*

ZR4	0.71	0.0091	0.06	0.4	0.56	1.0	0.07	0.8	0.83	503	18	455	7	445	7	89
ZR99	1.13	0.0056	0.06	0.8	0.56	1.1	0.07	0.6	0.58	477	36	450	8	445	6	93
ZR13	0.61	0.0022	0.06	0.6	0.57	1.0	0.07	0.7	0.72	516	26	456	7	444	6	86
ZR7	0.61	0.0037	0.06	0.6	0.56	1.1	0.07	0.8	0.72	493	28	452	8	444	7	90
ZR63	0.57	0.0042	0.06	0.5	0.56	0.9	0.07	0.6	0.69	511	24	455	7	443	5	87
ZR52	0.71	0.0036	0.06	0.7	0.56	1.2	0.07	0.8	0.70	499	32	452	8	443	7	89
ZR9	0.53	0.0031	0.06	1.0	0.55	1.6	0.07	1.2	0.75	458	42	446	11	443	10	97
ZR11	0.71	0.0033	0.06	0.9	0.55	1.2	0.07	0.7	0.58	452	39	444	8	443	6	98
ZR100	0.47	0.0022	0.06	1.2	0.56	1.6	0.07	1.0	0.65	487	51	450	12	443	9	91
ZR83	0.64	0.0053	0.06	0.8	0.55	1.2	0.07	0.8	0.70	463	34	445	9	442	7	96
ZR79	0.83	0.0025	0.06	0.8	0.56	1.2	0.07	0.7	0.64	503	35	450	8	439	6	87
ZR93	0.96	0.0035	0.06	0.8	0.57	1.1	0.07	0.8	0.67	545	33	456	8	438	6	80
ZR77	0.41	0.0021	0.06	0.8	0.55	1.1	0.07	0.7	0.64	500	33	446	8	435	6	87
ZR85	0.61	0.0028	0.06	0.7	0.55	1.1	0.07	0.8	0.71	484	29	443	8	435	6	90
ZR82	0.93	0.0019	0.06	0.9	0.55	1.3	0.07	0.9	0.65	490	41	443	9	434	7	89
ZR97	0.50	0.0017	0.06	0.9	0.55	1.3	0.07	0.9	0.68	488	38	442	9	433	7	89
ZR87	0.67	0.0035	0.06	0.6	0.54	1.2	0.07	1.0	0.81	488	26	438	8	429	8	88
ZR80	0.81	0.0065	0.06	0.9	0.54	1.4	0.07	1.0	0.73	481	40	435	10	427	9	89
ZR88	0.60	0.0026	0.06	0.6	0.54	1.2	0.07	0.9	0.78	507	28	437	8	424	8	84
ZR96	0.42	0.0029	0.06	0.8	0.55	1.2	0.07	0.8	0.69	565	35	445	9	422	7	75
ZR91	0.54	0.0028	0.06	1.1	0.52	1.9	0.07	1.5	0.80	469	47	426	13	418	12	89
ZR89	0.14	0.0098	0.06	0.7	0.46	1.0	0.06	0.7	0.69	463	29	384	7	371	5	80

					Radiogenic ratios					Apparent Ages (Ma)						
Spots	Th/U	^{206}Pb mV[1]	^{207}Pb/^{206}Pb	1σ %	^{207}Pb/^{235}U	1σ %	^{206}Pb/^{238}U	1σ %	Rho	^{207}Pb/^{206}Pb	2σ abs	^{207}Pb/^{235}U	2σ abs	^{206}Pb/^{238}U	2σ abs	Conc (%)
Group 4: Amphibole gneiss - sample BE32																
ZR27	1.28	0.0008	0.06	1.6	0.58	2.3	0.08	1.7	0.72	432	69	464	17	471	15	109
ZR25	1.28	0.0008	0.06	1.5	0.59	2.1	0.07	1.4	0.66	498	66	471	16	466	12	94
ZR22	1.13	0.0008	0.06	1.3	0.60	2.0	0.07	1.4	0.72	526	57	476	15	465	13	88
ZR20	1.24	0.0006	0.06	2.1	0.58	3.3	0.07	2.5	0.76	470	90	465	24	464	22	99
ZR23	1.31	0.0009	0.06	1.2	0.58	1.8	0.07	1.2	0.68	463	55	463	13	463	11	100
ZR8	1.19	0.0006	0.06	2.0	0.59	2.8	0.07	2.0	0.71	504	85	470	21	463	18	92
ZR24	1.43	0.0011	0.06	1.3	0.58	1.9	0.07	1.3	0.70	484	57	466	14	462	12	96
ZR16	1.23	0.0006	0.06	1.7	0.59	2.5	0.07	1.8	0.72	533	72	469	18	456	16	86
ZR12	1.19	0.0006	0.06	1.9	0.59	3.0	0.07	2.2	0.76	542	82	470	22	455	20	84

ZR28	1.48	0.0013	0.06	1.1	0.56	1.5	0.07	0.9	0.63	462	49	454	11	453	8	98
ZR10	1.14	0.0008	0.06	1.9	0.57	2.5	0.07	1.6	0.65	501	81	459	18	451	14	90
ZR2	1.24	0.0007	0.06	1.6	0.57	2.3	0.07	1.6	0.71	512	68	460	17	450	14	88
ZR21	1.14	0.0008	0.06	1.5	0.58	2.2	0.07	1.5	0.69	534	66	464	16	450	13	84
ZR1	1.40	0.0011	0.06	1.2	0.57	1.8	0.07	1.2	0.69	495	54	457	13	449	11	91
ZR3	1.42	0.0012	0.06	1.3	0.57	1.9	0.07	1.3	0.72	489	55	455	14	449	12	92
ZR19	1.14	0.0006	0.06	1.9	0.59	3.0	0.07	2.3	0.77	586	80	469	22	446	20	76
ZR5	1.15	0.0007	0.06	1.6	0.56	2.3	0.07	1.6	0.71	484	68	452	17	445	14	92
ZR17	*1.27*	*0.0008*	*0.06*	*1.4*	*0.59*	*1.8*	*0.08*	*1.1*	*0.60*	*421*	*63*	*470*	*14*	*480*	*10*	*114*
ZR18	*1.25*	*0.0008*	*0.06*	*1.4*	*0.61*	*2.1*	*0.08*	*1.5*	*0.73*	*493*	*61*	*481*	*16*	*478*	*14*	*97*
ZR15	*1.11*	*0.0009*	*0.06*	*1.6*	*0.60*	*2.4*	*0.08*	*1.7*	*0.71*	*507*	*72*	*479*	*18*	*474*	*16*	*93*
ZR13	*1.18*	*0.0008*	*0.06*	*1.8*	*0.60*	*2.7*	*0.08*	*2.0*	*0.74*	*495*	*78*	*476*	*20*	*473*	*18*	*95*
ZR11	*1.26*	*0.0007*	*0.06*	*2.4*	*0.58*	*3.4*	*0.08*	*2.4*	*0.69*	*414*	*107*	*462*	*25*	*472*	*21*	*114*
ZR30	*1.31*	*0.0009*	*0.07*	*1.6*	*0.67*	*2.2*	*0.07*	*1.4*	*0.65*	*788*	*67*	*519*	*18*	*460*	*12*	*58*
ZR14	*1.17*	*0.0008*	*0.06*	*1.9*	*0.57*	*2.8*	*0.07*	*2.0*	*0.72*	*522*	*83*	*457*	*21*	*444*	*17*	*85*
ZR26	*0.99*	*0.0006*	*0.06*	*2.1*	*0.56*	*3.1*	*0.07*	*2.2*	*0.73*	*498*	*90*	*452*	*22*	*443*	*19*	*89*
ZR6	*1.23*	*0.0008*	*0.06*	*1.3*	*0.56*	*1.9*	*0.07*	*1.3*	*0.72*	*516*	*55*	*453*	*14*	*441*	*11*	*85*
ZR4	*1.10*	*0.0008*	*0.06*	*1.5*	*0.55*	*2.3*	*0.07*	*1.6*	*0.72*	*498*	*67*	*445*	*16*	*435*	*14*	*87*
ZR7	*1.18*	*0.0008*	*0.06*	*1.7*	*0.55*	*2.5*	*0.07*	*1.8*	*0.72*	*485*	*73*	*442*	*18*	*434*	*15*	*90*
ZR29	*0.65*	*0.0008*	*0.06*	*1.5*	*0.56*	*2.2*	*0.07*	*1.6*	*0.71*	*551*	*65*	*453*	*16*	*434*	*13*	*79*
ZR9	*1.24*	*0.0009*	*0.06*	*1.0*	*0.54*	*1.6*	*0.07*	*1.1*	*0.73*	*495*	*44*	*440*	*11*	*429*	*10*	*87*

					Radiogenic ratios					Apparent Ages (Ma)						
Spots	Th/U	^{206}Pb mV[1]	$^{207}Pb/^{206}Pb$	1σ %	$^{207}Pb/^{235}U$	1σ %	$^{206}Pb/^{238}U$	1σ %	Rho	$^{207}Pb/^{206}Pb$	2σ abs	$^{207}Pb/^{235}U$	2σ abs	$^{206}Pb/^{238}U$	2σ abs	Conc (%)
Group 5: Amphibolite - sample BE10F																
ZR9	0.46	0.0020	0.06	0.8	0.62	1.2	0.08	0.8	0.69	476	34	488	9	491	8	103
ZR7	0.66	0.0020	0.06	1.6	0.64	1.8	0.08	0.7	0.40	551	70	500	14	489	7	89
ZR2	1.16	0.0037	0.06	0.6	0.62	0.9	0.08	0.6	0.63	515	27	488	7	482	5	94
ZR6	0.55	0.0041	0.06	0.6	0.61	1.2	0.08	1.0	0.82	486	26	482	10	481	9	99
ZR10	0.77	0.0039	0.06	0.3	0.61	0.7	0.08	0.5	0.71	498	15	484	6	481	5	97
ZR8	*0.16*	*0.0165*	*0.09*	*0.6*	*2.37*	*1.1*	*0.18*	*0.8*	*0.73*	*1500*	*23*	*1234*	*15*	*1088*	*15*	*73*
ZR11	*0.87*	*0.0038*	*0.05*	*1.3*	*0.57*	*1.5*	*0.08*	*0.8*	*0.51*	*378*	*56*	*456*	*11*	*472*	*7*	*125*
ZR5	*0.76*	*0.0028*	*0.06*	*2.3*	*0.61*	*2.4*	*0.08*	*0.7*	*0.28*	*544*	*97*	*484*	*18*	*471*	*6*	*87*

ZR4	0.87	0.0039	0.05	2.1	0.56	2.3	0.08	0.8	0.36	340	95	449	17	471	8	139
ZR13	0.91	0.0039	0.05	5.3	0.50	5.3	0.08	0.7	0.14	103	240	413	36	470	7	455
ZR1	0.93	0.0052	0.06	0.7	0.59	1.0	0.07	0.7	0.64	512	30	473	8	465	6	91
ZR3	0.69	0.0027	0.05	3.2	0.50	3.3	0.07	0.9	0.26	164	147	413	23	459	8	280

					Radiogenic ratios					Apparent Ages (Ma)						
Spots	Th/U	^{206}Pb mV[1]	^{207}Pb/^{206}Pb	1σ %	^{207}Pb/^{235}U	1σ %	^{206}Pb/^{238}U	1σ %	Rho	^{207}Pb/^{206}Pb	2σ abs	^{207}Pb/^{235}U	2σ abs	^{206}Pb/^{238}U	2σ abs	Conc (%)
Group 5: Amphibolite - sample BE16C																
ZR24	0.63	0.0037	0.06	0.5	0.61	1.3	0.08	1.1	0.87	471	23	486	10	489	11	104
ZR11	0.38	0.0023	0.06	0.5	0.60	1.0	0.08	0.8	0.79	470	21	477	7	478	7	102
ZR30	0.80	0.0020	0.06	2.0	0.61	2.7	0.08	1.8	0.67	499	86	480	21	477	17	96
ZR15	0.64	0.0050	0.06	0.4	0.60	0.9	0.08	0.7	0.78	478	19	475	7	475	7	99
ZR16	0.77	0.0024	0.06	0.7	0.59	1.0	0.08	0.7	0.65	458	31	471	8	474	6	103
ZR9	0.59	0.0039	0.06	1.4	0.58	2.5	0.08	2.0	0.81	452	62	468	19	471	18	104
ZR12	0.50	0.0022	0.06	0.6	0.59	1.0	0.08	0.7	0.68	475	27	470	7	469	6	99
ZR20	0.59	0.0018	0.06	1.2	0.58	1.7	0.08	1.2	0.68	454	54	465	13	467	11	103
ZR29	0.50	0.0015	0.06	1.0	0.59	1.8	0.08	1.5	0.82	496	42	472	13	466	13	94
ZR17	0.51	0.0017	0.06	1.0	0.58	1.6	0.07	1.1	0.70	449	46	463	12	466	10	104
ZR26	0.42	0.0012	0.06	0.8	0.58	1.2	0.07	0.9	0.70	466	35	466	9	465	8	100
ZR3	1.55	0.0039	0.06	0.5	0.59	1.0	0.07	0.7	0.74	488	24	468	7	464	6	95
ZR28	0.86	0.0019	0.06	0.9	0.58	1.5	0.07	1.2	0.75	466	41	464	11	464	10	100
ZR6	0.75	0.0027	0.06	0.5	0.58	1.0	0.07	0.7	0.73	492	24	467	7	462	6	94
ZR1	0.47	0.0021	0.06	0.7	0.58	1.1	0.07	0.8	0.71	478	31	464	8	461	7	96
ZR19	0.53	0.0015	0.06	1.5	0.68	2.3	0.08	1.8	0.76	670	62	529	19	497	17	74
ZR10	0.48	0.0017	0.07	0.9	0.72	1.3	0.08	0.9	0.65	841	39	548	11	480	8	57
ZR8	0.51	0.0017	0.05	1.1	0.58	1.5	0.08	0.8	0.58	411	50	465	11	475	8	116
ZR23	0.46	0.0010	0.05	2.7	0.57	3.6	0.08	2.4	0.66	385	119	456	27	471	22	122
ZR5	0.97	0.0036	0.06	0.4	0.61	0.8	0.08	0.6	0.73	554	18	483	6	469	5	85
ZR25	0.49	0.0014	0.06	1.2	0.57	1.7	0.08	1.1	0.66	413	53	459	12	468	10	113
ZR22	0.48	0.0015	0.05	1.8	0.55	2.1	0.07	1.1	0.50	338	80	443	15	463	9	137
ZR2	0.44	0.0018	0.06	2.7	0.62	3.1	0.07	1.6	0.50	629	113	491	24	462	14	74
ZR21	0.40	0.0013	0.05	2.3	0.55	2.9	0.07	1.8	0.61	372	100	447	21	461	16	124
ZR14	1.20	0.0039	0.06	0.3	0.58	0.7	0.07	0.5	0.73	487	15	464	5	459	5	94
ZR7	0.49	0.0015	0.06	1.3	0.57	1.6	0.07	1.0	0.60	466	55	460	12	459	9	99

ZR18	*0.79*	*0.0031*	*0.06*	*0.6*	*0.57*	*1.0*	*0.07*	*0.7*	*0.71*	*451*	*26*	*458*	*7*	*459*	*6*	*102*
ZR4	*0.52*	*0.0014*	*0.06*	*1.0*	*0.57*	*1.5*	*0.07*	*1.0*	*0.67*	*488*	*45*	*459*	*11*	*453*	*9*	*93*
ZR13	*1.36*	*0.0049*	*0.05*	*2.2*	*0.50*	*2.4*	*0.07*	*0.7*	*0.30*	*245*	*100*	*412*	*16*	*442*	*6*	*180*

					Radiogenic ratios					Apparent Ages (Ma)						
Spots	Th/U	^{206}Pb mV[1]	^{207}Pb/^{206}Pb	1σ %	^{207}Pb/^{235}U	1σ %	^{206}Pb/^{238}U	1σ %	Rho	^{207}Pb/^{206}Pb	2σ abs	^{207}Pb/^{235}U	2σ abs	^{206}Pb/^{238}U	2σ abs	Conc (%)
Group 5: Amphibolite - sample BE16C																
ZR24	0.87	0.0081	0.12	0.5	5.68	0.9	0.36	0.6	0.69	1881	19	1929	16	1974	21	105
ZR18R	0.43	0.0151	0.12	0.3	5.91	0.7	0.35	0.5	0.75	1975	10	1962	12	1950	18	99
ZR18C	0.48	0.0106	0.12	0.4	5.79	0.9	0.35	0.8	0.84	1968	13	1944	16	1923	26	98
ZR27	1.05	0.0104	0.06	0.4	0.59	1.0	0.08	0.9	0.84	458	18	474	8	477	8	104
ZR22C	1.02	0.0109	0.06	0.3	0.59	0.7	0.08	0.5	0.69	462	15	473	5	475	4	103
ZR6	0.59	0.0030	0.06	0.7	0.59	1.4	0.08	1.1	0.81	480	32	473	10	471	10	98
ZR20	1.35	0.0117	0.06	0.3	0.59	0.7	0.08	0.5	0.75	472	13	471	5	471	5	100
ZR4	0.75	0.0048	0.06	0.5	0.58	0.9	0.07	0.7	0.77	475	20	464	7	462	6	97
ZR11	0.97	0.0093	0.06	0.3	0.57	0.8	0.07	0.7	0.80	459	15	461	6	462	6	100
ZR26	0.66	0.0065	0.06	0.5	0.62	0.8	0.08	0.6	0.69	473	21	492	6	497	6	105
ZR23	0.75	0.0040	0.06	0.6	0.61	1.0	0.08	0.7	0.70	465	25	487	7	491	6	106
ZR21	0.53	0.0019	0.06	0.6	0.63	1.2	0.08	0.9	0.77	506	28	493	9	490	8	97
ZR25	0.51	0.0029	0.06	0.8	0.62	1.1	0.08	0.8	0.66	506	34	491	9	488	7	96
ZR22R	1.02	0.0130	0.05	2.4	0.58	2.5	0.08	0.6	0.26	374	105	466	18	485	6	130
ZR10	0.68	0.0025	0.06	0.6	0.60	1.1	0.08	0.8	0.77	449	26	477	8	483	8	108
ZR12	0.76	0.0038	0.06	0.4	0.60	1.1	0.08	1.0	0.88	492	16	478	8	475	9	97
ZR8	1.22	0.0170	0.06	0.4	0.58	0.8	0.07	0.6	0.76	479	16	465	6	462	5	96
ZR17	0.97	0.0157	0.06	0.4	0.57	0.7	0.07	0.5	0.66	472	17	461	5	458	4	97
ZR5	0.83	0.0014	0.06	1.0	0.57	1.5	0.07	1.0	0.69	472	44	459	11	456	9	97
ZR14	0.50	0.0023	0.06	0.8	0.57	1.1	0.07	0.7	0.61	508	36	461	8	452	6	89
ZR19	0.56	0.0016	0.06	1.0	0.57	1.3	0.07	0.8	0.61	500	42	459	10	451	7	90
ZR7	1.39	0.0257	0.06	0.4	0.51	1.1	0.06	1.0	0.87	488	19	418	8	406	8	83
ZR15	0.57	0.0036	0.07	2.6	0.58	2.8	0.06	0.9	0.32	803	108	466	21	400	7	50
ZR16	1.65	0.0241	0.06	0.4	0.41	0.8	0.05	0.6	0.72	495	17	349	5	327	4	66
ZR9C	1.29	0.0100	0.07	2.2	0.45	2.7	0.05	1.5	0.57	795	90	374	17	310	9	39
ZR1	1.39	0.0188	0.07	0.5	0.41	1.0	0.04	0.8	0.79	806	20	348	6	283	4	35
ZR9R	0.71	0.0266	0.06	0.4	0.34	1.3	0.04	1.2	0.91	558	17	297	7	265	6	47

ZR2C1	0.40	0.0207	0.07	0.8	0.36	1.2	0.04	0.8	0.66	779	33	316	6	256	4	33
ZR3C2	0.36	0.0225	0.07	1.9	0.36	2.4	0.04	1.3	0.56	872	79	311	13	241	6	28
ZR3C1	1.08	0.0221	0.06	4.1	0.29	4.3	0.04	1.2	0.28	566	173	260	20	228	5	40
ZR2C2	1.59	0.0302	0.06	4.1	0.29	5.1	0.03	3.0	0.60	599	172	257	23	221	13	37
ZR13	1.80	0.0000	12.50	146.6	4.38	149.3	0.00	28.6	0.19	8615	2312	1709	1616	16	9	0

Data report template (with modifications) from http://www.plasmage.org/recommendations

Notes: Convertion factor from mV to CPS is 62500000

Concentration uncertainty c.20%

Data not corrected for common-Pb

Concordance calculated as (206Pb/238U age / 207Pb/206Pb age) * 100

Decay constants of Jaffey et al 1971 used

Abreviations: C - core; R - rim and ZR - zircon.

Data not used to calculate ages are at the end in italics for each sample.

Supplementary Table 02: LA-ICP-MS Lu-Hf isotope data of zircon from northern BMC rocks.

Sample	*Measured*				$^{207}Pb/^{206}Pb$	*Calculated*				*Average*
	$^{176}Lu/^{177}Hf$	±2σ	$^{176}Hf/^{177}Hf$	±2σ	Ma	$(^{176}Hf/^{177}Hf)_T$	±2σ	εHf_0	εHf_T	T_{DM} Ga
Group 1: Quartz monzodiorite - sample BE16										
ZR7	0.029540	0.000375	0.282157	0.000027	469	0.282149	0.000027	-22.3	-12.1	2.0
ZR10	0.020288	0.001403	0.282145	0.000031	472	0.282141	0.000031	-22.7	-12.4	2.0
ZR11	0.024694	0.000309	0.282166	0.000029	469	0.282160	0.000029	-21.9	-11.7	1.9
ZR13	0.067891	0.002257	0.282263	0.000035	471	0.282246	0.000035	-18.5	-8.6	1.8
ZR18	0.016014	0.000222	0.282139	0.000027	474	0.282135	0.000027	-22.9	-12.5	2.0
Group 1: Amphibole gneiss - sample BE3C										
ZR5N	0.031016	0.000749	0.282255	0.000027	486	0.282247	0.000027	-18.8	-8.3	1.8
ZR6	0.021909	0.000372	0.282294	0.000031	487	0.282289	0.000031	-17.4	-6.8	1.7
ZR7	0.015826	0.000954	0.282210	0.000029	484	0.282206	0.000029	-20.4	-9.8	1.9
ZR16	0.060918	0.000684	0.282216	0.000034	487	0.282201	0.000034	-20.1	-9.9	1.9
Group 1: Amphibole gneiss BE14										
ZR1	0.031576	0.001296	0.282147	0.000028	471	0.282139	0.000028	-22.6	-12.4	2.0
ZR15	0.022135	0.000348	0.282180	0.000027	471	0.282174	0.000027	-21.4	-11.2	1.9
ZR16	0.042134	0.003773	0.282297	0.000035	472	0.282287	0.000035	-17.3	-7.2	1.7
ZR20	0.023651	0.000910	0.282208	0.000030	472	0.282202	0.000030	-20.4	-10.2	1.9
ZR21	0.028214	0.000570	0.282239	0.000027	466	0.282233	0.000027	-19.3	-9.2	1.8
Group 5: Amphibolite - sample BE10F										
ZR2	0.046601	0.002346	0.282287	0.000028	482	0.282275	0.000028	-17.6	-7.4	1.7
ZR6	0.037345	0.000541	0.282427	0.000096	481	0.282418	0.000096	-12.7	-2.3	1.4
ZR9	0.023758	0.001222	0.282210	0.000023	491	0.282204	0.000023	-20.4	-9.7	1.9
ZR10	0.040294	0.001741	0.282224	0.000028	481	0.282214	0.000028	-19.9	-9.5	1.8
Group 5: Amphibolite - sample BE16C										
ZR3	0.064667	0.001711	0.282159	0.000031	464	0.282143	0.000031	-22.2	-12.4	2.0
ZR16	0.044495	0.000497	0.282130	0.000032	474	0.282120	0.000032	-23.2	-13.1	2.0
ZR12	0.033750	0.000546	0.282302	0.000029	469	0.282293	0.000029	-17.1	-7.0	1.7
ZR29	0.033032	0.001473	0.282601	0.000063	466	0.282593	0.000063	-6.6	3.5	1.1
ZR9	0.021037	0.001238	0.282585	0.000032	471	0.282580	0.000032	-7.1	3.2	1.1

4 CAPÍTULO 4 – GEOQUÍMICA BMC

4.1 GEOQUÍMICA DAS ROCHAS PLUTÔNICAS DO COMPLEXO METAMÓRFICO BELÉN

Os dados geoquímicos das amostras dos grupos 1 a 5 do Complexo Metamórfico Belén indicam ampla variação dos teores de SiO_2, que os classifica como intermediários até ácidos (grupo 1 a 4) e como básico (grupo 5), com teores, respectivamente, grupo 1 (petrografia: quartzo monzodiorito e amphibolio gnaisse de composição quartzo monzodiorítica) 50,5 e 56,6 %, grupo 2 (petrografia: gnaisses e xistos de composição granodiorítica) 58,2 e 74,4 %, grupo 3 (petrografia: biotita gnaisse e xistos de composição granodiorítica) 63,8 e 65 %, grupo 4 (anfibólio gnaisse de composição tonalítica) 51,7 e 54,6 %, grupo 5 (anfibolitos de composição andesi-balsáltica a basáltica) 47,2 e 49,6 %. O Al_2O_3 varia para o grupo 1 de 16,4 e 19,35 %, grupo 2 de 12,9 a 13,85 %, grupo 3 de 15,8 a 16,05 %, grupo 4 de16 a 16,8 %, e grupo 5 de 12,8 a 15,9 %. O Fe_2O_3(t) varia para o grupo 1 de 8,3 a 10 %, grupo 2 de 0,25 a 7,59 %, grupo 3 de 5,46 a 6,2 %, grupo 4 de 7,92 a 10,6 %, e grupo 5 de 7,65 a 16,45 %. Para o MgO a variação é de: grupo 1 de 3,5 a 4,36 %, grupo 2 de 0,09 a 1,79, grupo 3 de 1,72 a 2,07 %, grupo 4 de 1,66 a 5,51 % e para o grupo 5 de 1,64 a 8,43 %.

Utilizando sílica como índice de diferenciação nos diagramas do tipo Harker (Figura 1), observam-se tendências bem definidas com correlações negativas entre SiO_2 e CaO, MgO, Fe_2O_3(t), TiO_2, Y e P_2O_5. Correlação positiva é identificada entre sílica K_2O, sugerindo o enriquecimento em feldspato alcalino dos litotipos mais evoluídos, Na_2O e Rb. Os diagramas binários da figura 2 exibem elementos traço como índice de diferenciação com tendências de correlação positiva de Zr por Hf, Nb por Ta, Nb por Zr e correlação negativa para La por Yb. O diagrama de Th por P_2O_5 apresenta correlação positiva e o binário de SiO^2 por LOI evidencia correlação negativa (fig. 2).

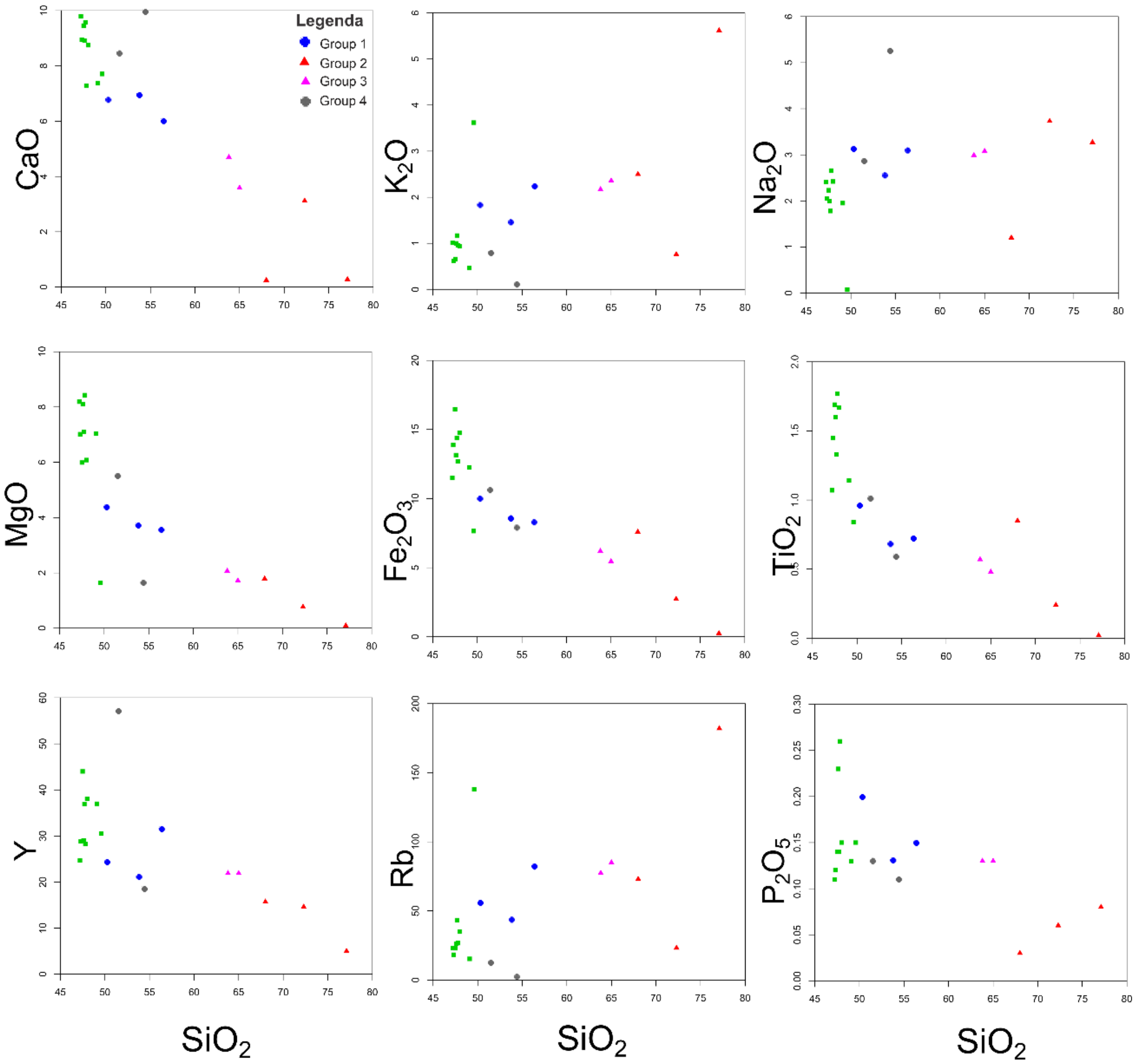

Figura 1 Diagramas de Harker de elementos maiores, expressos em óxidos (%) para as amostras do CMB.

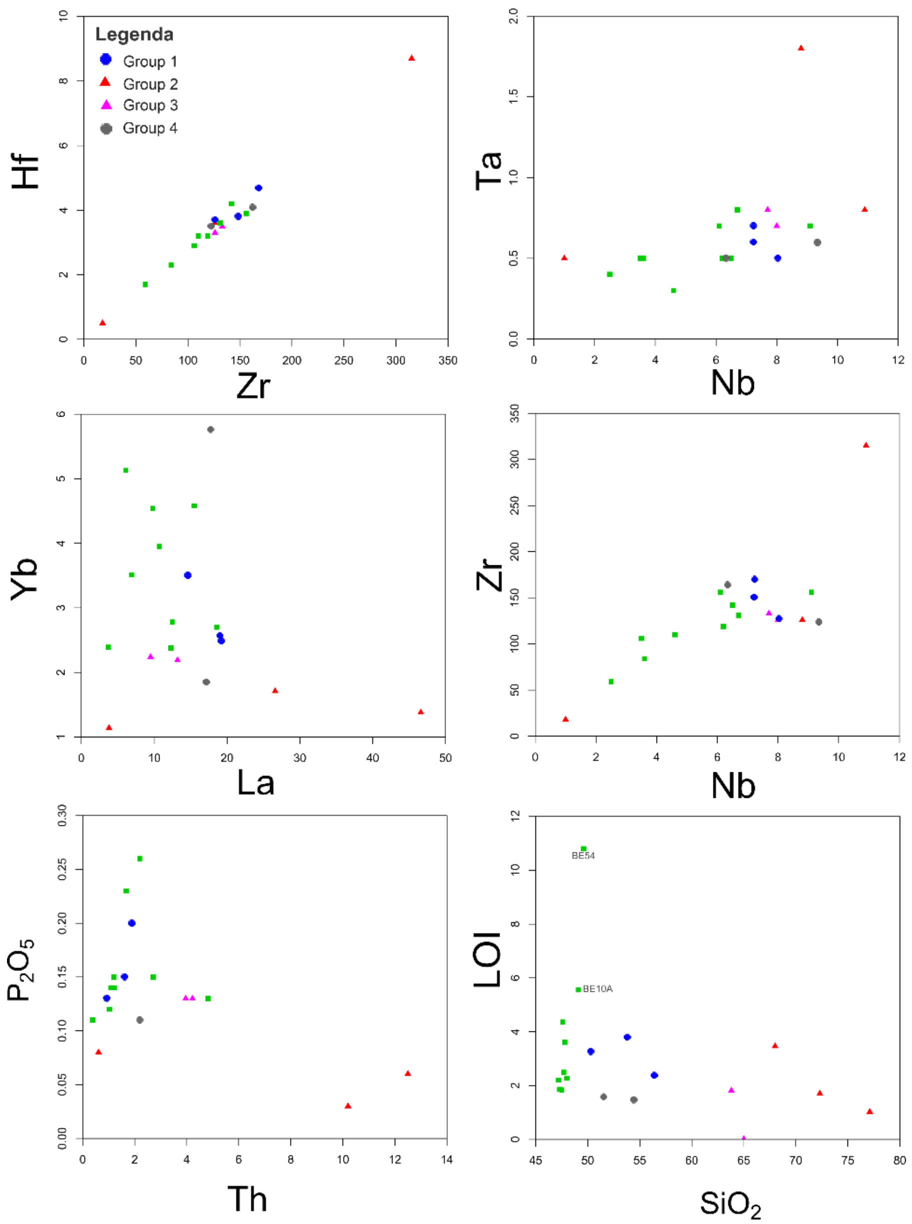

Figura 2 Diagramas binários para elementos traço e LOI por sílica das amostras do CMB.

Os dados geoquímicos sugerem classificação das rochas do grupo 1 como diorito, gabro-diorítico e monzogabro no diagrama de álcalis por sílica (TAS, Middlemost, 1994; Fig. 3A) e no diagrama P-Q (De Bon e Le Fort, 1983; Fig. 3B) as rochas do grupo 1 plotam como quartzo monzodiorito, quartzodiorito e gabro. As rochas do grupo 2 e 3 plotam como granito e granodiorito no diagrama de álcalis por sílica (TAS, Middlemost, 1994) e como granito, granodiorito e tonalito no diagrama P-Q (De Bon e Le Fort, 1983). As rochas do grupo 4 são classificadas como gabro-diorito no diagrama de álcalis por sílica (TAS, Middlemost, 1994) e como quartzo-diorito e gabro no diagrama P-Q (De Bon e Le Fort, 1983).

As amostras dos grupos 1 a 4 plotam no campo de séries cálcio-alcalinas, classificação corroborada pelo diagrama AFM (Figura 3C), de Irvine e Baragar (1971), com exceção do muscovita xisto com granada (BE10Q do grupo 2) e anfibólio gnaisse BE36 (grupo 4). Os grupos 1 e 4 são metaluminosos e os grupos 2 e 3 são peraluminosos quando plotados no diagrama A/NK versus A/CNK, proposto por Maniar e Piccoli (1989), a partir dos índices de Shand (Fig. 3D).

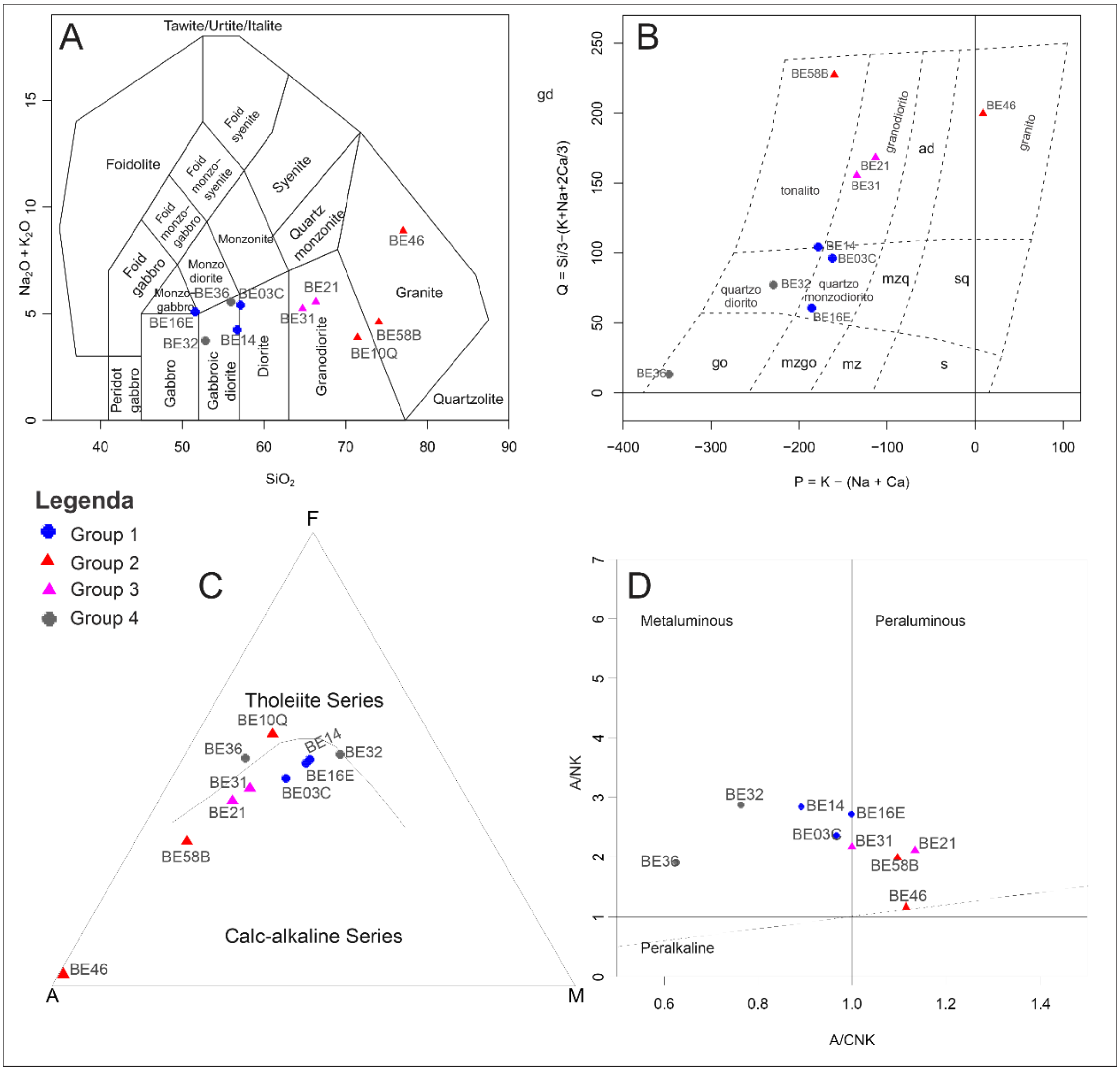

Figura 3 Diagramas classificatórios. A) diagrama de álcalis por sílica (TAS, Middlemost, 1994). B) Diagrama P-Q (De Bon e Le Fort, 1983). C) Diagrama AFM (Irvine e Baragar, 1971). D) Diagrama A/NK versus A/CNK, de Maniar e Piccoli (1989), a partir dos índices de Shand.

As rochas do grupo 5 foram classificadas (Fig. 4A) como basalto e andesito-basáltico pelo diagrama de álcalis versus sílica (TAS) de Le Bas et al. (1986). No diagrama de cátions de Jensen (1976) os anfibolitos plotam como basalto toleítico de alto Fe ou alto Mg (Fig. 4B).

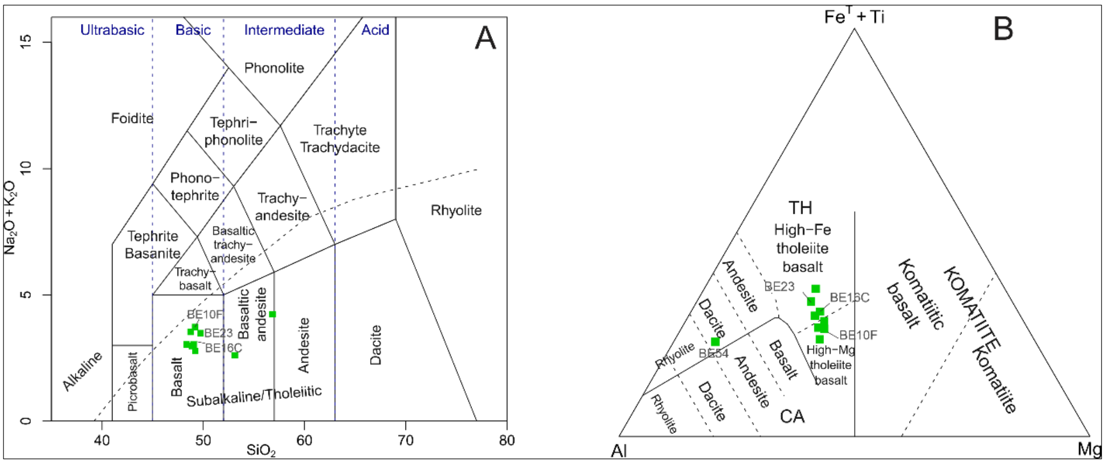

Figura 4 Classificação das rochas do grupo 5, anfibolitos do BMC. A) Diagrama de álcalis versus sílica de Le Bas et al. (TAS, 1986). B) Diagrama de cátions de Jensen (1976), usando concentrações de elementos maiores recalculados para composições 100% livres de voláteis.

Os diagramas discriminantes de ambiente tectônico de Pearce (1984) para Ta versus Yb (Fig. 5A) sugere protólitos gerados em arcos vulcânicos (VAG) e para Nb versus Y sugere protólitos gerados em ambiente sin-colisional (Fig. 5B).

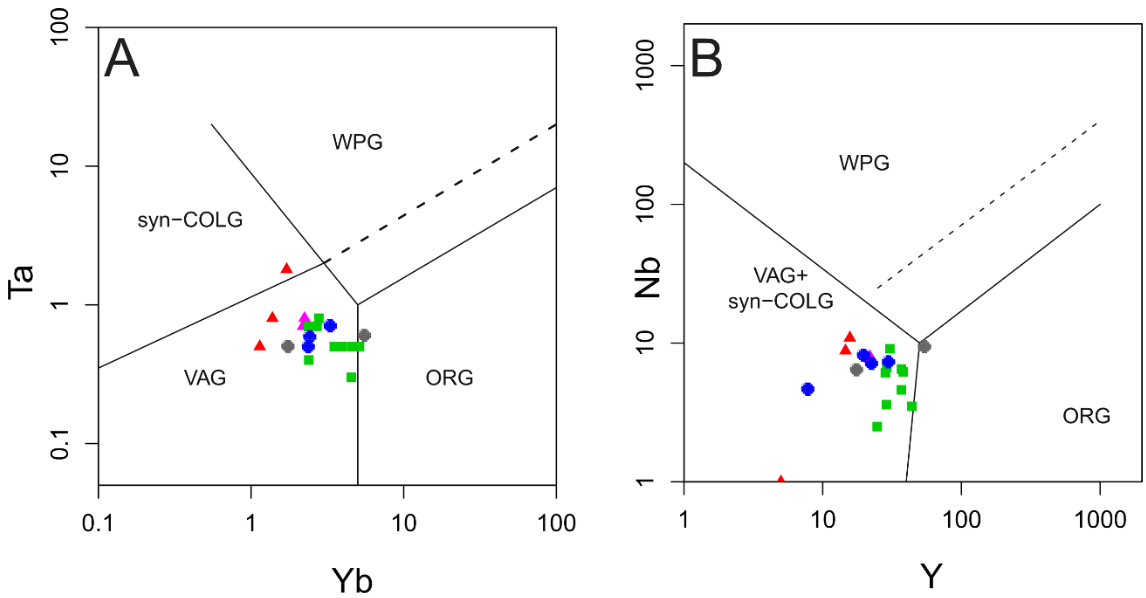

Figura 5 Diagramas discriminantes de ambiente tectônico de geração de granitos utilizando elementos traço em ppm (Pearce et al. (1984) para todas as rochas do BMC já classificas neste capítulo.

Os padrões de distribuição dos ETR para as rochas dos grupos 1 a 4, normalizados pelos valores condríticos de Boyton (1984; Figura 6A), exibem de maneira geral enriquecimento dos ETRL em comparação aos ETRP. O grupo mostra anomalia negativa de Eu e uma amostra com anomalias positivas de Tm, Yb e Lu. Observa-se que 2 amostras do grupo 2 possuem um padrão semelhante com leve anomalia negativa de Eu, mas uma das amostras do grupo 2 apresenta forte empobrecimento dos ETRL e parte dos ETRP, com anomalia positiva de Eu, mantendo-se no padrão do grupo apenas para Tm, Yb e Lu.

O grupo 3 mostra leve anomalia negativa de La, Ce e Pr em relação aos demais grupos, não exibe anomalia de Eu e tem anomalia levemente positiva de Tm, Yb e Lu. O grupo 4 tem uma amostra muito semelhante ao grupo 3 e uma amostra bastante variada e mais evoluída em relação aos ETR leves e pesados, sem anomalia de Eu.

A distribuição de elementos traço, normalizados N-MORB (Sun e McDonough 1989; Figura 6B), aponta enriquecimento de elementos LILE, em relação aos elementos de alto potencial iônico (HFSE). Observa-se nessa figura uma distribuição similar para a maioria das amostras, com anomalia negativa de Nb, positiva de Pb, positiva de Sr, negativa de P, negativa de Ti, à exceção do Rb com anomalia positiva em uma amostra do grupo 2 e K com anomalia negativa em uma amostra do grupo 4.

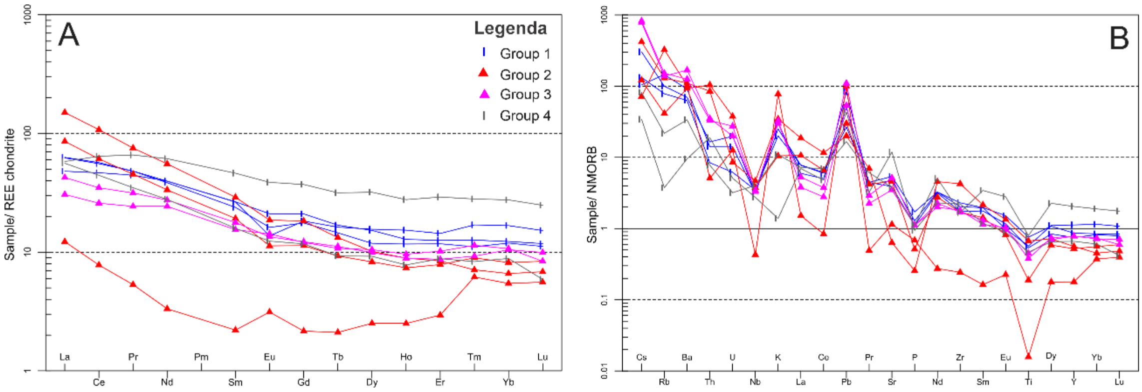

Figura 6 Caracterização geoquímica dos grupos 1 a 4 segundo A) elementos terras raras normalizados pelos valores de condrito de Boyton (1984) e B) elementos traço normalizados pelos valores de N-MORB de Sun e McDonough (1989).

Os padrões de distribuição dos ETR para o grupo 5, normalizados pelos valores de manto primitivo de McDonough e Sun (1995, Figura 7A), exibem enriquecimento dos ETRL em comparação aos ETRP para 6 amostras, sugerindo reciclagem de sedimento no manto profundo, e padrão plano para 3 amostras, indicando fusão parcial do manto. O grupo apresenta anomalia negativa de Eu, exceto por uma amostra que possui anomalia positiva de Eu. De maneira geral os ETRP mostram mais diferenças e os ETRL são homogêneos, exceto por uma amostra com leve anomalia negativa de Tm e Yb.

A distribuição de elementos traço, normalizados pelos valores de manto primitivo de Sun e McDonough (1989, Figura 7B), exibe enriquecimento dos elementos litófilos de íons grandes (LILE) Ce, Rb e Ba, em relação aos demais elementos LILE, com anomalia positiva de Th e U em relação ao grupo. Os elementos de alto potencial iônico (HFSE) estão horizontalizados, com forte anomalia positiva de Pb e uma única amostra apresenta-se fora do padrão, com anomalia negativa acentuada de Sr.

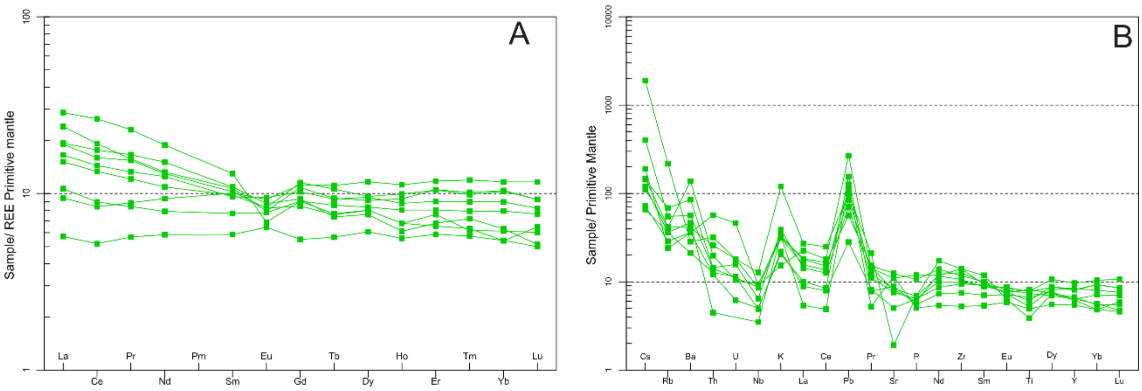

Figura 7 Caracterização geoquímica do grupo 5 segundo A) elementos terras raras normalizados pelos valores de manto primitivo de McDonough e Sun (1995) e B) elementos traço, normalizados pelos valores de manto primitivo de Sun e McDonough (1989).

Os dados de geoquímica apresentados neste capítulo estão em fase de interpretação para serem inseridos como um tópico do artigo apresentado no capítulo 2 da tese, ou então em um terceiro artigo.

Tabela 1 . Sumário dos dados de geoquímica das rochas dos grupos 1 a 5 do Complexo Metamórfico Belén.

	Grupo 1			Grupo 2			Grupo 3		Grupo 4		Grupo 5								
	BE03C	BE14	BE16E	BE46	BE58B	BE10Q	BE21	BE31	BE36	BE32	BE54	BE53	BE23	BE45	BE10A	BE16	BE10J	BE33	BE67
(%)																			
SiO2	56.6	54.0	50.5	77.1	72.3	68.0	65.0	63.8	54.6	51.7	49.6	47.5	48.0	47.3	49.1	47.7	47.6	47.2	47.8
TiO2	0.7	0.7	1.0	0.0	0.2	0.9	0.5	0.6	0.6	1.0	0.8	1.7	1.7	1.5	1.1	1.3	1.6	1.1	1.8
Al2O3	17.8	16.4	19.4	13.4	13.9	12.9	16.1	15.8	16.8	16.0	15.9	12.9	13.6	14.5	12.8	13.8	15.7	15.4	15.2
Fe2O3	8.3	8.6	10.0	0.3	2.7	7.6	5.5	6.2	7.9	10.6	7.7	16.5	14.8	13.9	12.3	14.4	13.2	11.5	12.7
MnO	0.2	0.2	0.2	0.0	0.1	0.1	0.1	0.1	0.1	0.3	0.1	0.3	0.2	0.3	0.2	0.3	0.2	0.2	0.2
MgO	3.5	3.7	4.4	0.1	0.8	1.8	1.7	2.1	1.7	5.5	1.6	6.0	6.1	7.0	7.0	7.1	8.1	8.2	8.4
CaO	6.0	7.0	6.8	0.3	3.1	0.3	3.6	4.7	10.0	8.5	7.7	9.5	8.8	9.0	7.4	9.6	8.9	9.8	7.3
Na2O	3.1	2.5	3.1	3.3	3.7	1.2	3.1	3.0	5.3	2.9	0.1	2.2	2.4	2.1	2.0	1.8	2.0	2.4	2.7
K2O	2.2	1.5	1.8	5.6	0.8	2.5	2.4	2.2	0.1	0.8	3.6	0.7	0.9	0.6	0.5	1.2	1.0	1.0	1.0
P2O5	0.2	0.1	0.2	0.1	0.1	0.0	0.1	0.1	0.1	0.1	0.2	0.1	0.2	0.1	0.1	0.1	0.2	0.1	0.3
LOI	2.4	3.8	3.3	1.0	1.7	3.5	0.0	1.8	1.5	1.6	10.8	1.8	2.3	1.9	5.6	2.5	4.4	2.2	3.6
Total	101.0	98.5	100.6	101.2	99.4	98.7	98.1	100.5	98.7	99.0	98.1	99.1	98.9	98.1	98.1	99.8	102.0	99.1	100.9
(ppm)																			
La	14.9	19.5	19.3	3.8	26.6	46.6	9.5	13.2	17.4	18.0	18.6	6.1	10.7	6.9	15.5	9.8	12.5	3.7	12.3
Ce	37.7	46.0	45.0	6.3	49.4	87.0	20.9	28.2	35.9	52.0	44.3	14.1	24.1	15.0	32.1	22.3	29.5	8.7	26.7
Pr	5.4	5.9	5.9	0.7	5.5	9.2	3.0	3.9	4.3	8.0	5.8	2.3	3.4	2.1	4.0	3.1	4.2	1.4	3.9
Nd	23.8	23.1	23.8	2.0	20.1	33.3	14.6	16.5	16.7	36.8	23.5	11.7	15.6	9.9	16.5	13.6	18.8	7.3	16.2
Sm	5.2	4.7	5.2	0.4	3.8	5.7	3.0	3.5	3.1	9.0	5.3	4.1	3.9	3.1	4.4	4.0	4.4	2.4	4.2
Eu	1.0	1.2	1.6	0.2	0.8	1.4	1.1	1.0	0.9	2.9	1.1	1.4	1.5	1.2	1.2	1.3	1.4	1.0	1.3
Gd	4.7	4.6	5.4	0.6	2.9	4.7	3.1	3.2	3.0	9.6	4.9	6.1	5.6	4.9	5.9	6.3	5.1	3.0	4.6
Tb	0.8	0.7	0.8	0.1	0.4	0.6	0.5	0.5	0.4	1.5	0.8	1.1	0.9	0.9	0.9	1.1	0.7	0.6	0.8
Dy	5.0	3.8	4.9	0.8	2.7	3.3	3.4	3.2	3.0	10.3	5.4	7.9	6.4	5.6	6.2	6.5	5.1	4.1	5.4
Ho	1.1	0.8	0.9	0.2	0.5	0.6	0.7	0.6	0.6	2.0	1.0	1.7	1.3	1.2	1.4	1.5	0.9	0.8	1.0
Er	3.0	2.5	2.6	0.6	1.7	1.8	2.1	1.8	1.9	6.1	3.3	5.1	4.0	3.5	4.6	4.6	3.0	2.6	2.9
Tm	0.6	0.4	0.4	0.2	0.3	0.2	0.4	0.3	0.3	0.9	0.4	0.8	0.6	0.5	0.7	0.7	0.5	0.4	0.4

Yb	3.5	2.5	2.6	1.1	1.7	1.4	2.2	2.2	1.9	5.8	2.7	5.1	4.0	3.5	4.6	4.5	2.8	2.4	2.4
Lu	0.5	0.4	0.4	0.2	0.3	0.2	0.3	0.3	0.2	0.8	0.4	0.8	0.6	0.5	0.6	0.6	0.4	0.3	0.4
Sr	425.0	351.0	485.0	103.0	416.0	57.2	315.0	465.0	1070.0	341.0	40.4	106.5	175.5	188.5	169.5	160.0	263.0	244.0	231.0
Ba	574.0	397.0	439.0	644.0	587.0	696.0	790.0	1060.0	60.1	212.0	199.0	148.0	394.0	252.0	251.0	596.0	964.0	325.0	287.0
Cs	0.7	0.9	2.1	0.5	0.9	2.9	5.8	5.5	0.2	0.6	15.0	0.5	3.2	0.6	1.5	1.1	0.9	1.0	1.2
Rb	81.4	43.8	55.9	182.0	23.2	73.0	85.0	77.4	2.1	12.2	138.0	22.9	34.9	18.3	15.3	43.4	26.3	23.0	26.7
U	0.7	0.3	0.9	0.6	1.8	0.4	1.3	0.9	0.2	0.2	0.4	0.2	0.0	0.1	1.0	0.3	0.2	0.0	0.4
Th	1.7	1.0	2.0	0.6	12.5	10.2	4.0	4.2	2.3	0.9	2.7	1.1	1.2	1.0	4.8	1.2	1.7	0.4	2.2
Hf	3.8	3.7	4.7	0.5	3.6	8.7	3.5	3.3	4.1	3.5	3.9	2.9	3.2	2.3	4.2	3.2	3.6	1.7	3.9
Nb	7.3	8.1	7.3	1.0	8.8	10.9	7.7	8.0	6.4	9.4	9.1	3.5	6.2	3.6	6.5	4.6	6.7	2.5	6.1
Ta	0.7	0.5	0.6	0.5	1.8	0.8	0.8	0.7	0.5	0.6	0.7	0.5	0.5	0.5	0.5	0.3	0.8	0.4	0.7
Ni	8.0	39.0	20.0	2.0	1.0	47.0	1.0	1.0	3.0	40.0	10.0	50.0	59.0	110.0	90.0	66.0	92.0	123.0	113.0
Co	49.0	47.0	59.0	57.0	116.0	85.0	61.0	112.0	36.0	65.0	52.0	62.0	62.0	75.0	61.0	64.0	70.0	57.0	87.0
Zr	150.0	128.0	170.0	18.0	126.0	315.0	133.0	126.0	164.0	124.0	156.0	106.0	119.0	84.0	142.0	110.0	131.0	59.0	156.0
V	214.0	194.0	228.0	6.0	29.0	120.0	94.0	124.0	178.0	283.0	204.0	479.0	459.0	376.0	298.0	402.0	346.0	313.0	297.0
Y	31.5	21.0	24.2	5.0	14.6	15.7	21.9	21.9	18.5	57.2	30.5	44.0	38.1	28.8	37.0	36.9	29.0	24.7	28.3
Ga	21.0	17.9	22.0	9.8	13.9	18.8	16.5	16.0	23.6	18.4	19.0	18.9	19.6	19.6	18.0	19.9	20.2	15.8	19.2
Sn	2.0	2.0	1.0	1.0	3.0	4.0	2.0	2.0	1.0	2.0	1.0	2.0	2.0	1.0	2.0	2.0	1.0	1.0	1.0
W	210.0	208.0	373.0	468.0	777.0	711.0	426.0	536.0	207.0	313.0	154.0	142.0	136.0	163.0	172.0	137.0	213.0	94.0	110.0
Cu	37.0	75.0	37.0	13.0	11.0	61.0	11.0	21.0	25.0	84.0	59.0	260.0	135.0	474.0	92.0	178.0	61.0	104.0	75.0
Zn	99.0	92.0	130.0	6.0	16.0	114.0	204.0	64.0	30.0	98.0	72.0	132.0	136.0	167.0	130.0	152.0	122.0	85.0	108.0
Cr	30.0	70.0	50.0	20.0	20.0	110.0	20.0	20.0	30.0	170.0	40.0	130.0	130.0	160.0	130.0	110.0	250.0	300.0	280.0
As	14.0	5.9	4.6	5.0	*	2.4	*	5.0	13.0	*	0.0	0.0	0.0	8.0	3.8	3.4	0.0	0.0	0.0
Li	20.0	20.0	20.0	10.0	20.0	20.0	10.0	30.0	10.0	10.0	30.0	10.0	20.0	20.0	30.0	10.0	10.0	10.0	30.0
Pb	25.0	8.0	15.0	30.0	9.0	6.0	16.0	33.0	13.0	5.0	7.0	2.0	8.0	11.0	19.0	5.0	4.0	9.0	6.0
Sc	22.0	23.0	26.0	2.0	5.0	14.0	14.0	15.0	16.0	50.0	24.0	55.0	49.0	44.0	39.0	51.0	33.0	41.0	33.0
(La/Yb)N	3.1	5.6	5.4	2.4	11.2	24.2	3.0	4.3	6.7	2.2	4.9	0.9	1.9	1.4	2.4	1.5	0.6	0.2	0.7
Eu/Eu*	0.6	0.8	0.9	1.4	0.8	0.8	1.0	0.9	0.9	0.9	0.6	0.9	1.0	0.9	0.7	0.8	1.0	1.3	1.0

5 CAPÍTULO 5 – CONSIDERAÇÕES FINAIS

A tese apresenta novos dados geocronológicos e isotópicos para dois importantes representantes de orogenias estabelecidos atualmente nos Andes Centrais. O Complexo Metamórfico Cerro Uyarani apresentado no Capítulo 2 e o Complexo Metamórfico Belén apresentado no Capítulo3.

As idades U-Pb e isótopos de Hf em núcleos e bordas de zircão bem diferenciados neste trabalho contribuíram para o entendimento da evolução tectônica do Complexo Metamórfico Cerro Uyarani. Os dados de Hf sugerem a associação do CMCU com o terreno Arequipa, mas a correlação com o Cráton Amazônico e terreno Rio Apa não pôde ser totalmente descartada. Novos dados de Hf e outros métodos isotópicos podem fortalecer as sugestões feitas no artigo apresentado no capítulo 2. A continuidade na pesquisa dessa região é necessária para o entendimento dos embasamentos paleoproterozoicos situados hoje na América do Sul. Uma das questões que ainda permanece em aberto é a origem paleoproterozoica do CMCU, que já foi correlacionado por outros autores com o Cráton Amazônico e Laurentia, mas que também apresenta similaridades, em relação a isótopos de Lu-Hf e idade, com o Kalahari.

Pudemos, neste trabalho, definir uma faixa de idades de formação dos protólitos do Complexo Metamórfico Belén e estabelecer uma provável fase de pico magmático. Os poucos dados de Hf obtidos até o momento apontam para processos de geração com forte contribuição crustal, o que não é comum a todos os setores conhecidos do magmatismo Famatiniano, e deve ser mais bem compreendido. Os dados de Hf para outros litotipos do CMB podem contribuir para a história evolutiva do magmatismo Famatiniano nesta região e como um todo. A relação entre as rochas ordovicianas do complexo, as rochas metassedimentares pré-cambrianas e as rochas ultra-máficas expostas na área ainda não é clara.

Nossos dados possibilitam a correlação das duas áreas estudas nesta tese. O magmatismo Famatiniano retrabalha rochas provavelmente do embasamento paleoproterozoico do terreno Arequipa, que é o embasamento que o Complexo Metamórfico Cerro Uyarani é associado. Porém, os zircões herdados obtidos em duas das amostras do CMB datam de 1.97-1.95 Ga, essas idades são mais antigas que as idades obtidas no CMCU, ainda assim são idades encontradas no terreno Arequipa do Peru.

Recomendações futuras para o Complexo Metamórfico Cerro Uyarani:

1- Reconhecimento em campo dos setores não mapeados do Domínio Cristalino Indiferenciado (DCU).

2- Novos dados de Hf nos Domínios do CMCU como um todo, devido a pouca quantidade de dados obtidos até então, e expandindo os dados para as fácies ainda não analisadas.

3- Emprego de dados geoquímicos para um melhor entendimento dos ambientes geradores, provavelmente dos migmatitos gerados no ciclo 2 do segundo evento identificado neste trabalho, contribuindo assim para o melhor entendimento da evolução tectônica do CMCU.

4- Conciliar a interpretação de diversos dados isotópicos como Sm-Nd, Sr-Sr e Pb-Pb podem auxiliar no entendimento da origem paleoproterozoica do CMCU, possibilitando comparações com Laurentia e Kalahari, por exemplo, que são potenciais paleocontinentes já associados ao Arequipa por diversos autores e neste trabalho por meio de isótopos de Hf.

Recomendações futuras para o Complexo Metamórfico Belém:

1- É essencial que haja novas campanhas de campo. Pudemos identificar nas imagens de satélite, com a ajuda do mapeamento realizado neste trabalho, feições características de exposições do CMB. Estes potenciais stocks ainda não foram reconhecidos em outros trabalhos publicados.

2- Novos dados isotópicos como Hf e Li que contemplem as diversas litologias reconhecidas neste trabalho podem auxiliar no entendimento do magmatismo do CMB, buscando testar qual das hipóteses sugeridas no artigo do capítulo 3 se adequam melhor aos processos de geração do magmatismo Famatiniano no BMC.

3- A utilização dos dados de geoquímica, principalmente dos elementos terras raras e traços. Os padrões de elementos terras raras e traços, apresentados no Capítulo 4, diferenciam os grupos de rochas do CMB de maneira ligeiramente diferente dos grupos identificados por petrografia. A geoquímica também será importante para o entendimento da contribuição crustal mostrada pelos isótopos de Hf.

6 REFERÊNCIAS

Albarède, F., Telouk, P., Blichert-Toft, J., Boyet, M., Agranier, A., Nelson, B., 2004. Precise and accurate isotopic measurements using multiple collector ICPMS. Geochem. Cosmochim. Acta 68.

Bahlburg H, Carlotto V, Cardenas J., 2006. Evidence of Early to Middle Ordovician arc volcanism in the Cordillera Oriental and Altiplano of southern Peru, Ollantaytambo formation and Umachiri beds. J. S. Ame. Ear. Sci. 22, 52–65.

Berthelsen, A., Marker, M., 1986. Tectonics of the Kola collision suture and adjacent Archean and Early Proterozoic terrains in the northeastern region of the Baltic Shield. Tec. 126, 31-55.

Bertotti, A.L., 2012. Lu-Hf em zircão por LA-MC-ICP-MS, Porto Alegre, PhD Thesis, 162pp. Universidade Federal do Rio Grande do Sul, Porto Alegre.

Bertotti, A.L., Chemale Jr., F., Kawashita, K., 2013. Lu-Hf em Zircão por LA-ICP-MS: aplicação em Gabro do Ofiolito de Aburrá. Colômbia. Pesqui. Geoc. 40 (2), 117–127.

Bispos-Santos, F., D'Agrella-Filho, M., Janikian, L., Reis, N.J., Trindade, R.I.F., Reis, M.A.A.A., 2013. Towards Columbia: paleomagnetism of 1980-1960 Ma Surumu volcanic rocks, Northern Amazonia. Prec. Res. 244, 123-138.

Blichert-Toft, J., Albarède, F., 1997. The Lu–Hf isotope geochemistry of chondrites and the evolution of the mantle–crust system. Earth Planet Sci. Lett. 148, 243–258.

Boynton, W.V. 1984. Chapter 3 - Cosmochemistry of the Rare Earth Elements: Meteorite Studies, Editor(s): P. Henderson, Developments in Geochemistry, Elsevier, 2, 63-114.

Buchan, K.L., Ernst, R.E., Hamilton, M.A., Mertanen, S., Pesonen, L.J., Elming, S.A., 2001. Rodinia: the evidence from integrated paleomagnetism and U-Pb geochronology. Prec. Res. 110, 9-32.

Bühn, B.M., Pimentel, M.M., Matteini, M., Dantas, E.L., 2009. High spatial resolution analyses of Pb and U isotopes for geochronology by laser ablation multi-collector inductively coupled plasma mass spectrometry (LA-MC-ICP-MS). Ann. Acad. Bras. Ciencias 81, 1–16.

Burrett, C., Berry, R., 2000. Proterozoic Australia-Western United States (AUSWUS) fit between Laurentia and Australia. Geo. 28, 103-106.

Casquet, C., Fanning, C.M., Galindo, C., Pankhurst, R.J., Rapela, C., Torres, P., 2010. The Arequipa Massif of Peru: new SHRIMP and isotope constraints on a Paleoproterozoic inlier in the Grenvillian orogen. J. S. Ame. Ear. Sci. 29 (1), 128–142.

Cawood, P.A., Nemchin, A.A., Strachan, R., Prave, T., Krabbendam, M., 2007. Sedimentary basin and detrital zircon record along East Laurentia and Baltica during assembly and break up of Rodinia. J. Geo. Soc. Lon. 164, 257-275.

Chauvel, C., Blichert-Toft, J., 2001. A hafnium isotope and trace element perspective on melting of the depleted mantle. Earth Planet Sci. Lett. 190 (3–4), 137–151.

Chu, N.C., Taylor, R.N., Chavagnac, V., Nesbitt, R.W., Boella, R.M., Milton, J.A., German, C.R., Bayon, G., Burton, K., 2002. Hf isotope ratio analysis using multi- collector inductively coupled plasma mass spectrometry: an evaluation of isobaric interference corrections. J. Anal. At. Spectr. 17, 1567–1574.

Cobbing, E.J., Ozard, J.M., Snelling, N.J., 1977. Reconnaissance geochronoiogy of the crystalline basement rocks of the Coastal Cordillera of southern Peru. Geo. Soc. Ame. Bul. 88, 241-246.

Dalmayrac, B., Lancelot, J.R., Leyreloup, A., 1977. Two-Billion-Year Granulites in the Late Precambrian Metamorphic Basement Along the Southern Peruvian. Coa. Sci. 198, 49-51.

Dalziel, I.W.D., Forsythe, R.S., 1985. Andean evolution and the terrane concept. Ear. Sci. Ser., Circum-Pacific Council for Energy and Mineral Resources 1, 565-581.

Debon, F., & Le Fort, P. 1983. A chemical–mineralogical classification of common plutonic rocks and associations. Transactions of the Royal Society of Edinburgh: Earth Sciences, 73(3), 135-149.

Dopico C.I.M, Antonio P.Y.J., Rapalini A.E., López de Luchi M.G., Vidal C.G., 2021. Reconciling Patagonia with Gondwana in early Paleozoic? Paleomagnetism of the Valcheta granites, NE North Patagonian Massif, J. S. Ame. Ear. Sci. 106, 1-17.

Ducea M.N., Bergantz G.W., Crowley J.L., Otamendi J., 2017. Ultrafast magmatic buildup and diversification to produce continental crust during subduction. Geo. 45 (3), 235–238.

Ernst, R.E., Srivastava, R.K., 2008. India’s place in the Proterozoic world: constraints
from the Large Igneous Province (LIP) record. Ind. Dyk. 41–56.

Ernst, R.E., Wingate, M.T.D., Buchan, K.L., Li, Z.X., 2008. Global record of 1600-700 Ma Large Igneous Provinces (LIPs): Implications for the reconstruction of the proposed Nuna (Columbia) and Rodinia supercontinents. Prec. Res. 160, 159-178.

Ernst, R.E., Srivastava, R.K., Bleeker, W., Hamilton, M., 2010. Precambrian Large Igneous Provinces (LIPs) and their dyke swarms: new insights from high-precision geochronology integrated with paleomagnetism and geochemistry. Prec. Res. 183, vii-vxi.

Ernst, R.E., Bleeker,W., Soderlund, U., Kerr, A.C., 2013. Large Igneous Provinces and supercontinents: toward completing the plate tectonic revolution. Lit. 174, 1-14.

Franz G, Lucassen F, Kramer W, Trumbull RB, Romer RL, Wilke H-G, Viramonte JG, Becchio R, Siebel W., 2006. Crustal evolution at the Central Andean continental margin: a geochemical record of crustal growth, recycling and destruction. Fro. Ear. Sci. 1, 45–64

García, M., Gardeweg, M., Clavero, J., & Hérail, G., 2004. Hoja Arica, Región de Tarapacá. Servicio Nacional de Geología y Minería, Carta Geológica de Chile, Ser. Geo. Bás. Issue 84).

Gerdes, A., Zeh, A., 2006. Combined U–Pb and Hf isotope LA-(MC-) ICP-MS analyses of detrital zircons: comparison with SHRIMP and new constraints for the provenance and age of an Armorican metasediment in Central Germany. Earth Planet Sci. Lett. 249, 47–61.

Gerdes, A., Zeh, A., 2009. Zircon formation versus zircon alteration – new insights from combined U–Pb and Lu–Hf in situ LA-ICP-MS analyses, and consequences for the interpretation of Archean zircon from the Central Zone of the Limpopo Belt. Chem. Geol. 261, 230–243.

Hartz, E.H., Torsvik, T.H., 2002. Baltica upside down: a new plate tectonic model for Rodinia and the Iapetus Ocean. Geo. 30, 255-258.

Hoffman, P.F., 1991. Did the breakout of Laurentia turn Gondwanaland inside-out ?. Sci. 252, 1409-1412.

Jensen, L.S., 1976. A New Cation Plot for Classifying Sub-alkaline Volcanic Rocks. Ontario Division Mines Miscellaneous Paper, 66, 21.

Johansson, Å., 2009. Baltica, Amazonia and the SAMBA connection-1000 million years of neighbourhood during the Proterozoic?. Prec. Res. 175 (1), 221-234.

Johansson, Å., 2014. From Rodinia to Gondwana with the 'SAMBA' model—A distant view from Baltica towards Amazonia and beyond. Prec. Res. 244, 226-235.

Johansson Å., Bingen B., Huhma H., Waight T., Vestergaard R., Soesoo A., Skridlaite G., Krzeminska E., Shumlyanskyy L., Holland M. E., Holm-Denoma C., Teixeira W., Faleiros F.M., Ribeiro B.V., Jacobs J., Wang C., Thomas R.J., Macey P.H., Kirkland C.L., Hartnady M.I.H., Eglington B.M., Puetz S.J., Condie K.C., 2022. A geochronological review of magmatism along the external margin of Columbia and in the Grenville-age orogens forming the core of Rodinia. Prec. Res. 371, 106463.

Kuznetsov, N.M., Meert, J.G., Romanyuk, T., 2014. Ages of detrital zircons (U/Pb, LAICP- MS) from the latest Neoproterozoic-Middle Cambrian (?) Asha Group, the south-western Urals: a test of an Australia-Baltica connection within Rodinia. Prec. Res. 244, 288-305.

Le Bas, M.J., Le Maitre, R.W., Streckeisen, A., Zanettin, B., 1986. A chemical classification of volcanic rocks based on the total alkali-silica diagram. Journal of Petrology, 27, 745-750.

Loewy, S.L., Connelly, J.N., Dalziel, I.W.D., 2004. An orphaned basement block: The Arequipa-Antofalla Basement of the central Andean margin of South America. Geo. Soc. Ame. Bul. 116, 171-187.

Ludwig, K.R., Isoplot 3.75, 2012. A Geochronological Toolkit for Microsoft Excel, vol. 5. Berkeley Geochronology Center Spec. Publ., pp. 1–75.

Maniar, P.D, Piccoli, P;M. 1989. Tectonic discrimination of granitoids. GSA Bulletin, 101 (5): 635–643.

McDonough, W.F., Sun, S.S 1995. The composition of the Earth, Chemical Geology, 120, Issues 3–4, 223-253.

Meert J.G., 2001. Growing Gondwana and Rethinking Rodinia: A Paleomagnetic Perspective. Gon. Res. 4 (Issue 3), 279-288.

Meert, J.G., Torsvik, T.H., 2003. The making and unmaking of a supercontinent: Rodinia Revisited. Tec. 375, 261-288.

Middlemost E.A.K. 1994. Naming materials in the magma/igneous rocks system. Earth Sci Rev, 37, 215–224.

Mpodozis C, Ramos VA., 1990. The Andes of Chile and Argentina. In Geology of the Andes and its Relation to Hydrocarbon and Mineral Resources. Circum pacific Council for Energy and Mineral Resources. Ear. Sci. Ser. 11, 59–90.

Nebel, O., Nebel-Jacobsen, Y., Mezger, K., Berndt, J., 2007. Initial Hf isotope compositions in magmatic zircon from early Proterozoic rocks from the Gawler Craton, Australia: a test for zircon model ages. Chem. Geol. 241 (1–2), 23–37.

Oliveira, F.V., 2015. Chronus: Um novo suplemento para a redução de dados U-Pb obtidos por LA-MC-ICPMS. M.Sc. Diss. Inst. Geociencias, Universidade de Brasília, Brasilia, Brazil, p. 19559.

Oliveira J.R., Hauser N., Reimold W.U., Ruiz A.S. , Matos R., Werlang T., 2022. The Cerro Uyarani Metamorphic Complex on the Bolivian Altiplano: New constraints on the tectonic evolution of the Central Andean basement between ∼1.8 and 1.0 Ga, J. S. Ame. Ear. Sci. 116, 103843.

Pankhurst, R.J., Hervé, F., Fanning, M.C., Calderon, M., Niemeyer, H., Griem-Klee, S., Soto, F., 2016. The pre-Mesozoic rocks of northern Chile: U-Pb ages, and Hf and O isotopes. Ear. Sci. Rev. 152, 88–105.

Patchett, P.J., 1983. Importance of the Lu–Hf isotopic system in studies of planetary chronology and chemical evolution. Geochem. Cosmochim. Acta 47, 81–91.

Pearce, J.A., Harris N.B.W., Tindle, A.G. 1984. Trace Element Discrimination Diagrams for the Tectonic Interpretation of Granitic Rocks, Journal of Petrology, 25, Issue 4, 956–983.

Priem, H.N.A., Kroonenberg, S.B., Boelrijk, N.A.I.M., and Hebeda, E.H., 1989. Rb-Sr and K-Ar evidence for the presence of a 1.6 Ga basement underlying the 1.2 Ga Garzón-Santa Marta granulite belt in the Colombian Andes. Prec. Res. 42, 315–324.

Rainbird, R.H., Stern, R.A., Khudoley, A.K., Kropachev, A.P., Heaman, L.M., Sukhorukov, V.I., 1998. U-Pb geochronology of Riphean sandstone and gabbro from southeast Siberia and its bearing on the Laurentia-Siberia connection. Earth and Planetary Science Letters 164, 409-420.

Ramos VA. 1988. The tectonics of the Central Andes: 308 to 338 S latitude. Geo. Soc. Ame., GSA, Boulder. Special Paper 218, 31–54.

Ramos VA. 2008. The basement of the Central Andes: the Arequipa and related terranes. Annual Review on Ear. Plan. Sci. 36, 289–324.

Ramos VA. 2009. Anatomy and global context of the Andes: main geologic features and the Andean orogenic cycle. Geo. Soc. Ame. Memoir, GSA, Boulder 404, 31–65.

Ramos V.A., 2010. The Grenville-Age Basement of the Andes. J. S. Ame. Ear. Sci. 29, 77-91.

Rapela, C. W., Pankhurst, R. J., Casquet, C., Dahlquist, J. A., Fanning, C. M., Baldo, E. G., Galindo, C., Alasino, P. H., Ramacciotti, C. D., Verdecchia, S. O., Murra, J. A., & Basei, M. A. S., 2018. A review of the Famatinian Ordovician magmatism in southern South America: evidence of lithosphere reworking and continental subduction in the early proto-Andean margin of Gondwana. Ear. Sci. Ver. 187, 259–285.

Salminen, J., Mertanen, S., Evans, D.A.D., Wang, Z., 2013. Paleomagnetic and geochemical studies on the Sakunta dyke swarms, Finland, with implications for a northern Europe-North American (NENA) connection within the Nuna supercontinent. Prec. Res. 244, 170-191.

Scherer, E., Münker, C., Mezger, K., 2006. Calibration of the lutetium–hafnium clock. Science 293, 683–687.

Sempéré T., 1995. Phanerozoic evolution of Bolivia. In Petroleum Basins of South America. Am. Ass.. Pet. Geo. Mem. 62, 207–30.

Shackleton, R. M., Ries, A. C., Coward, M. P., Cobbold, P., 1979. Structure metamorphism and geochronology of the Arequipa Massif of coastal Peru. J. Geo. Soc. Lon. 136, 195-241.

Tosdal, R.M. 1996. The Amazon–Laurentian connection as viewed from Middle Proterozoic rocks in the central Andes, western Bolivia and northern Chile. Tec. 15, 827-842.

Sun, S.S., McDonough, W.F., 1989. Chemical and isotopic systematics of oceanic basalts: implications for mantle composition and processes, magmatism in the Ocean Basins. In: Geological Society of London, Special Publications, 42, 313-345.

Taylor, S.R., McLennan, S.M., 1985. The Continental Crust: its Composition and Evolution. Blackwell, Oxford, p. 312pp.

Turner, C.C., Meert, J.G., Pandit, M.K., Kamenov, G.D., 2014. A detrital zircon U-Pb and Hf isotopic transect across the Son Valley sector of the Vindhyan basin, India: Implications for basin evolution and paleogeography. Gon. Res. 26 (Issue 1) 348-364.

Wasteneys, A.H., Clark, A.H., Farrar, E., Langridge, R.J., 1995. Grenvillian granulite-facies metamorphism in the Arequipa Massif, Peru: a Laurentia-Gondwana link. Ear. Pla. Sci. Let. 132, 63–73.

Wedepohl, K.H., 1995. The composition of the continental crust. Geochem. Cosmochim. Acta 59 (7), 1217–1232.

Wiedenbeck, M., Allé, P., Corfu, F., Griffin, W.L., Meier, M., Oberli, F., Von Quadt, A., Roddick, J.C., Spiegel, W., 1995. Three natural zircon standards for U–Th–Pb, Lu–Hf, trace element and REE analyses. Geostand. Newsl. 19, 1–23.

Wilde, S.A., Zhao, G., Sun, M., 2002. Development of the North China Craton during the late Archean and its final amalgamation at 1.8 Ga: Some speculations on its position within a global Paleoproterozoic supercontinent. Gon. Res. 5, 85-94.

Wingate, M.T.D., Pisarevsky, S.A., Evans, D.A.D., 2002. Rodinia connections between Australia and Laurentia: no SWEAT, no AUSWUS?, Ter. Nov. 14, 121-128.

Wörner, G., Lezaun, J., Beck, A., Heber, V., Lucassen, F., Zinngrebe, E., Rössling, R., Wilke, H.G., 2000. Precambrian and Early Paleozoic evolution of the Andean basement at Belen (northern Chile) and Cerro Uyarani (western Bolivia Altiplano). J. S. Ame. Ear. Sci. 13, 717–737.

Wu, L., Dong, J., Haibin, L., Fei, D., Li, Y., 2010. Provenance of detrital zircons from the late Neoproterozoic to Ordovician sandstones of South China: implications for continental affinity. Geo. Mag. 147, 974-980.

Zhao, G., Cawood, P.A., Wilde, S.A., Sun, M., 2002. Review of global 2.1–1.8 Ga orogens: implications for a pre-Rodinia supercontinent. Ear. Sci. Rev. 59, 125-162.